Institut für Bio- und Geowissenschaften: Agrosphäre (IBG-3)
Forschungszentrum Jülich

In Silico Evaluation of the Water and Carbon Flows in the Soil-Rhizosphere-Plant Continuum

Dissertation

zur Erlangung des Grades

Doktor der Ingenieurwissenschaften (Dr.-Ing.)

der Agrar-, Ernährungs- und Ingenieurwissenschaftlichen Fakultät

der Rheinischen Friedrich-Wilhelms-Universität Bonn

von

Mona Giraud

aus

Saint-Martin-d'Hères, Frankreich

Bonn 2026

Referent:
Prof. Dr. Andrea Schnepf, Rheinische Friedrich-Wilhelms-Universität Bonn, Deutschland

1. Korreferent:
Prof. Dr. Guillaume Lobet, Université catholique de Louvain, Belgien

2. Korreferent:
Prof. Dr. Christine Beveridge, University of Queensland, Australien

3. Korreferent:
Prof. Dr. Holger Pagel, Rheinische Friedrich-Wilhelms-Universität Bonn, Deutschland

Tag der mündlichen Prüfung: 30.01.2026

Angefertigt mit Genehmigung der Agrar-, Ernährungs- und Ingenieurwissenschaftlichen Fakultät der Universität Bonn

Abstract

Background and Motivation: Water and carbon are fundamental to both plant development and the soil ecosystem. Water supports essential physiological processes of plants and soil microbes, while carbon plays a dual role: it acts as an energy source and biomass building block, but when released into the atmosphere, it contributes to the greenhouse effect. Changes in water and carbon balances both impact and are impacted by the processes of soil microbial communities and plants, creating complex feedback loops. Climate change is disrupting these cycles, leading to extreme weather events like droughts and floods that complicate agricultural resource management. This creates an urgent need to develop optimal genotype-environment-management (GxExM) strategies to enhance crop resilience. Setting up multi-scale, multi-domains, multi-physics models can yield new and relevant insights into the interrelated processes driving the resilience of environments to new climates and sustainable agricultural practices. Functional Structural Plant Models (FSPMs) can be an important part of such frameworks by simulating how structure and function interact at the scale of individual plants and their surrounding local environment.

Material and Methods: To better represent the water and carbon balance in the soil-rhizosphere-plant continuum, the existing CPlantBox model was extended by adding or adapting several modules related to water and carbon flow from roots to leaves while at the same time adjusting and improving the numerical schemes. As a first implementation, the plant model was embedded into an updated multiscale soil-rhizosphere model. In a parallel implementation, the plant model was linked to an auxin flow module and a hormonal regulation network to evaluate the effects of sucrose and auxin on branching patterns.

Technical results: The CPlantBox was extended to simulate the coupled water and carbon flow inside a growing plant, including distributed carbon sinks and sources. The model was also expanded to a coupled dynamic soil-rhizosphere-plant framework that represents three-dimensional carbon and water fluxes and their interactions with the soil and plant domains. The plant model includes modules for shoot and root growth, carbon and water transport, root

water uptake and carbon release, coupled transpiration and stomatal regulation, hormonal control on shoot branching, with emerging properties such as carbon partitioning. The multi-scale soil model accounts for biological and physical reactions, including adsorption and microbial interactions, enabling a realistic simulation of plant-soil carbon and water exchange. The multi-scale approach improves resolution near the root-soil interface while maintaining computational efficiency through fixed-point iteration and implicit time-stepping.

Scientific results: The implementation of the plant model (chapter 2) enabled us to observe the effects of dry spells on water and carbon flow within the plant. The developmental stage of the plant at the onset of a dry spell was a crucial factor influencing these effects. Initially, dry atmospheric conditions tended to trigger increased transpiration and respiration. However, the reduced plant growth resulting from water scarcity could lead to lower leaf area (and thus transpiration) and respiration over the long term, when the dry spell occurred earlier in the plant's development. Using the soil-rhizosphere-plant model (chapter 3), we could examine how plant-mediated dry spells impact soil carbon and water balance. Increased exudation from older plants during dry spells benefited active microbial communities limited by carbon, resulting in relatively higher microbial CO_2 emissions. Conversely, such conditions hindered carbon utilization in less active communities, as they were more constrained by water availability. In another line of research, we investigated auxin-mediated plant growth (chapter 4). We found that, by implementing a simplified auxin flow model within the CPlantBox FSPM, we could replicate key branching patterns observed in experimental studies and literature. These results underline the key role of carbon-dependent phytohormones for the development of plant shoot.

Conclusion: The newly developed soil-rhizosphere-plant model offers a novel integrated representation of water and carbon flows across domains and processes that are typically simulated in isolation. Through this integration we gained valuable insights into complex interaction processes. Furthermore, the multiscale implementation enabled us to precisely evaluate water and carbon flow, as well as reactions at the soil-plant interface, while limiting the increase of the computation time. The results from the branching model indicate that the representation of auxin and sucrose flow is sufficient to simulate bud release and branching patterns at the plant scale, provided the plant is not experiencing stress. However, these results represent only the first examples of model implementation. Later studies could focus more strongly on model calibration, validation and implementation for new research questions. Moreover, several key functional aspects could be incorporated to enhance the model's accuracy and robustness, particularly under limiting conditions such as nitrogen scarcity.

Zusammenfassung

Hintergrund und Motivation: Wasser und Kohlenstoff sind zentrale Elemente für das Wachstum von Pflanzen und das Funktionieren des Bodenökosystems. Wasser ist unverzichtbar für grundlegende physiologische Prozesse in Pflanzen und Mikroorganismen im Boden. Kohlenstoff übernimmt eine doppelte Funktion: Er liefert Energie und ist ein zentraler Baustein für Biomasse – gleichzeitig trägt freigesetzter Kohlenstoff in Form von CO_2 zum Treibhauseffekt bei. Veränderungen in der Wasser- und Kohlenstoffbilanz beeinflussen sowohl pflanzliche als auch mikrobielle Prozesse im Boden. Daraus entstehen komplexe *Feedback-Loops*. Der Klimawandel bringt diese Kreisläufe aus dem Gleichgewicht und führt zu extremen Wetterereignissen wie Dürren und Überschwemmungen. Das erschwert ein nachhaltiges und effizientes Management landwirtschaftlicher Ressourcen. Um die Widerstandsfähigkeit von Nutzpflanzen zu stärken, sind daher dringend optimierte *Genotype-Environment-Management* (GxExM) Strategien erforderlich. Modelle, die mehrere Skalen, Domänen und Prozesse abdecken, können helfen, neue Erkenntnisse über die gekoppelten Systemdynamiken zu gewinnen, die die Widerstandsfähigkeit von Ökosystemen beeinflussen–insbesondere im Hinblick auf ihre Reaktion auf den Klimawandel und nachhaltige Bewirtschaftungsformen. Funktional-Strukturelle-Pflanzenmodelle (FSPMs) spielen in solchen Frameworks eine wichtige Rolle: Sie zeigen, wie Struktur und Funktion von Pflanzen mit ihre lokale Umwelt interagieren.

Material und Methoden: Um die Wasser- und Kohlenstoffflüsse im Kontinuum zwischen Boden, Rhizosphäre und Pflanze besser abzubilden, wurde das bestehende CPlantBox-Modell um mehrere Module erweitert oder angepasst. Diese betreffen insbesondere den Transport von Wasser und Kohlenstoff von den Wurzeln bis in die Blätter. Gleichzeitig wurden auch die numerischen Verfahren verbessert. In einem ersten Schritt wurde das Pflanzenmodell in ein aktualisiertes, multiskaliges Boden-Rhizosphären-Modell integriert. Parallel dazu wurde das Pflanzenmodell mit einem Auxin-Transportmodul und einem hormonellen Regulationsnetzwerk verbunden, um den Einfluss von Saccharose und Auxin auf das Verzweigungsmuster der Pflanze zu untersuchen.

Technische Ergebnisse: CPlantBox wurde erweitert, um den gekoppelten Wasser- und Kohlenstoffffluss in einer wachsenden Pflanze zu simulieren, einschließlich verteilter Kohlenstoffquellen. Zudem wurde das Modell zu einem gekoppelten, dynamischen Boden-Rhizosphäre-Pflanze-Framework erweitert, das 3D Wasser- und Kohlenstoffflüsse sowie deren Interaktionen in Boden- und Pflanzen abbildet. Das Pflanzenmodell umfasst Module für das Wachstum von Spross und Wurzeln, den Transport von Wasser und Kohlenstoff, die Wasseraufnahme durch die Wurzeln, die Kohlenstofffreisetzung, die gekoppelte Transpiration mit stomatärer Regulation sowie die hormonelle Steuerung der Verzweigung. Ein neues Ergebnis ist zum Beispiel die Kohlenstoffverteilung in der Pflanze. Das Bodenmodell berücksichtigt sowohl physikalische als auch biologische Prozesse–etwa Adsorption und mikrobielle Interaktionen–und erlaubt dadurch eine Simulation des Austauschs von Wasser und Kohlenstoff zwischen Pflanze und Boden. Die Multiskalenmethode verbessert die Auflösung in der Nähe der Wurzel-Boden-Grenzfläche und ermöglicht eine effiziente Berechnung mithilfe von Fixpunkt-Iteration und einem impliziten Zeitschritt.

Wissenschaftliche Ergebnisse: Mit dem neu entwickelten Pflanzenmodell (Kapitel 2) konnten die Auswirkungen von Trockenperioden auf den Wasser- und Kohlenstoffffluss der Pflanze vorhergesagt werden. Ein entscheidender Einflussfaktor war das Entwicklungsstadium der Pflanze zu Beginn der Trockenphase. Trockene atmosphärische Bedingungen führten zunächst zu erhöhter Transpiration und Exsudation. Wenn die Trockenperiode in einem frühen Entwicklungsstadium der Pflanze auftrat, konnte aber das durch Wassermangel bedingte geringere Wachstum langfristig zu einer reduzierten Blattfläche–und damit zu geringerer Transpiration und Respiration–führen. Die Veränderungen im Wasser- und Kohlenstoffhaushalt der Pflanzen wirken sich wiederum auf den Wasser- und Kohlenstoffhaushalt im Boden sowie auf die Aktivität des Bodenmikrobioms aus (Kapitel 3). Treten Trockenperioden in einem späteren Wachstumsstadium auf, kann dies zu erhöhter Exsudation führen. Davon profitieren aktive, kohlenstofflimitierte mikrobielle Gemeinschaften, was zu einem Anstieg der mikrobiellen CO_2-Emissionen führt. Weniger aktive Gemeinschaften hingegen, die stärker von der Wasserverfügbarkeit abhängig sind, zeigen unter denselben Bedingungen eine eingeschränkte Kohlenstoffnutzung. Als weitere wissenschaftliche Frage wurde die Rolle von Auxin bei der pflanzlichen Verzweigungsrate untersucht (Kapitel 4). Das Modell war in der Lage, zentrale Verzweigungsmuster erfolgreich zu reproduzieren, wie sie in unseren experimentellen Studien und in der Fachliteratur beobachtet wurden.

Schlussfolgerung: Das neu entwickelte Boden-Rhizosphäre-Pflanze-Modell bietet einen neuartigen, integrierten Ansatz zur Darstellung von Wasser- und Kohlenstoffflüssen über verschiedene Bereiche und Prozesse hinweg, die normalerweise getrennt simuliert werden. Durch die Integration dieser Module wurden wertvolle Einblicke in komplexe Wechselwirkungen gewonnen. Die multiskaliges Modellstruktur ermöglichte zudem eine präzise Analyse der Wasser- und Kohlenstoffflüsse sowie der Reaktionen an der Wurzel-Boden-Grenzfläche. Die Ergeb-

nisse des Verzweigungsmodells zeigen, dass die Abbildung des Auxin- und Saccharoseflusses ausreicht, um die Knospenfreisetzung und das Verzweigungsmuster auf Pflanzenebene zu simulieren–sofern keine Stressbedingungen vorliegen. Diese Ergebnisse sind jedoch ein erster Ausblick auf die Möglichkeiten des Modells. Zukünftige Arbeiten könnten sich stärker auf die Kalibrierung, Validierung und Anwendung des Modells für neue Fragestellungen konzentrieren. Darüber hinaus ließe sich die Genauigkeit und Belastbarkeit des Modells weiter verbessern, indem zusätzliche funktionale Aspekte integriert werden, insbesondere für Stressbedingungen wie Stickstoffknappheit.

Table of Contents

List of Figures

List of Tables

Chapter 1

Introduction

In this first section, we will introduce the thesis and formulate its different objectives.

Why should proud summer boast
Before the birds have any cause to sing?
Why should I joy in any abortive birth?
At Christmas I no more desire a rose
Than wish a snow in May's new-fangled shows
But like of each thing that in season grows.

William Shakespeare *Love's Labour's Lost*

Water and carbon are vital components of plant development and the broader soil ecosystem. Water is indispensable for key physiological processes in plants, while carbon plays a dual role: it can be a valuable resource, serving as an energy source, building block, or component of soil organic matter, but, once released as CO_2, also one of the main greenhouse gases (Bonan, 2019d, De Swaef et al., 2022). The soil ecosystem, which is home to numerous microorganisms, plays a critical role in recycling nutrients, enhancing soil productivity, and detoxifying harmful substances. These organisms, along with plant species, are highly responsive to changes in the water and carbon balance, which can modify soil characteristics and influence the abundance and richness of microbial and plant species (Aqeel et al., 2023, Bardgett and Caruso, 2020, Bardgett et al., 2013).

Climate change is expected to significantly disrupt global water and carbon cycles, leading to profound consequences for plant phenotypes, fitness, and agricultural productivity (de Vries, 2021, FAO, 2021, Galindo-Castañeda et al., 2022). Extreme weather events, such as droughts and floods, are becoming more frequent, complicating the management of water and carbon resources in agricultural systems. This creates a pressing need to adapt resource management strategies to address issues like water scarcity and excess while safeguarding food production and ecosystem health.

Understanding how carbon and water cycles will evolve in the face of climate change is essential, but predicting these changes is highly complex. These cycles influence climate patterns and are impacted by them, creating feedback loops that are difficult to evaluate accurately (Schnepf et al., 2022, Silva and Lambers, 2021a). Assessing the resilience of ecosystems under these changing conditions requires studying interactions between processes at different scales. In agriculture, this translates into finding optimal genotype-environment-management (GxExM) combinations to improve crop performance. However, at the field scale, the genotype (G) is affected by both the environment (E) and management (M), making it challenging to pinpoint the most suitable genotype for a given set of conditions (Soualiou et al., 2021).

A finer understanding of the interactions between water and carbon fluxes at the plant scale, particularly across the soil-rhizosphere-plant continuum, is crucial to address this challenge. Such knowledge will enable the development of resilient GxExM combinations that can withstand environmental stress, thereby contributing to sustainable agricultural practices and mitigating the negative impacts of climate change (De Swaef et al., 2022, de Vries, 2021, Galindo-Castañeda et al., 2022, Soualiou et al., 2021).

To achieve this, integrated modelling frameworks are powerful tools. They can enhance our understanding of complex interactions within the soil-plant system and help breeders, farmers, and decision-makers make informed choices. By simulating various scenarios, models can predict optimal plant phenotypes under

unknown GxExM conditions, offering a way to manage uncertainty in a rapidly changing climate (Benes et al., 2020, De Swaef et al., 2022, Soualiou et al., 2021, Stock et al., 2024).

This thesis focuses on developing an integrated multi-scale, multi-physics framework to represent the carbon and water balance within the soil-rhizosphere-plant continuum. This approach aims to provide deeper insights into the intricate processes driving plant performance, resilience, and ecosystem services, with the ultimate goal of supporting more informed decision-making in agriculture and beyond.

1-1 Mechanistic bio-physical models

Models are essential tools for studying the water and carbon balance in ecosystems. For instance, they are widely recognized as useful predictive instruments, particularly in scenarios where long-term forecasts are needed but no experimental data is available (Benes et al., 2020, Bonan, 2019d, Stock et al., 2024, Thornley and Cannell, 1997). Beyond predictions, models can also generate synthetic data for observations that are difficult to measure experimentally, such as exudation rates or plant respiration (Benes et al., 2020, Lacointe and Minchin, 2019). This has driven the development of digital twins as a method for real-time monitoring of dynamic systems (Bouvry and Lebeau, 2023, Stock et al., 2024, Verdouw et al., 2021).

Models can additionally enhance experimental research by helping scientists design experiments (Benes et al., 2020, Bonan, 2019d). Indeed, models can be used to explore in put parameter space and select experimental conditions likely to yield informative outputs.

Models can be categorized based on how explicitly they represent underlying processes. Mechanistic models provide am explicit representation of biological, chemical, and physical processes, while empirical or statistical models rely on observed relationships between input and output variables (Stock et al., 2024, Tardieu et al., 2020). Although all models incorporate some empirical aspects, more mechanistic models are generally expected to maintain accuracy in untested environmental scenarios, making them particularly useful for predicting plants' resilience to climate change, which introduces novel climate conditions and extreme weather events (Tardieu et al., 2020).

In addition to generating quantitative data, mechanistic models also serve as educational tools, helping to formalize the representation of a network of interrelated processes (Bonan, 2019d). The selection of domains, assumptions, and simplifications is itself a key component of model development (Cieslak et al., 2022).

Additionally, the outputs of mechanistic models can improve our understanding of process interactions: While researchers may know the direct relationships influencing observed outcomes, the resulting dynamics can sometimes be complex and counter-intuitive (Cieslak et al., 2022, Stock et al., 2024). Researchers can use the qualitative and quantitative model outputs to understand better underlying mechanisms and distinguish between correlation and causality in experimental data (Beveridge et al., 2023, Putten et al., 2013, Schnepf et al., 2022, Silva and Lambers, 2021a, Stock et al., 2024, Wass et al., 2023). Processes in ecosystems are often overlapping and redundant, and nature does need to adhere to Occam's razor (Beveridge et al., 2023). Mechanistic models, therefore, provide a framework for assessing which biological, chemical, and physical processes are most relevant under specific conditions and scales (Beveridge et al., 2023, Bonan, 2019d), a critical consideration in the context of the ever increase of knowledge available (Beveridge et al., 2023).

Mechanistic models are also valuable when direct relationships between observed outputs are only partially known. By testing different networks of processes, researchers can identify which configurations produce the most accurate and robust results (Bonan, 2019d, Louarn and Song, 2020, Schneider et al., 2020). Thus, both successful and unsuccessful model calibration can improve our understanding of the studied systems.

1-2 Functional Structural Plant Models

The characteristics of functional structural plant models (FSPMs) are linked to the history of their development. The creation of FSPMs was preceded by that of the structural plant models, created in the 1960s, with the notable example of the L-System–or Lindenmayer-System (Prusinkiewicz and Lindenmayer, 2012, Vos et al., 2009, 2007). The L-System takes advantage of the of the geometric characteristics of plants, such as bilateral and circular symmetry in some leaves and flowers, helical symmetry in some stems, and scale symmetry (fractals) for some plant topologies (Prusinkiewicz and Lindenmayer, 2012). These geometries allow the plants structure to be defined using a set of empirical rules that are repeated cyclically (Vos et al., 2009).
The first FSPMs were created in the 1990s and have two main origins: structural models with added functional modules, and non-structural process-based models with added functions (Vos et al., 2007, preface). We observed in the following years the emergence of FSPMs and related frameworks that are still widely used in within the community today, such as GroIMP (Vos et al., 2007, chap. 4), GreenLab (Wang et al., 2024) and OpenAlea (Pradal et al., 2008), Vlab/L-studio with the cpfg, lpfg simulators[1] (Vos et al., 2007, chap. 3). These models were initially used to evaluate the effect of structure on functions (no feedback), specifically resource capture: the effect of the 3D roots on water uptake (Dunbabin et al., 2013) and the effect of shoot on light interception (Vos et al., 2009,

[1] see https://algorithmicbotany.org/papers/

2007). FSPMs also raised interest by their reliance on mechanistic rules defined at the local (cell, organ) level to obtain emerging properties at the plant level (Vos et al., 2009). The models grew in complexity to represent a wider range of functions and scales as well as feedback loops between plant structure and functions and with the local environment (Schnepf et al., 2022).
For a time, shoot and root systems were simulated separately (Dunbabin et al., 2013, Leitner et al., 2010, Vos et al., 2007). Indeed, the mode of representation of the structures (long and thin tubes for the roots, more complex 3D geometry for leaves and fruits), processes of interest (e.g., photosynthesis against root water uptake), and surrounding environment (atmosphere or soil), made the coupling of the plant shoot and root system more arduous. Shoot-atmosphere and root-soil coupling were more common than root-shoot coupling. However, some models like GRAAL (Drouet and Pagès, 2003) already offered a full plant structure simulation. The question of root-shoot coupling became more important as plant processes, such as transpiration, can be better studied by accounting for the full plant transport (Lacointe and Minchin, 2019). For similar reasons as the ones given above (difference in process modelled and research questions), we observed the development of two diverging FSPM groups: for crops and smaller annual plants on the one side against trees and perennial plants on another side (DeJong, 2022, Sievänen et al., 2014). However, some frameworks, such as GreenLab (Wang et al., 2024) and Vlab/L-studio (DeJong, 2022, Prusinkiewicz et al., 2009) are able to represent both crops and trees.

FSPMs are usually agent-based models, where each section of the plant interacts directly with its environment, creating a distribution of the decision centres–modular implementation (Dubitzky et al., 2013, Soualiou et al., 2021, Stock et al., 2024, Vos et al., 2009). Therefore, the resulting phenotype of a simulation results from those separated, partially independent interactions. This makes FSPMs especially able to recreate phenotypic stochasticity, a key aspect of a plant's development (De Reffye et al., 2010, Louarn and Song, 2020, Stock et al., 2024).
FSPMs operate generally at the tissue, plant and "group of plants" scale (see Fig.1-1). However, using up- and down-scaling, they can also represent processes at a lower (cell) and higher (field) scale (Soualiou et al., 2021). FSPMs can be categorized according to the plant sections represented–e.g., root system, shoot, branch, full plant. Moreover, while some framework aim to remain generic (e.g., CPlantBox, CN-Maiz, PiafMunch), others specialize on a specific plant type (e.g., GRAAL, CN-Wheat, L-PEACH) (Allen et al., 2005, Barillot et al., 2016, Drouet and Pagès, 2003, Dubitzky et al., 2013, Lobet et al., 2014a, Lu et al., 2024, Soualiou et al., 2021, Wang et al., 2024).
Other important aspects that define FSPMs are the sets of functional processes implemented (plant transpiration, solute uptake, plant growth) and their position along the phenomenological (empirical)–physiological (mechanistic) modelling axis (Dubitzky et al., 2013, Ruiz et al., 2021).
Several programming languages have been developed specifically for FSPMs, such as the "L" and "L+C" for L-system models and the "XL" language of GroImp (Dubitzky et al., 2013, Soualiou et al., 2021), which makes them specifically

adapted for the needs of plant modellers. Other models use common programming languages (Fortran, C++, Python, Julia) that can lead to higher computing speed and easier coupling with and implementation by, respectively, models and modellers outside of the FSPM nexus (Dubitzky et al., 2013, Schnepf et al., 2018b, Soualiou et al., 2021).

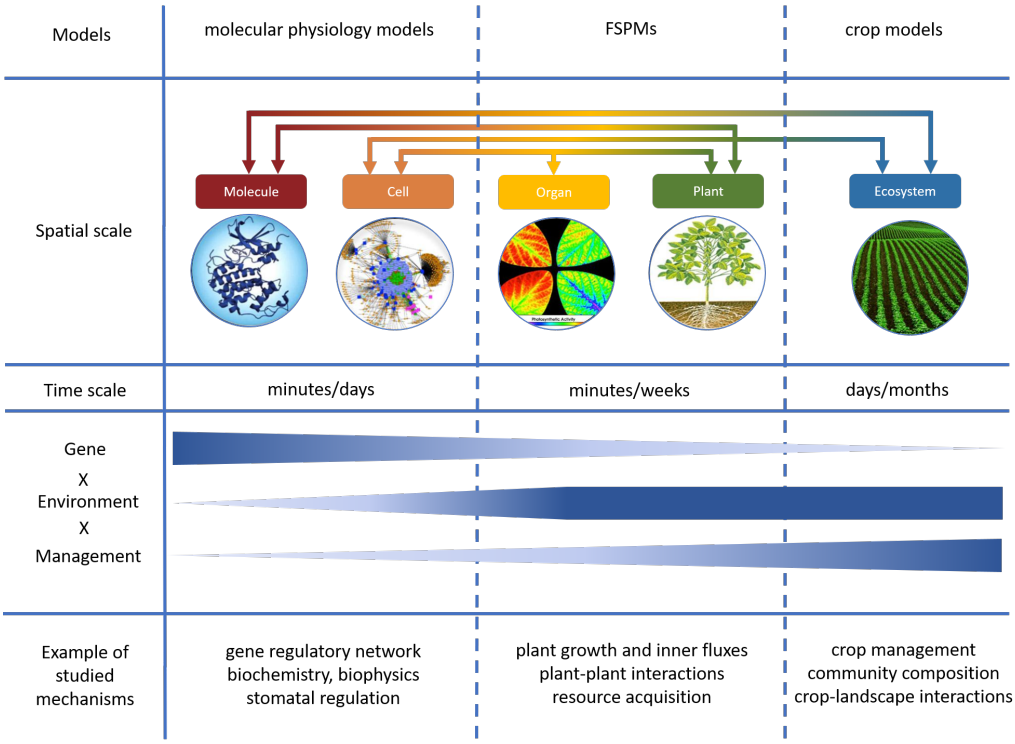

Figure 1-1: Types of biological models for plants. Adapted from Tardieu et al. (2020) and Marshall-Colon et al. (2017). Each model type is linked to its usual spatial and temporal scale, and examples of mechanisms studied with such models. The dashed vertical lines and arrows between scales illustrate the fluid boundaries between model types, enabled by approaches such as multiscale modelling, hybrid modelling, or model coupling. For simulating phenotypes resulting from specific G×E×M combinations, molecular physiology models are more suited to capturing gene-level effects, whereas crop models are better at representing the impacts of agricultural management at the field or farm level. Additionally, crop models can link the results to broader climatic conditions, while functional-structural plant models account for interactions with the plant's local environment.

FSPMs are complementary to existing model types and can answer a new set of questions at the sub-organ, plant, and field scale (Cieslak et al., 2011, De Reffye et al., 2010, Schneider et al., 2020, Soualiou et al., 2021, Vos et al., 2009). They are specially adapted to account for plant micro-climates and represent plant scale processes, such as resource allocation and exchanges of resources with the environment (Gauthier et al., 2020), as well as plant-plant interactions (Evers et al., 2011). Phyllotaxie is another plant scale process that can be well studied *in silico* using

FSPMs (Prusinkiewicz et al., 2009, Vos et al., 2009). Indeed, the growth rates can be dependent on semi-mechanistic processes (De Swaef et al., 2022, Gauthier et al., 2020, Schnepf et al., 2018b). Although less common, some FSPMs also use processes-based modules to define the branching dynamic of shoots (Prusinkiewicz et al., 2009, Renton et al., 2012). FSPMs can be used to simplify and observe the effect of molecular or cellular level processes at the plant scale (Vos et al., 2009). Likewise, FSPMs can link the gene scale with the plant scale, mixing empirical and mechanistic modules (Vos et al., 2009). FSPMs are therefore an interesting tool to evaluate Gene x Environment x Management combinations. The explicit three-dimensional plant structure offers a unique opportunity to reach a higher accuracy in the representation of plant flows (like water and carbon) using computational fluid dynamic (De Swaef et al., 2022, Stock et al., 2024). Through these simulations of inner-plant flows, it is possible to set up new framework linking processes across plant sections (Vos et al., 2009).

FSPMs face several challenges inherent to their characteristics and that were, for the most part, identified early in their development (Vos et al., 2007). A main issue is the computing speed (Soualiou et al., 2021, Vos et al., 2009, 2007): FSPMs offer by definition a high spatial resolution and some of the processes represented (transpiration) require a high temporal resolution. Covering a spacial and temporal scale relevant for agronomists (whole field over the growing period) can then require a high computing time. Processes relying on differential equations (like resource allocation) can be especially time-intensive (Vos et al., 2007). Moreover, the ideal boundaries of a model should be the areas and processes that are not noticeably affected by the evaluated scales of the model. Because of the high interconnectedness of biological processes, this condition when defining a model cannot be easily respected (Vos et al., 2007). Biological modellers need therefore to rely on empirical parameters representing implicitly non-simulated processes, define simplifying assumptions and the range of applicability of a calibrated model. As resilience analysis require the simulation of more complex systems (Silva and Lambers, 2021b), representing several spatial scales and processes remains both a challenge and an objective for FSPMs (Schnepf et al., 2022). The level of precision of FSPMs also makes their calibration difficult as plant- and tissue-level data is needed rather than aggregated field-level observations.

These challenges are being addressed by the FSPM community. Indeed, an increase in cooperation between research groups allowed for the development of model couplings, hybrid modelling and benchmarking of existing models (Gaudio et al., 2021, Schnepf et al., 2023, Wang et al., 2024). These higher interactions between models make the creation of multi-scale multi-physic platforms easier, using the advantages of each model over a large range of scales (Silva and Lambers, 2021b). Biological modeling has also been profiting from input from other science fields, such as software engineering, mathematics and physics (Radde and Hütt, 2016, Stock et al., 2024).Thanks to software engineering, we observed an improvement of models that reached higher speed and overall better scalability. The usage of machine learning and surrogate modeling are part of new tools that

can help better calibrate models.

1-3 CPlantBox

The development of the CPlantBox framework follows the trends described above for FSPMs (Fig.1-2). CPlantBox started as the RootBox model in 2010, using the L-system language (Leitner et al., 2010). CRootBox (Schnepf et al., 2018b) presented a re-implementation of RootBox in C++ with Python binding to allow for a high computing speed coupled with a flexible interface, and did not require a MatLab licence. Thanks to this faster framework, a larger number of plants could be simulated at once. CRootBox has since then been used in several studies, and in some cases coupled with other models, for instance to simulate root-soil coupling (Mai et al., 2019). Zhou et al. (2020) presented the extension of CRootBox to a full plant model and coupled with the plant flow solver PiafMunch (Lacointe and Minchin, 2019) to link the carbon and water flow of a static plant. Similarly to other root models (Schnepf et al., 2023), CPlantBox offers a precise computation of the inner plant flows and root water uptake, based on differential equations. CPlantBox represents a framework that can be coupled with a range of other models to represent the plant's local environment, or coupled with lower and higher scale models (Baker et al., 2025, Giraud et al., 2023, Vanderborght et al., 2024). A more detailed description of CPlantBox is given in section 2-2-1 of this thesis.

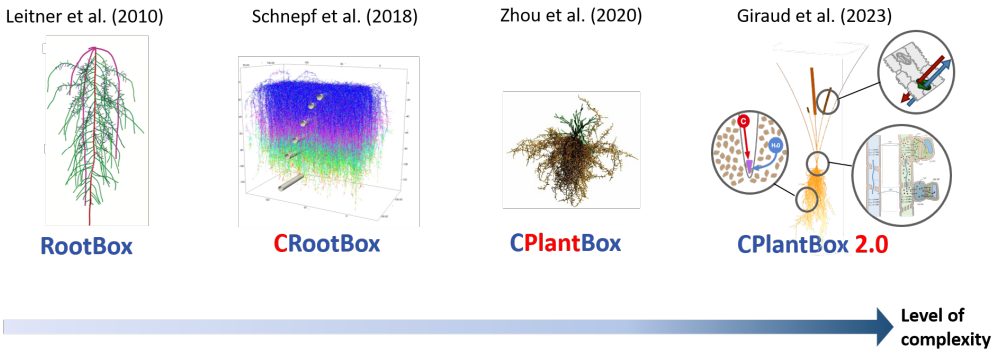

Figure 1-2: Graphical representation of the development of RootBox into CPlantBox. Each image represents a significant update of the framework's code, with the relevant reference given above.

1-4 Computational fluid dynamic for functional structural plant models

1-4-1 Water potential and flow

Water potential corresponds to the potential energy of a set amount of water–per unit of e.g., volume (hPa) or weight (cm)–compared to a reference state. It is an important value to define water-related processes: it gives information on the water status of the domain and its gradient drives the water flow and exchange (De Swaef et al., 2022, Nobel, 2009b). We present below the different types of water potential.

The total water potential, ψ_t (hPa), can be defined as:

$$\psi_t = \frac{\eta - \eta_{\text{ref}}}{\bar{V}} = \psi_p + \psi_g + \psi_o, \tag{1-1}$$

where η $(hJ\ mol^{-1})$ is the chemical potential of the water under study, and η_{ref} $(hJ\ mol^{-1})$ is that of a reference water. Here, ψ_p (hPa) represents the pressure potential, ψ_g (hPa) is the gravitational potential, and ψ_o (hPa) is the osmotic potential, dependent on the concentration of solutes in the liquid (De Swaef et al., 2022, Nobel, 2009b). $\bar{V}$ is molar volume of water $(m^3\ mol^{-1})$.

The pressure potential ψ_p includes all contributions except osmotic and gravitational effects. It can take positive values when $|\psi_p| > |\psi_{p,\text{ref}}|$, or negative values when $|\psi_p| < |\psi_{p,\text{ref}}|$. In unsaturated soils, the pressure potential is given by:

$$\psi_{p,\text{soil}} = \psi_{m,\text{soil}} + \psi_{a,\text{soil}} < 0, \tag{1-2}$$

where ψ_m (hPa) is the matric potential and ψ_a (hPa) is the pneumatic potential. The pneumatic potential accounts for air pressure differences and is expressed as:

$$\psi_a = P_{\text{atm}} - P_{\text{soil air}}, \tag{1-3}$$

with P_{atm} (hPa) representing the atmospheric pressure at ground level, which depends on the total pressure exerted by gases in the atmosphere.

The reference water, indicated by the subscript "ref," is pure, located at ground level ($z_{\text{ref}} = 0$), and its hydrostatic potential equals the atmospheric pressure.

In plants, the pressure potential ψ_p is equivalent to the hydrostatic potential ψ_h. Typically, ψ_p is positive in plant tissues, where it is referred to as turgor pressure. However, in specific plant structures like the xylem, the pressure potential,

denoted $\psi_{p,x}$, is usually under negative tension.

While many FSPMs concentrate on water flow either in the roots (Schnepf et al., 2023) or the shoot (Albasha et al., 2019), simulating both simultaneously can provide a more accurate representation of the interconnected water dynamics and transmission of signals along the continuum via water potential. Precise computation of the water potential can link to a better representation of the domain interactions across the soil-plant-atmosphere continuum, for instance, via root water uptake and plant transpiration (De Swaef et al., 2022). Water is also an important component of the carbon balance. It regulates plant growth (carbon usage) and stomatal opening (carbon source) (Bonan, 2019c, De Swaef et al., 2022). The soil water content also defines the soil advective flow and concentration of solutes around the root. This will influence both the plant's passive carbon release and the access of the microbial community to that carbon. Too low soil water content will also lower the activity and fitness of the soil microbes (Moyano et al., 2013, Wang et al., 2021), affecting the soil carbon balance.

1-4-2 Carbon transport

Many plant models assume that carbon transport throughout the plant is instantaneous ("common assimilate pool") (Reyes et al., 2019). However, explicitly modelling the flow of carbon through the plant can offer deeper insights into carbon allocation patterns (Lacointe and Minchin, 2019). Models differ in their representation of this flow, with some, though in the minority, assuming a steady-state flow for sucrose (analytical solution) (Hall and Minchin, 2013, Seleznyova and Hanan, 2018). While this allows for simpler simulations, it imposes a stronger assumption than the steady-state representation of water flow, as phloem flow is slower (Zhou et al., 2020), which consequently limits the time resolution that can be used.

Many models focus on specific plant organs such as the root system (Bidel et al., 2000, Rees et al., 2023a), the shoot (Seki et al., 2014, Uys et al., 2021), or the fruit (Allen et al., 2005). However, some models represent both the root and shoot, as in studies of wheat (Rees et al., 2023a), morning glory (Zhou et al., 2020), or generic C3 monocots (Giraud et al., 2023). While phloem flow in trees may require three-dimensional representations (Hölttä et al., 2006, Mammeri and Sellier, 2017, Sellier and Harrington, 2012), axial flow in crops is typically represented using one-dimensional models that neglect lateral gradients in transport tissues (Bidel et al., 2000, Lacointe and Minchin, 2019, Postma and Lynch, 2012, Uys et al., 2021).

Some models simplify the sink-source interaction by assuming that carbon is loaded into the phloem at specific source points and unloaded at specific sink points (Seleznyova and Hanan, 2018, Thorpe et al., 2011, Zhou et al., 2020). Others model carbon transport in more detail, incorporating distributed sinks

and sources (Giraud et al., 2023, Lacointe and Minchin, 2019) and complex reactions within tissues containing the carbon solute (Sze et al., 2013, Uys et al., 2021). To balance model accuracy with simplicity, detailed biochemical and physical representations of phloem solutes across different tissue types often treat plant sections as compartments (no explicit axial flow) (Gauthier et al., 2020, Grafahrend-Belau et al., 2013) or simulate simpler plant topologies (Uys et al., 2021). Commonly modelled types carbon sink include growth, respiration, maintenance, storage as starch or in fruits and seeds (Barillot et al., 2016, Daudet et al., 2002, Giraud et al., 2023, Nikinimaa et al., 2013, Seki et al., 2014), and, when the root system is modelled, exudation (Barillot et al., 2016, Giraud et al., 2023, Rees et al., 2023a, Thorpe et al., 2011, Zhou et al., 2020).

Another critical aspect is the representation of the carbon source, which can be empirical and constant (Lacointe and Minchin, 2019, Uys et al., 2021, Zhou et al., 2020), or variable and dependent on environmental or plant-related factors (Giraud et al., 2023, Nikinmaa et al., 2014). Additionally, carbon loading can be either passive or active, depending on the plant represented (De Schepper et al., 2013, Sze et al., 2013).

The concentration of carbon in the phloem solution also significantly affects model outputs (Cabrita, 2011). Models may assume either constant solution viscosity (Bidel et al., 2000, Daudet et al., 2002, Seki et al., 2014, Uys et al., 2021) or make viscosity dependent on carbon concentration (Allen et al., 2005, Giraud et al., 2023, Hall and Minchin, 2013, Lacointe and Minchin, 2019, Nikinimaa et al., 2013, Seleznyova and Hanan, 2018). Similarly, the osmotic pressure may be modelled as a non-linear function of solute concentration (Cabrita, 2011, De Swaef et al., 2022, Seleznyova and Hanan, 2018), though some models approximate this relationship as linear over the relevant concentration range (Van't Hoff equation) (De Swaef et al., 2022, Hall and Minchin, 2013).

Phloem advection is another element that varies between models. Some implementations, make advection dependent solely on the osmotic potential gradient (Hall and Minchin, 2013, Seleznyova and Hanan, 2017, 2018, Uys et al., 2021), while others couple xylem and phloem flow, making advection dependent on the pressure gradient affected by xylem, under the assumption of water potential equilibrium between the two tissues (Daudet et al., 2002, Giraud et al., 2023, Hölttä et al., 2017). Certain models also account for non-equilibrium conditions between xylem and phloem (Hölttä et al., 2006, Lacointe and Minchin, 2019, Zhou et al., 2020).

Finer representations of phloem flow may also include mechanisms like carbon solute leakage-retrieval (De Schepper et al., 2013), the reduced phloem conductivity caused by small sieve pore radii (Thompson, 2006), or the representation of carbon solute molecules other than sucrose.

Cabrita (2011) provide a review of the mathematical modelling of phloem flow that can inform the assumptions and simplifications used in computational models of this process.

1-4-3 The advection-diffusion-reaction equation

Partial differential equations (PDEs) are equations that depend on more than one independent variable (e.g., time and spatial coordinates). The order of the highest derivative term defines the order of the equation. A PDE is said to be linear if its coefficients do not vary according to the dependent variable. A particular kind of PDE is the advection-reaction-dispersion (ARD) equation. This equation can be used in mathematical models to represent the flow and balance of a specific element X in a domain.

The advection-diffusion-reaction is made of four types of terms (Guyer et al., 2009):

$$\frac{\partial X}{\partial t} = \nabla \bullet (\vec{u}X) + \nabla \bullet D\nabla X + S_X \tag{1-4}$$

The terms on the left-hand side correspond to the changes in the concentration of X according to time at one specific coordinate. The first term on the right-hand side corresponds to the advective transport of the component X due to the movement of the solution.The second term on the right-hand side corresponds to the diffusion (and dispersion) term, driven by the concentration radiant. The last term represents the net source of X. This equation can be used as the basis for the transport of solutes in a saturated medium (such as the carbon transport in the phloem). Once adapted for a multi-phase transport, it can also be used to represent the solute flow in an unsaturated soil.

1-4-4 Plant axial flux

According Newton's second law of motion, we have per unit of an arbitrary volume V of liquid with constant density (Blyth and Morris, 2018, Radcliffe and Simunek, 2010):

$$m\overrightarrow{a} = \overrightarrow{F}, \tag{1-5}$$

$$\int_V \rho \frac{dj}{dt}\, dV = \int_V \overrightarrow{F}_V\, dV, \tag{1-6}$$

with $\overrightarrow{F}$ (MLT^{-2}) the sum of the forces on that liquid. $\overrightarrow{a}$ (L/T^2) is the acceleration of the flow (j (L/T)) and ρ (M/L^3) the density of the liquid.

As per Reynolds' transport theorem, we get:

$$\int_V \rho \frac{dj}{dt} dV = \int_V \rho \frac{\partial j}{\partial t} dV + \int_S (\rho j)(j \cdot \mathbf{n})\ dS \tag{1-7}$$

And from the divergence theorem:

$$\int_S (\rho j)(j \cdot \mathbf{n})\ dS = \int_V (\rho j) \nabla \cdot j\ dV \tag{1-8}$$

Consequently:

$$\int_V \left[\rho \left(\frac{\partial j}{\partial t} + (j \cdot \nabla) j \right) - \overrightarrow{F}_V \right] dV = 0, \tag{1-9}$$

$$\rho \left(\frac{\partial j}{\partial t} + (j \cdot \nabla) j \right) - \overrightarrow{F}_V = 0, \tag{1-10}$$

Following Cauchy's momentum equation, we divide the volume-specific forces $\overrightarrow{F}_V$ in two groups (Blyth and Morris, 2018, Radcliffe and Simunek, 2010): volume-specific body forces (gravity, $\nabla \psi_g$) and the surface forces. The surface forces correspond to the volume-specific pressure ($\nabla \psi_p$) and to the stress deviator tensor. We apply the simplification that not only the xylem but also the phloem solutions are Newtonian fluids with constant viscosity (μ) over the (sufficiently small) evaluated distance. It is then possible to define the stress deviator tensor as $\mu \nabla^2 j$. In summary:

$$\rho \left(\frac{\partial j}{\partial t} + (j \cdot \nabla) j \right) = -\nabla \psi_g - \nabla \psi_p + \mu \nabla^2 j \tag{1-11}$$

For incompressible fluids $\nabla \cdot j = 0$. Therefore:

$$\rho \frac{\partial j}{\partial t} = -\nabla \psi_g - \nabla \psi_p + \mu \nabla^2 j \tag{1-12}$$

As the xylem and phloem flow is laminar ($\mathrm{Re} \ll 1$), the inertia of the fluid is negligible compared with the viscosity term ($\rho \frac{\partial j}{\partial t} \ll \mu \nabla^2 j$) (Thompson, 2006). And consequently:

$$\mu \nabla^2 j = \nabla \psi_g + \nabla \psi_p \tag{1-13}$$

Because the xylem and phloem tissues do not make a perfect tube, it is not possible to apply the Poiseuille equation derivation (Cabrita, 2011). Instead, following the recommendation of Bear and Bachmat (1967, Eqn. 12) and Narsilio et al. (2009, Eqn. 4), we assume that the viscous resisting force ($\mu \nabla^2 j$) is proportional (and of opposite sign) to the velocity in a laminar flow. We thus obtain $\mu \nabla^2 j = -\frac{\mu}{\kappa} j$, which yields:

$$j = -\frac{\kappa}{\mu} (\nabla \psi_g + \nabla \psi_p) \tag{1-14}$$

This equation follows Darcy's law for a flow in a porous medium (ISSS, 1976, defn. 21), which fits with the representation of the phloem and xylem tissues as many sieve elements strung together (Batchelor and Batchelor, 2000, Uys et al., 2021).

1-4-5 Spatial discretisation

In mechanistic models, the flow and reactions of different represented solutes and fluids can be computed by partial differential equations, such as ones described in section 1-4-3.
The partial differential equations can be solved with a numerical solver using a cell-centered finite volume method (Koch et al., 2021, Succi, 2015), where the represented domain is discretized as a mesh made of cells. We then approximate a mean value for each of the represented element at the center of each cell (Eulerian approach). The diffusion and advection fluxes are computed at each boundary between two cells, called a face.
According to the Gauss theorem, the change in the mean value of the dependent variable for a cell is equal to the flux across the faces of that cell (Succi, 2015). For faces that link a cell and the border of the domain, it is possible to implement a set of boundary conditions when solving the domain.

The geometry of faces, cells, and meshes varies according to the dimension of the mesh. A graphical representation of those three classes for 3D, 2D, and 1D rectilinear meshes are given in Fig. 1-3. We also present the specific terminology used in CPlantBox, the plant model implemented in this study.

Definition	name	CPlantBox nomenclature	dimensions		
			3D	2D	1D
Boundary between two subcontrol volumes	(inner) face	node	rectangle 	segment	point
Subcontrol volume	cell	segment	parallelepiped 	rectangle 	segment
Simulated domain	mesh	plant	parallelepipeds 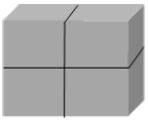	rectangles 	segments or network 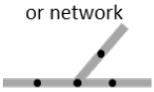

Figure 1-3: Graphical representation of a rectilinear mesh and its components (face, cell) according to the number of represented dimensions. The third column gives the specific nomenclature used in the 1-dimensional CPlantBox plant model. With the cell-centred finite element method, the solution of the computed variables is approximated at the centre of the cell.

An alternative to the cell-centered finite volume method is the vertex-centered finite volume method. For a 1D mesh, this means that the unknown variable is solved for each face of the model and the flux is evaluated in the segments. This method is akin to the graph discretization, where the 1D mesh-cell corresponds

to a graph-edge and the 1D mesh-face corresponds to a graph-node.

For FSPMs, this finite volume discretization can allow for the representation of the different phytomeres (Vos et al., 2009) or for the implementation of "big cell" method (Cieslak et al., 2022). The "big cell" is a straight forward link between the cell and the plant scale, where each plant subcontrol volume is simulated according to (bio-physical) cell-scale rules.

In the roots and stems of plants, the transport tissues can be represented as a 1-dimensional line (no radial-gradient) (Lacointe and Minchin, 2019, Renton et al., 2012, Reyes et al., 2019, Schnepf et al., 2023). The plant can, therefore, be discretized as a directed 1D network (or tree graph)in a 3D space (mixed-dimensional coupled scheme) (Koch et al., 2018, Schnepf et al., 2023). This simplification allows for higher computational efficiency (Koch et al., 2018) while yielding accurate results (Schnepf et al., 2023). Some models simulating plant inner flow use 2D or 3D discretisation schemes (Sellier and Harrington, 2012) but tend to focus on only part of a plant or on simpler topologies because of the higher computation cost (Ruiz et al., 2021). In this study, we, therefore, used a 1D cell-centered method for the phloem solution flow (Giraud et al., 2023, Lacointe and Minchin, 2019) and the 1D vertex-centered method for the xylem solution flow (Giraud et al., 2023, Schnepf et al., 2023).

We, moreover, use both a 3D and 1D cell-centered method for the computation of the water flow and carbon balance in the soil.

1-5 Model coupling and temporal discretisation

Multi-scale, multi-domain, and multi-physics models allow us to represent the complex feedback effects and emerging properties in an ecosystem and can yield precious insights on how specific environments will react to changes in climate (Benes et al., 2020, Gaudio et al., 2021, Louarn and Song, 2020, Schnepf et al., 2022).

It is, therefore, needed to find a balance between model simplicity and accuracy when representing processes and domain structure to reach the level useful for scientific understanding (Bonan, 2019d, Cieslak et al., 2022, Louarn and Song, 2020). Model coupling can be a powerful tool to reach such objective (Benes et al., 2020, Gaudio et al., 2021, Stock et al., 2024). It allows the framework to represent different interrelated processes across domains and scales and with different levels of precision (mixed-dimensional coupled schemes) (Koch et al., 2018), and the modular aspect of such coupling can allow the complexity of the framework to be adapted for each specific study.

These coupled models and modules create a set of equations that, in most cases, must be approximated using a numerical solver (Bonan, 2019a). In some models, when the time step is slow enough or when there are no feedback effects, the modules can be implemented sequentially. To take better into account interactions, a straightforward approximation method is the fixed-point iteration, where the modules are run until convergence criteria are met (Bonan, 2019a).

For fixed-point iterations, the forward and backward Euler methods are common time-stepping schemes (Bonan, 2019a, Guyer et al., 2009, Koch et al., 2021). For the forward Euler method, the changes in X between the time step k and $k+1$ is evaluated using the output of a set of equation $\boldsymbol{f}$ with the *initial* conditions X_k at time t_k. Written as an equation, it yields:

$$\frac{X_{k+1} - X_k}{\Delta t} - \boldsymbol{f}(X_k, t_k) = 0, \tag{1-15}$$

For this method to be stable (i.e. to reach convergence for the fixed point iteration), very small time step may be necessary, increasing thus the computation time.
With the backward or implicit Euler method, the changes in X between the time step k and $k+1$ is evaluated using the output of a set of equation $\boldsymbol{f}$ to the *final* conditions X_{k+1} at time t_{k+1}. Written as an equation, it yields:

$$\frac{X_{k+1} - X_k}{\Delta t} - \boldsymbol{f}(X_{k+1}, t_{k+1}) = 0, \tag{1-16}$$

Although the implicit calculation allows for a larger time step, a too-high time step might not be detected and could lead to erroneous results.

1-6 Aims and objectives

The overall aim of this thesis was to develop an integrated soil-rhizosphere-plant modeling framework to simulate water and carbon dynamics in response to genotype-management-environment interactions. This framework should connect plant physiological processes with soil-microbe interactions, allowing for the assessment of the system's responses to environmental fluctuations such as droughts.

To achieve this, the following technical and research objectives were pursued:

- Extend the CPlantBox model to simulate water transport and carbon balance in roots and shoots under varying environmental conditions. Implement the model to assess changes in plant water and carbon dynamics during dry spells.
- Setup a coupled framework to represent the soil-microbes-plant interactions regarding the water and carbon balances. Implement the model to assess changes in plant water and carbon dynamics during dry spells, with soil carbon dynamic and bulk soil-rhizosphere interactions taken into account.

- Develop a semi-mechanistic model linking plant carbon balance with hormonal regulation of shoot branching, using auxin and sucrose as key regulatory signals. Evaluate the impact of resource availability and environmental stress on branching patterns by comparing simulation outputs with experimental data and the literature.

1-7 Thesis outline

Chapter II of this thesis presents a new version of the pre-existing CPlantBox functional strutural plant model. We first give an overview of modules and the equations implemented in the new version of CPlantBox, as well as the solving scheme. We then present an implementation of new model for a generic C3 monocot under different weather scenarios. The model results are used to evaluate the effects of a dry spell of one week on the plant's growth according to the plant development stage. We then evaluate the results and compare them against observations from the literature.

Chapter III of the thesis presents the coupling of CPlantBox with a multiscale soil model, which includes water flow and the carbon balance between several represented pools (microbial, solutes, emitted microbial CO_2). We present each part of the framework, focusing on the adaptation done for the coupling. We then give an overview of the coupling method, especially the fixed point iteration with implicit time stepping. The coupled model is implemented using the scenarios defined in chapter II of the thesis, for different microbial traits. The results are used to untangle the dynamic interactions between the different processes and domains. These observations are then compared with the literature.

Chapter IV of this thesis presents the implementation of a regulatory network within CPlantBox. We first give an overview of the assumptions used based on a literature review and the resulting model equations. We then present the experimental setup used to calibrate and test the model. Afterwards, we present the results of the laboratory and simulation studies. The results of both are also compared against the literature. The similarities and discrepancies are used to evaluate the strength and weaknesses of the model.

Chapter V of the thesis discusses the findings of the thesis within the wider research landscape.

Chapter VI of this thesis gives an overview of the main findings and conclusion obtained from the different work packages. We conclude with recommendations for further research paths to better reach the over-arching aim of simulating genotype-management-environment interactions across the soil-rhizosphere-plant continuum.

Chapter 2

CPlantBox: a fully coupled modelling platform for the water and carbon fluxes in the soil–plant–atmosphere continuum

In this section, we present the new version of the functional structural plant model CPlantBox, which simulates the connected inner plant water flow and carbon balance.

In Nature's temple, living pillars rise,
Speaking sometimes in words of abstruse sense;
Man walks through woods of symbols, dark and dense,
Which gaze at him with fond, familiar eyes.

Charles Baudelaire, Jacques LeClercq
Flowers of Evil

This chapter is a modified version of a scientific article published as:

> Giraud, M., Le Gall, S., Harings, M., Javaux, M., Leitner, D., Meunier, F., Rothfuss, Y., van Dusschoten, D., Vanderborght, J., Vereecken, H., Lobet, G., and Schnepf, A. (2023). CPlantBox: a fully coupled modeling platform for the water and carbon fluxes in the Soil-Plant-Atmosphere-Continuum. in silico Plants, diad009 (cit. on pp. 59, 63, 66, 68, 76).

2-1 Introduction

Terrestrial carbon and water cycles are, amongst others, affected by plant development (De Schepper et al., 2013, De Swaef et al., 2022, de Vries, 2021). Climate change is expected to alter the global water and carbon balances (Swart et al., 2019) and thus plant phenotype and fitness (de Vries, 2021). A better understanding of the mechanisms driving the plant carbon- and water-fluxes, and their relations to the environment is key to selecting phenotypes and management practices, that are adapted to these altered environmental conditions and therefore to mitigate the negative effects of climate change and maintain or even increase food production (De Swaef et al., 2022, de Vries, 2021, Galindo-Castañeda et al., 2022, Soualiou et al., 2021).

However, the complex spatio-temporal interactions between the water and carbon fluxes in the soil-plant-atmosphere continuum make predictions and analyses of experimental results difficult. First of all, cellular scale characteristics (like the shape and size of the xylem and phloem tissues) need to be considered to understand emerging effects seen at larger scale (like the evapotranspiration and biomass production of a field) (Bramley, 2006, Cabrita, 2011, Coussement et al., 2020, Thompson and Holbrook, 2003). Moreover, feedback loops and threshold effects make the influence of plant physiological traits on the water and carbon cycles site-specific (de Vries, 2021). For these same reasons, we can also observe differences between short- and long-term effects of climatic shifts on the water and carbon cycles (Damour et al., 2010, de Vries, 2021) and experimental studies are not sufficient to predict the equilibrium of ecosystems in the distant future.

Mechanistic modelling can help evaluate plant behaviour for as yet non-existing genotype-environment-management combinations and can help decipher underlying interrelated processes leading to experimental observations (Soualiou et al., 2021, Stanfield and Bartlett, 2022, Tuzet et al., 2003). Modelling can therefore be used to investigate the benefits and drawbacks of novel crop management practices and to set objectives for plant breeders (Louarn and Song, 2020, Soualiou et al., 2021, Stanfield and Bartlett, 2022).

From three-dimensional functional structural plant models (3D FSPMs) properties emerge at the organism scale that can be scaled up to the field or ecosystem (De Swaef et al., 2022, Louarn and Song, 2020, Soualiou et al., 2021). FPSMs that represent the transport functions of plant tissues are especially adapted to simulate plant carbon and water fluxes in the plant and link these fluxes to [a] the water and carbon transfer in the environments (soil and atmosphere), [b] the smaller and larger scale structures of the plant, and [c] its growth and development (Cannell and Thornley, 2000, Coussement et al., 2020, Lacointe and Minchin, 2019).
For instance, axial flow (along the transport tissues) can be represented by Darcy's law. Likewise, lateral flow (leaving or entering the transport tissues), which involves transport across selective plant cell membranes, can be represented by a membrane transport equation (Meunier et al., 2017, Thompson and Holbrook, 2003, Zhou et al., 2020) and depends on pressure or osmotic potential gradients. The plant water and carbon fluxes are hence the results of [a] cellular-scale characteristics, like the number of cell layers between the vascular bundles and the epidermis (Bramley, 2006), [b] plant-scale characteristics, like the topology of the xylem and phloem networks (Lacointe and Minchin, 2019), and [c] water potentials in the soil and atmosphere and photosyntesis and local sink terms that determine sugar concentrations in the phloem. Therefore, FPSMs with transport functions should be able to predict the fluxes of carbohydrates and water from sources to sinks and determine organ growth as a function of plant-external conditions. This implies that these FSPMs should be able to reproduce phenotypic plasticity in different climates and could complement crop models by supplying plant structure parameters, like the ratio of shoot-to-root biomass, computed semi-mechanistically under specific genotype-environment-management combinations.

The quality and applicability of an FSPM depends on the processes and domains it considers: linking different mechanisms (like the flow and use of carbon), domains (soil, plant, atmosphere), and organs (root, shoot, ...) via dynamic feedback loops is essential to understand the short- to long-term effects of specific plant traits on the plant capacity to adapt to the environment (Louarn and Song, 2020, Tuzet et al., 2003). For instance, the short feedback loop between the plant stomatal regulation, water and carbon flows needs to be represented. Indeed, the photosynthesis (source of plant carbon) and transpiration (loss of plant water) occur through the same path and are both influenced by the stomatal opening (Corso et al., 2020, Damour et al., 2010, Dewar, 2002). This loss of water (resp. source of carbon) is interlinked with the xylem (resp. phloem) turgor pressure gradients that drive the flow in the transport tissues (Thompson and Holbrook, 2003). As the stomatal opening depends also on the leaf water status, it is itself influenced by the flow of water in the xylem (Damour et al., 2010, Dewar, 2002, Tuzet et al., 2003). An important longer-term feedback loop involves the plant growth: carbon and water flows regulate the partitioning of assimilated carbohydrates between the different organs (and resulting shoot-to-root ratio) (De Swaef et al., 2022, Lacointe and Minchin, 2019). The growth will, in turn,

indirectly influence the water and carbon fluxes in the soil-plant-atmosphere continuum by changing plant transport network topology and morphology (like the number of roots, leaf area...) and with this, its photosynthetic and water uptake capacities (Chen et al., 2020, Damour et al., 2010, Galindo-Castañeda et al., 2022).

In this work, we present the latest implementation of CPlantBox, a 3D FSPM (Zhou et al., 2020), with PiafMunch (Lacointe and Minchin, 2019) and DuMu^{x} (Koch et al., 2021) coupling. The novel aspect of this CPlantBox implementation lies in the tight coupling with PiafMunch's carbon flow module, in the implementation of CRootBox modules (like plant growth) (Schnepf et al., 2018b) and in the addition of new modules, such as the coupled photosynthesis-transpiration-stomatal regulation (Bonan, 2019c, Tuzet et al., 2003) and water- and carbon-limitation on growth (De Swaef et al., 2022, Schopfer, 2006). While the earlier version of CPlantBox could simulate the effect of a static plant, soil, and user-defined transpiration rate on the plant water and carbon fluxes, the new model can also simulate the influence of the plant water and carbon fluxes on the soil water flow, the plant growth, and the stomatal regulation. The model can consequently represent semi-mechanistically the interactions between the growth of a 3D plant (discrete structure) and the water and carbon fluxes in the soil-plant-atmosphere continuum (continuum equations). CPlantBox offers thus a generic and precise (high spatial and temporal resolution) framework that can be used to test the interaction between known or hypothetical processes (dynamic of plant carbon and water uptake, flow and usage), and understand the causes of emergent behaviours (exudation rate, carbon partitioning). This new development of the model aims to be user-friendly and adapted to a wide variety of plant types.

In this paper, we present:

1. An overview of the equations implemented in the new version of CPlantBox and the schemes used to solve them.
2. An application of the model for a generic C3 monocot. The parameters were set using experimental, literature, and illustrative data. The model was then implemented to look at the effect on the plant's development of a dry spell of one week of at different plant development stages.

2-2 Material of methods

2-2-1 Description of the model

Figure 2-1 gives an overview of the different processes simulated in CPlantBox. In summary: CPlantBox aims to represent the soil-plant-atmosphere continuum and the interactions between those three domains. The environmental conditions are represented by atmospheric forcing (Figure 2-1A.1) and by the soil water initial conditions. The soil water flow equations are then computed during the simulation

via the the open source simulation framework DuMu^x (Koch et al., 2021) (Figure 2-1A.3, see Section 2-2-1-5). The plant domain is represented by a discrete structure made of nodes linked by segments (Figure 2-1A.2a, see Section 2-2-1-2). The atmospheric, leaf boundary layer, and soil variables affect the stomatal opening, which regulates transpiration (water sink) and photosynthesis (sucrose source) (Figure 2-1A.4, see Section 2-2-1-4-1 and Appendix A.3-3). CPlantBox simulates the resulting xylem water flow, lateral root (and leaf) fluxes and soil-root water exchanges (Figure 2-1A.6, see Section 2-2-1-4-2). CPlantBox simulates likewise the resulting mesophyll and sieve tube sucrose flow (Figure 2-1A.5, see Section 2-2-1-4-3). The sucrose dynamic is also influenced by the sucrose usage (or sink), which yields the plant water- and carbon-limited growth, respiration (linked to maintenance and growth), and sucrose exudation (Figure 2-1A.7, see Section 2-2-1-4-5).
The CPlantBox modules have the following dependency order: plant growth $<$ plant water flow $<$ photosynthesis-stomatal regulation $<$ plant sucrose balance. Therefore, it is possible for the user to run only the lower-level modules (for example: plant growth and water flow). Likewise, the user can choose whether or not to run the dynamic soil water flow module.

The main differences between the CPlantBox version presented by Zhou et al. (2020) and the current version are presented in section 2-2-1-1.

In the following sections, we define how plants are represented as a discrete structure in the model (Section 2-2-1-2). Following this, the equations of the implemented modules are listed (Sections 2-2-1-2-2-2-1-5). Finally, we describe the computation loop (Section 2-2-1-6). The schemes used to solve these continuum models on the discrete plant structures are presented in appendix A.6 and a sensitivity analysis of the water-related modules and carbon-related modules are presented in appendix A.7. A definition of the water potential components and of the conductance or conductivity variables used in this paper as well as their notations are given in Appendix A.1. Tables presenting the lists of symbols used with their respective units and (when applicable) values can be found in Appendix A.5-2.

2-2-1-1 Comparison with the former CPlantBox implementation

The functional-structural plant model CPlantBox was first presented by Zhou et al. (2020). The differences between the version of Zhou et al. (2020) and the current version of the model are presented in Figure 2-2.

In summary, the following modules were added or adapted compared with the original model: (a) The plant meristems can be intercalary, as opposed to apical only (see Section 2-2-1-3) and the prescription of the plant topology was unified and made more flexible; (b) water- and carbon-limited growth was implemented (see Section 2-2-1-4-5-2); (c) the pre-existing xylem water flux analytical solver

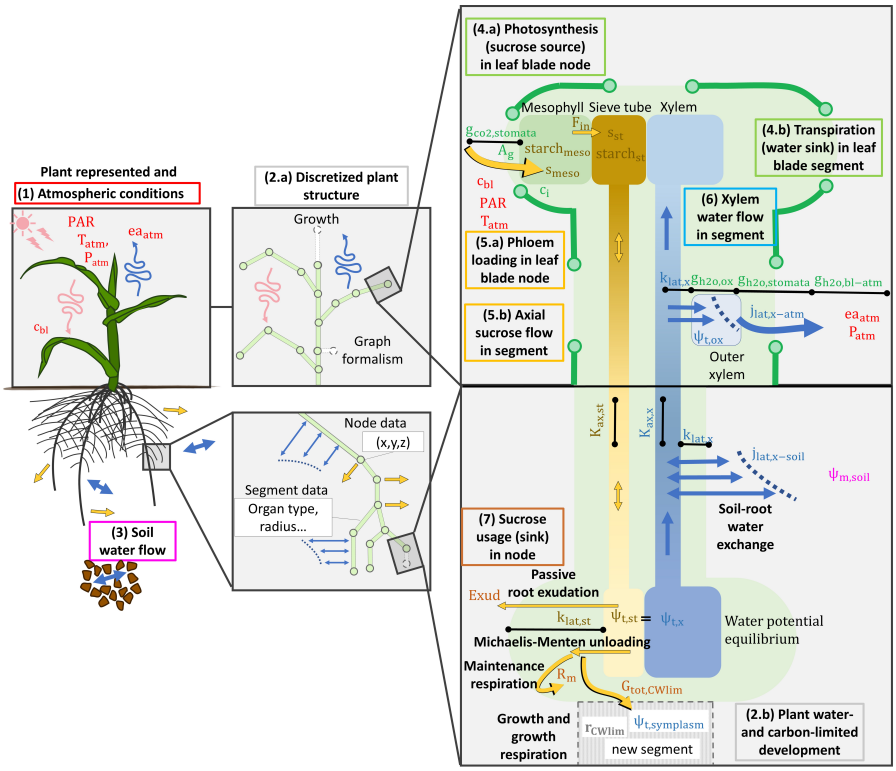

(a) Graphical overview. The water content and flow are defined along the segments. The sucrose concentration and sink or source rates are defined for each plant node. Growth-related sinks can occur in all meristem nodes, maintenance can occur in all nodes, and exudation can occur in all root nodes. Assimilation can occur in all leaf-blade nodes.

- Atmospheric conditions **(1)** influence the model via the atmospheric water potential ea_{atm}, temperature T_{atm} , the incoming light PAR, and CO2 concentration on the leaf surface c_{bl}
- The plant structure (2) affects the segment shape data and node's 3D position and the sucrose demand for growth. It is affected by the water- and carbon-limited growth $G_{tot,CWlim}$ **(7)**
- Soil water potential $\psi_{m,soil}$ **(3)** and xylem water potential $\psi_{p,x}$ **(6)** are linked via the root water uptake rate $j_{lat,x-soil}$
- $\psi_{p,x}$ **(6)** and stomatal opening $g_{h2o,stomata}$ **(4)** are coupled via the outer-xylem water potential $\psi_{t,ox}$ and leaf transpiration rate $j_{lat,x-atm}$
- The sieve-tube sucrose concentration s_{st} **(5)** is influenced by the xylem water potential $\psi_{t,x}$ **(6)** and the gross assimilation rate A_g **(4)**

(b) Written summary of the interactions between the modules.

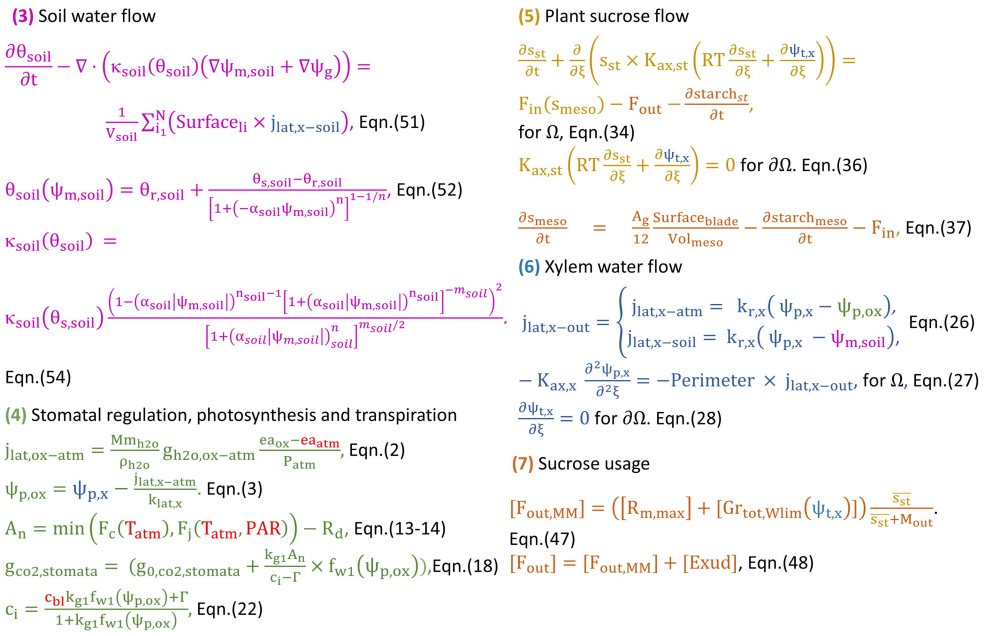

(c) Main driving equations for a C3 plant.

Figure 2-1: Representation of the domains and processes simulated within CPlantBox.

(Meunier et al., 2017) was expanded from the root to the whole plant and implemented (see Section 2-2-1-4-2); (d) the implicit numerical solver PiafMunch (Lacointe and Minchin, 2019) for phloem flows driven by hydrostatic pressure gradients was adapted for tight coupling to CPlantBox (see Section 2-2-1-4-3); (e) the DuMu^x PDE solver (Koch et al., 2021) simulating soil water fluxes with a cell-centered finite volume method (see Section 2-2-1-5); and (f) a coupled photosynthesis (FvCB)-stomatal opening (Tuzet et al., 2003) was added (see Section 2-2-1-4-1).
The tighter coupling between CPlantBox and PiafMunch leads to a higher computation speed, and simpler implementation for the end user. Moreover, the changes done to the PiafMunch code allow its implementation with a dynamic (growing) plant.

2-2-1-2 Structure of the plant

Figure 2-3A.1 presents a conceptual plant, which is defined as an ensemble of organs. We consider the organs: "seed", "root", "stem", or "leaf". The organ class could be extended to include also other organ categories like, for instance, flowers, or fruits. The shape variables are defined with subscripts: *seed*, *root*, *stem*, *leaf*, *st* (sieve tube tissues), *x* (xylem tissues), *seg* (segment), *org* (organ), *sheath* (leaf sheath), or *blade* (leaf blade).

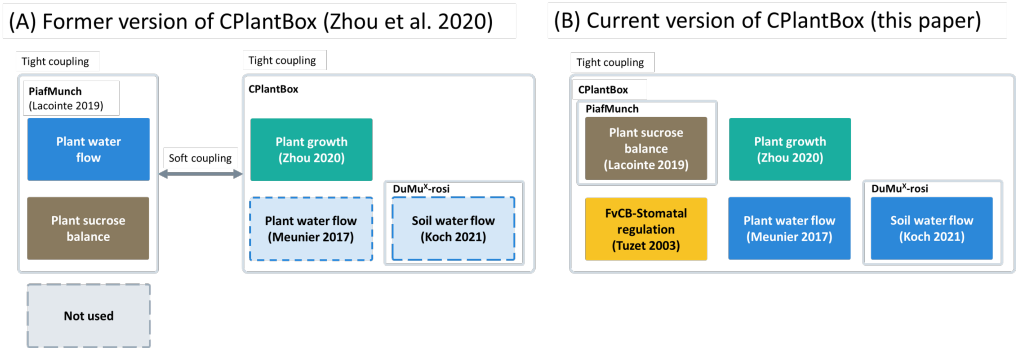

Figure 2-2: Evolution of the CPlantBox framework. Representation of (A) the former and (B) current version of CPlantBox. Main changes include: an expansion of the root water flow module to shoot organs, implementation of a photosynthesis (FvCB) and stomatal opening module, adaptation and implementation within CPlantBox of a phloem flow module. The tighter coupling between the phloem and plant module allows us to use the CPlantBox water module and the DuMu^x-rosi soil flow module.

As represented in Figure 2-1A.2a and Figure 2-3B, plant organs are seen as a series of cylinders (root or stem segments) or cuboids (leaf segments).

As shown in Figure 2-3C, the conceptual plant topology is represented in a discrete way in CPlantBox using graph formalism: the organs are made of 1-D segments, which are defined by their begin- and end-nodes (directed tree). Each node has 3-D coordinates. The orientation of the segments has an effect on the sign of the inner plant flows (see appendix A.6-1).
CPlantBox stores one mean value per segment of each variable defining the plant's morphology, like cylinder radius (or cuboid thickness) a, and cuboid width w, both in cm. Although the sieve tubes and xylem tissues are not explicitly represented, their data are also stored, for instance: number of xylem vessels per cross section (n_x) and radius (a_x). This allows us to directly use or compute at run-time the necessary plant variables.

More information regarding the plant conceptual shape and the related equations can be found in the appendix A.2.

The plant growth rate can either follow an empirical function or, when the water and sucrose modules are run, the water- and sucrose-limited growth rate (r_{CWlim} in $cm\ d^{-1}$), can be used (Figure 2-1A.2b). The equations used to compute r_{CWlim} are presented in the appendix 2-2-1-3. In brief, the initial potential (maximum) organ growth rate is user-defined. CPlantBox then computes the current potential organ growth rate, the limitation caused by the symplast turgor-pressure ($\psi_{p,symplasm}$ in hPa) and by the supply of sucrose. This yields r_{CWlim}, the actual growth rate. This growth is represented via the elongation of existing segments or via the creation of new segments.

The lateral growth of the xylem and phloem tissues can be represented by setting a time-dependent axial conductance, lateral conductivity, as well as a time-dependent cross sectional area of the phloem vessels ($A_{cross,st}$ in cm^2). We neglect the elastic (reversible) variation of the tissue volumes (v in cm^3) according to the turgor pressures (ψ_p in hPa).

The explicit representation of the plant segment and their growth in CPlantBox is presented in more detail by Schnepf et al. (2018b).

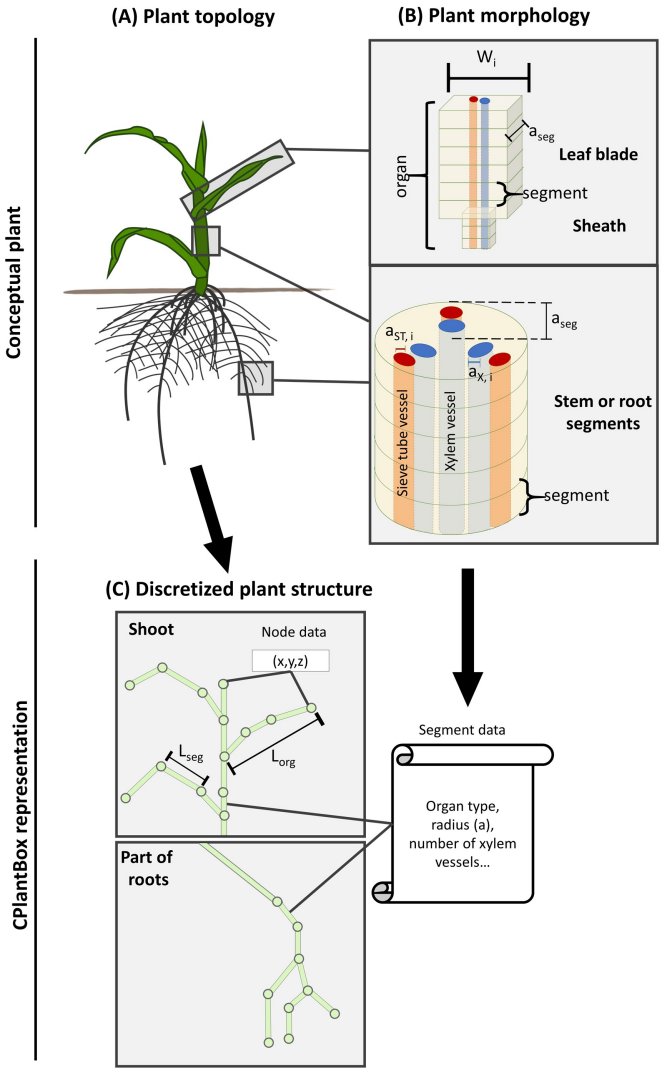

Figure 2-3: Representation of a conceptual plant's topology (A), the morphology of its organs (B) and its discretised representation in CPlantBox (C). The plant topology is represented by the nodes' 3-D coordinates and by their connections (segments). The morphological data are stored in arrays with one value per segment. Note: for better visibility, the cross section of the xylem and phloem vessels are not at the scale of the organs' cross sections.

2-2-1-3 Maximum and carbon and water limited growth rate

$r_{max,org}$ ($cm^3\ d^{-1}$) is the maximum irreversible growth rate of the organ's growing zone when the cell's symplast are at full turgor and the xylem is at the reference water potential ($\psi_{t,x} = 0$). To compute from this the carbon need for growth ($G_{tot,max}$, $mmol\ sucrose\ d^{-1}$), we first divide this growth demand between the nodes of the segments within the growing zone (using the dimensionless f_{length} factor). The water limited growth rate ($r_{Wlim,i}$, in $cm^3 d^{-1}$) and carbon need ($G_{tot,Wlim}$, $mmol\ sucrose\ d^{-1}$) are computed for the node i as follows:

$$r_{Wlim,i} = r_{max,org} \times f_{w2} \times f_{length} \tag{2-1}$$

$$f_{w2} = \frac{max(\psi_{p,symplast}, \psi_{p,crit,2}) - \psi_{p,crit,2}}{-\psi_{o,symplast} - \psi_{p,crit,2}} \tag{2-2}$$

$$r_{max,org} = \frac{v_{t_{end},org} - v_{t_{init},org}}{t_{end} - t_{init}} + \frac{v_{t_{end},org,child} - v_{t_{init},org,child}}{t_{end} - t_{init}} \tag{2-3}$$

$\psi_{p,symplast}$ (cm) is the turgor water pressure within the symplast of the cell. $\psi_{p,crit,2}$ is the minimum symplast turgor potential below which no growth occurs (the "wall yield threshold"). We assume that the aploplast has the same water potential values as the xylem tissues and that the permeability of the membrane between the apoplast and the symplast is high: $\psi_{t,symplast} = \psi_{t,apoplast} = \psi_{t,x}$ (De Swaef et al., 2022, Schopfer, 2006). We thus obtain $\psi_{p,symplast} = \psi_{t,x} - \psi_{o,symplast}$. Also, we do not represent the osmotic regulation to drought. Therefore, we consider that the osmotic water potential in the symplast $\psi_{o,symplast}$ is constant. f_{w2} increases consequently linearly with $\psi_{t,x}$.
As we neglect the elastic flexibility of the cell walls, Eqn.(2-2) is conceptually similar to Zubairova et al. (2016, Eqn.(6)). To facilitate the calibration from empirical data, we normalised the gradient between $\psi_{p,symplast}$ and $\psi_{p,crit,2}$ to obtain the dimensionless f_{w2} which can be multiplied by $r_{max,org}$. The variation of $r_{max,org}$ according to a negative exponential function (Schnepf et al., 2018b, Zhou et al., 2020) can be used to represent implicitly the variation of the irreversible wall extensibility.

The volume of the organs according to their length can be computed from the formulas given in appendix A.2.

$v_{org,child}$ corresponds to the volume of the child (lateral) organs attached to the node i and which are too small to be explicitly represented in the plant structure. They therefore use the sucrose of parent organ's node they are connected to.

As shown in Figure 2-4, the growth zone ($l_{growingZone}$ in cm) of roots are located at the organs' tip (Bramley, 2006), while the leaf growing zone is within the first centimeters at the base of the leaf (Zubairova et al., 2016). For the stem, the growing zone is within the growing phytomer (Kirby, 1988). These growing

zones correspond to the organ nodes where $G_{tot,max} > 0$. Therefore:

$$f_{length} = \frac{l_{seg \cap growingZone}}{l_{growingZone}} \tag{2-4}$$

With $l_{seg \cap growingZone}$ the part of the segment which is within $l_{growingZone}$.

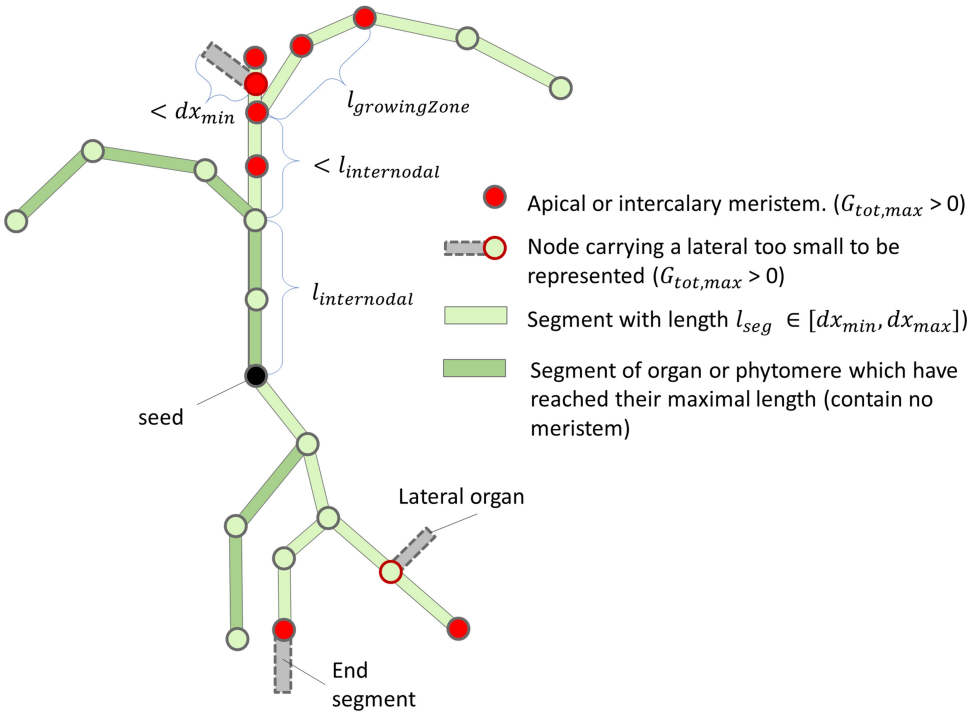

Figure 2-4: Location of a plant's meristems (red-filled points). Roots have apical meristem. Leaves have intercalary meritem at their base. Stems with internode longation have intercalary meristems in each phytomere. These meristem-nodes are carbon sinks used in the sucrose flow module. When segments with meristems are too small to be represented ($l_{seg} < dx_{min}$), like for small laterals or end-segment of organs, the nearest node is used as carbon sink (points with red outline).

After running the phloem module, the water- and carbon-limited growth rate ($r_{CWlim,i}$, $cm^3\ d^{-1}$) for the node i is computed thus:

$$r_{CWlim,i} = \frac{G_{tot,CWlim,i} \times Y}{\rho_s} \tag{2-5}$$

with ρ_s ($mmol\ sucrose\ cm^{-3}$) the plant tissue sucrose density, Y ($-$) the efficiency of the plant sucrose usage for growth. $G_{tot,i}$ ($mmol\ sucrose\ d^{-1}$) is the actual (carbon- and water-limited) plant sucrose usage rate for growth and growth-related respiration given by the sucrose module (see Eq.(2-59)). $r_{CWlim,i}$ of the nodes in the growing zone (cell division and cell elongation) will then be

used by CPlantBox to simulate the organ growth.
For leaves and stems, this representation creates a small growth-compensation (artificial carbon flow) within the organ's growing zone (first centimeters of the leaf or growing phytomer of the stem). For example: carbon used for growth at the start of the growth section can lead to an elongation at the end of the growth section.

A precise description of the methods used in CPlantBox to create segments and define their orientation is presented in Schnepf et al. (2018b). In brief, each time a new node is added, the tropism (resp. bending) function is called *TropismN* (resp. *bendingN*) times. Sets of α and β (*rad*) angles are drawn from, respectively, a normal distribution with zero mean and standard deviation *TropismS* (resp. *bendingS*, in cm^{-1}) and a uniform distribution between 0 and 2π. The α and β set leading to the optimization of the tropism (resp. bending) function is kept (see Figure 2-5.1).
Some functionalities were added in the new version of CPlantBox. It is now possible for existing nodes to be shifted (see Figure 2-5.2), elongating thus the length of the prior segment. For intercalary meristems, this leads to the shift of all the subsequent nodes. In such cases, the directions of the following segments are re-computed.

2-2-1-4 Functions within the plant

2-2-1-4-1 Stomatal regulation, photosynthesis, and transpiration

In the following section, we present the FvCB-stomatal regulation module (see Figure 2-1A.4) (Bonan, 2019c, Farquhar et al., 1980, Leuning, 1995, Tuzet et al., 2003). Transpiration and photosynthesis outside of the leaf blades were neglected. Outputs include [a] the net assimilation rate (A_n in $mmol\ C\ cm^{-2}d^{-1}$), which is the source term used by the sucrose flow module (see Eqn.(2-46)), and [b] the leaf outer-xylem water potential ($\psi_{t,ox}$ in hPa), which is used by the xylem module (see Eqn.(2-35)).

2-2-1-4-1-1 Leaf transpiration rate and stomatal hydraulic conductivity

As presented in Figure 2-6 the water vapor has to go through several compartments, defined by their respective conductances $g_{h2o,Y}$ ($mmol\ cm^{-2}\ d^{-1}$); with Y standing for the outer-xylem pathway to the stomata (ox), the stomata ($stomata$), the leaf boundary layer (bl), the canopy above the leaf ($canopy$), or the air between the top of the canopy and the point of measurement (atm). The total conductance between the outer xylem compartment and the point of humidity measurement ($g_{h2o,ox-atm}$ in $mmol\ cm^{-2}\ d^{-1}$) is obtained by analogy with electric resistances in series:

$$g_{h2o,ox-atm} = (g_{h2o,ox}^{-1} + g_{h2o,stomata}^{-1} + g_{h2o,bl}^{-1} + g_{h2o,canopy}^{-1} + g_{h2o,atm}^{-1})^{-1} \quad (2\text{-}6)$$

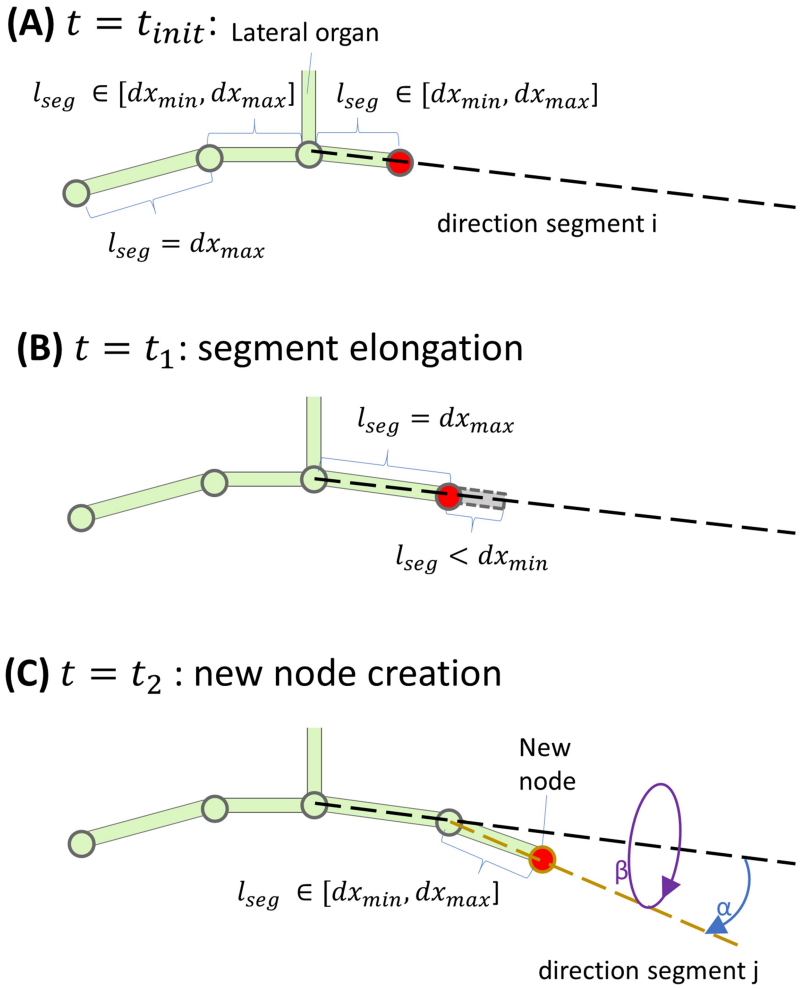

Figure 2-5: Growth of the discretized plant structure. (A) All segments have a length $l_{seg} > dx_{min}$. (B) All segments are elongated until reaching $l_{seg} = dx_{max}$, unless the internodal distance is reached beforehand. Segments of length $l_{seg} < dx_{min}$ are not represented. (C) Once a segment has reached it maximum length, the organ is further elongated by adding a new node. The position of the new node is selected according to the result of the tropism (roots) or bending (shoot) function. Adapted from Schnepf et al. (2018b, Figure A1)

$g_{h2o,ox}^{-1}$ includes the resistances of different leaf elements, such as the mesophyll. The computation of $g_{h2o,stomata}$ and $g_{h2o,ox}$ are presented in Section 2-2-1-4-1-3. The evaluation of the other H_2O conductances is presented in Appendix A.3-3.
The area-specific water vapor flow rate ($j_{lat,ox-atm}$ in $cm^3\ cm^{-2}\ d^{-1}$) corresponds to the water flow from the outside of the vascular bundle-sheath to the point of measurement of atmospheric variables. It be obtained from Fick's law applied to ideal gases (Nobel, 2009c, Tuzet et al., 2003):

$$j_{lat,ox-atm} = \frac{Mm_{h2o}}{\rho_{h2o}} \times g_{h2o,ox-atm} \times (\frac{ea_{ox} - ea_{atm}}{P_{atm}}) \quad (2\text{-}7)$$

With Mm_{h2o} ($kg\ mmol^{-1}$) and ρ_{h2o} ($kg\ cm^{-3}$) respectively the water molar mass and density, ea (hPa) the actual vapor pressure, P_{atm} (hPa) the atmospheric air pressure. ea_{ox} can be obtained from $\psi_{t,ox}$ using Eqn.(A-6). We do not represent the variations in water storage along the evaporation pathway. We have consequently: $j_{lat,ox-atm} = j_{lat,x-ox} = j_{lat,x-atm}$. All the elements of the considered leaf tissue are at the same height ($\psi_{g,ox} = \psi_{g,x}$) and we neglect the xylem osmotic potential ($\psi_{o,x}$). $\psi_{p,ox}$ can therefore be obtained from:

$$\psi_{p,ox} = \psi_{p,x} - \frac{j_{lat,x-atm}}{k_{lat,x}} \quad (2\text{-}8)$$

with $k_{lat,x}$ the lateral conductivity of the vascular bundle sheath ($cm\ hPa^{-1}\ d^{-1}$). The exact method used to compute $\psi_{p,ox}$ is presented in Eqn.(A-33).

2-2-1-4-1-2 Carbon assimilation

In this section, we present the evaluation of A_n as limited by the rate of carboxylation by Rubisco (F_c in $mmol\ C\ cm^{-2}d^{-1}$) and by the rate of RuBP regeneration via electron transport (F_j in $mmol\ C\ cm^{-2}d^{-1}$).

2-2-1-4-1-2-1 Rubisco activity at the sites of carboxylation

Rubisco activity at the sites of carboxylation

F_{cmax}^{25} ($mmol\ cm^{-2}\ d^{-1}$) corresponds to the maximum F_c for $T = 298.15\ K$. Qian et al. (2021) defined F_{cmax}^{25} according to the leaf chlorophyll content (Chl in $mmol\ cm^{-2}$):

$$F_{cmax}^{25} = k_{chl1} \times Chl + k_{chl2} \quad (2\text{-}9)$$

with k_{chl1} and k_{chl2} fitting parameters representing the empirical relationship between F_{cmax}^{25} and Chl. k_{chl1} and k_{chl2} can be set according to the assimilation rate when F_c is limiting for photosynthesis. Chl is currently an input parameter and can be used to represent the effect of plant nitrogen uptake.
F_{cmax} ($mmol\ cm^{-2}\ d^{-1}$) is the maximal F_c ($mmol\ cm^{-2}\ d^{-1}$) at a temperature T:

$$F_{cmax} = F_{cmax}^{25} \times Arrhenius(T_{seg}, E_{a,v}) \times TempInhib(T_{seg}, E_{d,v}) \quad (2\text{-}10)$$

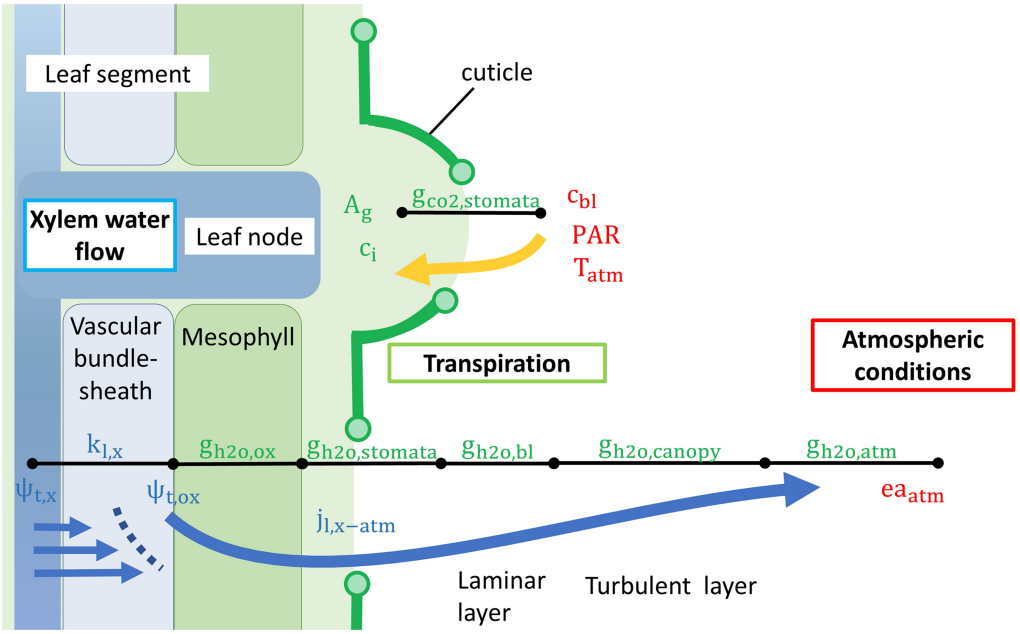

Figure 2-6: Water flow between the leaf xylem and the point of humidity measurement. The numbering of the image sections were kept identical to those presented in Figure 2-1A. The xylem total water potential ($\psi_{t,x}$) varies along the plant segments while each segment has one mean outer-xylem water potential ($\psi_{t,ox}$).

$E_{a,v}$ and $E_{d,v}$ ($mJ\ mmol^{-1}$) are respectively the activation and deactivation energy for F_{cmax}. $Arrhenius(T_{seg}, E_{a,v})$ represents the result of the Arrhenius function (see Eqn.(A-7)) and $TempInhib(T_{seg}, E_{d,v})$ represents the result of the temperature inhibition function (see Eqn.(A-8)).
F_c is affected by $\Gamma*$ ($mmol\ CO_2\ mmol\ air^{-1}$), the CO_2 compensation point (equilibrium CO_2 level reached when $A_n = 0$) in the absence of mitochondrial respiration (R_d in $mmol\ cm^{-2}\ d^{-1}$). $\Gamma*$ and R_d are obtained from Eqn.(A-9) and (2-21), respectivelly.

F_c follows a Michaelis-Menten function and depends on the CO_2 and O_2 molar fractions in the substomatal cavity, respectively c_i ($mmol\ CO_2\ mmol\ air^{-1}$) and o_i ($mmol\ O_2\ mmol\ air^{-1}$).

F_c can then be computed using Eqn.(2-11) (Bonan, 2019c, Tuzet et al., 2003):

$$F_c = \begin{cases} max(F_{cmax} \times \frac{c_i - \Gamma*}{c_i + M_{co2}(1 + \frac{o_i}{M_{o2}})}, 0) & \text{, for C3 plants} \\ F^{25}_{cmax} \times Q10^{\frac{T - T_{refq10}}{10}} \times \frac{1}{1 + e^{s1(T - s2)}} \frac{1}{1 + e^{s3(s4 - T)}} & \text{, for C4 plants} \end{cases} \tag{2-11}$$

(2-12)

With M_{co2} and M_{o2} ($mmol\ mmol^{-1}$) the Michaelis coefficients for, respectively, CO_2 and O_2 (see Eqn.(A-9)). $Q10$ is a coefficient widely used in the scientific literature and defines the temperature sensitivity of chemical reactions: a higher $Q10$ value leads to a steeper temperature-caused increase. T_{refq10} defines the reference temperature: $|Q10^{\frac{T - T_{refq10}}{10}}|_{T=T_{refq10}} = 1$. $s1$ (resp. $s3$) ($-$) defines the rate of decrease in F_c with increasing (resp. decreasing) T. $s2$ and $s4$ (K) are the values of T at which $F_c = \frac{F^{25}_{cmax}}{2}$. The computation of c_i is presented in Section 2-2-1-4-1-4.

2-2-1-4-1-2-2 Electron transport rate

Electron transport rate

$Je^{25}_{max}(mmol\ cm^{-2}\ d^{-1})$ is the the maximum electron transport rate for $T = 298.15\ K$. It is assumed to be proportional to F^{25}_{cmax} (Tuzet et al., 2003):

$$Je^{25}_{max} = k_{jmax} F^{25}_{cmax} \tag{2-13}$$

with k_{jmax} ($-$) a set coefficient which can be defined according to the light saturation point for photosynthesis under well-watered conditions. Je_{max} ($mmol\ cm^{-2}\ d^{-1}$) is the the maximum electron transport rate and is computed with the following equation:

$$Je_{max} = Je^{25}_{max} \times Arrhenius(T_{seg}, E_{a,j}) \times TempInhib(T_{seg}, E_{d,j}) \tag{2-14}$$

with $E_{a,j}$ and $E_{d,j}$ ($mJ\ mmol^{-1}$), respectively the activation and deactivation energy for Je_{max}.

We can then obtain Je ($mmol\ cm^{-2}\ d^{-1}$), the electron transport rate for a value of photosynthetically active radiation absorbed (PAR in $mmol\ photons\ cm^{-2}\ d^{-1}$):

$$\omega Je^2 - (\alpha PAR + Je_{max})Je + \alpha PAR \times Je_{max} = 0 \tag{2-15}$$

with ω $(-)$ a parameter that determines the shape of the parabola and α $(-)$ the quantum yield of whole-chain electron transport.
Je corresponds to the smaller root of the quadratic equation (Bonan, 2019c):

$$Je = \frac{\alpha PAR + Je_{max} - \sqrt{(\alpha PAR + Je_{max})^2 - 4\omega\alpha PAR Je_{max}}}{2\omega} \tag{2-16}$$

From Je, we can compute F_j :

$$F_j = \begin{cases} max(\frac{Je}{4} \times \frac{c_i - \Gamma*}{c_i + 2\Gamma*}, 0) & \text{, for C3 plants} \\ \alpha PAR & \text{, for C4 plants} \end{cases}, \tag{2-17}$$

2-2-1-4-1-2-3 Carbon fixation by PEP

Carbon fixation by PEP

For C4 plants, we compute an additional PEP-limited assimilation rate, following the description given below, taken from Bonan (2019c).

F_{kp}^{25} ($mmol\ cm^{-2}\ d^{-1}$) is the initial slope of the CO_2 response curve for F_p at $T = 298.15\ K$. Bonan (2019c) defined F_{kp}^{25} according to F_{cmax}^{25}:

$$F_{kp}^{25} = F_{cmax}^{25} \times 0.02 \times 1e6 \tag{2-18}$$

At a temperature T, we have:

$$F_{kp} = F_{kp}^{25} \times Q10^{\frac{T - T_{refq10}}{10}} \tag{2-19}$$

From F_{kp} we obtain F_p:

$$F_p = \begin{cases} 0 & \text{, for C3 plants} \\ (c_i - \Gamma*) \times F_{kp} & \text{, for C4 plants} \end{cases}, \tag{2-20}$$

Contrary to Bonan (2019c), we make F_p dependent on $(c_i - \Gamma*)$ instead of c_i. Indeed, we could otherwise have $A_n > 0$ when $c_i < \Gamma*$, leading to a negative value of g_{co2}, the stomatal opening.

2-2-1-4-1-2-4 Gross and net assimilation rates

Gross and net assimilation rates

The gross and net CO_2 assimilation rates (respectively A_g and A_n in $mmol\ cm^{-2}\ d^{-1}$) correspond to the quantity of sucrose gained by the plant per

unit of leaf exchange surface and time. They are computed from F_c (Eqn.(2-11)), F_j (Eqn.(2-17)), and F_p (Eqn.(2-20)):

$$R_d = \begin{cases} R_d^{25} \times Arrhenius(T_{seg}, E_{a,R_d}) & \text{, for C3 plants} \\ Rd^{25} \times Q10^{\frac{T-T_{refq10}}{10}} \frac{1}{1+e^{s5(T-s6)}} & \text{, for C4 plants} \end{cases}, \quad (2\text{-}21)$$

$$A_g = min(F_c, F_j, F_p) \quad (2\text{-}22)$$

$$A_n = A_g - R_d \quad (2\text{-}23)$$

A_n is then used as source term for the sucrose flow (see Section 2-2-1-4-3-2). When $A_g < R_d$, we have a negative sucrose source in the mesophyll (see Eqn.(2-46)). In such cases, R_d is also limited by the amount of sucrose available in the mesophyll and can be lower than the value obtained from Eqn.(2-21).

2-2-1-4-1-3 Leaf water and CO_2 conductance

The molar conductances of the domain Y to CO_2 and H_2O (respectively $g_{co2,Y}$ and $g_{h2o,Y}$ in $mmol\ cm^{-2}d^{-1}$) correspond to the flow of gaseous CO_2 (resp. H_2O) per unit of CO_2 concentration (resp. water vapor pressure). $g_{co2,stomata}$ depends on the gradient between c_i and the CO_2 compensation point (Γ in $mmol\ CO_2\ mmol\ air^{-1}$). Γ is obtained from Eqn.(2-24).

$$\Gamma = \frac{\Gamma * + M_{co2} R_d (1 + \frac{o_i}{M_{o2}})/F_{cmax}}{1 - R_d/F_{cmax}} \quad (2\text{-}24)$$

A low $\psi_{t,ox}$ will lead to lower $g_{co2,stomata}$ and $g_{h2o,ox}$. This response is represented empirically via a dimensionless water scarcity factor (f_{w1}):

$$f_{w1} = f_{w1r} + (1 - f_{w1r}) \frac{1 + e^{k_{fw1}\psi_{t,crit,1}}}{1 + e^{k_{fw1}(\psi_{t,crit,1} - \psi_{t,ox})}} \quad (2\text{-}25)$$

with $\psi_{t,crit,1}$ (hPa) the critical water potential. k_{fw1} ($-$) is a sensitivity parameter. A higher value of k_{fw1} leads to a stronger variation of f_{w1} around $\psi_{t,crit,1}$, whereas a lower value leads to a more gradual response.

$g_{h2o,ox}$ ($mmol\ cm^{-2}d^{-1}$), the conductivity to water of the pathway between the xylem membrane and the substomatal cavity, is computed from its maximum value ($g_{h2o,ox,max}$, assumed constant) and the water scarcity factor f_{w1}: $g_{h2o,ox} = g_{h2o,ox,max} \times f_{w1}$.
$g_{h2o,stomata}$ and $g_{co2,stomata}$ are computed following the model of Tuzet et al. (2003):

$$g_{h2o,stomata} = k_{g2,stomata} \times g_{co2,stomata} \quad (2\text{-}26)$$

$$g_{co2,stomata} = g_{0,co2,stomata} + \frac{k_{g1} A_n}{c_i - \Gamma} \times f_{w1} \quad (2\text{-}27)$$

with $g_{0,co2,stomata}$ ($mmol\ cm^{-2}d^{-1}$) the residual stomatal opening. k_{g2} accounts for the H_2O to CO_2 ratio of molecular diffusivity—$k_{g2,stomata} = 1.6$ (Tuzet et al., 2003). As opposed to the model of Leuning (1995), the model of Tuzet et al.

(2003) model uses c_i and not c_{bl} ($mmol\ CO_2\ mmol\ air^{-1}$), the CO_2 molar fraction at the leaf surface. Indeed, c_i was shown to have a stronger influence on $g_{co2,stomata}$ (Damour et al., 2010). k_{g1} $(-)$ is a fitting parameter representing the effect of A_g on $g_{co2,stomata}$. It can be computed from the expected $\frac{c_i}{c_{bl}}$ ratio when $f_{w1} = 1$ using Eqn.(2-31) presented in the next section.

2-2-1-4-1-4 Substomatal CO_2 molar fraction

Following an Ohm's law adaptation of Fick's law of diffusion, c_i ($mmol\ mmol^{-1}$) can be calculated with the "CO_2 supply function" (Damour et al., 2010, Dewar, 2002):

$$c_i = c_{atm} - \frac{A_n}{g_{co2,stomata-atm}} \tag{2-28}$$

with c_{atm} ($mmol\ mmol^{-1}$) the CO_2 molar fraction at the point of measurement. However, when A_g is low, our fixed-point iteration solving scheme (see Section 2-2-1-6) does not converge and gives unrealistic c_i value ($c_i \leq 0$ or $c_i \gg c_{bl}$). For this reason, similarly to Dewar (2002), we use the CO_2 molar fraction on the leaf surface (c_{bl} in $mmol\ mmol^{-1}$).

$$c_i = c_{bl} - \frac{A_n}{g_{co2,stomata}} \tag{2-29}$$

With c_{bl} an input parameter.
We then combine Eqn.(2-27) and Eqn.(2-29) and we neglect $g_{0,co2,stomata}$:

$$c_i - c_{bl} = \frac{A_n}{\frac{k_{g1}A_n}{c_i-\Gamma} \times f_{w1}} \tag{2-30}$$

$$c_i = \frac{c_{bl}k_{g1}f_{w1} + \Gamma}{1 + k_{g1}f_{w1}} \tag{2-31}$$

If we assume that c_{bl} and k_{g1} are set parameters and $\Gamma \ll c_{bl}$, the c_i value then mainly depends on f_{w1} $(-)$, the water scarcity factor of the stomatal model. This follows field observations, where $\frac{c_{bl}}{c_i}$ is usually seen to be constant, except in case of water scarcity (Damour et al., 2010).

2-2-1-4-2 Xylem water flow

Darcy's law is seen as a good approximation to compute the axial flux of water in the xylem ($J_{ax,x}$ in $cm^3\ d^{-1}$) (Roose and Fowler, 2004). Moreover, we assume that the xylem solution has physical characteristics similar to that of pure water. We therefore neglect $\psi_{o,x}$ (hPa), the xylem osmotic potential. We thus have $\psi_{t,x} = \psi_{p,x} + \psi_{g,x}$, with $\psi_{t,x}$ the total xylem solution potential, $\psi_{p,x}$ the xylem hydrostatic

potential and $\psi_{g,x}$ the gravitational potential, all in hPa. For a straight xylem segment we obtain:

$$J_{ax,x} = -K_{ax,x}\left(\frac{\partial \psi_{p,x}}{\partial \xi} + \frac{\partial \psi_{g,x}}{\partial \xi}\right), \quad (2\text{-}32)$$

$$J_{ax,x} = -K_{ax,x}\frac{\partial \psi_{t,x}}{\partial \xi}, \quad (2\text{-}33)$$

$$K_{ax,x} = \frac{\pi}{8\mu_{h2o}} \times \sum_{i}^{n_x} a_{x,i}^4 \quad (2\text{-}34)$$

$K_{ax,x}$ ($cm^4\ hPa^{-1}d^{-1}$) is the xylem intrinsic axial conductance and ξ (cm) corresponds to the local axial coordinate of the plant. μ_{h2o} ($hPa\ d$) is the temperature-dependent viscosity of pure water. $a_{x,i}$ (cm) is the radius of the xylem vessel number i in the segment cross-section, n_x is the number of xylem vessels in the cross-section.
The sink and source for water are given by the lateral water flow ($j_{lat,x-out}$ in $cm\ d^{-1}$), which corresponds to the xylem-soil ($j_{lat,x-soil}$) or xylem-atmosphere ($j_{lat,x-atm}$) water exchange:

$$j_{lat,x-out} = \begin{cases} j_{lat,x-soil} = k_{lat,x}(\psi_{p,x} - \psi_{m,soil}) & \text{, if root} \\ j_{lat,x-atm} = k_{lat,x}(\psi_{p,x} - \psi_{p,ox}) & \text{, if leaf blade} \end{cases}, \quad (2\text{-}35)$$

where $k_{lat,x}$ ($cm\ hPa^{-1}\ d^{-1}$) is the lateral hydraulic conductivity of the root cortex (for roots) or of the vascular bundle-sheath (for leaves). $\psi_{m,soil}$ is the soil matric water potential in hPa. $\psi_{m,soil}$ is given by the soil water flow module (see Section 2-2-1-5) and $\psi_{p,ox}$ is given by the FvCB-stomatal regulation module (see Section 2-2-1-4-1, Eqn.2-8). CPlantBox offers several options for setting $k_{lat,x}$ and $K_{ax,x}$ (constant, age dependent, organ type dependent...). $j_{lat,x-out} > 0$ represents a water loss for the plant.
We do not currently represent the effect of cavitation on the xylem conductivity. Likewise, we do not represent the effect of the water flow between the phloem and the xylem on the xylem water balance. This lateral water exchange is very low when compared with the xylem flow during the day (Hölttä et al., 2006, Windt et al., 2006, Zhou et al., 2020, Fig.2.B). However, because of this simplification, we cannot simulate the "Münch's counterflow" (xylem water flux driven by the phloem water flux) although it is the main force driving the xylem solution at night (Hölttä et al., 2006, Windt et al., 2006, Zhou et al., 2020, Fig.2.B). However, this flow remains low and has a limited effect on our output variables of interest (transpiration rate, growth rate, carbon partitioning).

We neglect the variation of water storage in the plant. The mass balance gives us thus the following driving equation for the xylem solution flow (see Figure 2-1A.6):

$$-K_{ax,x}\frac{\partial^2 \psi_{p,x}}{\partial^2 \xi} = -p_{seg} \times j_{lat,x-out} \text{ for } \Omega \backslash \partial\Omega, \quad (2\text{-}36)$$

$$\frac{\partial \psi_{p,x}}{\partial \xi} = 0 \text{ for } \partial\Omega \text{ (all organ end-nodes)} \quad (2\text{-}37)$$

with p_{seg} (cm) the perimeter of the plant exchange zone, Ω the domain considered (here the plant), and $\partial\Omega$, the domain's boundary (here: the tip or end-node of each organ). Thus, the soil (Section 2-2-1-5, Figure 2-1A.3), xylem (Figure 2-1A.6), and photosynthesis-stomatal opening subproblems (Section 2-2-1-4-1-1, Figure 2-1A.4b) are coupled via Eqn.(2-36).

2-2-1-4-3 Sucrose balance

In the following section, we present the equations defining the plant sucrose dynamic (Figure 2-1A.5), yielding the sucrose concentration in the sieve tube (s_{st} in $mmol\ sucrose\ cm^{-3}$) and in the leaf mesophyll (s_{meso} in $mmol\ sucrose\ cm^{-3}$). The flow and concentration of sucrose in other tissues (such as the parenchyma) is not explicitly represented. The module also yields $[F_{out}]$ $(mmol\ sucrose\ cm^{-3}d^{-1})$, the s_{st} loss rate, which gives the exudation rate and the plant water- and carbon-limited growth (see Section 2-2-1-4-5).

2-2-1-4-3-1 Sucrose in the phloem

Similarly to Section 2-2-1-4-2, we compute $J_{ax,st}$ $(cm^3\ d^{-1})$, the sieve tube axial solution flow, by implementing Darcy's law (see Eqn.(2-32)). We therefore obtain (Thompson and Holbrook, 2003):

$$J_{ax,st} = -K_{ax,st}\left(\frac{\partial\psi_{p,st}}{\partial\xi} + \frac{\partial\psi_{g,st}}{\partial\xi}\right) \tag{2-38}$$

$$K_{ax,st} = \frac{\pi}{8\mu_{st}} \times \sum_{i}^{n_{st}} a_{st,i}^4 \times \beta \tag{2-39}$$

$K_{ax,st}$ $(cm^4\ hPa^{-1}d^{-1})$ is the sieve tube axial intrinsic conductance and $\psi_{p,st}$ (hPa) is the sieve tube hydrostatic pressure.
μ_{st} $(hPa\ d)$ is the viscosity of the sieve tube solution and it is computed from the temperature and sucrose concentration according to the method of Mathlouthi and Reiser (1995, Eqn. (6.29)) as implemented by Lacointe and Minchin (2019).
$a_{st,i}$ (cm) is the radius of the sieve tube number i in the segment cross-section, n_{st} is the number of sieve tubes in the cross-section.
Following the recommendation of Thompson and Holbrook (2003), we added the parameter β $(-)$ to the computation of $K_{ax,st}$ to represent the ratio of axial conductance with sieve plates to that without. β can be evaluated via empirical data or from images of phloem and sieve plates (Thompson and Holbrook, 2003). This parameter is not needed for the xylem tissues as the opening in its cells' end walls are much larger (Nobel, 2009a). CPlantBox offers several options for defining a_{st} (constant, organ type dependent...).

We assumed water equilibrium between the xylem and phloem (see appendix A.4 for more explanations). We therefore obtain:

$$\psi_{t,st} = \psi_{t,x} \tag{2-40}$$

We assume that there is a semi-permeable membrane (permeable to water but not to sucrose) between the phloem and the xylem. The total potential in the phloem, $\psi_{t,st}$, is equal to the sum of sieve tube solution's hydrostatic ($\psi_{p,st}$, hPa), gravitational ($\psi_{g,st}$, hPa), and osmotic potential ($\psi_{o,st}$, hPa). We consequently obtain:

$$\psi_{p,st} + \psi_{g,st} = \psi_{t,x} - \psi_{o,st} \tag{2-41}$$

We consider that sucrose makes up the largest fraction of solutes in the sieve tube solution (De Schepper et al., 2013). The $\psi_{o,st}$ can therefore be computed according to van't Hoff relation: $\psi_{o,st} = -RT_{seg}s_{st}$. With T_{seg} the segment's temperature in K. As explained by Hall and Minchin (2013) and Cabrita (2011, Section 2.2.3.1), the van't Hoff relation may not be appropriate when $s_{st} > 0.5$ $mmol\ sucrose\ cm^{-3}$. We kept nonetheless that definition of $\psi_{o,st}$ for this first implementation of the model.
Eqn.(2-38) becomes:

$$J_{ax,st} = -K_{ax,st}\left(\frac{\partial \psi_{t,x}}{\partial \xi} + RT_{seg}\frac{\partial s_{st}}{\partial \xi}\right) \tag{2-42}$$

Using the relations defined above, we do not need so solve another equation for $\psi_{p,st}$ but can at all times compute it from other known state variables, namely $\psi_{t,x}$ (see Eqn.(2-36)) and s_{st}.

Assuming then that sucrose is transported within the phloem by advection only, with no lateral gradient, constant initial conditions and no-flux boundary conditions, we obtain:

$$\frac{\partial s_{st}}{\partial t} + \frac{\partial}{\partial \xi}\left(s_{st} \times K_{ax,st}\left(RT_{seg}\frac{\partial s_{st}}{\partial \xi} + \frac{\partial \psi_{t,x}}{\partial \xi}\right)\right) - [F_{in}] + [F_{out}] + \frac{\partial starch_{st}}{\partial t} = 0 \quad \text{for } \Omega \backslash \partial\Omega,\ t > t_0 \tag{2-43}$$

$$s_{st} = s_{st,0} \quad \text{for } t = t_0, \tag{2-44}$$

$$K_{ax,st}\left(RT_{seg}\frac{\partial s_{st}}{\partial \xi} + \frac{\partial \psi_{t,x}}{\partial \xi}\right) = 0 \quad \text{for } \partial\Omega \tag{2-45}$$

with $[F_{in}]$ and $[F_{out}]$ ($mmol\ sucrose\ cm^{-3}d^{-1}$), respectively the source and sink of s_{st} (see sections 2-2-1-4-3-2 and 2-2-1-4-5 respectively), $starch_{st}$ ($mmol\ sucrose\ cm^{-3}$) the concentration of starch in the sieve tube (see sections 2-2-1-4-4), and t_0 the time at the beginning of the simulation.

2-2-1-4-3-2 Sucrose in the mesophyll

Like s_{st}, we solve s_{meso} ($mmol\ sucrose\ cm^{-3}$), the sucrose concentration in the leaf source compartments (considered to be the mesophyll cells). As represented in

Figure 2-1A.5a, A_n is obtained from the photosynthesis module (see Section 2-2-1-4-1) and leads to a variation of s_{meso}. Then occurs an active phloem loading from the mesophyll to the sieve tube ($[F_{in}]$ in *mmol sucrose* cm^{-3} d^{-1}) (De Schepper et al., 2013), defined according to Stanfield and Bartlett (2022). We do not simulate axial flow within the mesophyll compartments. In summary:

$$\frac{\partial s_{meso}}{\partial t} = \frac{A_n}{12}\frac{p_{blade} \times l}{v_{meso}} - [F_{in}] - \frac{\partial starch_{meso}}{\partial t}, \text{ for } t > t_0 \quad (2\text{-}46)$$

$$s_{meso} = s_{meso,0} \quad \text{for } t = t_0, \quad (2\text{-}47)$$

$$[F_{in}] = \frac{F_{in,max}}{v_{st}} \times \frac{s_{meso}}{M_{meso} + s_{meso}} \times e^{-\beta_{meso} s_{st}} \quad (2\text{-}48)$$

p_{blade} (cm) and v_{meso} (cm^3) are respectively the leaf blade perimeter and mesophyll volume. The factor 12 allows us to go from *mmol C* d^{-1} to *mmol sucrose* d^{-1}. $F_{in,max}$ (*mmol sucrose* d^{-1}) is the maximum loading rate into the sieve tube, β_{meso} $(-)$ is a factor indicating the strength of the s_{st} down-regulation for loading. M_{meso} (*mmol sucrose* cm^{-3}) is the Michaelis-Menten coefficient for the sucrose loading. $starch_{meso}$ (*mmol sucrose* cm^{-3}) is the concentration of starch in the mesophyll (see sections 2-2-1-4-4). When $A_n < 0$, the sucrose in the mesophyll is used for mitochondrial respiration (R_d, see Eqn.(2-21)).

2-2-1-4-4 Sucrose storage

We represent the storage of sucrose as starch ($s_{starch,X}$ in *mmol sucrose* cm^{-3}) via Eqn.(2-49), taken from Lacointe and Minchin (2019):

$$\frac{\partial starch_X}{\partial t} = \frac{F_{max,starch,X} \times s_X}{M_{starch,X} + s_X} - k_{hyd,starch,X} \times starch_X + k_{targ,starch,X}(s_X - s_{targ,X}) \quad (2\text{-}49)$$

with the X subscript standing for *st* or *meso*. As Lacointe and Minchin (2019) explained in their paper, this equation allows the user to represent several dynamic. A Michaelis-Menten synthesis dynamic can be represented by setting a non-zero (a) maximum value of *starch* synthesis ($F_{max,starch,X}$ in *mmol sucrose* cm^{-3} d^{-1}) and (b) Michaelis constant ($M_{starch,X}$ in *mmol sucrose* cm^{-3}). Relative starch hydrolyse rate is given by $k_{hyd,starch,X}$ (d^{-1}). Starch metabolism is dependent on a target s_X ($s_{targ,X}$ in *mmol sucrose* cm^{-3}) if the related constant $k_{targ,starch,X}$ (d^{-1}) is not null.

2-2-1-4-5 Sucrose usage

In this section, we present how to compute the maximal or water-limited sucrose usage rates for each sink categories. From this we obtain the total sucrose sink term ($[F_{out}]$ in *mmol sucrose* cm^{-3} d^{-1}) used in the s_{st} balance equation (see Eqn.(2-43) and Figure 2-1A.7). We also present how $[F_{out}]$ is used to compute the realized (s_{st}-limited) sinks (Figure 2-1A.2b).

In the plants, s_{st} can be used for growth (Gr, in *mmol sucrose* d^{-1}), root exudation ($Exud$, in *mmol sucrose* d^{-1}) and respiration (Dilkes et al., 2004, Galindo-Castañeda et al., 2022, Thornley and Cannell, 2000). s_{st} respiration can be divided in two conceptual categories: growth respiration (R_{gr}, in *mmol sucrose* d^{-1}), which is linked to Gr; and maintenance (or residual) respiration (R_m, in *mmol sucrose* d^{-1}). This conceptual representation follows the growth-maintenance paradigm (Amthor, 2000, Roux et al., 2001, Thornley and Cannell, 2000). Other sucrose sinks, notably starch synthesis, are not represented (discussed in Section 2-4-2). Each carbon sink X (*mmol sucrose* d^{-1}) can also be given in concentration units (with $[X]$ in *mmol sucrose* cm^{-3} d^{-1}), obtained from $[X] = \frac{X}{v_{st}}$, with v_{st} (cm^3) the volume of the sieve tube.

2-2-1-4-5-1 Exudation

The root exudation rate ($Exud$, in *mmol sucrose* d^{-1}) is assumed to be a passive process (Galindo-Castañeda et al., 2022), dependent on the lateral sucrose gradient:

$$Exud = k_{lat,st} \times p_{seg} \times l \times max(\bar{s_{st}} - s_{soil}, 0) \quad (2\text{-}50)$$

$$\bar{s_{st}} = min(s_{st} - s_{st,min}, 0.) \quad (2\text{-}51)$$

with $k_{lat,st}$ (cm d^{-1}) the lateral sieve tube conductivity for sucrose. Similarly to $k_{lat,x}$, CPlantBox offers several options for setting $k_{lat,st}$ (constant, root order dependent...). s_{soil} (*mmol sucrose* cm^{-3}) is the mean soil carbon concentration in equivalent sucrose. l (in cm) is the evaluated length. $s_{st,min}$ (*mmol sucrose* cm^{-3}) is the minimum sucrose concentration below which no usage of sucrose occurs. This parameter allows the user to define more easily a minimum sucrose concentration to follow experimental observations and to respect the necessary conditions for water equilibrium between xylem and phloem (see appendix A.4).

2-2-1-4-5-2 Water-limited growth and growth respiration

The water-limited (or potential) growth-related sink ($G_{tot,Wlim}$, in *mmol sucrose* d^{-1}) corresponds to the potential carbon used for growth (Gr_{Wlim}) and growth related respiration ($R_{gr,Wlim}$). It is computed as follows:

$$G_{tot,Wlim} = R_{gr,Wlim} + Gr_{Wlim}, \quad (2\text{-}52)$$

$$Gr_{Wlim} = r_{Wlim}\rho_s A_{cross,seg}, \quad (2\text{-}53)$$

$$R_{gr,Wlim} = Gr_{Wlim}\frac{1-Y}{Y} \quad (2\text{-}54)$$

with Y ($-$) the sucrose use efficiency for growth. ρ_s (*mmol sucrose* cm^{-3}) is the volumetric structural carbon content of this tissue in unit of sucrose. $A_{cross,seg}$

(cm^2) is the cross-sectional area of the segment. r_{Wlim} ($cm\ d^{-1}$) is the water limited growth rate, computed via Eqn.(2-2). The sucrose used for Gr_{Wlim} will become part of the plant's structural sucrose content (sucrose making up the plant cells' walls).

2-2-1-4-5-3 Maximal maintenance respiration

$R_{m,max}$ ($mmol\ sucrose\ cm^{-3}\ d^{-1}$) corresponds to the maximal (non-carbon limited) value of R_m. It represents for instance the sucrose usage to replace the structural carbon (re-synthesis), secondary growth, the phloem leakage and futile cycles (Lacointe and Minchin, 2019, Thornley and Cannell, 2000). $R_{m,max}$ is obtained empirically from Eqn.(2-55):

$$R_{m,max} = v_{seg}(\rho_s k_{m1} + \bar{s_{st}} \times k_{m2}) \times Q10^{\frac{T-T_{refq10}}{10}} \tag{2-55}$$

with v_{seg} (cm^3) the volume of the plant tissues. k_{m1}, k_{m2} are fitting parameters defining $R_{m,max}$ according to, respectively, the structural (for wall re-synthesis) and non-structural carbon content. Following the example of Gauthier et al. (2020), we added the short-term effect of temperature on $R_{m,max}$ via $Q10$ ($-$) and T_{refq10} (K) (Amthor, 2000). $Q10$ is a coefficient which is widely used in the scientific literature and which defines the temperature sensitivity of chemical reactions: higher $Q10$ value leads to steeper increase with temperature. T_{refq10} defines the reference temperature: $|Q10^{\frac{T-T_{refq10}}{10}}|_{T=T_{refq10}} = 1$. As other modules are added to CPlantBox (like nitrogen uptake and flow) their related respiration may be added to the computation of $R_{m,max}$.

2-2-1-4-5-4 Sucrose-limited sinks

$[F_{out,MM}]$ ($mmol\ sucrose\ cm^{-3}\ d^{-1}$) is the sucrose usage rate for growth and maintenance. It follows a saturation-dynamic and is computed from the Michaelis-Menten respons function (Gauthier et al., 2020, Jones and Cox, 2019, Lacointe and Minchin, 2019):

$$[F_{out,MM}] = ([R_{m,max}] + [G_{tot,Wlim}]) \times \frac{\bar{s_{st}}}{\bar{s_{st}} + M_{out}}, \tag{2-56}$$

with M_{out} the Michaelis-Menten coefficient. After adding the passive $Exud$, we obtain $[F_{out}]$ ($mmol\ sucrose\ cm^{-3}\ d^{-1}$) the total sucrose usage rate:

$$[F_{out}] = [F_{out,MM}] + [Exud] \tag{2-57}$$

A high increase in s_{st} will only affect the maintenance and growth rate if the sink cells are not saturated, while the exudation will not be demand-limited.
$F_{out,MM}$ gives us the value of $[R_m]$ and $[G_{tot,CWlim}]$ ($mmol\ sucrose\ cm^{-3}\ d^{-1}$), the realized sucrose usage rate for maintenance and growth respectively :

$$[R_m] = min([R_{m,max}], [F_{out,MM}]) \tag{2-58}$$

$$[G_{tot,CWlim}] = [F_{out,MM}] - [R_m] \tag{2-59}$$

Eqn. (2-58) indicates that maintenance has priority over growth, which is a common assumption (Roux et al., 2001, Fig. 1).

2-2-1-5 Soil water flow

The variation in soil water content ($\frac{\partial \theta_{soil}}{\partial t}$) is computed thanks to the DuMu^{x} module (see Figure 2-1A.3) using the Richards equation, which describes the movement of water in an unsaturated soil (Koch et al., 2021, Richards, 1931):

$$\frac{\partial \theta_{soil}}{\partial t} - \nabla \cdot (\kappa_{soil}(\theta_{soil})(\nabla \psi_{m,soil} + \nabla \psi_{g,soil})) = \frac{1}{V_{soil}} \sum_{i}^{N} (p_i \times l_i \times j_{lat,x-soil,i}) \quad (2\text{-}60)$$

with $\sum_i^N (p_i \times l_i \times j_{lat,x-soil,i})$, the root-soil water exchange for all roots i in the considered soil domain (Neumann boundary condition obtained from Section 2-2-1-4-2), V_{soil} (cm^3) the volume of the considered soil domain, and $\kappa_{soil}(\theta_{soil})$ (in $cm^2\ hPa^{-1}\ d^{-1}$) the soil conductivity for a specific water content.
The soil water content (θ_{soil} in $cm^3\ cm^{-3}$) and $\kappa_{soil}(\theta_{soil})$ are obtained from the van Genuchten-Mualem equations (Mualem, 1976, van Genuchten, 1980):

$$\theta_{soil} = \theta_{r,soil} + \frac{\theta_{s,soil} - \theta_{r,soil}}{[1 + (\alpha_{soil}|\psi_{m,soil}|)^{n_{soil}}]^{m_{soil}}} \text{ if } \psi_{m,soil} < 0 \quad (2\text{-}61)$$

$$\theta_{soil} = \theta_{s,soil} \text{ if } \psi_{m,soil} \geq 0 \quad (2\text{-}62)$$

$$\kappa_{soil}(\theta_{soil}) = \kappa_{soil}(\theta_{s,soil}) \frac{\left(1 - (\alpha_{soil}|\psi_{m,soil}|)^{n_{soil}-1}[1 + (\alpha_{soil}|\psi_{m,soil}|)^{n_{soil}}]^{-m_{soil}}\right)^2}{\left[1 + (\alpha_{soil}|\psi_{m,soil}|)^{n}_{soil}\right]^{m_{soil}/2}} \quad (2\text{-}63)$$

$$\psi_{m,soil} = \psi_{m,soil,0} \quad \text{for } t = t_0 \quad (2\text{-}64)$$

$$m_{soil} = 1 - \frac{1}{n_{soil}} \quad (2\text{-}65)$$

with α_{soil} (hPa^{-1}) a parameter related to the inverse of the air-entry suction, n_{soil} and m_{soil} ($-$) parameters representing the soil pore-size distribution, $\theta_{s,soil}$ and $\theta_{r,soil}$ ($cm^3\ cm^{-3}$) the saturated and residual soil water content, $\kappa_{soil}(\theta_{s,soil})$ (in $cm^2\ hPa^{-1}\ d^{-1}$) the saturated soil conductivity. We neglect the effect of $\psi_{o,soil}$ and $\psi_{o,x}$ (the osmotic potential in the soil and in the xylem) on the flow. $\psi_{m,soil}$ can thus be used by the xylem module (Dirichlet boundary condition), see Eqn.(2-35). The coupling between CPlantBox and DuMu^{x} is made available via a python binding within the root-soil interaction module DuMu^{x}-ROSI (Khare et al., 2022). The method for the soil discretisation and interface with the xylem flow is given in appendix A.6-2-1.

We do no represent in this implementation the variation of soil carbon concentration.

2-2-1-6 Numerical solution and computational loop

The numerical solutions of each CPlantBox modules and of the DuMu^{x} soil water flow module are described in the appendix A.6 and in Koch et al. (2021) respectively. Briefly, the soil water flow is solved by a cell-centered finite volume method (CC-FVM) (Koch et al., 2021). The xylem water flow is solved using the hybrid analytical method of Meunier et al. (2017). The sucrose balance (sucrose usage

and transport in the sieve tube and mesophyll) is computed by discretising the continuous equation into a series of ODEs solved numerically (Newton iterations with implicit time stepping) on each plant-node (vertex-centered finite volume method, VC-FVM) (Hindmarsh et al., 2005). The xylem water flow and FvCB-Stomatal regulation are computed together via fixed-point iterations. For these two modules, an iterative calculation of c_i, A_g, g_{co2}, $j_{lat,x-out}$, $\psi_{t,ox}$, and $\psi_{t,x}$ for each plant segment is carried out (in that order). Convergence is said to have been reached when the relative difference between two consecutive loops in each segment for each of these variables is bellow 1% or when the absolute difference is below a set threshold. The other modules are run sequentially at each user-defined time step. The user can run all the modules at each loop or increase the time step of some modules by running them every set number of loops (operator splitting). The optimal time step for the data exchange between the modules is strongly problem-dependent and to be selected by trial and error. Figure 2-7 gives a graphical representation of the simulation loop and main exchange of data between the modules.

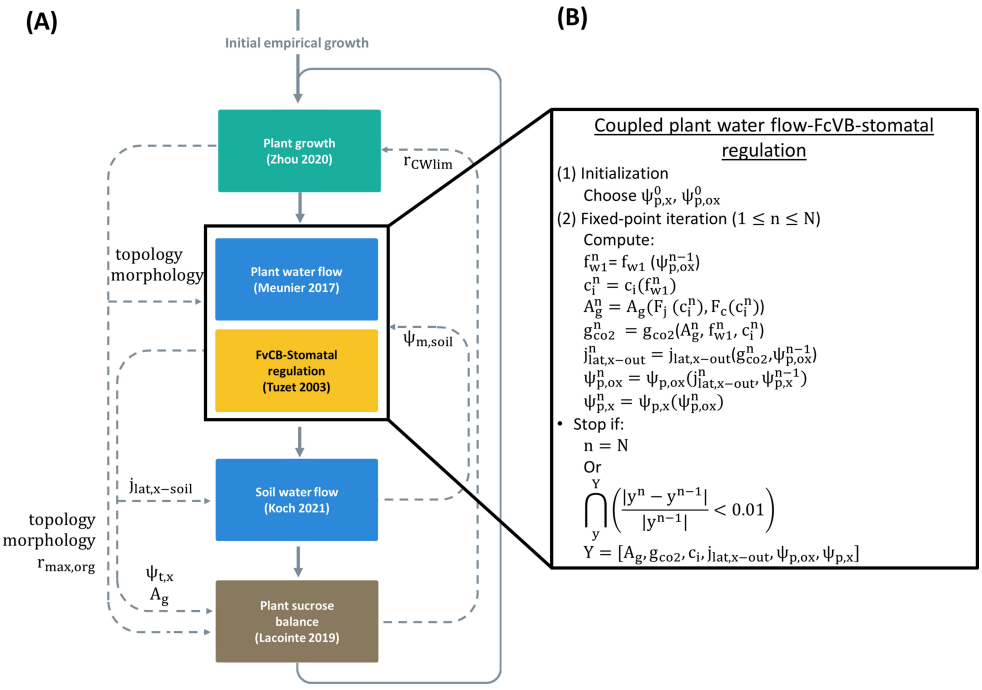

Figure 2-7: Representation of the simulation loop of the model with (A) the overall loop, and (B) the fixed-point iteration loop used for the coupled plant water flow-FvCB-stomatal regulation modules. The dashed arrows represent the exchange of data between the modules. The full arrows give the sequence of the modules in the loop. At each time step, each part of the model is computed sequentially, except for the water flow-FvCB-stomatal regulation modules which are looped over until convergence.

2-2-2 System modelled

The model was calibrated for C3 monocots using experimental (see Appendix A.5-1), literature, or illustrative data. The list of the parameters, with their value and source, are given in Appendix A.5-2.
Notably, for this implementation, different $k_{lat,st,root}$ and $k_{lat,x,root}$ were defined for each root order. Moreover, we set

$$k_{lat,root,l} > 0 \text{ if } l \in [0, l_{rootExchange}]$$

where l is the distance from the root tip and $l_{rootExchange} = 0.8\ cm$. This means that root water uptake and exudation are assumed to occur in the immature portion of the root (Bramley, 2006, Chap. 4).

We simulated the growth of a C3 monocot under a control scenario (hereafter called *baseline*) compared with dry spells at two stages of development of the plant.

The environmental variables (see Table 2-1) of *baseline* (resp. the dry spell periods) were set from the data of Swart et al. (2019) for Germany in June of 2010 (resp. 2100, under the $SSP5-8.5$ scenario), making *baseline* relatively wetter and colder (resp. the dry spell periods relatively drier and warmer). $\theta_{mean,soil}$ for *baseline* was set near saturation. $\theta_{mean,soil}$ during the dry spells was set 30% lower, which corresponds to the relative decrease in moisture in the upper soil column between June 2010 and 2100 (Swart et al., 2019).

Both dry spells were represented by a period of one week without rainfall: 11 to 18 days and 18 to 25 days after sowing, hereafter called *early dry spell* and *late dry spell*.

The virtual plants were obtained by running CPlantBox up to day 10 (after sowing) using a mean empirical growth rate (neither dependent on the carbon- nor water-flow) and without simulation of the water and carbon fluxes. Indeed, the plant leaf blades (the carbon source and water sink) had to be large enough before starting the carbon- and water-limited growth. After three hours of burn-in time, we simulated the carbon and water fluxes and of the carbon- and water-limited growth. The plants all grew under the *baseline* conditions with a static soil (constant mean $\psi_{m,soil} = 0.4\ cm^3 cm^{-3}$ at hydraulic equilibrium), except during the dry spel between day 10 and (for *early dry spell*, reps. *late dry spell*) the start of the dry spells (11d, resp. 18d). At the start of the dry spells, the dynamic soil water flow module was implemented. For the plants under *drier&warmer*, the alternative initial soil conditions were used (initial $\psi_{m,soil} = 0.28\ cm^3 cm^{-3}$). The soil water flow was simulated until the end of the dry spells (18d, resp. 25d). After the dry spells, the *baseline* environmental and static soil variables were used. Table 2-2 summarises the above-given timeline of the four simulations.

The minimum plant segment length was set to 1 cm. The θ_{soil} per voxel is (until the start of the dry spells) constant per layer and varies with the depth (hydraulic equilibrium). The mean θ_{soil} value is given in table 2-1. The voxel size (resolution) was set to 1 cm^3.

The Van Genuchten parameters are presented in Appendix A.5-2, Table A.1. The mean soil soluble carbon concentration was set as a unique constant value. In order to represent the effect of the water uptake by neighboring root systems, we defined the lateral dimensions of the simulation domain to be equal to the inter plant distance, 3×12 cm^2, and used a laterally periodic domain. The depth of the simulation domain was 60 cm. During the dynamic soil simulation, no rainfall occurred and we assumed that the soil was covered with gravel (negligible evaporation). We could thus set a no-flux upper boundary condition for the soil water flow module. We moreover set a free-flow lower boundary condition.
Although we represented the air humidity gradient between the middle of the canopy and the point of measurement, the atmospheric conditions were represented by a set of mean values, equal for the whole canopy. This means that the same c_{bl}, PAR, T_{atm}, and ea_{atm} were set for all shoot segments. We assumed a constant wind speed 2 m above ground u_{2m} of $8.467e+7$ $cm\ d^{-1}$ (or 2 $m\ s^{-1}$ in SI units). The CO_2 concentration on the leaf surface (c_{bl}) was set constant at $350e-6$ $mmol\ mmol$, an illustrative value based on measurements from the TERENO- observatory network in Selhausen (Puetz et al., 2016). We simulated a unified temperature in the whole system $T_{plant} = T_{soil} = T_{atm}$. PAR, T_{atm} and h_{atm} (relative air humidity 2 m aboveground) went from their minimum to their maximum value via a sinusoidal function with a period of 1 day.

The time step for the main simulation loop was of 1 hour. Within this loop, the time step for the exchange of data between the plant and the soil water modules was 1 minute.

Table 2-1: Environmental variables

	min-max of sinusoidal function[a]			$\theta_{mean,soil}$
	PAR	T_{atm} (K)	h^b_{atm} (%)	$(cm^3\ cm^{-3})$
baseline	0-940	288.95-295.15	0.6-0.88	0.4
dry spell		293.85-303.42	0.44-0.74	0.28

[a] T_{atm}, PAR and h_{atm} go from their minimum to their maximum value via a sinusoidal function with a period of 1 day to represent the day-night cycle. All the atmospheric variables correspond to values 2 m aboveground.
[b] relative air humidity.
the *baseline* variables were used for all simulations before and after the dry spells

Table 2-2: Timeline of the simulations. The grey (resp. blue) cells indicate the empirical (resp. semi-mechanistic) growth period and "ds" the implementation of the dynamic soil. The blue gradient during the dynamic soil simulation represent the decreasing soil water content. The sharp shift from dark to light (resp. light to dark) blue at the beginning (resp. end) of the dry spells represent the implementation of the *dry spell* (resp. *baseline*) atmospheric and initial (resp. constant) soil variables.

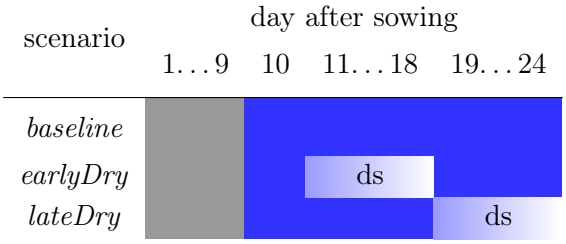

2-3 Results

2-3-1 Simulation of the time-course of water and carbon flows

The model was implemented on a Lenovo Thinkpad T490, with an Intel(R) Core(TM) i5-8265U processor, using the Windows subsystem linux Ubuntu20.04. The run-time of the simulation was about 1 hour 10 minutes for *baseline*, 2 hours 40 minutes for *early dry spell*, and 5 hours 25 minutes for *late dry spell*. The number of plant nodes went up to 2448 (for *baseline*). The relatively high run-time of the simulation was linked to the high number of nodes and will be lower for plants with smaller root systems or when decreasing the resolution (increasing the minimum plant segment length). It is also possible to adapt the absolute and relative error tolerances of the phloem module.

Figure 2-8 illustrates the simulated plant structure and output by the model. Figure 2-8A shows a 3-dimensional visualisation of the monocot at 18d for *baseline*. Figure 2-8B shows examples of run-time variables for selected nodes: the total water potential in the xylem ($\psi_{t,x}$, in cm) and the mean concentration of sucrose in the sieve tubes (s_{st}, in $mmol\ cm^{-3}$).
The development of the plant led to a higher $\psi_{t,x}$ because of the improved water uptake capacity. We can also observe an increased gradient of s_{st} between the shoot and roots.

2-3-2 Sucrose usage and non-structural sucrose content

Figure 2-9 presents the sucrose partitioning between the different sinks. Figure A.2 in Appendix A.8 presents the same data but over a shorter period to give a clearer example of the daily s_{st} variations. During the dry spells, the

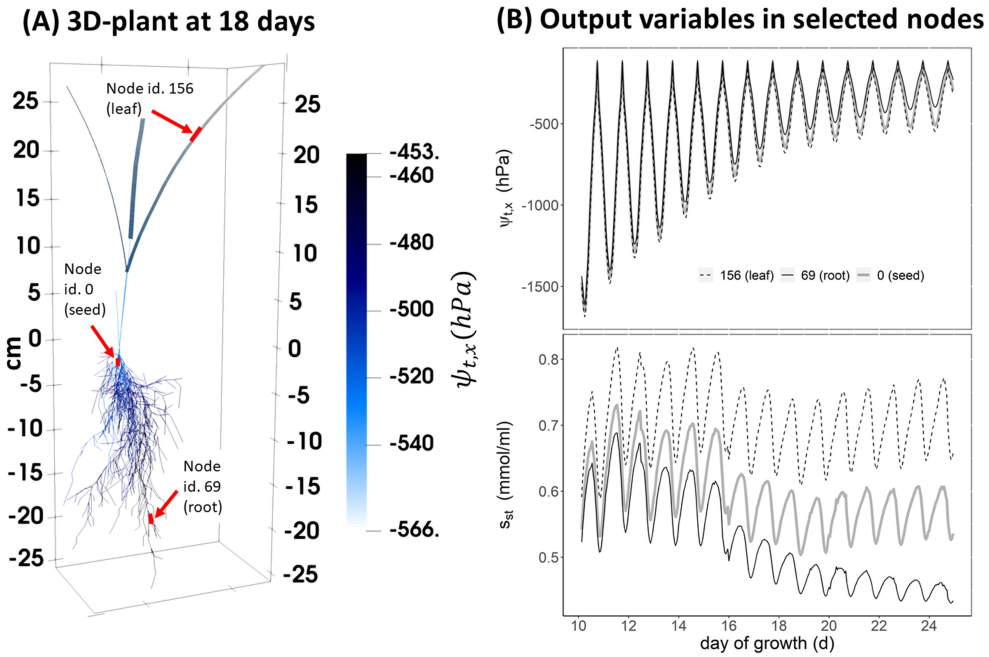

Figure 2-8: Sample of CPlantBox outputs (A) a 3-dimensional image of a C3 monocot at 18 day under *baseline* (B) values for three specific plant nodes of the xylem water potential ($\psi_{t,x}$) and phloem sucrose concentration (s_{st}). The red arrows and rectangles indicate the selected nodes.

absolute value of maintenance respiration (R_m) was higher because of the higher temperature, leading to a higher enzyme activity. The daily R_m peak was likewise caused by the higher temperature at midday.

Because of the sink prioritisation (maintenance > growth), in case of low assimilation (night time) or high R_m (midday), growth respiration ($G_{tot,CWlim}$) diminished to fulfil the R_m need.

The minimum soil matric potential ($\psi_{m,soil}$) remained constant at $-129\ hPa$ for *baseline* and outside of the dry spell periods. At the beginning of the dry spells (11d or 18d) minimum $\psi_{m,soil}$ ($\psi_{m,soil}$ in the upper soil layer) was $-467\ hPa$. At the end of the dry spell simulations (18d or 25d) minimum $\psi_{m,soil} = -1376\ hPa$ for *early dry spell* and $-1984\ hPa$ for *late dry spell*. $\psi_{m,soil}$ and h_{atm} affected the symplasm turgor potential ($\psi_{p,symplast}$): the minimum $\psi_{p,symplast}$ was 8537 hPa for *baseline*, 7119 hPa for *early dry spell* and 8095 hPa for *late dry spell*. For *early dry spell*, $\psi_{p,symplast}$ was closer to the critical symplasm turgor potential for growth below which no growth occurs ($\psi_{p,crit,2}$, set to 2000 hPa), leading to a lower $G_{tot,CWlim}$. Soil and air water content had therefore a moderate effect on $G_{tot,CWlim}$.

$Exud$ varied according to s_{st} and was lower at night time. Moreover, we saw similar variations of $Exud$ during the dry spells. Indeed, The higher R_m and the lower assimilation rate (see Figure 2-14) for *early dry spell* and *late dry spell* were not compensated by the decrease in $G_{tot,CWlim}$ and led to a lower daily maximum $Exud$ when compared with *baseline*.

Table 2-3 gives the absolute values of the cumulative R_m, $G_{tot,CWlim}$, and $Exud$ at the end of the simulations. Compared with *baseline*, *early dry spell* and *late dry spell* led to a strong decrease of cumulative $G_{tot,CWlim}$ (-17% and -21% respectively), and $Exud$ (-30% and -26% respectively). *early dry spell* led to a slight decrease of cumulative R_m (-5%) while *late dry spell* led to a strong increase of cumulative R_m ($+20\%$).

Table 2-3: Total value of the cumulative sucrose sinks at the end of the simulation in $mmol$ for maintenance respiration (Rm), growth and growth respiration ($G_{tot,CWlim}$), root exudation ($Exud$).

scenario	R_m	$G_{tot,CWlim}$	$Exud$
baseline	2.44	5.37	4.23
early dry spell	2.30	4.47	2.97
late dry spell	2.93	4.22	3.14

Figure 2-10 presents the mean s_{st} per organ type. s_{st} did not vary strongly during the simulation: it always remained between 0.42 $mmol\ cm^{-3}$ and 0.82 $mmol\ cm^{-3}$. For this simulation, the starch dynamic in the sieve tube was dependent on the gradient between s_{st} and $s_{targ,st}$. As we set $s_{targ,st} = 0.4\ mmol\ cm^{-3}$, the starch reserves of the plant only increased during

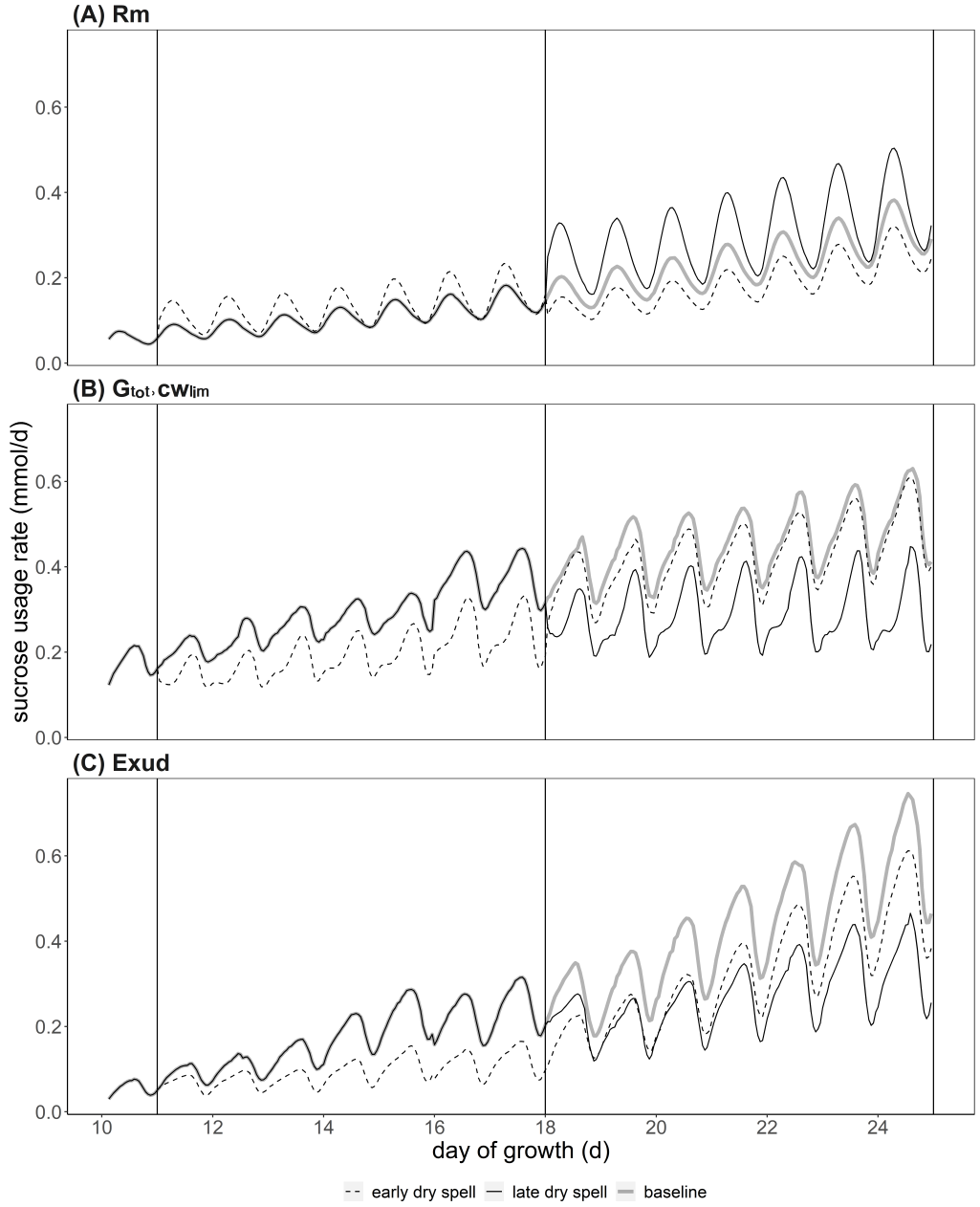

Figure 2-9: Partitioning of the carbon loss between the three sinks according to time: maintenance respiration (Rm), growth and growth respiration ($G_{tot,CWlim}$), root exudation ($Exud$). The black vertical lines define the start and end of the atmospheric dry spells (11d to 18d or 18d to 25d). We compare an early (thin dashed lines) and late dry spells (thin lines) against against a baseline scenario (thick lines).

the simulation. During the dry spells the lower assimilation rate and higher R_m led to a lower s_{st} compared with *baseline*. For *early dry spell*, the difference in s_{st} was maintained aven after the end of the dry spell. These differences in s_{st} in the roots caused the different $Exud$ observed in Figure 2-9.

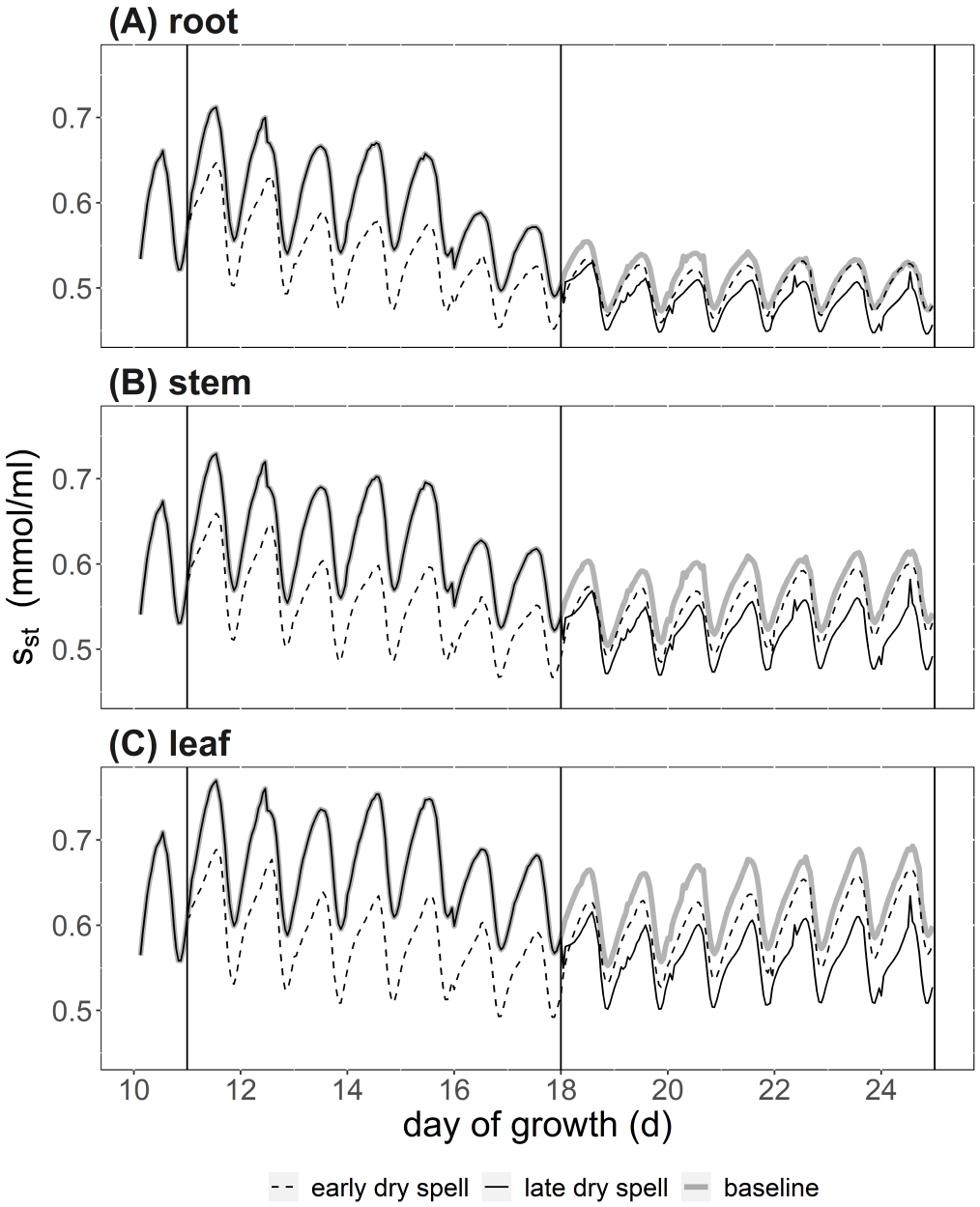

Figure 2-10: Mean sucrose concentration (s_{st}) according to time in the (A) root, (B) stem, and (C) leaf organs. The black vertical lines define the start and end of the dry spells (11d to 18d or 18d to 25d). We compare an early (thin dashed lines) and late dry spells (thin lines) against against a baseline scenario (thick lines).

2-3-3 Structural sucrose content

Figure 2-11 presents the absolute structural sucrose content for each organ type and subtype.

At the beginning of the dry spell (11d, resp. 18d) the monocots under *early dry spell* (resp. *late dry spell*) and *baseline* were exactly identical. We can observe several growth plateaus in the development of the stems. This was caused by the user-defined growth delay of the main stem and tillers. It was used to represent the period after the first appearance of the stem and before the stem elongation phase.

Moreover, the lower $G_{tot,CWlim}$ under *early* and *late dry spell* (see Figure 2-9) led to a lower growth for all organ types. Especially, we see a lower growth for *late dry spell* compared with *baseline*, which fits with the lower $G_{tot,CWlim}$ observed in Figure 2-9. For all simulation scenarios, we can observe that the growth rate of the 2^{nd} order laterals is much higher after day 18.

Figure 2-12 presents the relative structural sucrose content for each organ type and subtype.
For all simulations, the root-to-shoot ratio of structural sucrose content increased during the simulation. We observed that the dry spell intensities had a slight effect on the relative structural sucrose partitioning.
For instance, the final relative sucrose content in the root was 53% for *baseline*, 51% for *early dry spell*, 50% for *late dry spell*.
Because the growth of the 2^{nd} order roots was much more important after day 18, *late dry spell* had the lowest relative structural sucrose content of 2^{nd} order roots (30%) when compared with *baseline* (33%).

Figure 2-13 shows the 3-dimensional representation of the plants at the end of the simulation. Under *baseline* (2-13A) we observed a higher development of the leaves and root systems compared to *early dry spell* and *late dry spell* (2-13B and 2-13C). Indeed, the lower increase in root structural carbon is reflected by the different total root lengths per root order at day 25: we obtained 3456 *cm* for *baseline*, 2793 *cm* for *early dry spell*, and 2586 *cm* for *late dry spell*.

Likewise, we can observe the different total leaf length per plant at day 25: we obtained 161 *cm* for *baseline*, 148 *cm* for *early dry spell*, and 145 *cm* for *late dry spell*.

Moreover, Figure 2-13 allows us to see the s_{st} gradient along the plant's organs. For instance, longer mature leaves had the highest s_{st} values.

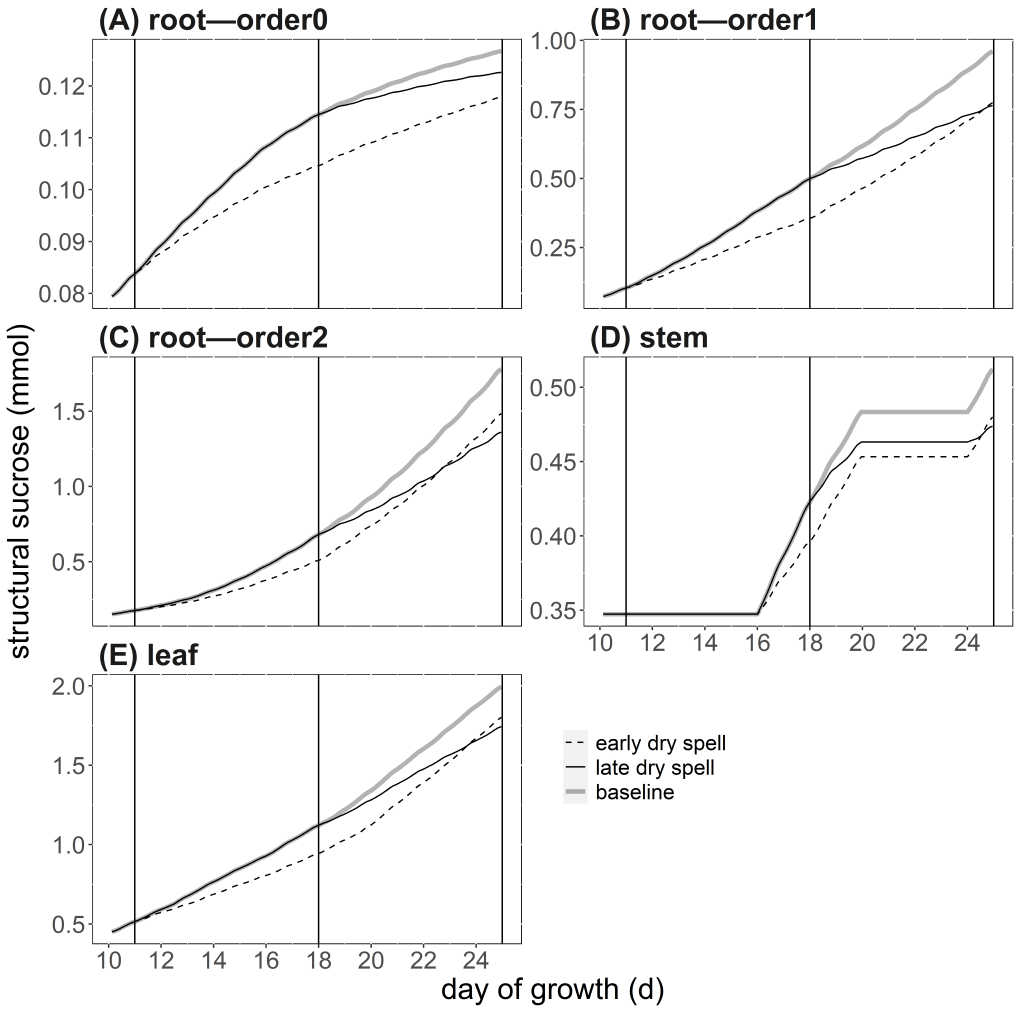

Figure 2-11: Absolute structural sucrose content per plant organ type and subtype according to time, with (A) 0-order roots; (B) 1^{rst} order roots, (C) 2^{nd} order roots, (D) stem, (E) and leaf organs. Structural sucrose corresponds to the carbon in the plant tissues, in equivalent sucrose. The black vertical lines define the start and end of the dry spells (11d to 18d or 18d to 25d). We compare an early (thin dashed lines) and late dry spells (thin lines) against against a baseline scenario (thick lines).

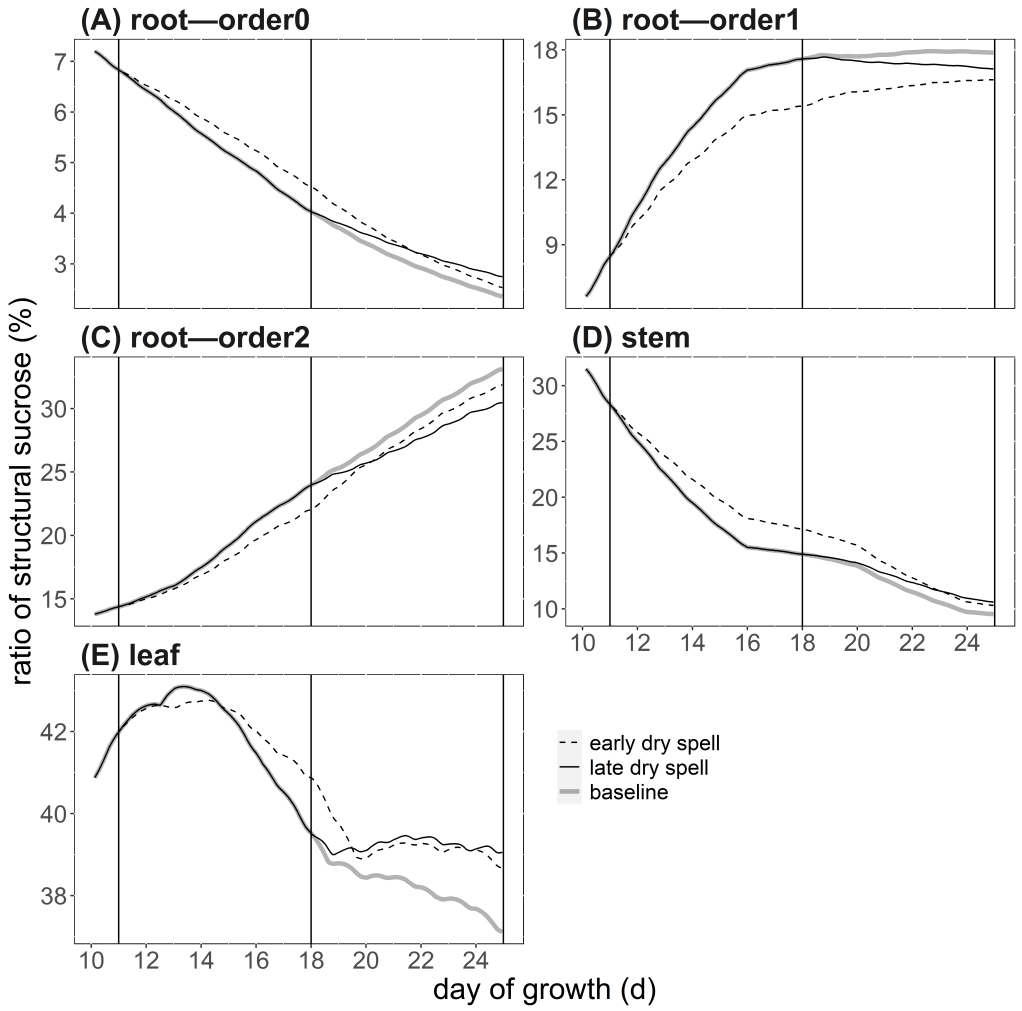

Figure 2-12: Relative structural sucrose content per plant organ type and subtype according to time, with (A) 0-order roots; (B) 1^{rst} order roots, (C) 2^{nd} order roots, (D) stem, (E) and leaf organs. Structural sucrose corresponds to the carbon in the plant tissues, in equivalent sucrose. The black vertical lines define the start and end of the dry spells (11d to 18d or 18d to 25d). We compare an early (thin dashed lines) and late dry spells (thin lines) against against a baseline scenario (thick lines).

Finally, we could observe that the root system of *late dry spell* is less fibrous than under *baseline*, as observed in section 2-3-3. This was linked with to lower development of the higher-order roots.

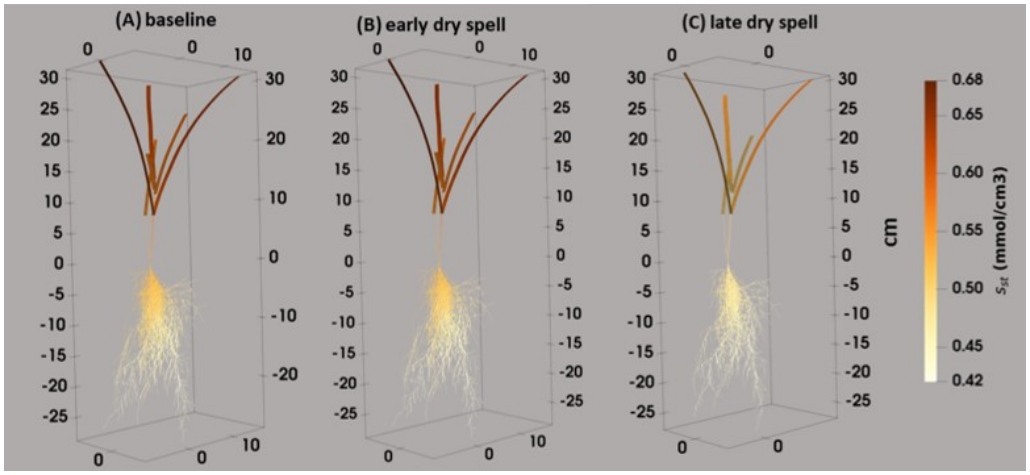

Figure 2-13: 3D representation of the virtual plants at 25d after a (A) baseline wetter and colder scenario, or drier and warmer dry spells (B) between days 11 and 18, (C) between days 18 and 25. Each segment is colored according to its sucrose concentration in the sieve tube (s_{st}, $mmol\ cm^{-3}$).

2-3-4 Instantaneous water use efficiency

Figure 2-14 presents the cumulative transpiration and sucrose assimilation (cumulative $A_{g,plant}$, in $mmol$) for all scenarios (*baseline*, *early dry spell*, and *late dry spell*).

The dry spells had a negative effect on cumulative $A_{g,plant}$: -19 % for *early dry spell* and -15 % for *late dry spell*, when compared with *baseline*. This is caused by the lower leaf development (see Section 2-3-3) and by the lower assimilation rate per unit of leaf area (A_g).

For all simulations we observed a small closing of the stomata because of the leaf water potential near midday. The water scarcity factor for stomatal opening (f_{w1}) went down to 0.94 for *baseline* scenarios, 0.86 for *early dry spell* and 0.91 for *late dry spell*. A smaller opening of the stomata led to a lower substomatal CO_2 concentration (c_i) and through this also caused the lower A_g for *drier&warmer*. Likewise, for *early dry spell* and *late dry spell*, maximum air temperatures of 303.42 K, above the optimum value of 298.15 K, led to a lower A_g.
Moreover, the higher leaf to air vapor pressure deficit during the dry spells led to a higher cumulative transpiration compared with *baseline*: +16% for *early dry spell* and +58% for *late dry spell*.

Overall, we observed a decrease in instantaneous water use efficiency ($A_{g,plant}$-to-transpiration ratio) at the end of the simulation for the dry spells scenarios compared with *baseline*: -30% for *early dry spell* and -46% for *late dry spell*.

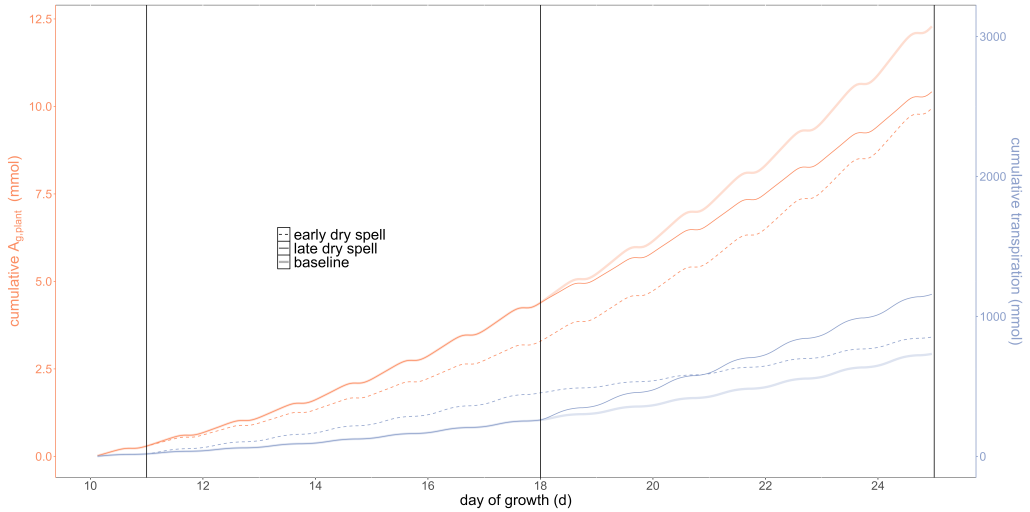

Figure 2-14: Cumulative assimilation of sucrose and transpiration, respectively $A_{g,plant}$ (orange) and transpiration (blue). The black vertical lines define the start and end of the dry spells (11d to 18d or 18d to 25d). We compare an early (thin dashed lines) and late dry spells (thin lines) against against a baseline scenario (thick lines).

2-4 Discussion

2-4-1 Results of the simulation

In this study, we used our model to look at the effect of a dry and warm spell of one week on plant water flow, carbon flow, and growth, based on the expected temperature, air relative humidity, and relative variation in soil water content in Germany for June of 2100 (but without changes of CO_2 concentrations).
We could observe a lower growth rate for all organs, fitting with the results of Chen et al. (2021) for monocots under drought stress. In this simulation, the moderately lower turgor pressure during the drought affected the growth negatively. However, the lower growth was mainly caused by a lack of sucrose. This is contrary to the literature consensus as water stress is linked to a higher sucrose concentration because the lower growth rate over-compensates the lower assimilation (Lemoine et al., 2013, Michelena and Boyer, 1982). This change in osmotic potential leads in turn to a higher turgor pressure in the symplast (Lemoine et al., 2013, Michelena and Boyer, 1982). The effect of the water stress on the plant's sucrose concentration can however be adapted by recalibrating the phloem module. Moreover, the coupling between the sucrose concentration and symplast turgor pressure can be represented by implementing the symplast pressure and solution flow of PiafMunch (Lacointe and Minchin, 2019).

We observed a lower assimilation-to-transpiration ratio during and after the dry spells compared with the baseline. This was also observed experimentally by Tshikunde et al. (2018) for a monocot. The influence of the leaf area on the plant's photosynthetic capacities confirms the assumption of Damour et al. (2010) in their review of stomatal regulation models.

During the simulation, the ratio of exudation to total carbon usage remained within the range found in the literature for monocots: $3 - 40\%$ (Dilkes et al., 2004). However, as soil soluble carbon concentration was a constant during the simulation, we could not model the feedback effects of different exudation levels. The plant sucrose concentration varied between 0.4 $mmol\ cm^{-3}$ and 0.9 $mmol\ cm^{-3}$, which fits with the values reported by (Jensen et al., 2013, Thompson and Holbrook, 2003). The low pressure gradient between source and sinks follows as well the current assumption for herbaceous angiosperms (De Schepper et al., 2013).

Contrary to other modelling studies, the dry spells did not lead to a decrease in transpiration (Bingham and Wu, 2011, Tuzet et al., 2003). Indeed, the slight closing of the stomata did not compensate the higher evaporative demand caused by the lower air relative humidity. Additionally, the initial soil water potential remained high. The chosen grid resolution for the soil (1 cm^3) was also relatively coarse and might have led to an over-estimation of the plant water uptake and thus of the transpiration (Khare et al., 2022). As shown by Khare et al. (2022), representing rhizosphere drying helps simulate more accurately the flow of soil water and root water uptake under dry conditions. A module representing this process is currently available within CPlantBox, but was not used within this study. Moreover, we did not represent the loss of conductivity caused by cavitation and this process can strongly affect the transpiration rate (Corso et al., 2020, De Swaef et al., 2022). Likewise we did not simulate the stomatal closure linked to an increase in s_{meso} (De Schepper et al., 2013), which would have lead to a lower assimilation and transpiration for the plants at the beginning of the simulation, when s_{st} is higher. Divergences between our model and other observed or simulated results remain however useful as they can give insight into which processes are key to representing emerging properties.

2-4-2 Current limitations of the model and future perspectives

The increasing number of modules in CPlantBox leads to a high number of parameters and (intermediary) outputs. Also, several variables and parameters cannot be measured experimentally (like the separation of the respiration between maintenance and growth (Thornley, 2011)) making their experimental evaluation more complex.
A first sensitivity analysis (see appendix A.7) was therefore done to evaluate the most important parameters. Moreover, several controls were setup in CPlantBox

to warn the user in case of impossible outputs (like negative transpiration rate and too high sucrose concentration in the sieve tube). Building on this work, the development of an effective calibration pipeline and parameter database would be an important step towards making this model more readily usable (Louarn and Song, 2020). On the experimental side, new (field) experiments will be conducted to parameterize the model for a specific wheat genotype rather than a generic C3 monocot. When CPlantBox is not precisely parameterized, it can be used to do qualitative tests rather than quantitative predictions. Until the new modules are calibrated and tested against real data, this new version of CPlantBox should moreover be used to do qualitative evaluations rather than quantitative predictions.

The fixed-point approach used for the plant water flow-photosynthesis-stomatal regulation modules (Sections 2-2-1-4-2 and 2-2-1-4-1) always converged for our simulations (convergence reached in $<$ 5000 loops). However, in case of a slow convergence (small variable variation between two consecutive loops), the computation time might become very high or the software might assume prematurely convergence. Adapting the computation scheme would make flow-photosynthesis-stomatal regulation modules more robust to a wide range of setup. Moreover, the other modules are solved sequentially. Therefore, the selected time step needs to be small enough to avoid divergence. In the future, other parts of the module coupling which are more susceptible to diverge (like the coupled plant-soil water flow) will be solved with an implicit time stepping.

Regarding the functional processes represented, the accuracy of the phloem flow outputs could be further improved by adapting the representation of the sucrose usage. First of all, the plant's respiration is currently following the widely-used growth-maintenance paradigma. As other processes/functional modules are added into CPlantBox (like nitrogen uptake and flow), it will be possible to shift to a process-based definition of the respiration rate, as recommended by Cannell and Thornley (2000) and implemented by Gauthier et al. (2020). This would also improve the evaluation of the feedbacks between the environmental conditions and the plant's processes. Also, the representation of the sucrose exudation rate, and of the chlorophyll-dependent assimilation offers the first elements of a more explicit representation of the nutrient flow within the plant, which are an important aspects of a plant's adaptation to its environment (Galindo-Castañeda et al., 2022). Moreover, the representation of sucrose-induced closing of the stomata would help evaluate the plant's sucrose-related adaptation capacity to a changing environment (De Schepper et al., 2013). The negative feedback of the sucrose on photosynthesis would on the other hand help better represent the decrease of photosynthetic capacity in case of low sucrose usage. Representing tissue death caused by water and/or carbon scarcity would allow CPlantBox to simulate plant development under more extreme weather conditions.

It would moreover be possible to update the internal CPlantBox-PiafMunch module to represent other processes available in PiafMunch, such as the osmotic and elastic adjustments of the plant tissues to its water content. Integrating these processes would allow us to simulate more precisely possible compensation between the total and osmotic potential in the symplast in case of drought (Michelena and Boyer, 1982). While elastic deformation of the xylem (Corso et al., 2020) and phloem (Thompson, 2006) were not found to have a strong effect on their respective conductivities, elastic adjustment of the symplast can however lead to a higher resilience to droughts by maintaining a higher water potential in the plant (shrinking) (Kramer and Boyer, 1995) or by increasing its water storage capacity (expansion) (Saliendra and Meinzer, 1991).
Moreover, water stress can lead to a lower growth even when turgor pressure and sucrose concentration are high Michelena and Boyer (1982), via for instance phytohormones, which we cannot yet represent in CPlantBox.

Regarding the 3-dimensional representation of the plant, a first description of graminaceous shoot growth was implemented: the leaf sheaths grow together upward, making a pseudo stem. We have moreover a stem elongation phase. The user can then setup an age-dependent tropism function to have the bending of the leaf blade once they have reached a specific age. The explicit 3-dimensional representation of the shoot organs makes it possible to simulate precisely the atmospheric variables (like PAR, T, g_{bl}, g_{canopy}) for each leaf segment. Next implementations of the model could include the simulations of the canopy micro-climate.

2-5 Conclusion

In this paper, we presented the latest version of CPlantBox and implemented it to represent the effect of atmospheric dry spells of one week, starting at different days (11 against 18 days after sowing) and compared the results with a baseline wetter and colder scenario. We could observe that the dry spells led to lower growth and exudation rates. The model also showed that the early dry spell affected the plant processes (higher transpiration, lower assimilation, lower organ growth) less than the late dry spell when compared with the wetter and colder climate.

The model was therefore capable of computing plant variables at a sub-diurnal scale and for each plant control volume in a complex architecture (fully grown monocot with distributed water and carbon sink and sources). The model could moreover simulate semi-mechanistically the interplay between the 3-dimensional plant topology and the environmental conditions via the water and carbon flows in the soil-plant-atmosphere continuum by representing a growing plant in a

dynamic environment. The computed variables at small time and spatial scales led to emerging properties that are usually less precisely defined in plant models (growth rate, carbon partitioning).

CPlantBox is a versatile open-source tool that can be used to test hypotheses and understand the underlying relations between selected processes leading to specific phenotypes under different genotype-environment-management combinations.

Next steps in the development of CPlantBox will include the setup of a calibration pipeline and the gathering of field and laboratory data to represent a specific plant phenotype, in order to test the model's capacity to mimic experimental outputs.

Model availability

The CPlantBox code used to run the simulations is available at `https://github.com/Plant-Root-Soil-Interactions-Modelling/CPlantBox/releases/tag/v2.0`. All the files used to run the simulations and plot the results are also available on Zenodo: 10.5281/zenodo.8106144.

Acknowledgement

The authors thank S. Moyo, M. Humza, C. Tempelmann, E. Vogt and A. Hollweg for their technical assistance during this work. The authors also thank T. Feron for his help setting up the initial equations of the photosynthesis model.

Author contributions

SLG, YR, and MG conceived the experiments. SLG and MH ran the experiments under the supervision of YR and DvD. MG implemented the model changes described in Appendix A under the supervision of AS, GL, DL and JV. SLG and MG calibrated the model. MG ran the simulations under the supervision of AS and GL. DL, AS, FM, and MJ set up the equations (and wrote) Part I.2.2 and Appendix H.2.1. SL wrote Appendix G.1. MG wrote the other parts of the manuscript under the supervision of AS and GL. All authors provided critical feedback and helped shape the research, analysis and manuscript.

Chapter 3

In silico analysis of carbon and water dynamics in the rhizosphere under drought conditions

In this section, we present the coupling of CPlantBox with a multi-scale soil model, including microbial dynamic.

Behold this compost! behold it well! [...] What chemistry! [...]
Now I am terrified at the Earth, it is that calm and patient,
It grows such sweet things out of such corruptions,
It distills such exquisite winds out of such infused fetor,
It renews with such unwitting looks its prodigal, annual, sumptuous crops

Walt Whitman *This compost*

This chapter is a modified version of a scientific article:

Giraud, M., Sircan, A., Streck, T., Leitner, D., Lobet, G., Pagel, H., and Schnepf, A. (2025, preprint). In silico analysis of carbon stabilisation by plant and soil microbes for different weather scenarios. EGUsphere, https://doi.org/10.5194/egusphere-2025-572.

3-1 Introduction

Understanding the dynamics driving the water and carbon (C) balances in the soil-plant-atmosphere continuum is key to predict, mitigate, and adapt agroecosystems to climate change (George et al., 2024, Silva and Lambers, 2021b). While water plays an important role as a resource and as an intra- and inter-domain signalling carrier (De Swaef et al., 2022), C compounds can serve as an essential energy source or a biomass building block (George et al., 2024, Lynch et al., 2021).

Plants link the water and C balances in the soil and atmosphere via plant-related processes, such as coupled stomatal regulation-photosynthesis-transpiration, C and water transport and storage in plant tissues, C usage (growth, maintenance, exudation) root-soil water exchanges and root C release (De Swaef et al., 2022, Lacointe and Minchin, 2019, Silva and Lambers, 2021b). The plant's capacity to capture, transport and release water (resp. C) across domains (e.g., C fixation leading to rhizodeposit hotspots distribution (Landl et al., 2021a)) or within one domain (e.g., hydraulic lift, (Lynch et al., 2021)) is also strongly defined by the topology of its shoot (de la Fuente Cantó et al., 2020) and root system (de la Fuente Cantó et al., 2020, Galindo-Castañeda et al., 2023, George et al., 2024)–e.g., lateral root branching density, number of root tips (Galindo-Castañeda et al., 2023, Lynch, 2021). Likewise, plant anatomical characteristics (e.g., number and nature of the concentric root cells, number and size of the phloem and xylem vessels) strongly affect the flow within the plant (Lynch et al., 2021) and the plant-soil exchanges (Galindo-Castañeda et al., 2023, Lynch et al., 2021).

The quantity and quality of the C released by the plant influence the transfer of nutrients and energy to the soil (de la Fuente Cantó et al., 2020) and thus microbial activity (de la Fuente Cantó et al., 2020, Galindo-Castañeda et al., 2022, Galindo-Castañeda et al., 2023, Schnepf et al., 2022) directly as energy and biomass input and indirectly by changing the properties of the soil (de la Fuente Cantó et al., 2020, George et al., 2024, Schnepf et al., 2022). Root water uptake changes the soil moisture (Ruiz et al., 2021), which eventually triggers drought stress responses of soil microbial communities (Bardgett and Caruso, 2020). Plant-soil feedbacks drive inter and intra-specific plant interactions (Putten et al., 2013) (e.g., competition for soil resources). Plants can also exert

direct feedback effects on themselves (e.g., aboveground-belowground feedback) which will influence their fitness. Those feedbacks depend on soil organic matter (SOM) content and texture, which determine soil water holding capacity and hence moisture availability under drought (Bardgett and Caruso, 2020, George et al., 2024).

Plant-soil exchanges lead to the creation of the rhizosphere, an area of soil around the root with biotic (rhizodeposition, microbial communities) and abiotic (structure, water content) characteristics distinctive from the bulk soil (de la Fuente Cantó et al., 2020, George et al., 2024). The hydraulic conductance of the rhizosphere is the primary constraint for plant water transport, especially in water-limited environments (De Swaef et al., 2022, Khare et al., 2022, Roose et al., 2016), leading to abiotic stress and stomatal closure (Damour et al., 2010, George et al., 2024) or better drought resilience in case of favorable abiotic conditions (Lynch et al., 2021).

The rhizosphere is also the most important hotspot of microbial activity on the planet (George et al., 2024, Lynch et al., 2021). Soil microbes control SOM decomposition and CO_2 release (Pagel et al., 2020) and regulate soil C allocation to the different organic and mineral pools. Rhizosphere microbes are relevant to soil C cycling as the activation-deactivation processes allow for rapid responses to the input of C and energy provided by rhizodeposits (George et al., 2024). Soil microbes are therefore a significant sink of photoassimilates, influencing root C release, root-to-shoot C allocation and overall plant growth (Lynch et al., 2021).

Due to the tight coupling of water and C cycling between soil, microbes and plant, it becomes relevant to design integrated plant-microbiome traits adapted for specific soils to promote resource capture by plants and ensure the resilience of plant-soil systems to environmental stressors (de la Fuente Cantó et al., 2020, Galindo-Castañeda et al., 2022, Silva and Lambers, 2021b). A thorough unterstanding of interactions between soil-microbes-plant (Bardgett et al., 2013, Galindo-Castañeda et al., 2022, Gaudio et al., 2021, George et al., 2024, Roose et al., 2016) that can lead to intra- and inter-specific competition (for light, water and nutrients), complementarity (spatio-temporal and niche processes) and facilitation (improving access to resources) is therefore essential to inform breeding choices (De Swaef et al., 2022, Gaudio et al., 2021).

Mechanistic biogeochemical modelling facilitates the analysis of complex systems (Putten et al., 2013, Schnepf et al., 2022). Especially Functional Structural Plant Models (FSPMs) link the plant structure with its function and simulate processes at the plant level (Ruiz et al., 2021, Schnepf et al., 2022). Coupling an FSPM with a soil model in a multiscale modelling framework leverages the strengths of different models and increase model accuracy (Gaudio et al., 2021, Roose et al., 2016, Schnepf et al., 2022). Small-scale models provide effective properties and predict emerging behaviour at higher scales, while models at coarser scales provide the initial and boundary conditions to the small scale models (Schnepf

et al., 2022).

Although many studies looked at water and flow of (usually one) nutrient (especially phosphorus) in soil and rhizosphere (Mai et al., 2019, Roose et al., 2016, Ruiz et al., 2021), few focused on both water and C (Ruiz et al., 2021) and accounted for physiochemical processes (Pot et al., 2022). Moreover, many of the spatially explicit rhizosphere models ignore microorganisms (Roose et al., 2016) although the increasing resolution of those models make a detailed characterisation of the soil biochemistry more relevant (Lynch et al., 2021, Roose et al., 2016). FSPMs simulating C (Rees et al., 2023a,b) and water flow were also developed (Giraud et al., 2023, Lacointe and Minchin, 2019) but simulating neither the soil C nor water flows (Lacointe and Minchin, 2019, Rees et al., 2023a,b) or only the water flow (Giraud et al., 2023).

This study aimed to set up and implement a fully integrated plant-soil-microbiome model that accounts for root-microbiome interactions directly and enables the in-depth analysis of drought responses of C cycling in plant-soil systems. We present an extended version of the FSPM CPlantBox (Giraud et al., 2023). CPlantBox is a 3D functional structural full plant model and was used to model several processes across the plant, single root, ans pore scales (Giraud et al., 2023, Landl et al., 2021a, Mai et al., 2019). Root system simulations were also implemented to evaluate the effect of root system structure on the root-soil exchange of water (Khare et al., 2022), C (Landl et al., 2021a), or water and phosphorous (Mai et al., 2019). We coupled CPlantBox with TraiRhizo (Sircan et al., 2024), a 1D axisymmetric soil model based. TraiRhizo offers a unique balance between complexity and precision for the C and microbial dynamic and a simplified representation of the soil structure–see review of Pot et al. (2022) for an evaluation of the analogous SpatC (Pagel et al., 2020) against other soil models. For this study, TraiRhizo was adapted and re-implemented in DuMu^x (Koch et al., 2021) for a faster and more adaptable simulation setup. The two models were coupled using an updated version of the multiscale setup of Mai et al. (2019) to obtain higher accuracy and stability.

In the first part of the paper, we present the equations of the model, with emphasis on the soil processes. We then present the scheme for the coupling of the different domains and modules. In the second section of the paper, we implement the model to evaluate how short dry spells at different stages of the plant's development affect the soil C balance and, in particular, the C stabilisation according to the biokinetic characteristics of the microbial community. In the last section of the paper, we discuss the output of the coupled model against experimental and *in silico* results, and we compare our framework against other existing simulation tools.

3-2 Material and methods

3-2-1 Overview of the multiscale framework

3-2-1-1 Individual models

For the plant domain, we use the FSPM CPlantBox, as presented by Giraud et al. (2023). In CPlantBox, the plant is represented as a series of connected 1-dimensional segments, making a branched network of nodes in a 3-dimensional space (Fig. 3-1(a)). CPlantBox simulates the plant water flow using the analytical solution of (Meunier et al., 2017), and the coupled the stomatal regulation (Leuning, 1995) and FvCB-photosynthesis (Farquhar et al., 1980) models. The plant C balance is evaluated with a numerical solver (Lacointe and Minchin, 2019), which yields the semi-mechanistic plant growth rate.
For the soil domain, Sircan et al. (2024) developed a 1-dimensional axisymmetric soil model that computes the C transport and microbial dynamics according to a set C release rate from a root segment. Their model was re-implemented within the existing soil framework of the FSPM (Mai et al., 2019) and adapted to take into account variations of water content. It was expanded to represent the 3-dimensional macroscale (Fig. 3-2) (Khare et al., 2022, Koch et al., 2021, Mai et al., 2019). The macroscale model is made of 3-dimensional sub-control volumes (i.e., voxels), while the microscale model is comprised of axisymmetric 1D sub-control volumes (i.e., segments). A list of the symbols of the soil models, their units and meanings can be found in appendix B.1. The explicitly represented soil C pools are: low molecular weight organic compounds (dissolved and sorbed), high molecular weight organic compounds, copiotrophic and oligotrophic microorganisms with active and dormant metabolic states, emitted CO_2 due to microbial respiration. In the following section, we give an overview of the spatial and temporal coupling of these models within a multiscale framework.
The hydraulic conductance of the soil–root interface is the primary constraint for plant water transport when the soil is dry. Achieving realistic results requires, therefore, high spatial resolution near the soil-root interface, leading to computationally expensive simulations (Khare et al., 2022, Roose et al., 2016). To balance computing speed and model accuracy, we therefore coupled the models presented in this section in a multiscale framework where the spatial resolution is set according to the distance from the soil-root interface.

3-2-1-2 Spatial coupling

Figs. 3-1 and 3-2 give a graphical representation of the spatial coupling method, adapted from the approach presented by Mai et al. (2019) and Khare et al. (2022). Each root segment below-ground is allocated to a macroscale voxel, selected according to the location of the segment centre when it was first created. For each root segment, we initialise a microscale model that computes the water flow, C transport, and microbial dynamics based on the plant-soil water and C exchanges prescribed by the root segment. Other than in Sircan et al. (2024), in which

the plant-soil exchange was prescribed as boundary conditions at the root-soil interface, the net releases of water and C in this coupled model come from the simulation outputs of the FSPM, driven by inner plant flows and processes, such as photosynthesis, transpiration, and growth (Giraud et al., 2023).
The volume of the macroscale voxel is divided between the microscale domains it contains. Therefore, the maximum possible volume of a single microscale domain is the volume of the containing voxel. The total perirhizal volume around a root system (bulk soil) corresponds to the total volume of all the microscale domains. It is also equal to the sum of the volumes of all macroscale voxels containing at least one root segment. Therefore, the bulk soil volume depends on the root system structure and on the user-defined resolution at the macroscale rather than an *a priori* evaluation of the rhizosphere volume. The microbial reactions and adsorption are computed at the voxel scale for voxels that do not contain root segments. The biochemical reactions are computed at the microscale for voxels containing at least one segment. The resulting variation rates are represented at the macroscale as a sink term. The flow of water and transport of solutes between the voxels is computed at the macroscale and given as sink term to the microscale segments. Moreover, we scale the size of the microscale segments, meaning that the segments near the root surface are smaller than the ones further away. The macroscale domain is divided into subdomains whose concentrations and flows are computed in parallel while the microscale domains are distributed between processes run in parallel. The plant processes are not simulated in parallel.

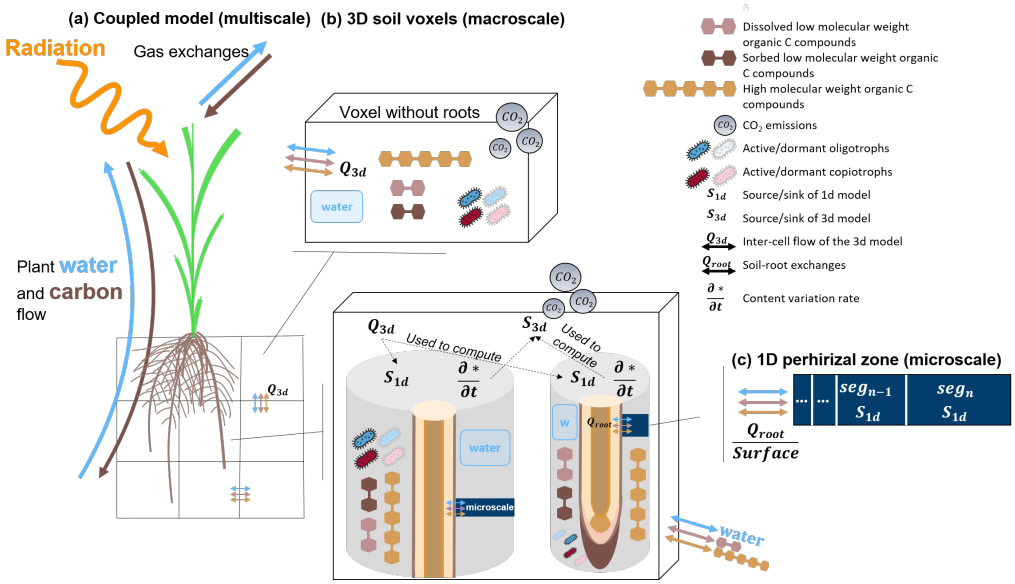

Figure 3-1: Representation of the multiscale coupling with (a) the whole multiscale model, (b) example of 3D macroscale soil voxels, (c) example of a 1D microscale model. The 3D soil model (black grid) is made up of 3D voxels (transparent rectangles with black borders). The 1D model is represented using the dark blue line in the 3D voxels. It lies between a root segment and the end of the implicitly-represented perirhizal zone (grey hollow cylinder).

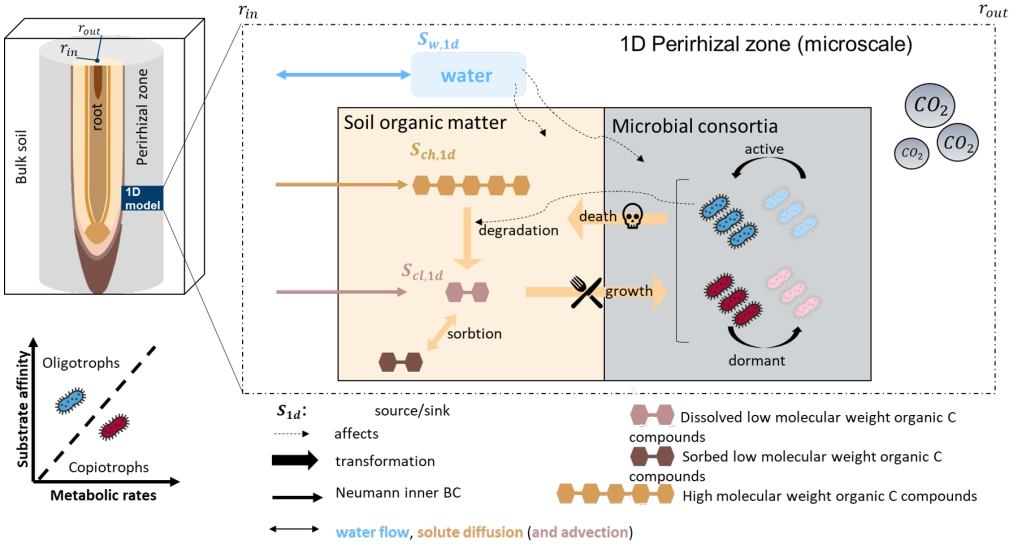

Figure 3-2: Representation of the updated microscale model (Sircan et al., 2024) reimplemented within the multiscale framework (Koch et al., 2021, Mai et al., 2019). The model represents the soil domain around the root (perirhizal zone). Eight carbon pools are represented: carbon from organic compounds with a low molecular weight (dissolved and sorbed), organic compounds with a high molecular weight, active and dormant copiotrophs and oligotrophs, emitted microbial CO_2. Water flow and content are also represented. The graphic was adapted from Sircan et al. (2024).

Fig. 3-3 gives a representation of the hard-coded direct interactions between the atmospheric conditions and the C and water pools represented in the plant and soil. For instance, for a set soil water content, high transpiration leads to a lower plant water potential and, thus, to a lower growth. In contrast, growth leads to a larger root system and leaf surface, allowing for higher transpiration. It is the interactions between those processes that drive the water and C balances of the overall system.

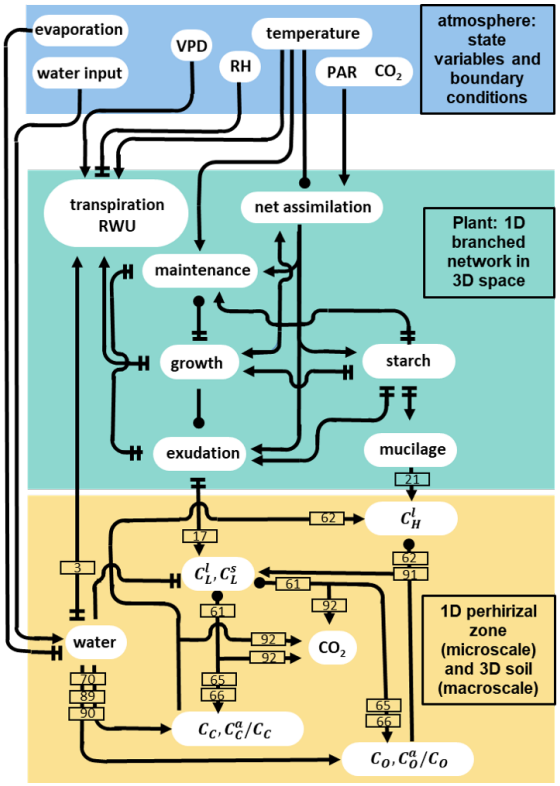

Figure 3-3: Graphical representation of the direct interactions represented between the different carbon and water pools plant model (green rectangle), soil models (yellow rectangle) and the atmospheric conditions given as input (blue rectangle). The lines ending with an arrow represent a positive effect, two perpendicular lines represent a negative effect, and a circle represents both a positive and negative effect (the net effect depends on the simulated conditions). The numbers in the rectangles give the indexes of the equations describing the corresponding process. The equations affecting the plant domain are defined in Giraud et al. (2023). The atmospheric conditions are represented by user-defined state variables and boundary conditions, e.g. vapour pressure deficit (VPD), relative humidity (RH), and incoming photosynthetically active radiations (PAR). Soil carbon pool data include the concentration of carbon from low molecular weight organic compounds in the soil and water phase (resp. C_L^s, C_L^l), high molecular weight organic compounds in the water phase (C_H^l), total or active copiotrophs (resp. C_C, C_C^a) and oligotrophs (resp. C_O, C_O^a).

3-2-1-3 Temporal coupling

The modules of the plant and soil models are implemented sequentially. The order of the implementation is presented in Fig. 3-4. Each "outer" loop (encompassing all the modules) represents one time-step. Within each time step, two nested fixed-point iterations are implemented:

1. the "first fixed point iteration" contains the interactions between the [a] soil water flow and solute transport (for the microscale and macroscale domains) and [b] plant water flow and stomatal regulation.

2. the "second (inner) fixed point iteration" links the steady state plant water flow and stomatal regulation. This iteration loop was presented in Giraud et al. (2023) and will not be detailed further here.

These two nested iteration loops allow for a higher computing speed. Indeed, the inner fixed point iteration for the stomatal opening can necessitate several hundred iterations before convergence (especially in the case of water-induced stomatal closing). While the FvCB-stomatal regulation module can compute these iterations quickly, the code section evaluating the water flow at the macro- and microscale is much slower. Moreover, in the first iterations of the FvCB-stomatal computation, strong over- or under-estimation of the transpiration may occur, especially in case of sharp changes in environmental conditions. Using these inputs directly for soil flow computation could lead to non-convergence errors. Processes in the C and water cycles can operate on different timescales (Gaudio et al., 2021). Specifically, the speed of plant growth and phloem transport tends to be slower than the plant and soil water flow. When running a simulation, it may consequently be necessary to use a smaller time step within the fixed-point iteration. Thus, we set up an adaptive operator splitting between the outer time step and the first fixed-point iteration, with an automatic adaptation of the fixed-point iteration time step. Moreover, we used an implicit time stepping within the fixed-point iteration, which means that the output of the previous loop is used as initial and boundary conditions for the next loop of the iteration. This implicit time stepping is more stable than the explicit alternative and allows us to use larger time steps. Currently, the plant sucrose flow and growth are outside the iteration loop. Indeed, adding these modules to the fixed-point iteration would significantly slow the simulation. Also, for time steps $< 1\ h$, changes in plant shape and sucrose transport remain limited.

3-2-2 Governing Equations

These sections present the method used to simulate water and carbon turnover within the plant and the soil. Each section is divided between the plant-specific and soil-specific equations. For the soil part, the common equations for both the macro- and microscale are presented, followed by equations specific to each

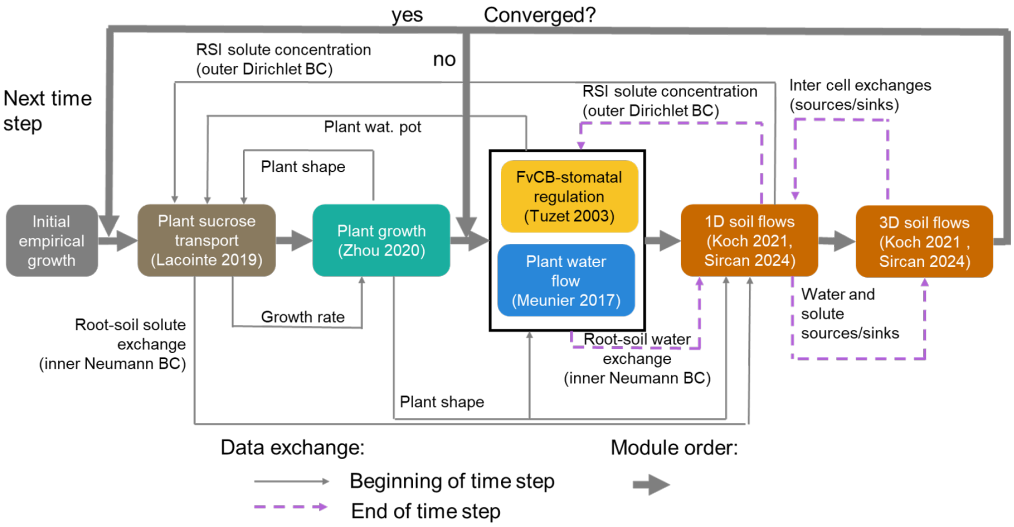

Figure 3-4: Representation of the time loop, as well as the implementation order and exchange of data between the modules. The loop including the soil flows (orange rectangles) corresponds to the outer iteration loop. The black rectangle outline containing the plant water flow (blue rectangle) and stomatal regulation (yellow rectangle) corresponds to the inner iteration loop. The plant sucrose transport and balance (brown rectangle) and growth (green rectangle) are not included in the iteration loop. Adapted from Giraud et al. (2023).

domain. The soil volume (volume of the solid and pores) is written in cm^3 *scv* (sub-control volume). The amounts of solutes and microbes are given in units of equivalent carbon ($mol\ C$). As the equations describing the microbial reactions remain similar to those set up by Sircan et al. (2024), these ordinary differential equations are included in appendix B.4.

3-2-2-1 Plant water flow

The plant water model is described in Giraud et al. (2023). Briefly, we compute the plant xylem water flow as:

$$-K_{ax,x}\frac{\partial^2 \psi_{h,x}}{\partial^2 \xi} = -p_{seg} \times q_{w,plant-out} \text{ for } \Omega \backslash \partial\Omega, \tag{3-1}$$

$$\frac{\partial \psi_{h,x}}{\partial \xi} = 0 \text{ for } \partial\Omega \text{ (all organ end-nodes)} \tag{3-2}$$

$K_{ax,x}$ ($cm^4\ hPa^{-1}d^{-1}$) is the xylem intrinsic axial conductance and ξ (cm) is the local axial coordinate of the plant. p_{seg} (cm) is the perimeter of the plant exchange zone, Ω the domain considered (here the plant), and $\partial\Omega$, the domain's boundary (here: the tip or end-node of each organ). We assume a no-flux boundary condition here as the plant-exterior water exchanges occur along the segments.

The net water sink is given by the lateral water flow ($q_{w,plant-out}$ in $cm\ d^{-1}$), which corresponds to the xylem-soil ($q_{w,root-soil}$) or xylem-atmosphere ($q_{w,leaf-air}$) water exchange:

$$q_{w,plant-out} = \begin{cases} q_{w,root-soil} = min(K_{lat,x}, K_{sri})(\psi_{h,x} - \psi_{m,1DS}) & \text{, if root} \\ q_{w,leaf-air} = K_{lat,min}(\psi_{h,x} - \psi_{h,ox}) & \text{, if leaf blade} \end{cases} \quad (3\text{-}3)$$

With $K_{lat,x}$ ($cm\ hPa^{-1}\ d^{-1}$) the lateral hydraulic conductivity of the root cortex (for roots) or of the vascular bundle-sheath (for leaves). K_{sri} ($cm\ hPa^{-1}\ d^{-1}$) is the equivalent lateral hydraulic conductivity and $\psi_{m,1DS}$ (hPa) is the soil matric potential at the inner boundary of the corresponding 1D microscale soil domain (root-soil interface). $\psi_{h,ox}$ (hPa) is the water potential in the outer-xylem compartment, computed by the FvCB-stomatal regulation module. Note that, as changes in plant water storage are neglected, root water uptake equals transpiration at any given time step: $\sum_i^{segs} p_i q_{w,root-soil,i} = \sum_i^{nr} p_i q_{w,leaf-air,i}$, with p_i (cm) the perimeter of the segment i within the set $segs$.

K_{sri} is computed from the soil and plant data:

$$K_{sri} = \begin{cases} \frac{K_{sat}\kappa_m(S_{sat})}{\Delta r_{root-1DS}} & \text{if } q_{w,root-soil} \leq 0 \\ \frac{K_{sat}}{\Delta r_{root-1DS}} & \text{else} \end{cases}, \quad (3\text{-}4)$$

$$K_{sat} = \frac{\kappa}{\mu_w} \quad (3\text{-}5)$$

With K_{sat} ($cm\ hPa^{-1}\ d^{-1}$) the soil saturated hydraulic conductivity, μ_w ($hPa\ d$) the viscosity of the soil water solution, assumed equal to that of pure water at $20°C$. κ (cm^2) is the intrinsic permeability of the soil and κ_m ($-$) the relative conductivity loss, dependent on the soil water saturation (S_{sat}, $-$). $\Delta r_{root-1DS}$ (cm) is the distance in radial coordinate between the root surface and the centre of the inner segment of the microscale domain. Net root water release ($q_{w,root-soil} > 0$) is only limited by K_{sat} in the soil, while net root water uptake ($q_{w,root-soil} < 0$) is also limited by κ_m.

3-2-2-2 Soil water flow

The variation in volumetric soil water content (θ in $cm^3\ water/cm^3\ scv$) is defined according to the Richards equations (Richards, 1931):

$$\frac{\partial \theta}{\partial t} = \nabla \cdot (K(S_{sat})(\nabla \psi_{m,XDS} - \nabla \psi_{g,XDS})) + S_\theta \quad (3\text{-}6)$$

With $K(S_{sat})$ ($cm^2\ hPa^{-1}\ d^{-1}$) the unsaturated hydraulic conductivity (hereafter written as K for simplicity), $\nabla \psi_{m,XDS}$ and $\nabla \psi_{g,XDS}$ (hPa/cm) are the gradients of matric and gravitational water potentials in either the macroscale (ψ_{3DS}) or microscale (ψ_{1DS}) domain, respectively.
S_θ ($cm^3\ water\ cm^{-3}\ scv\ d^{-1}$) is the net source of water in the domain. ∇ is the

nabla operator, either for the 1D axisymmetric (radial derivative $\frac{\partial}{\partial r}$) or for the 3D domain ($\frac{\partial}{\partial x} + \frac{\partial}{\partial y} + \frac{\partial}{\partial z}$). We moreover have:

$$\theta = \phi S_{sat} \tag{3-7}$$

with ϕ ($cm^3\ pore/cm^3\ scv$) the soil porosity (assumed constant). for simplicity, we assume that $\phi = \theta_s$, with θ_s ($cm^3\ water/cm^3\ scv$) the θ value at saturation. θ_r ($cm^3\ water/cm^3\ scv$) is the lowest possible θ value (residual water content). The hydraulic conductivity is defined using the pore size distribution model of Mualem (1976) and the water retention function is computed according to van Genuchten (1980):

$$S_{sat} = \left(\frac{1}{1 + (\alpha\ \psi_{c,XDS})^n}\right)^{1-1/n} \tag{3-8}$$

$$\psi_{c,XDS} = \psi_{n,XDS} - \psi_{m,XDS} \tag{3-9}$$

$$K = \kappa_m(S_{sat}) K_{sat} \tag{3-10}$$

$$\kappa_m(S_{sat}) = S_{sat}^{l_{soil}} \times [1 - (1 - (S_{sat})^{n/(n-1)})^{1-1/n}]^2 \tag{3-11}$$

ψ_n (hPa) is the reference pressure, set to 1000 hPa, and ψ_c (hPa) is the capillary pressure. α (cm^{-1}) is related to the inverse of the air entry suction, n ($-$) is a shape parameter, l_{soil} ($-$) is the soil tortuosity. The implementation of Eq. (3-6) for the macroscale 3D soil and microscale 1D soil are given respectively in appendices B.2-1 and B.2-2.

3-2-2-3 Plant carbon transport

The plant sucrose model used for this study is based on the one presented by Giraud et al. (2023). The model was adapted to simulate mucilage release. The variation of sucrose-carbon concentration in the sieve tube (C_L^{st} in $mol\ C\ cm^{-3}\ st\ d^{-1}$, with $cm^3\ st$ the sieve tube volume) is computed from Eq. (3-12):

$$\begin{aligned}\frac{\partial C_L^{st}}{\partial t} + \frac{\partial}{\partial \xi}\left(C_L^{st} \times K_{ax,st}(RT_{seg}\frac{\partial C_L^{st}}{\partial \xi} + \frac{\partial \psi_{h,x}}{\partial \xi} + \frac{\partial \psi_{g,x}}{\partial \xi})\right) \\ -S_{exud,st} - S_{starch,st} - S_{other,st} = 0 \\ \text{for } \Omega \backslash \partial\Omega,\ t > t_0,\end{aligned} \tag{3-12}$$

$$K_{ax,st}(RT_{seg}\frac{\partial C_L^{st}}{\partial \xi} + \frac{\partial \psi_{h,x}}{\partial \xi} + \frac{\partial \psi_{g,x}}{\partial \xi}) = 0 \quad \text{for } \partial\Omega \tag{3-13}$$

$$C_L^{st} = C_{L,0}^{st} \quad \text{for } t = t_0, \tag{3-14}$$

With R ($hPa\ cm^3\ K^{-1}\ mol^{-1}$) the ideal gas constant, $K_{ax,st}$ ($cm^4\ hPa^{-1} d^{-1}$) the sieve tube axial intrinsic conductance, T_{seg} (K) the temperature of the plant segment. $S_{exud,st}$ ($mol\ cm^{-3}\ st\ d^{-1}$) is the loss of C_L^{st} by exudation of low molecular weight organic carbon compounds, S_{starch} ($mol\ cm^{-3}\ st\ d^{-1}$) is the loss or gain

of C_L^{st} by starch synthesis or degradation, $S_{other,st}$ ($mol\ cm^{-3}\ st\ d^{-1}$) represents other net sinks of C_L^{st}–like gain by assimilation and inflow from the mesophyll compartment.
We assume that the exudation of low molecular weight organic carbon occurs via a passive diffusion (Ma et al., 2022, Rakshit et al., 2021), represented by a mass transfer approach:

$$S_{exud,st} = q_{exud}\frac{2\pi\ r_{in}\ L}{V_{st}} \tag{3-15}$$

$$q_{exud} = K_{lat,st}\ (C_L^{st} - C_L^l) \tag{3-16}$$

With $K_{lat,st}$ ($cm\ d^{-1}$) is the lateral sieve tube conductivity for sucrose, V_{st} ($cm^3\ st$) is the sieve tube volume. We assume that exudation occurs mainly near the root tip (Badri and Vivanco, 2009, Neumann and Römheld, 2009, Rakshit et al., 2021). Therefore, $K_{lat,st} > 0$ only for the last segment of growing roots. C_L^l ($mol\ C/cm^3 water$) corresponds to the concentration of dissolved low molecular weight organic carbon in the soil water at the root-soil interface. It is obtained from the inner segment of the microscale soil domain assigned to the root segment.
We assume that the mucilage is made from starch (*starch*, in $mol\ C/cm^3$) before being released via an active process (Kutschera-Mitter et al., 1998, Nguyen, 2009, Rougier, 1981). The production and release processes are represented in the following equations:

$$\frac{\partial starch}{\partial t} = S_{starch,st} - S_{mucil,st} \tag{3-17}$$

$$S_{starch,st} = k_{targ,starch}(C_L^{st} - C_{L,targ}^{st}) \tag{3-18}$$

$$S_{mucil,st} = q_{mucil}\frac{2\pi\ r_{in}\ L_i}{V_{st}} \tag{3-19}$$

$$q_{mucil} = k_{mucil}starch \tag{3-20}$$

With $k_{targ,starch}$ ($1/d$) and k_{mucil} (cm/d) parameters controlling respectively the synthesis and decay rate of starch and the release of mucilage. $C_{L,targ,st}^l$ defines the target C_L^{st} and thus the threshold between starch synthesis and desynthesis. As in Hirschberg et al. (1998), the release of mucilage is represented via a simple first-order kinetic. We then obtain S_{mucil} ($mol\ cm^{-3}\ st\ d^{-1}$), the release rate of mucilage. $k_{mucil} > 0$ only at the tip (in our model: the last segment) of growing roots. Both q_{exud} and q_{mucil} ($mol\ cm^{-2}\ d^{-1}$) can then be used by the microscale soil domains (see Eq. (B-27), Eq. (B-31)).

3-2-2-4 Soil carbon transport

The changes in solute concentration are computed using the advection-diffusion-reaction equation—see Ahusborde et al. (2015) and Helmig (1997, Eq 3.100):

$$\frac{\partial\theta C_X^l}{\partial t} - \nabla\cdot\left(C_X^l\vec{u}_X\right) - \nabla\cdot(D_X(\theta,\phi)\nabla C_X^l) - S_X\ (-S_{1DS-3DS,X}) = 0 \tag{3-21}$$

$$S_{ads,X} + S_{microbe,X} = S_X \tag{3-22}$$

C_X^l (mol/cm^3 $water$) is either the concentration of carbon from dissolved low molecular weight organic compounds (C_L^l) or high molecular weight organic compounds (C_H^l) in the soil liquid solution. S_X ($mol\ C\ cm^{-3}\ scv\ d^{-1}$) is the net source of C_X^l, and it encompasses the adsorption of C_X^l ($S_{ads,X}$, $mol\ C\ cm^{-3}\ scv\ d^{-1}$, see section 3-2-2-5) and the changes caused by microbial reactions ($S_{microbe,X}$, $mol\ C\ cm^{-3}\ scv\ d^{-1}$, see appendix B.4 and Eq. (B-15)). $S_{1DS-3DS,X}$ is an additional source term only used at the microscale and presented in Eq. (B-21). $\vec{u}_X$ is the advective flux.

$D_X(\theta, \phi)$, the effective dispersion in the porous medium (caused by molecular diffusion and hydrodynamic dispersion), is obtained from Millington and Quirk (1961), as implemented by Koch et al. (2021):

$$D_X(\theta, \phi) = D_{Xw} \frac{\theta^{\frac{10}{3}}}{\phi^2} \tag{3-23}$$

With D_{Xw} (cm^2/d) the diffusion coefficient of the carbon compound in water. Low molecular weight organic C compounds can be modelled as true solutes and are thus subject to convection. High molecular weight carbon compounds correspond to the plant mucilage releases, a gel-like substance when hydrated (Kutschera-Mitter et al., 1998, Ma et al., 2022). To simulate the rheology of mucilage slime, we adopt a simplified approach with a null advective flux ($\vec{u}_H$) and a lower diffusion coefficient ($D_{H,w} < D_{L,w}$). The implementation of Eq. (3-21) for the macroscale 3D soil and microscale 1D soil are given respectively in appendices B.3-1 and B.3-2.

3-2-2-5 Adsorption

We describe in this section the adsorption of low molecular weight organic C compounds (C_L) from the liquid phase (C_L^l) onto the solid phase (C_L^s). As Sircan et al. (2024), we describe the adsorption as linear. However, instead of equilibrium sorption, we used linear first-order kinetics. This was necessary in order to obtain the same result at the micro- and the macroscale. Moreover, not assuming instantaneous equilibrium allows us to set lower time steps during the simulations. We further assume that only the low molecular weight organic substances can be sorbed. Adsorption was implemented according to Ahrens et al. (2020):

$$\frac{\partial C_L^s}{\partial t} = k_{ads} C_L^l (C_{L,max}^s - C_L^s) - k_{des} C_L^s \tag{3-24}$$

$$C_{L,max}^s = C_{L,max}^s = \rho_b \frac{k_{clsmax}\ k_{clay+<20\mu msilt}}{M_{mass,C}} \tag{3-25}$$

with k_{ads} ($23265.14\ cm^3\ scv\ mol^{-1}\ C\ d^{-1}$) and k_{des} ($4.47\ d^{-1}$) the adsorption and desorption rates, defined according to the values given by Ahrens et al. (2020). $C_{L,max}^s$ ($mol\ C\ cm^3\ scv$) is the maximal concentration of adsorbed C_L^s, ρ_b ($1.51\ g$ mineral soil$/cm^3\ scv$) is the soil bulk density, $M_{mass,C}$ ($12.011\ g\ C\ mol^{-1}\ C$) is the molar mass of carbon, $k_{clay+<20\mu msilt}$ (0.45−, Wang

et al. (2018)) is the fraction of clay and silt smaller than 20 μm. k_{cssmax} $(-)$ is an empirical factor defined according to the make up of the clay minerals in the soil. According to Jiang et al. (2014), the Selhausen soil (used to calibrate the model) is dominated by illites, a 2 : 1 mineral. Consequently, $k_{cssmax} = 0.079$ (Ahrens et al., 2020). This yields $C^s_{L,max} = 4.5e^{-3}\ mol\ C\ cm^{-3}\ scv$). From the adsorption dynamic, we get the adsorption net sink for dissolved low molecular weight organic carbon: $S_{ads,L} = -\frac{\partial C^s_L}{\partial t}$, used in Eq. (3-22). As high molecular weight organic carbon compounds represent the mucilage gel, no adsorption is represented: $S_{ads,H} = 0$.

3-2-2-6 Plant growth and perirhizal zone

We simulate dynamic plants that grow according to input parameters (representing plants genetically determined characteristics) and to their water and sucrose status (see Giraud et al. (2023)). This leads to changes in root segment lengths and to the creation of new root segments. The method used to define the shape, water and solute content of new or growing microscale domains is presented below.

Currently, each root segment (and associated microscale domain) is allocated to the soil voxel containing its centre when the segment is first created, even if one or both segment extremities are out of the voxel. In order for the output to be realistic, it is therefore important for the maximum root segment size to be lower or near the length of a soil voxel. Moreover, for the current setup, root segments will remain in the same soil voxel even if the centre of an existing segment (because of segment elongation) moves to another voxel. We assume that these simplifications will have a limited influence on the results if the resolution is high enough. After simulating plant growth for the time step N, we obtain the new lengths (L, cm) and radius (r_{in}, cm) of the roots, which are, respectively, the lengths and inner boundary of the microscale domains. From these shape data, we recompute the outer radial boundary of the 1D domains (r_{out}, cm) according to the volume of the soil voxels ($V_{3DS,scv}$) and the number of microscale domains contained within (nr). For the microscale domain k in the voxel i:

$$r^N_{out,k} = \sqrt{\frac{r^2_{in,k}\ L^N_k}{\sum_j^{nr_{i,N}}\ r^2_{in,j}\ L^N_j}\frac{V_{3DS}}{\pi\ L^N_k} + r^2_{in,k}} \tag{3-26}$$

Consequently, creation of new roots or changes in L and r_{in} of existing roots in a voxel can lead to changes in the perirhizal zone volume allocated to an individual microscale soil domain. From the soil point of view, a higher density of roots in the voxel leads to smaller perirhizal zones for each of the root segments contained in it. The description of the method used to update the amounts of water and carbon in the microscale models as they are created and change shape is presented in the appendix B.5. In brief, the gradient of existing 1D domains with decreasing volume is preserved. We then compute the volume of newly freed soil for each voxel. From the amount of water and carbon lost by the 1D models, we obtain the mean water content and carbon concentration in the freed space. This volume

(and corresponding water and solute contents) is distributed between the new and expanding microscale domains to respect the results of Eq. (3-26).

3-2-3 Model application: The effect of dry spells on soil carbon and microbial dynamics near a growing plant

The implementation setup for the coupled model follows the one used in Giraud et al. (2023), with Van Genuchten parameters measured from one testing site of the Research Center Jülich, located in Selhausen (50.8659 N, 6.4471 E). We simulated the growth of a C3 monocot under a control scenario (hereafter called *baseline*) and compared it with dry spells at two plant development stages. Both dry spells were represented by a period of one week without rainfall: 11 to 18 days and 18 to 25 days after sowing, hereafter called *earlyDry* and *lateDry*. The virtual plants were obtained by running the plant model up to day 10 (after sowing) using a mean empirical growth rate (neither dependent on the carbon- nor water-flow) and without simulation of the water and carbon fluxes. From the 10^{th} day onward, we simulated the carbon and water fluxes and of the carbon- and water-limited growth, as well as the soil carbon dynamic. The plants all grew under the *baseline* conditions with a static soil (constant mean $\psi_{m,soil} = -100\ cm$ at hydraulic equilibrium), except during the dry spells: day of growth 11 to 18 for *earlyDry*, and 18 to 25 for *lateDry*). At the start of the dry spells, the mean soil water potential was lowered to $-450\ cm$ and warmer and drier atmospheric conditions were simulated. After the dry spells, the *baseline* environmental and static soil water conditions were used. We used a no-flux boundary condition for the macroscale soil. Fig. 3-1 summarises the timeline of the three scenarios.

Table 3-1: Timeline of the simulations. The grey (resp. blue) cells indicate the empirical (resp. semi-mechanistic) growth period and "ds" the implementation of the dynamic soil. The blue gradient during the dynamic soil simulation represents the decreasing soil water content. The sharp shift from dark to light (resp. light to dark) blue at the beginning (resp. end) of the dry spells represents the implementation of the *dry spell* (resp. *baseline*) atmospheric and initial (resp. constant) soil variables. Table taken from Giraud et al. (2023)

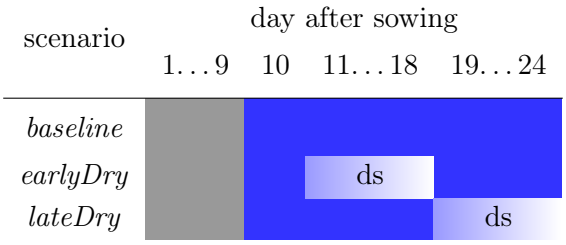

For the plant model, the calibration of Giraud et al. (2023) was adapted to better follow our assumptions regarding the plant mucilage and carbon dynamic (e.g., preferential carbon usage for growth over exudation), and to address the divergences between the outputs of Giraud et al. (2023) and experimental observation (light dry spells caused carbon rather than water scarcity). Changes

were also made to the lateral conductivity ($k_{lat,x}$, $cm\ hPa^{-1}\ d^{-1}$) in the mature root zone: the constant value was computed according to Bramley et al. (2007, Fig. 4.15) and set to 1.5% of $k_{lat,x}$ within the immature root zone, see appendix B.8 for a more detailed description.

The selection of the biokinetic parameter sets is given in appendix B.9. Briefly, Sircan et al. (2024) computed 1650 parameter sets respecting parameter and process constraints defined according to a literature review. Those sets were divided into three groups according to the resulting C_L^l radial profile for the microscale domains. 33 sets were selected randomly from each group and a simulation was run for four days. We then selected three parameter sets giving diverging results. Table 3-2 presents the characteristics of the selected sets. The first set, thereafter called *highCO2*, led to a high CO_2 production in spite of a low microbial development. The second set, thereafter called *highMB*, led to the highest microbial development. The third set, thereafter called *lowMUptake*, led to the highest soil solute concentration (low microbial solute uptake).

Table 3-2: Qualitative summary of the characteristics of the selected biokinetic parameter sets (*highCO2*, *highMB*, *lowMUptake*). O: oligotrophs, C: copiotrophs, (de)act.: activation and deactivation, *VS*: compared against. The evaluation has the following order (representing the low-to-high gradient): $- < . < + < ++$

denomination	**fitness**		**act. *VS* deact.**		**(de)act. *VS* growth + decay**		**O *VS* C**		**CO_2 losses**
	O	**C**	**O**	**C**	**O**	**C**	**(de)act.**	**fitness**	
highCO2	+	−	.	.	+	+	.	+	++
highMB	+	.	+	+	++	.	−	+	+
lowMUptake	−	.	−	−	.	.	.	−	-

3-2-4 Analysis of the outputs

The data were treated and visualised with Python3.10 (Van Rossum and Drake Jr, 1995).

3-2-4-1 Scale definition for model evaluation

To take advantage of the multiscale setup, we evaluated the model outputs at four different scales: macroscale, bulk soil, perirhizal$_{trunc}$, microscale. We define the macroscale as the soil voxels (Fig. 3-1(b)) that contain at least one root at the end of the simulations in any of the scenarios. This soil space is therefore constant and equal for all the simulations. We define the bulk soil as the macroscale data of voxels containing at least one root at each time step, potentially different for each simulation. For the perirhizal$_{trunc}$ analysis, we aggregated the mean concentrations for each microscale domain truncated at a specified distance from the root surface, denoted as $\Delta r_{analysis}$. The value of $\Delta r_{analysis}$ was pragmatically set

to 0.06 *cm*. It corresponds to the minimum distance between the inner and outer boundaries of the microscale domains obtained during the simulation. By setting a consistent distance between the inner and outer boundaries of the truncated domains, we obtained a partial uniformity between the domains that reduced variations that could arise from differences in soil allocation to each domain (see Eq. (3-26)). Moreover, using these truncated 1D models allowed us to evaluate a soil area nearer to the root surface, for comparison with the bulk soil scale. At the microscale, we evaluated the data for each segment of the 1D models (Fig. 3-1(c)) individually.

3-2-4-2 Vertical concentration profiles

To evaluate the vertical concentration profiles, we computed the total soil volume, water volume, and C content (for each C pool) for each depth at the bulk soil scale. This allowed us to determine the corresponding mean C concentration and water content around the root systems. Additionally, we present the minimum and maximum C concentrations (for each C pool) and water content values at each soil depth to capture the lateral variability.

3-2-4-3 Complementary cumulative volume distributions

We created complementary cumulative volume distribution plots of the concentration at the perirhizal$_{trunc}$ scale. In these plots, the x-axis represents different concentration values. The y-axis shows the absolute or relative volume of the selected perirhizal zone (up to 0.06 *cm* from the root surface) with concentrations equal to or greater than the corresponding x-axis value. This representation provides insight into the spatial variability and distribution of concentrations within the specified zone. Additionally, these graphs allow us to evaluate how much of the perirhizal zone volume exceeds certain concentration levels, such as hotspot thresholds.

3-2-4-4 Relative change of soil carbon distribution

To evaluate the change in plant-soil C turnover for the different weather scenarios and biokinetic parameter sets, we categorised C into four pools: solutes (dissolved and sorbed low molecular weight organic C and high molecular weight organic C), microbes (including total oligotrophic and copiotrophic C), active microbes (including active oligotrophic and copiotrophic C), and emitted CO_2 (microbial respiration). We evaluated the C content at the macroscale for each of these pools at each time step and normalised the values for *earlyDry* and *lateDry* under each biokinetic parameter set according to the corresponding baseline scenario: $(C_{X,spell} - C_{X,baseline})/C_{X,baseline}$, with X the name of the C pool.

3-2-4-5 Soil organic carbon hotspots

One important effect of plant C releases is the resulting changes in soil organic C (SOC). Using the study of Poeplau and Don (2023), we set three SOC thresholds defined according to the $SOC/SOC_{expected}$ ratio: 0.65, 0.83, 1.16. $SOC_{expected}$ ($mol\ C\ cm^3\ scv$) is the average expected SOC according to the soil clay content. Following the method of Poeplau and Don (2023) and the Selhausen clay content data of Wang et al. (2018), we set $SOC_{expected} = \frac{\rho_b}{1000 M_C}(0.0288 k_{clay} + 13.674) = 2.36e^{-3}\ mol\ C\ cm^3\ scv$, with k_{clay} the soil clay content in $g\ kg^{-1}$, ρ_b ($g/cm^3\ scv$) the soil bulk density, M_C ($g\ C/mol\ C$) the C molar mass. The 1/1000 factor is used to go from $g\ kg^{-1}$ to $g\ g^{-1}$.

A first evaluation of the outputs showed that our simulated values were almost always in the lowest SOC class and significantly below the mean Selhausen SOC reported by Wang et al. (2018). For the hotspot analysis, we therefore added an SOC_{slow} class representing the very slow decomposing SOC, assumed to be constant over the study period. We set $SOC_{slow} = SOC_{theoric} - SOC_{simulated,init}$, with $SOC_{simulated,init}$ the total SOC explicitly simulated in our model (solute and microbial pools) at the beginning of the simulation, and $SOC_{theoric}$ the value from Wang et al. (2018). We then set the variable $SOC = SOC_{simulated} + SOC_{slow}$, computed at the microscale. This is the value used to compare with the SOC thresholds given by Poeplau and Don (2023). We use a stacked area graph to represent the SOC hotspots, as soil above the higher thresholds is also above the lower thresholds. As presented by Landl et al. (2021a), we computed the volume-normalised hotspot volume to obtain a metric for the efficiency of the rhizodeposition.

3-2-4-6 Radial concentration profiles

Finally, for the microscale, we presented C concentration data for all segments of the 1D domains on one scatter plot per weather scenario and parameter set, giving, on the x-axis, the radial coordinate of the segment centers according to the root surface.

3-3 Results

3-3-1 Three-dimensional simulation of microbial carbon dynamics in the soil-plant system

The integrated plant-soil-microbiome model extends the FSPM model of Giraud et al. (2023)) by implementing microbial carbon (C) dynamics in soil. Consequently, the extended FSPM model now provides 3D simulations of plant architecture, water and C dynamics in the plant and the soil, and microbial dynamics in the soil, including the rhizosphere. While this study focuses on C cycling and microbial dynamics at the root-soil interface, more detailed simulation results regarding water and C flow in a plant for the three considered weather scenarios

are given in Giraud et al. (2023). Fig. 3-5 shows a typical simulation after 24.5d of plant growth (midday) for a biokinetic parameterisation that results in high microbial CO_2 production (*highCO2*) under the *baseline* scenario. The simulation highlights an increasing concentration of dissolved low molecular weight organic C (C_L^l) and active copiotrophs (C_C^a) in response to root exudation in the upper part of the root system, near its centre.

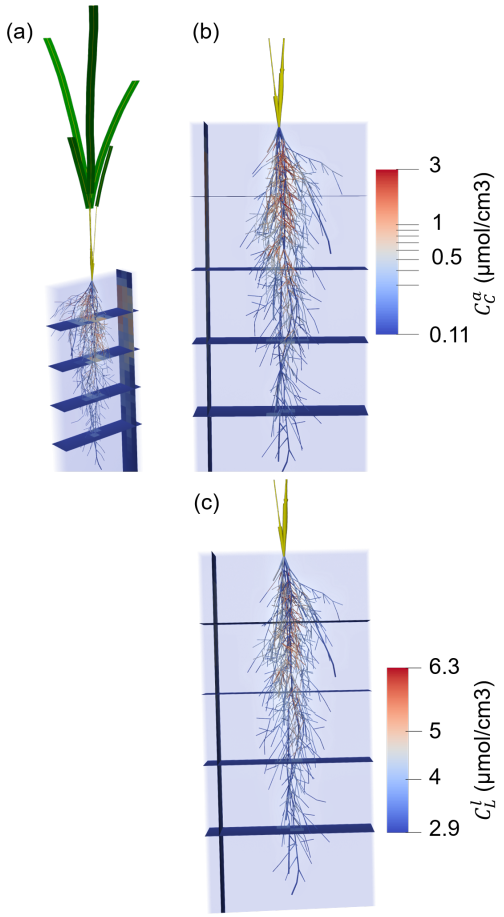

Figure 3-5: 3D representation of the plant and soil domains for microbial biokinetic parameterisation *highCO2* under the *baseline* scenario at 24.5d of growth, with (**A**) the whole plant, (**B**, **C**) zoom on the root system. (**A**, **B**) present the concentration of active copiotrophic biomass C (C_C^a) and (**C**) that of dissolved low molecular weight organic C (C_L^l). The soil colours give the concentration in the bulk soil. The root colours give the concentration at the soil-root interface. Unified colours were given to the aboveground roots, shoot segments and leaf blades.

3-3-2 Plant processes

Fig. 3-6.A presents the plant xylem mean water potential (ψ_x, cm) for each biokinetic parameterisation and weather scenario. The simulation results reflect

the diurnal dynamics of ψ_x in response to the truncated sinusoidal curve used to describe the atmospheric conditions (light input, air relative humidity and temperature). These boundary conditions affected the plant stomatal regulation and, thus, the C assimilation and transpiration rate. We observed an increase of ψ_x over time for *baseline* as the leaf:root ratio decreased. With drought, ψ_x rapidly decreased at the beginning of the dry spells and recovered after its end in response to changes in soil water content and mean air relative humidity during the dry spells (see Giraud et al. (2023, Table 1)). Towards the end of the simulation with *earlyDry*, ψ_x converged to the values of *baseline*, indicating a full recovery of the plant water uptake capacity. As a consequence of the lower leaf:root ratio, ψ_x was lower at the beginning of the dry spells for *earlyDry* (11^{th} day) than for *lateDry* (18^{th} day). However, in comparison to *earlyDry*, the higher plant transpiration under *lateDry* with higher total leaf and root surface area led to a quicker decrease in soil water content. This mechanism induced lower ψ_x in the *lateDry* compared to the *earlyDry* scenario from the third day after the start of the dry spells onward (13^{th} and 20^{th} day).

Fig. 3-6.B shows the cumulative amount of C used for growth (and growth respiration) during the simulation. The diurnal cycle of ψ_x affected the plant growth. During the day, the transpiration-induced lower ψ_x limited plant growth compared to the night, where increased ψ_x permitted faster, albeit still water-limited, C assimilation and biomass production. The required C was taken from the starch reserves built up during the day. We can also observe trends over the simulation. Unlike younger plants, older plants could maintain growth during the diurnal period outside of the dry spells. During the dry spells, growth occurred only at night and at a severely reduced rate. On the last three nights of the late dry spell, we observed no night-growth due to lower plant night ψ_x.

Plant maintenance respiration increased during the spells due to the higher air temperatures. In the *earlyDry* scenario, plant growth was severely limited compared to *baseline*, resulting in a lower plant maintenance respiration rate after the dry spell ended (18^{th} day). For *lateDry*, we saw a lower maintenance respiration rate from the fourth day of the spell. The total cumulative respiration (growth and maintenance related) at the end of the simulation was highest for the *baseline* scenario. It was about 29% lower for *earlyDry* and 18% lower for *lateDry*. The biokinetic parameterisation had no significant effect on the plant water processes or growth and maintenance.

Figs 3-6.C and D present the cumulative amount of C used for (respectivelly) passive exudation and active mucilage release during the simulation. The plant water balance affected the exudation rate. During the simulation, exudation occurred only under limited C use for growth in response to low ψ_x. Although the mucilage release was not always maintained at night (e.g., at the end of the *earlyDry* simulation), this process was less affected by the diurnal cycle than the exudation. This led to qualitative changes in the type of C released by the plant throughout the day. In comparison to *baseline* the early dry spell led to a lower total exudation at the end of the simulation: -32%, -35%, and -37% for *highCO2*, *highMB*, and *lowMUptake*, respectively. Conversely, the late dry spell resulted in higher exudation compared to *baseline*: $+29\%$ for *highCO2* and *highMB*, $+26\%$

for *lowMUptake*. Thus, the dry spells triggered both positive and negative effects on exudation. On the one hand, more C became available for exudation with decreasing plant growth. On the other hand, the lower ψ_x led to a closing of the stomata, causing a lower assimilation rate per unit of leaf area.
Lower plant growth also led to lower leaf and total root surface area compared to *baseline*, which limited exudation. The effect of the simulated spells on total exudation was, therefore, dependent on the stage of plant growth at the start of the spell. After the end of the early dry spell (days 18-23), the daily plant exudation for *earlyDry* was higher than for *baseline*, partially reducing the exudation gap between the two. The total mucilage release under *earlyDry* at the end of the simulation was close to that under *baseline*: -11%, -2%, and $+6\%$ for parameter sets *highCO2*, *highMB*, and *lowMUptake*, respectively. In contrast, mucilage release reached $+139\%$ for *highCO2* and *highMB* and $+170\%$ for *lowMUptake* under *lateDry*. We found an effect of the biokinetic parameterisation on exudation and mucilage release. The *highCO2* and *highMB* parameterisation, associated with high microbial C usage rates resulted in lower concentrations of dissolved low molecular weight organic C (C_L^l $mol\ C/cm^{-3}$). This lower C_L^l increased passive exudation. The higher exudation was then compensated by the plant starch reserves (in the mesophyll and around the plant transport tissues) and did not affect the plant growth or maintenance. As the mucilage release rate is a function of the plant starch content, higher exudation induced lower mucilage release.
These differences in exudation and mucilage release appeared only after the onset of the dry spells. The release rates between the biokinetic parameterisations for *earlyDry* became similar again from the third day after the end of the dry spell onward. The highest exudation rate per unit of root surface for a single segment was obtained at 11 day $5hrs$ with *baseline* and *lateDry* (0.153 $mmol\ C\ cm^{-2}\ d$), at 10 day $21hrs$ for *highCO2* and *lowMUptake* with *earlyDry* (0.145 $mmol\ C\ cm^{-2}\ d$), and at 12 day $8hrs$ for *highMB* with *earlyDry* (0.148 $mmol\ C\ cm^{-2}\ d$).

3-3-3 Vertical concentration profiles

Fig. 3-7 presents the vertical concentration profiles of organic C, microbial pools and produced CO_2 from microbial respiration at the end of the simulation for the bulk soil scale. The root system structure affected the concentration profiles. The peaks of organic C between 0 cm and 13 cm of depth corresponded with the location of the highest root length density (Fig. 3-7(a), (b), (c) and Fig. B.6). A second peak of maximum C concentration was observed at the bottom of the profile close to the tips of primary roots. That second peak is especially strong for *lateDry* due to lower root growth, i.e., very few root segments reached 20 cm, such that the mean C concentration equals the maximum concentration. Conversely, the higher lateral dispersion of the roots in the upper soil layers led to a stronger lateral variability in the concentration profile (larger min-max ranges). Stronger plant growth under *baseline* resulted in perirhizal zones and rhizodeposition at lower depths such that the C accumulation at the root tips was much less pronounced compared to the dry spell scenarios.

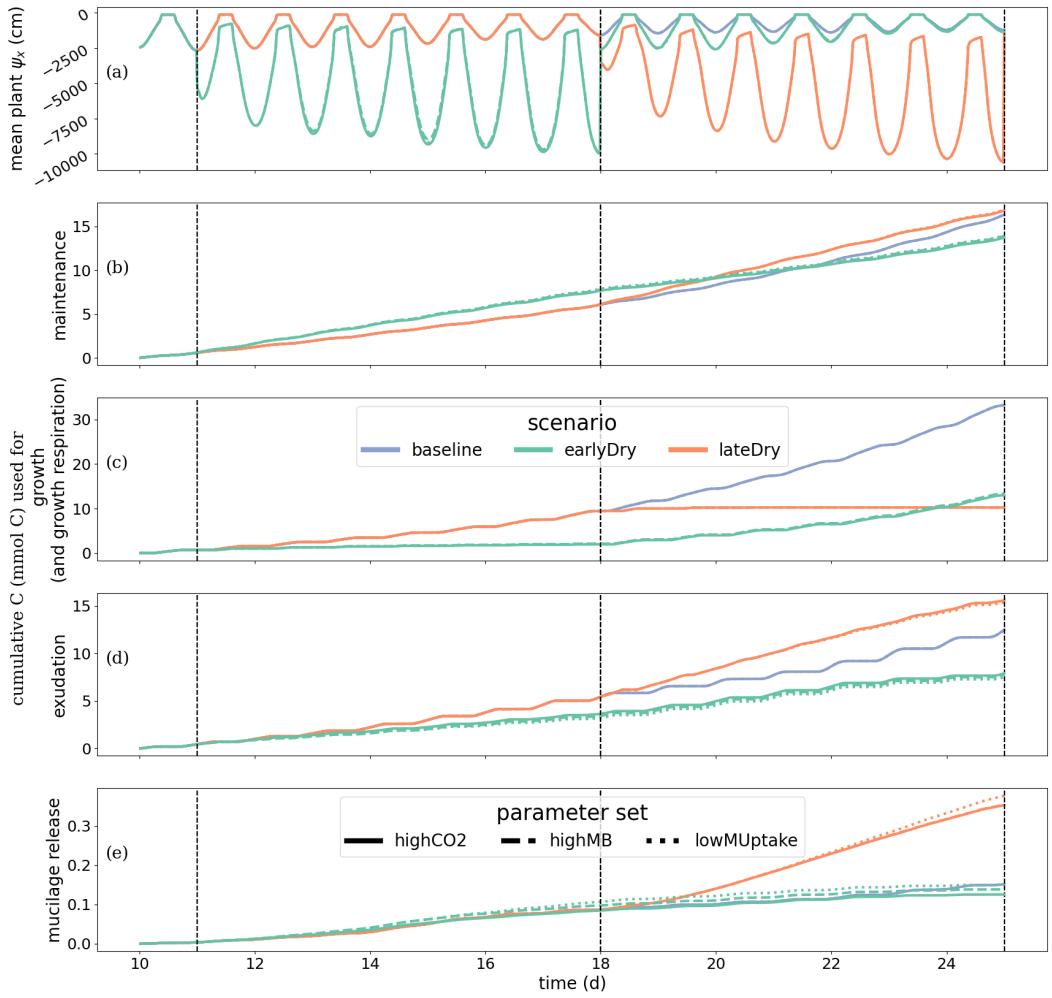

Figure 3-6: Dynamics of Plant water- and carbon-related metrics: (**A**) the mean plant xylem water potential (ψ), (**B**) cumulative carbon growth and growth respiration, (**C**) exudation, (**D**) mucilage release. Line colours indicate the weather scenarios: baseline (blue) against an early (green) and late (red) dry spell. Line types represent different biokinetic parameter sets. The vertical dotted lines show the beginning and end of the early (day 11 to 18) and late (day 18 to 25) dry spells. Please note that the scales of the y-axis differ in each subplot.

The biokinetic parameterisation strongly influenced the C concentration profiles (Fig. 3-7(e)-(j)). With *highCO2*, solute and microbial C concentrations (C_L^l, C_L^s, C_H^l, C_C, C_O) were lowest. The *highMB* parameterisation also led to low solute concentrations but triggered increased microbial C due to higher microbial C consumption. With *lowMUptake*, solute concentrations were highest because of low microbial C uptake. These results are consistent with the observations obtained during the model conditioning (see appendix B.9).
Although the weather scenarios had a less pronounced effect on the concentration profiles than the biokinetic parameterisation, the dry spells induced distinct effects. Under *earlyDry*, the concentration profiles were close to that of *baseline* (e.g., C_C, Fig. 3-7(e)), or between *baseline* and *lateDry* (e.g., C_H^l, Fig. 3-7(b)). This shows the resilience soil C cycling to the early dry spell. In particular, despite the lower total exudation, the concentration of C_L^l for *earlyDry* is close to that of the *baseline* due to the increased exudation rate during the second half of the simulation (Fig. 3-7(a)). Under *lateDry*, we observed higher C_H^l. This can be attributed to higher plant mucilage release for this scenario (Fig. 3-7(b)). The highest C_C^a and C_O^a values at the last time step are obtained with *baseline* (Fig. 3-7(g), (h)). The differences in the microbes' activation can partly be explained by the water content remaining at the high default value ($-100\ cm$) during the whole simulation under *baseline*. C uptake by copiotrophs was higher (high C_C, and microbially respired C as CO_2 but lower C_L^l) under *lateDry* for *highCO2* and *highMB* (Fig. 3-7(d), (e)). This results can be linked to the higher total exudation and lower water content, making the C ressources more readily available to the microbes. However, for *lowMUptake*, the higher C uptake by copiotrophs occurred under *baseline*. Thus, water was relatively more limiting than C supply for copiotrophic growth with *lowMUptake* (compared with *highCO2* and *highMB*) because of a lower maximum uptake rate. For that same reason, maximum C_O for each parameter set is very slightly higher ($< +0.7\%$) under *baseline*.

Due to the short simulation time, C_O (Fig. 3-7(f)) showed no significant growth at the bulk soil scale ($< 3\%$ of growth), but the dry spells weakly affected the proportion of active and dormant oligotrophs (Fig. 3-7(h), (j)).

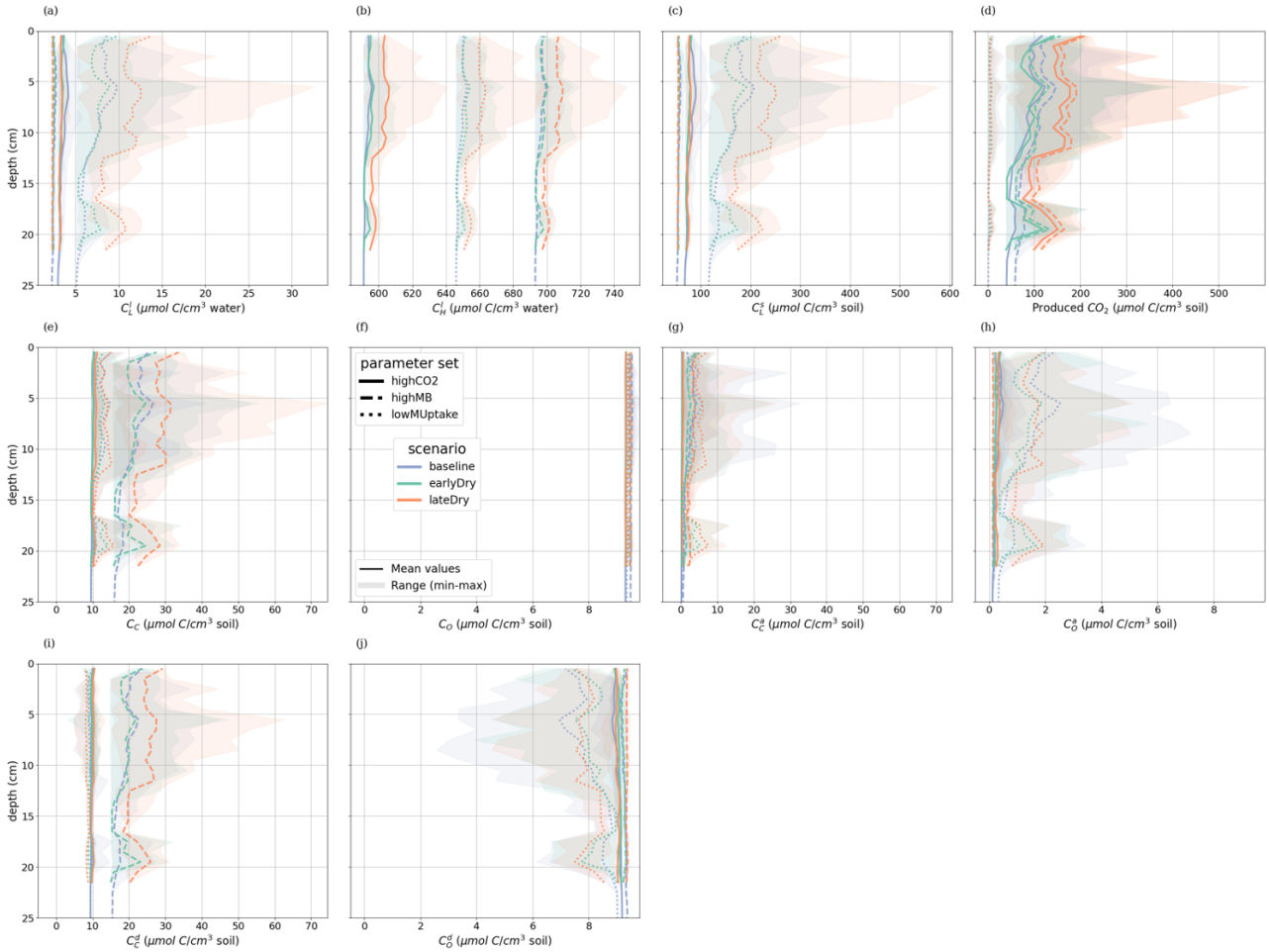

Figure 3-7: Mean bulk soil concentrations of the soil carbon with depth
(**a**) dissolved and (**c**) sorbed (C_L^s) low-molecular-weight organic molecules, (**b**) high-molecular-weight organic molecules(C_H^l), (**d**) produced CO_2, (**e, g, i**) total (C_C), active (C_C^a) and dormant (C_C^d) copiotrophs, (**f, h, j**) total (C_O), active (C_O^a) and dormant (C_O^d) oligotrophs. Line colours indicate the weather scenarios: baseline (blue) against an early (green) and late (red) dry spell. Line types represent different biokinetic parameter sets. The semi-transparent bands give the range between the minimum and maximum concentration in soil voxels with at least one root segment at each depth.

3-3-4 Complementary cumulative volume distributions

Fig. 3-8 shows the perirhizal$_{trunc}$ volume with a concentration inferior or equal to the value on the x-axis. The description and motivation of the evaluation method for this figure are given in section 3-2-4-4. Root exudation and mucilage release triggered concentration peaks of solutes and microbial C in the perirhizal$_{trunc}$ volume (Fig. 3-8). Particularly copiotrophs were strongly stimulated reaching high abundances up to 580 $\mu mol/cm^3$ *soil* for *lateDry* with *highMB*. Both dry spells led to strongly reduced total perirhizal$_{trunc}$ volumes at the end of the simulation of 42% for *earlyDry* and 34% for *lateDry* in relation to *baseline*. As a consequence, maximum C_H^l and C_C^l concentrations were lowest with *baseline* because the released plant C triggering copiotrophic growth was distributed in a larger volume.

While *lateDry* with *highCO2* and *highMB* caused the highest CO_2, C_C and C_C^d peaks at the bulk soil scale (see respectively Fig. 3-7(d), (e), (i)), for the perirhizal$_{trunc}$ zone the highest values for these parameter sets were obtained with *earlyDry* (Fig. 3-8(c), (d), (f)). The simulated copiotroph growth during the dry spell occurred earlier under *earlyDry*, creating a larger pool of C_C^d ready to be re-activated and grow during periods of high exudation. As the growth rate is a function of the current C_C^a, high C_C^d early in the simulation favoured the overall growth in those hotspots.

Parameterizing the model with *highMB* under *lateDry* caused an especially high C_C over most of the perirhizal$_{trunc}$ volume with an increase of active and a strong build-up of dormant copiotrophs (Fig. 3-8(d), (e), (f)). Conversely, although *highMB* under *lateDry* also led to a slight increase in the total and dormant oligotrophic concentrations (Fig. 3-8(g), (i)), it resulted in a decrease in the amount of active oligotrophs (Fig. 3-8(h)). This simulated pattern indicates a pronounced competition between oligotrophs and copiotrophs for this scenario-parameter set combination. Indeed, the C_O^a values started decreasing strongly during the second half of the late dry spell, when the exudation rate became also lower.

3-3-5 Carbon pool distribution

We wished to evaluate the changes in C turnover within the plant-soil system, according to the weather scenarios and for the different biokinetic parameter sets. Consequently, Fig. 3-9 gives the relative changes of C content in different C pools, compared with the *baseline* scenarios. The relative increases of activated microbes-C and solutes-C (Figs. 3-9.B and 3-9(c)) correspond to the night periods, when less C was exudated with *baseline* compared with the other scenarios. These periods also corresponded to higher soil matric potentials, diminishing the negative effects of the low soil θ on microbial activation during the dry spells. This relatively higher activated microbes-C pool was observed for the *highMB*

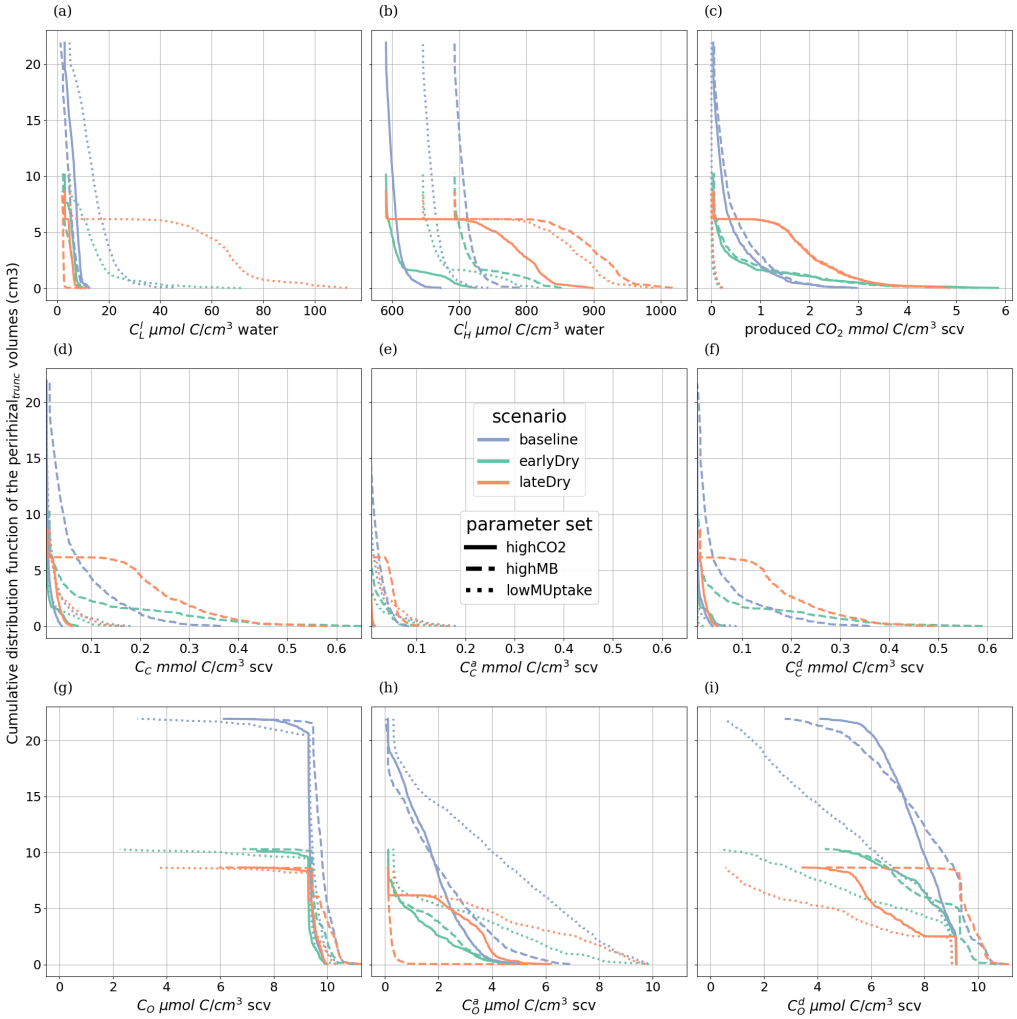

Figure 3-8: Perirhizal zone volume according to the minimal concentration of organic carbon in the truncated perirhizal zones, for (**A**) carbon of low-weight dissolved organic molecules (C_L^l), and (**B**) carbon of high-weight organic molecules in the water phase (C_H^l), (**C**) emitted CO_2, (**D**) total (C_C) (**E**) active (C_C^a) (**F**) dormant (C_C^d) copiotrophs in the soil phase, (**G**) total (C_O) (**H**) active (C_O^a) (**I**) dormant (C_O^d) oligotrophs in the soil phase. The line colors give the weather **scenario**: baseline (blue) against an early (green) and late (red) dry spell. The line types represent the different biokinetic parameterisation. Subplots D, E, F and G, H, I have the same scale on the x-axis.

and *highCO2* parameter sets with *lateDry*, although the values were lower than for *baseline* at the last time step. The *lateDry* scenario led consequently to a redistribution of C in the microbial and emitted CO_2 pools. Therefore, in spite of the higher total exudation, the solutes-C pool is lower compared with the corresponding *baseline* scenarios. On the contrary, for *lowMUptake*, the *lateDry* scenario led to a higher accumulation of C within the solutes pools (Fig. 3-9(d)). We can also note that, while we have converging relative solutes-C values between *earlyDry* and *lateDry* for *highMB* and *highCO2* by the end of the simulations, the values for *lowMUptake* are diverging. For all *earlyDry* scenarios, we observe that less C enters the soil domain, leading to relatively lower values compared with *baseline* for all pools by the end of the simulations. We also found a small relative uptick of activated microbes-C for the *highMB* and *highCO2* parameter sets after the spell (Fig. 3-9(b)), linked with the increased soil water content and plant exudation (Fig. 3-6).

3-3-6 SOC hotspots

To evaluate the root systems' exudation efficiency, Fig. 3-10 presents the relative volumes of the SOC hotspots (see definition in 3-2-4-5) in the bulk soil. We observed distinct characteristics over the whole simulation for each biokinetic parameterisation. For *highCO2*, the absolute hotspot volume remained low and decreased with growth (after an initial increase during the dry spells). For *highMB*, the total absolute hotspot volume ($SOC \geq 0.65SOC_{expected}$) peaked in the first half of the simulation before becoming stable under *baseline*. With this biokinetic parametrisation, we observed the portion the relative hotspot volume within the highest class ($SOC \geq 1.16SOC_{expected}$): 8%, 32%, and 29% of the hostpot volume belonged to the highest class under, respectively, *baseline*, *earlyDry*, and *lateDry*. Because of the low microbial activity, we observed the highest relative SOC hotspot volume for *lowMUptake* for all weather scenario: $2.9e-2$, $2.8e-2$, and 0.11 under *baseline*,*earlyDry*, and *lateDry*.

Outside of the dry spell, diurnal cylcing in the hotspot volume followed the plant C releases during the day and soil C mineralisation without replenishment at night. This dynamic is especially strong with *highCO2* as the hotspot volume is (almost) back to 0 at the end of the day periods. The dry spells buffered the diurnal cycle for all scenarios as the exudation became more stable. Moreover, the biggest hotspot volume and intensity were obtained with the *lateDry* spell, following the higher exudation and mucilage release. *earlyDry* did not lead to a higher total hotspot volume (with $SOC \geq 0.65SOC_{expected}$) for the *highMB* and *lowMUptake* parametrisation at day 25 of growth. However, a bigger portion of the SOC hotspost belonged to the higher hotspot classes ($\geq 0.83SOC_{expected}$ or $\geq 1.16SOC_{expected}$).

For *highCO2* and *highMB*, we observed an increase in hotspot volume during the first half of the dry spells, followed by a decrease during the second half. This can be partly explained by the decrease in daily plant C releases during the second half of the spell. The decreasing SOC hotspot volume in the second half of the

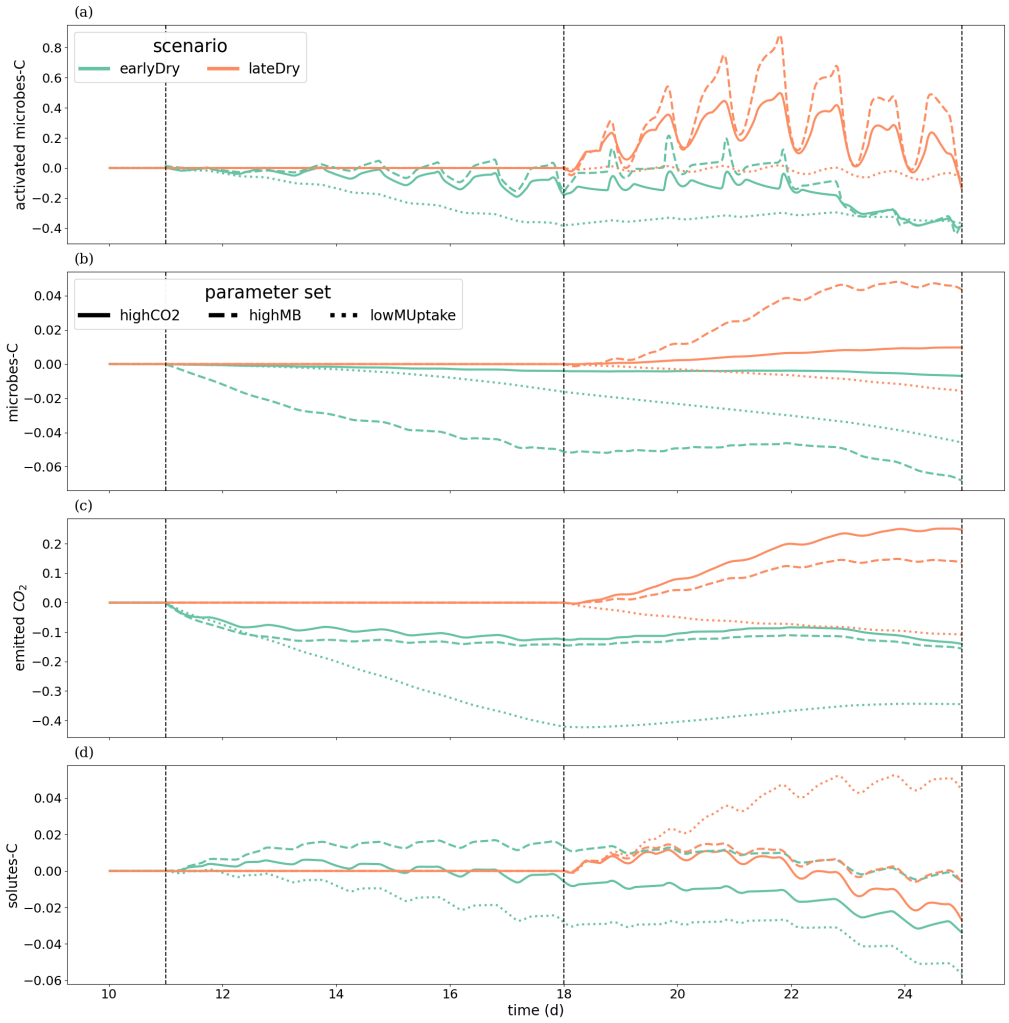

Figure 3-9: Relative change of root-released carbon use in response to drought scenarios according to the biokinetic parameters at the macroscale.
The panels present the difference of C between each drought treatment and the baseline in relation to the baseline C usage for (a) microbes-C, (b) activated microbes-C, (c) CO_2 emitted by microbes, (d) soil solutes-C. The line types represent the different biokinetic parameterisation. The dotted lines show the beginning and end of the early (day 11 to 18) and late (day 18 to 25) dry spells. Please note that the scales of the y-axis differ in each subplot.

spells was also due to the activation and growth of the microbial communities and C utilization after the first strong influx of plant C releases, followed by partial dormancy. Upon the next influx of C (the following day), the microbes reactivated and used the C more quickly. For *lowMUptake*, characterised by its lower microbial activity, we observed a continuous increase in hotspot volume throughout the spells.

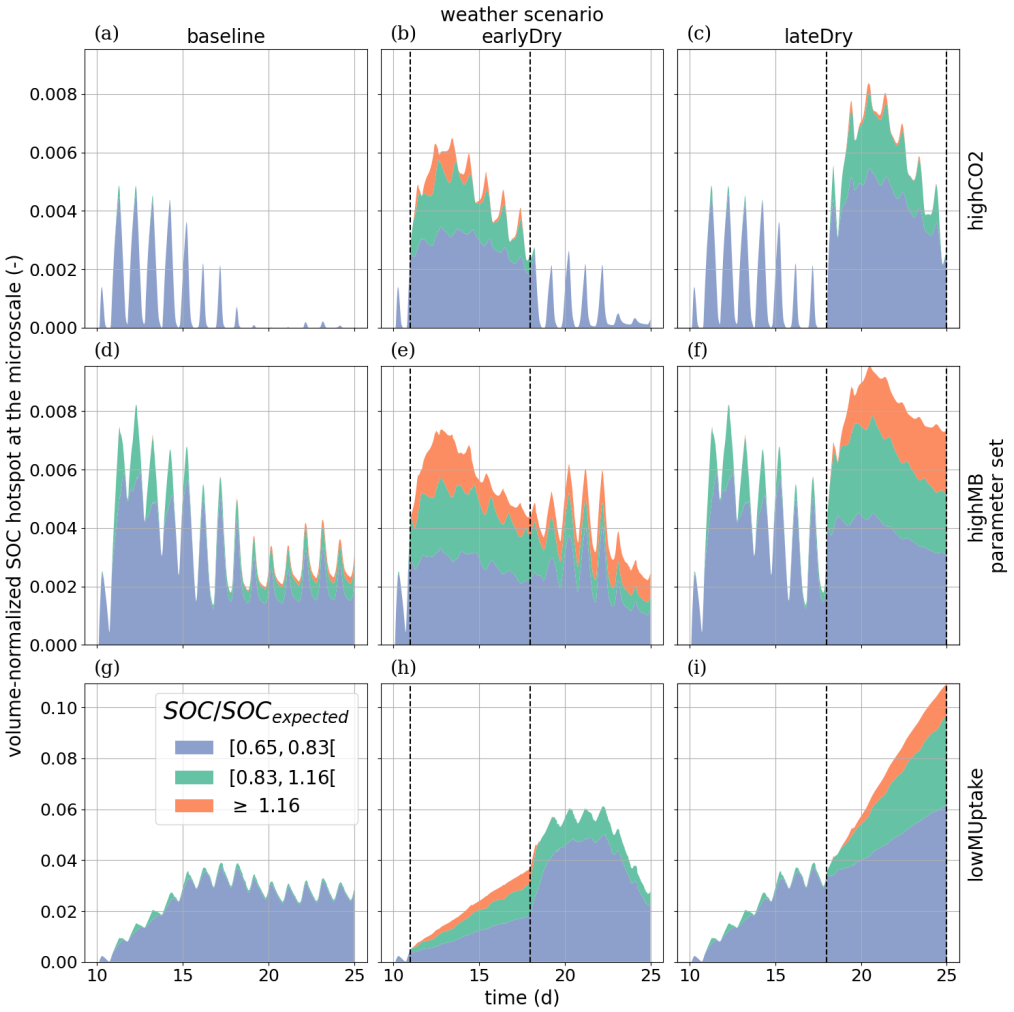

Figure 3-10: Relative SOC hotspot volume in the perirhizal zone according to time for the three $SOC/SOC_{expected}$ classes. The classes' ranges were defined according to Poeplau and Don (2023). The dotted lines show the beginning and end of the early (day 11 to 18) and late (day 18 to 25) dry spells. The third row is on a scale different from the first and second rows.

3-3-7 Radial carbon concentration profiles

To analyse how plant-soil system responses to drought affect the carbon stabilisation in the perirhizal zone, Fig. 3-11 shows the connection between the extent of the microscale domains and dissolved low-weight organic molecules concentrations C_L^l at the end of the simulation. Just as for the bulk soil and perirhizal$_{trunc}$ scales, the highest C_L^l were obtained under *lateDry* for *lowMUptake* and under *baseline* for *highCO2* and *highMB* (see Fig. B.7). For *lowMUptake*, microscale domains with shorter outer radii (segment index eight, which is nearer to the root surface) had higher radial concentrations. These shorter outer radii were caused by several microscale domains sharing a single macroscale voxel. Therefore, the higher concentrations underline the additive effect on the C_L^l profile due to proximity to the perirhizal zone, which can indicate an overlap of the rhizospheres. This proximity effect was less noticeable for *highCO2* and *highMB*, where we observed concentration profiles less dependent on the extent of the microscale domain. Indeed, with those biokinetic parameter sets, the microbial C uptake was highest and reacted fastest to high influxes of dissolved low molecular weight organic carbon. Therefore, the C_L^l was closer to an asymptote at the outer boundaries of the 1D domain. These steeper gradients can cause a the rhizosphere extent to be smaller, limiting the rhizosphere overlaps. The effect of rapid microbial C uptake with *highMB* is also visible in Fig. 3-11(d) and E, where some concentration profiles show lower C_L^l values closer to the root surface, where the concentration of C_C is highest (see Fig. B.11). The C_L^l radial profiles are strongly linked to the C_C profiles, as presented in appendix B.11.
We found a high microbial growth during the first pulse of added C followed by a transition to dormancy due to reduced C availability. Microbes remained mostly dormant until reactivated by the next C input pulse while also slowly dying. Reactivation of the microbes during the periods of high C_L^l led to a rapid consumption of the carbon in dissolved low-weight organic molecules near the root surface. As a result, C_L^L became lower than it initially was once the C input pulse diminished–at night (e.g., day 24.69 of growth) and during the second half of the dry spells. We can also observe how, during the dry spells, C_L^L were higher than for the other two scenarios due to lower water content, favouring microbial C uptake.

3-4 Discussion

3-4-1 Plant processes

In this implementation of the model, we simulated a simplified plant C dynamic compared with the one described in the literature, while still being able to recreate qualitative plant dynamic.

Regarding the plant's C release, exudation was found to be positively correlated with plant growth (Canarini et al., 2019, Přikryl and Vančura, 1980). In our

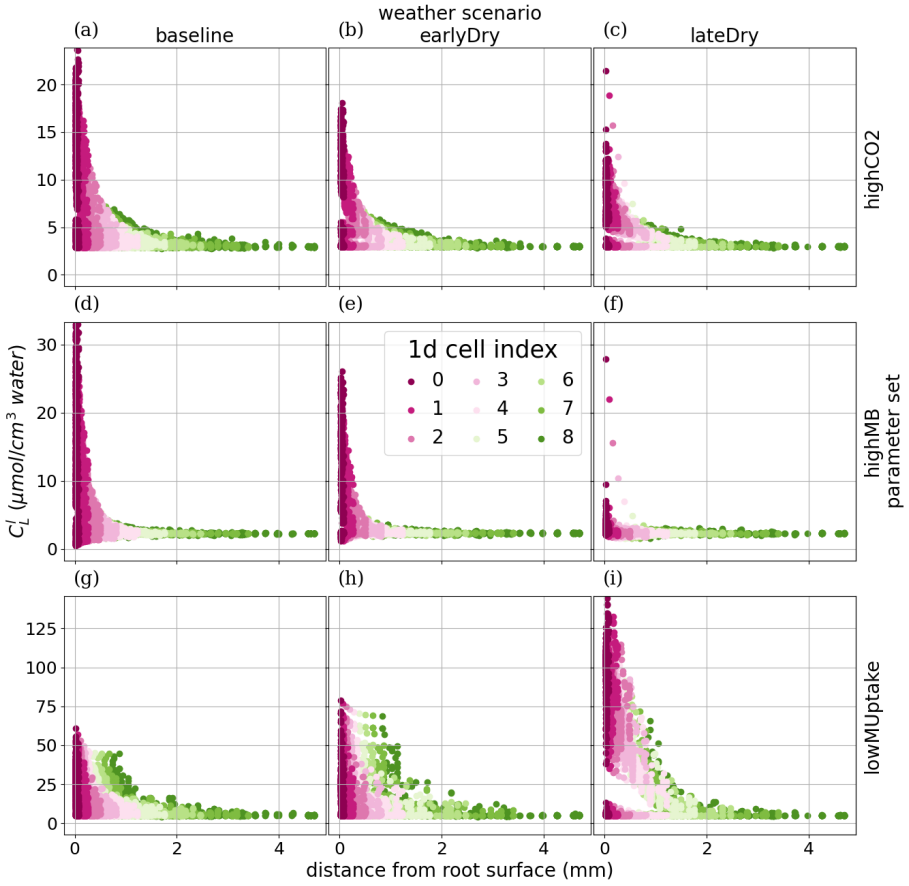

Figure 3-11: Radial concentration profile of carbon from low molecular weight organic compounds at the end of the simulation for each plant perirhizal zone. r (mm) corresponds to the distance to the root surface. The colour gives the segment index of the 1D domain. Each column corresponds to a specific weather scenario and each row corresponds to a specific biokinetic parameterisation.

study, we assumed that exudation occurs only at the growing root tip, making the two correlated on the diurnal- and weekly-scales for a specific weather scenario. However, lower growth allowed more C to be available for exudation, making the two anti-correlated on the hourly scale (day vs. night dynamics) and when comparing dryer against wetter scenarios. Moreover, in experimental studies, a decrease of rhizodeposits was also observed at night (Kuzyakov and Cheng, 2004). This dynamic was particularly strong in our simulations, as we observed no exudation in the middle of the night outside of the dry spell periods. However, we could still recreate qualitative observations made in other studies. Indeed, plants to regulate internal C concentrations and adjust C allocation for growth and maintenance under fluctuating environmental conditions by modulating starch storage (Bazot et al., 2005, Tixier et al., 2023) and C release rates (Canarini et al., 2019, Prescott et al., 2020). The upper range of our exudation rates per unit of root surface ($\approx 0.16\ mmol\ C\ cm^{-2}\ d$) was superior to the averaged rates given in the experimental study of Kravchenko et al. (2004) ($0.018\ mmol\ C\ cm^{-2}\ d$) or Trofymow et al. (1987) ($0.01\ mmol\ C\ cm^{-2}\ d$, as presented by Darrah (1991)). However, we could find similar values in the study of Personeni et al. (2007, Fig3A), due in part to its higher temporal resolution: $\approx 0.68\ mmol\ C\ cm^{-2}\ d$ under high light input and assuming an exuding root tip of 1 cm. The modelling study of Thorpe et al. (2011) for a dwarf bean plant yielded $\approx 0.69\ mmol\ C\ cm^{-2}\ d$, assuming and exuding root tip of 1 cm with radius of 0.02 cm. Moreover, microbial C uptake acted as a C sink and could affect the exudation rate (Canarini et al., 2019). We also observed a change in the type of organic C released by the plant (in our model, exudation-to-mucilage release ratio) under dry spell (Bazot et al., 2005, Hartmann et al., 2020). In spite of those changes, mucilage remained between 1-10% of exudation, consistent with the observations of Nguyen (2009), and exudation represented between 3-40% of assimilated C (Dilkes et al., 2004, Lynch and Whipps, 1990).
Regarding the plant water balance, the outputs of the model differ from that presented by Giraud et al. (2023), in part because of the implementation of the multiscale setup with fixed-point iteration, in part because of the update of the plant parameters, as decribed in section 3-2-3.

3-4-2 Distribution of soil carbon

3-4-2-1 Spatial and temporal distribution of microbial functional groups

Regarding the spatial resolution, we observed a smooth gradient of low-weight dissolved organic molecules-C (C_L^l) along the radial axis for the different biokinetic parametrisation. This suggests that our resolution for the microscale domains is sufficient to represent the C flow in the 1D soil models. For simulations of solutes with low diffusion rates (e.g. phosphorus) and a lower advection (low plant water uptake rate), the root's uptake rate would become strongly dependent on the size of the 1D segment at the root-soil interface. A study could be conducted to evaluate the minimum number of segments necessary to accurately represent the selected soil processes according to the range of

expected advection and diffusion rates of solutes under specific scenarios. The output of the simulations showed diverging results according to the studied scales (macroscale, bulk soil, perirhizal$_{trunc}$ and microscale). For instance, compared with the bulk soil scale, the perirhizal$_{trunc}$ scale showed a higher influence of the weather scenarios on the soil C balance. Moreover, the microscale showed a high gradient of the C concentration along the radial coordinate of the 1D domains that could not be represented via the perirhizal$_{trunc}$ scale. These scale-dependent results underline the advantage of using a multi-scale simulation and having a higher precision at the root-soil interface, following the observations of Mai et al. (2019). Moreover, the model showed a strong horizontal and vertical variability in the concentrations, making a 3D evaluation relevant before, for instance, aggregating the results to a 2D or 1D sink term to be used by higher-scales models. As mentioned in the first implementation of the multiscale framework (Mai et al., 2019), the low resolution near the root soil interface (at the *mm* scale) raises the issue of including lower-scale processes, such as the influence of pore size on the water and C balance (Kuppe et al., 2022). As in the study of Landl et al. (2021a), the interactions between the 1D and 3D soil models also allowed us to represent the additive effect of perirhizal zone proximity, which led to higher solute concentration under specific biokinetic parameterisation (*lowMUptake*) and favored C hotspot formation from plant releases. Landl et al. (2021a) also evaluated the influence of root traits on the soil's normalised hotspot volume. Our study complements those findings and shows that root and microbial traits have to be evaluated together, as high concentration of soil organic C can be reached for different exudation rates according to the traits of the microbial community.

Other characteristics of the microbial activity were studied with our model. With the biokinetic parameter sets *highCO2* and *highMB*, we observed a diurnal dynamic of high microbial growth under higher exudation (daytime), leading to a high consumption of C for microbial growth and maintenance. This was followed by microbial dormancy (high dormant-to-total microbe ratio at nighttime). This dynamic has been observed in the literature and can be described as a "starving-survival lifestyle", where microbes enter dormancy in a low-nutrient environment and quickly react to new inputs of resources (Hobbie and Hobbie, 2013). We found a specific reaction to resource scarcity for the parameter set *highMB* with *lateDry*. For this simulation, we found an especially high copiotroph growth and a high ratio of dormant oligotrophs. This diverging results between the two communities are indicative of a possible intra-microbial competition. This follows over studies where plant exudation and root growth affected microbial composition (Bonkowski et al., 2021, de la Fuente Cantó et al., 2020). Biokinetic parameter sets describing more active microbes (*highCO2* and *highMB*) were also linked to a higher usage of soil solutes in case of higher exudation, when compared with the *baseline* scenarios. This higher usage rate led to a form of "rhizosphere priming effect" (Bonkowski et al., 2021, Kuzyakov and Cheng, 2004) where the root exudation caused an increase in mineralisation of the pre-existing soil organic matter, leading ultimately to a relatively lower amount of C in the

solute pool compaired with the *baseline*. A more precise evaluation of a possible rhizosphere priming effect could be conducted with this setup, by dividing each C pool between the C originating from the plant additions and the C already present in the system at the beginning of the simulation. Our simulation of the microbial dynamic and competition was however limited by not accounting for other stresses than C and water scarcity, such as nitrogen, phosphorus (Brown et al., 2022, Drake et al., 2013), or oxygen (Wiesenbauer et al., 2024) scarcity. Likewise, the diurnal aspect of microbial activity would also be better represented by accounting for soil temperature (Kuzyakov and Cheng, 2004). However, over the time period of this study (two weeks), we assumed the soil temperature varied little. Regarding the spatial distribution of the microbes, the prescribed exudation near the plant root tips also led to a higher microbial growth in those areas, resulting in a vertical distribution similar to the one observed by McDougall and Rovira (1970). At the microscale, simulations also resulted in very high concentrations of copiotrophs near the root surface. Although high copiotrophic concentration near the root surface following exudation is expected (Bonkowski et al., 2021), representing microbial motility (Kuppe et al., 2022, Schnepf et al., 2022) would help smooth these concentration peaks. Representing motility could also potentially lead to a better representation of the priming effect as the microbes (especially from mature roots) might diffuse and consume C in areas further away from the root-soil interface (Dupuy and Silk, 2016).

3-4-2-2 Effect of dry spells on carbon stabilisation

The biokinetic parameterisation strongly influenced the effects of the weather scenarios on soil C balance. For more active biokinetic parameter sets (*highCO2* and *highMB*), the microbial growth was limited by C resources. The higher plant C releases *lateDry* had therefore a positive effect on the microbial community. On the contrary, for non-C limited microbial communities (*lowMUptake* parameter set), the water stress of *lateDry* affected negatively the microbial growth. These opposite reactions influenced how the soil domain was impacted by the short dry spells (see below). The microbial dynamic will have an even stronger impact on the simulated water and C balance once soil-to-plant feedback mechanisms are implemented, such as nutrient uptake (de la Fuente Cantó et al., 2020) and organic C-dependent soil hydraulic parameters (de la Fuente Cantó et al., 2020, Landl et al., 2021b).
Our *earlyDry* and *lateDry* weather scenarios led to a short decrease in soil water content, creating a wetting-drying cycle. According to the meta-analysis of Borken and Matzner (2009), these wetting drying cycles should lead, under specific environmental conditions and microbial communities, to lower microbial respiration during the spells, followed by a respiration pulse once the soil is rewetted. These pulses may or may not compensate for the earlier CO_2 emission decrease (Borken and Matzner, 2009). In our simulation, the early dry spell always led to a decrease in overall emitted microbial CO_2 at the macroscale when compared with the *baseline* scenarios. We then observed in the week following the end of the

spell a slight uptick in emitted CO_2 compared with the baseline, which did not compensate the lower earlier emissions. For the later dry spells with *highCO2* and *highMB* parametrisation, the emission pulses occurred during the spells. Indeed, while the drying led to a lower portion of microbes being dormant, the soil water content often remained too high to cause high microbial death or deactivation, especially for soil zones further away from the roots (macroscale). The lower water stress was, therefore, partly compensated by the higher C_L^l. We did not simulate an increase of plant and microbial necromass to be used by the soil microbes at the end of the spell (increasing thus the respiration once the soil is rewetted). Another explanation for the divergence is that we do not represent the easier access to "previously protected organic matter" caused by sudden soil rewetting. Moreover, we represented short dry spells (seven days) while longer spells (two weeks) may be necessary to see stronger effects on the microbial community (Borken and Matzner, 2009). The higher C mineralisation during the drying phase of the later dry spell could also be linked to the method used to represent microbial sensitivity to water stress. Indeed, for simplicity, we did not represent the direct effect of soil water content on the potential microbial death (k_{max}). Moreover, we used the same value to calibrate the sensitivity of copiotrophs and oligotrophs to water stress, although oligotrophs could be assumed to be more resistant to low soil water content. Finally, the water scarcity parameters could be recalibrated using experimental data.
We could reproduce qualitatively processes measured by Deng et al. (2021) for the C balance under limited water resources. Indeed, we observed a decrease in root biomass during the dry spells, with, under some scenarios, an increased exudation. The lower root growth then led to lower plant respiration, while the higher concentration of dissolved organic C under the late dry spell (with *highCO2* and *highMB*) led to a higher microbial respiration by the end of the simulation. Contrary to Deng et al. (2021), we did not observe a decrease in total soil organic C. They linked this decrease to a lower soil C addition from plant residue, which is not represented in our model. Under $earlyDry$, we could observe (limited) differences in concentration compared with the *baseline* seven days after the end of the dry spells, underlining the resilience of the simulated environment, especially for the soil zones nearer the roots. The $lateDry$ scenario led to the lowest plant growth but to a higher SOC hotspot volume, indicating a more resource-efficient root system exudation. We had, therefore, a trade-off in the C usage strategy.

3-5 Conclusions

In this paper, we presented the equations and implementation of a coupled model representing carbon and water flow in the soil-rhizosphere-plant continuum, influenced by atmospheric conditions through plant transpiration and photosynthesis. This framework accounts for the effects of water content variation on carbon flow and microbial activity. The multiscale implementation enables precise evaluation of fluxes and reactions at the soil-plant interface and can capture feedback across domains and scales. Despite the simplified representation of plant and mi-

crobial processes and limited calibration, the model reproduces trends reported in the literature, such as the "starving-survival" lifestyle of some microbial communities. We found that the effect of water scarcity on soil carbon turnover is an emergent property arising from 1D-scale feedbacks between plants, microbes, and local environmental conditions. The varied impacts of water stress highlight the strong influence of local soil and plant characteristics in determining whether carbon or water limitation dominates turnover. By representing multiple sources of plant and microbial stress, the model provides a mechanistic explanation for variability in plant and soil carbon allocation under combined stresses. The model yields a wide range of variables (e.g., short-term carbon storage) across the soil-rhizosphere-plant continuum that can be used to assess the performance of plant phenotypes and management measures under dynamic conditions. By computing the resulting soil and plant conditions and identifying the key processes driving ecosystem responses, this model can both provide parameters for larger-scale models and inform the design of simplified models that focus on the most influential processes. Moreover, this work lays the foundation for a more comprehensive model of the plant-soil interaction cycle, including nutrient exchanges, which are essential to accurately represent the feedback of soil on plant processes. Finally, this model is uniquely adapted to re-create the experimental observations of isotopic carbon allocation in the plant and soil.

3-6 Code availability

For this study, we used the plant model CPlantBox (Schnepf et al., 2025b) and the corresponding soil module (Schnepf et al., 2025a). The full setup is available at: Giraud2025_CarbonStabilisation

Chapter 4

Representation of hormonal control at the plant scale on pea plants' branching patterns

In this section, we implement a semi-mechanistic simulation of the plant branching pattern affected by auxin and sucrose concentrations.

You are bewildered, my beloved, by the rich profusion
Of this floral tumult spread throughout the garden;
[...]
All shapes alike, yet none equal,
And thus the chorus hints at a secret law,
A sacred riddle. Oh, could I, my lovely friend,
Convey to you at once the happy solving word!

Goethe *Die Metamorphose der Pflanzen*

This chapter is a modified version of a scientific article in preparation:

> Giraud, M., Lobet, G., Schnepf, A., Conway, S., Auzmendi, I., Amoo, O., Dun, E., Hanan, J., and Beveridge, C. (in preparation). Computational Evaluation of Key Processes Affecting Apical Dominance at the Plant Scale.

4-1 Introduction

Branching (or tillering) influences the productivity of crop plants and their resilience in a changing environment (Barbier et al., 2017, Evers et al., 2011). Indeed, branching is strongly linked with the total area and three-dimensional location of the plant leaf, affecting its photosynthetic capacity, and both light interception and water use efficiency (Barbier et al., 2017, 2019, Damour et al., 2010, Evers et al., 2011). Moreover, branching can positively and negatively impact the plant yield by changing the carbon repartition between production and storage organs (Barbier et al., 2017, 2019, Evers et al., 2011)—e.g., number of seeds, size and sweetness of fruits.

This branching depends in parts on whether existing auxiliary buds (see definition in section C.1) are able to grow until reaching the branch stage (Barbier et al., 2019, Evers et al., 2011). Additionally to being crucial to a crop yield and resource usage efficiency, bud releases and growth is a plastic emergent properties, affected by complex and interrelated processes (Evers et al., 2011, Evers and Vos, 2013, Qiushuang et al., 2021).

There is, first of all, a genetic control: bud release and growth are influenced by several quantitative trait locus (QTL). Indeed, several mutants of wild type plants in pea produce strongly diverging branching patterns (Arumingtyas et al., 1992, Beveridge et al., 2003, Ferguson and Beveridge, 2009, McKay et al., 1995). Environmental conditions (and plant management) also affect the emergence and elongation of branches: a high assimilation rate leads to a high sucrose concentration that favours branching (Fichtner et al., 2017). Other stimuli like light quality, temperatures, nitrogen availability, water stress also affect the branching pattern (Beveridge et al., 2003, Qiushuang et al., 2021). The combination of a plant genetic build up and the exterior stimuli make up the genome – environment – management combinations (GxExM).
The effects of the GxExM on a plant phenotype in general and branching, in particular, are in part mediated by complex and overlapping hormonal processes (Beveridge et al., 2023, Evers et al., 2011, Evers and Vos, 2013). Indeed, phytohormones are influenced by environmental stimuli and act both downstream and upstream of gene release (Qiushuang et al., 2021, Schneider et al., 2019). Hormones can affect branching negatively (auxin, strigolactone) or positively (cytokinin, trehalose 6-phosphate) (Barbier et al., 2019, 2015b, Fichtner et al., 2017).

In order to understand better the mechanisms behind branching regulation, many experiments have been conducted on pea (*Pisum sativum*) (Barbier et al., 2019). Indeed, pea branching is strongly affected by apical dominance (see definition in section C.1) and limiting the interactions between the shoot upper section with the rest of the plant (e.g., decapitation, see definition in section C.1) can lead to the outgrowth of several or all branches (Barbier et al., 2015b, Ferguson and Beveridge, 2009). Studying metabolism changes in the plants before and after the (partial) removal of the apical dominance has helped us understand how the different processes of branching regulation interact.

For several years, it was believed that auxin was the key hormone for branching regulation (Barbier et al., 2017, Husain and Linck, 1966, Schneider et al., 2019): it acts upstream of strigolactone and cytokinin and inhibits bud outgrowth. However, more recent experiments have shown that the auxin flow moved too slowly down the main shoot to cause the bud growth observed within hours of decapitation (Chabikwa et al., 2018, Muldoon, 2022, Renton et al., 2012).

More recently, the central role of sucrose (nutritional and signalling) was brought forward (Barbier et al., 2019, 2015b, Fichtner et al., 2017). Several hypotheses have been made regarding how sucrose and auxin interact with other hormones (cytokinine, strigolactone, gibberellic acid and abscisic acid ABA) in branching regulation within the different zones of the plants and for different stages of the branch development. Although precise descriptions of the dynamic regulatory networks were developed, it remains unclear whether some hormonal changes are correlative or causative to observed branching patterns (Beveridge et al., 2023). Moreover, the interaction across plant organs and their relative importance for different GxExM also needs to be better understood (Barbier et al., 2019, Beveridge et al., 2023).

Fig. 4-1 offers a simplified network representing of the main hormonal interactions affecting bud release (see definition in section C.1) and branch development. For the shoot, auxin is produced mainly in young growing leaves of the plant. It is transported down the shoot by active transporters (PIN proteins). The presence of auxin in the main shoot up regulates strigolactone (SL) production and down-regulates cytokinin (CK) and shoot branching (Fig. 4-1 (A)). Sucrose is produced by photosynthetic active leaves. It can move up and down the shoot, according to the pressure gradient. sucrose down-regulates SL production and up-regulates CK and shoot branching (Fig. 4-1 (A)). Under low sucrose and high auxin concentration, the lateral buds remain dormant (Fig. 4-1 (B)). However, even without removing the auxin sources, high sucrose concentration can remove lateral buds dormancy (Fig. 4-1 (C), see definition in section C.1). A more exhaustive representation of the hormonal regulation networks is presented by Beveridge et al. (2023).

Numerous modelling studies have explored the role of auxin at cellular and

tissue levels, focusing on processes such as leaf vein formation, shoot primordium development, and root tip growth (Allen and Ptashnyk, 2020, Cieslak et al., 2022, van Berkel et al., 2013). Less common are studies investigating the auxin's influence on phyllotaxy. For instance, Bertheloot et al. (2020) aggregated the interactions of auxin, strigolactone, cytokinin, and sucrose at the bud level in roses, reducing them to a single variable based on auxin and sucrose concentrations. While these findings have advanced our understanding of plant branching regulation, translating them to the whole-plant scale remains an important and non-trivial step (Cieslak et al., 2022, Wass et al., 2023), integrating hormonal regulatory networks into Functional Structural Plant Models (FSPMs) offers several advantages.
First, it can enhance our understanding of branching by considering interactions with other key processes and limiting factors, such as water pressure, nutrient availability, and carbon balance (Beveridge et al., 2023, De Swaef et al., 2022, Evers et al., 2011, Evers and Vos, 2013, Schneider et al., 2019). Modelling these processes under field conditions is essential, especially for selecting genotypes under changing environmental conditions that affect carbon and water balances. Additionally, noted by Beveridge et al. (2003) and Cieslak et al. (2022), the increasing complexity of regulatory networks makes them harder to understand and implement. In silico simulations allow researchers to evaluate which processes most significantly affect desired outcomes in specific GxExM scenarios, simplifying the models where possible. Finally, incorporating hormonal networks into plant-scale models bridges the gap between research and practical applications, benefiting stakeholders such as breeders.

In recent years, several functional structural shoot models, particularly L-system models, have simulated plant phyllotaxy based on auxin flow (Cieslak et al., 2022, Prusinkiewicz et al., 2009, Renton et al., 2012, Schneider et al., 2019). For instance, Renton et al. (2012) introduced a "big cell model" to scale polar auxin transport to the whole plant level, while Powell et al. (2022) reimplemented Bertheloot et al. (2020)'s model in a genotype-to-phenotype framework to link genotype to phenotypic traits. However, despite the central roles of growth, branching, and their complexity, no plant model offers yet a precise and mechanistic representation of the entire plant's carbon and water balance (Beveridge et al., 2023, Cieslak et al., 2022).

In this work, we develop a regulatory network based on a literature review, encompassing key stages of branch (see definition in section C.1) development, and implement it into an FSPM (Giraud et al., 2023). Our model simulates an entire plant in three-dimensional space, accounting for carbon and water flow and balance at a sub-organ level, and incorporates a simplified representation of auxin flow.

The study is divided into three parts. First, we describe the characteristics and calibration of the extended model. Second, we present the experimental setup

and results from a laboratory experiment, where four pea phenotypes were tested under three different light levels. Finally, we compare the *in silico* results with *in vivo* observations to assess whether the modelled processes are sufficient to replicate the observed outcomes.

4-2 Material and methods

4-2-1 Experimental setup

In this section, we present the materials and methods for the *in vivo* laboratory experiment.

4-2-1-1 Plant material

Four pea (*Pisum sativum*) phenotypes (obtained from three genotypes) were selected for this experiment (see Table tab:phenotypes). The first was the wild-type *WT* Torsdag cultivar (line L107). The second was the *WT* strigolactone mutant *SLM* (line K524, mutant on locus rms1-2T), previously described by Arumingtyas et al. (1992). The third was the *WT* dwarf mutant *DW* (line NGB5839, mutant on locus le^{5839}), described by McKay et al. (1995). The fourth phenotype was the decapitated wild-type, *WTD*, and was obtained by decapitating *WT* above node 6. An example scan for each phenotype can be found in the appendices (Figs. C.3-C.6).

The expected branching patterns at the end of the experiment for each phenotype and light level (with relevant references) are described in the second column of table 4-4. Overall, we expect *WT* and *DW* to have smooth branching patterns, while *WTD* and *SLM* should have one or more branching gaps. Moreover, *DW* should yield a more bushy phenotype than *WT* as less carbon is used for the main shoot. Finally, higher light levels were expected to cause more bushy phenotypes. A description of smooth branching patterns and branching gaps, as well as a graphical representation of the pea plant structure, are given in the appendix C.1.

4-2-1-2 Growth conditions and Measurements

The plants were grown one per pot (width: 67 mm top, 47 mm bottom, and height: 96 mm) with UQ23Arab soil mix under a 16 h photoperiod at 23°C daytime, 18°C night-time temperatures in climate-controlled chambers.

Three groups of eighteen *WT*, nine *DW*, and nine *SLM* plants were grown on three different shelves of the climate chamber. Each shelf received a different level of light during the photoperiod: low, medium or high level, corresponding to an average of, respectively, 90 lx (64%), 120 lx (86%), and 140 lx (100%) at

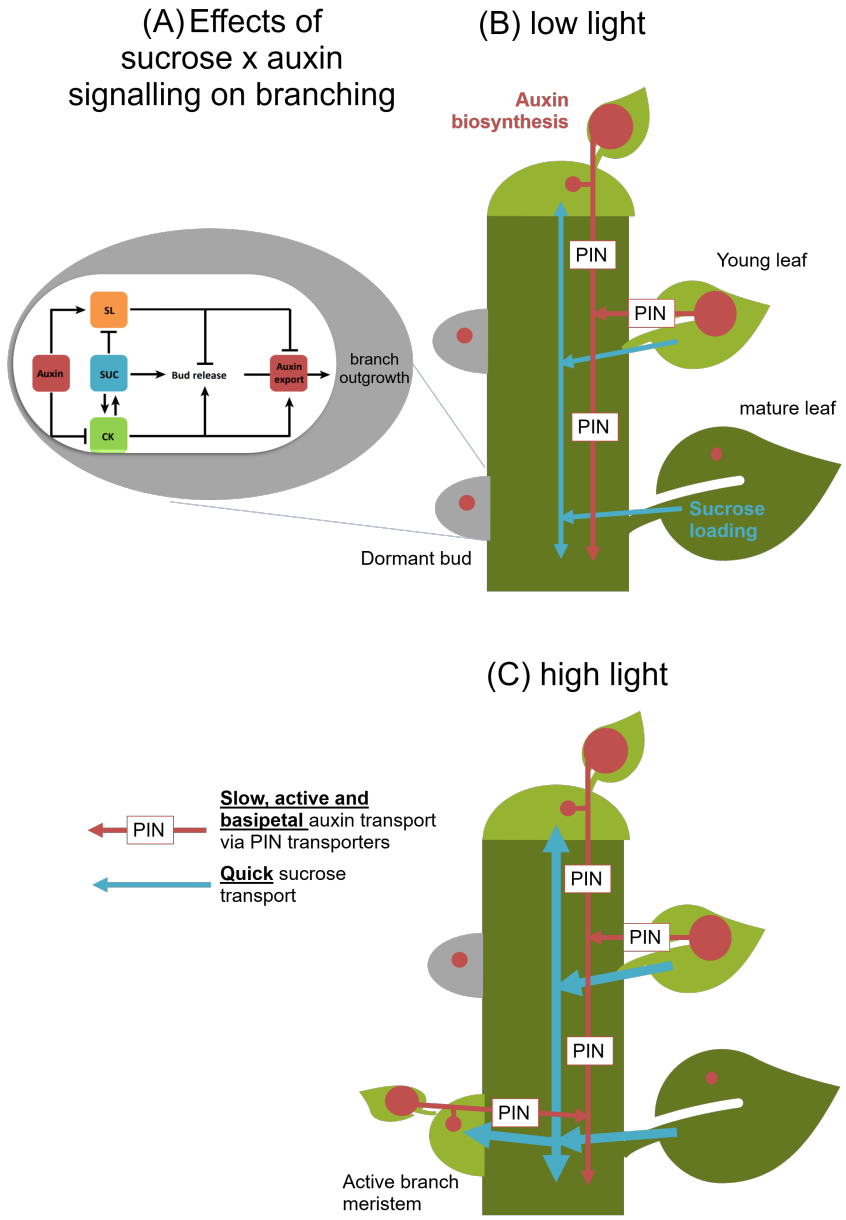

Figure 4-1: Representation of the role of auxin and sucrose on shoot branching for pea, with (A) a focus on the hormonal regulatory network in the bus, a representation of bud release along a shoot under a (B) low against (C) high light scenarios. Auxin is produced in the meristem of leaves and shoots and transported outside the meristem or bud and down the shoot by active PIN transporters. A high auxin gradient upregulates auxin transport and correlates with branching. High auxin concentration in the main shoot impedes the export of the bud auxin and, thus, its release. A high concentration of sucrose can lead to the release of dormant bud despite high auxin concentration. Adapted from Barbier et al. (2019).

Table 4-1: Description of the genotypes *in vivo* and representation *in silico*

phenotype name	genotype reference	representation *in silico*
WT: wild type	L107 (Arumingtyas et al., 1992)	baseline
WTD: wilde type decapitated		decapitation 1 *cm* above node 6
DW: dwarf	le^{5839} (McKay et al., 1995) mutant	lower internodal distance lower growth rate lower light input (see section 4-3-1)
SLM: strigolactone mutant	rms1-2T (Arumingtyas et al., 1992) mutant	$s_{lim,release} = 0$ $k_{lim,specialisation} = \text{Inf}$ $k_{lim,deactivation} = \text{Inf}$

the base of the shelves.

Pots were watered to saturation at planting, and twice weekly after seedling emergence. The pots were fertilized once per week with 250 mL of FlowFeedX liquid nutrients (Grow Force; 5g per 10L of water). As the light intensity varied according to the position of the plants on the shelves, the pots were moved once a week on the surface of their respective shelves.

At day 14, nine of the *WT* plants for each light level were decapitated: Their stems were cut approximately 1 *cm* above node 6 to remove the shoot tip. All the plants were harvested 21 days after sowing.

At the end of the experiments, the plants were harvested and scanned (RICOH scanner, IMC3500A) with a resolution of 600 dpi. The plants' laterals' lengths and position along the main shoot were then measured with the Fiji software (Schindelin et al., 2012).
The shoot scans were also used to calibrate the plant model–see section 4-2-3-3.

4-2-1-3 Statistical analysis

The statistical analyses were performed with R (R Core Team, 2019) to compare the mean total lengths of the branches for each group. The branches' lengths were the dependent continuous variables and plant types were set as categories. We assumed that the replicates gave independent samples.
We first set the light levels as categories. We used the non-parametric Mann–Whitney U test (with the correction method of Benjamini and Hochberg (1995)) to evaluate whether two groups had significantly different distributions.

Indeed, each combination of light level and phenotype only had nine or fewer replicates, making the results of the Shapiro normality test less trustworthy (Adusah and Brooks, 2011). Moreover, a visual evaluation of the histograms showed that the normal distribution was not respected.

We then considered the light input as an integer variable (corresponding to a mean number of lux measured at the bottom of each shelf). This yielded between 22 and 27 replicates per categorical group, allowing us to use the Shapiro normality test. As the residual of the ANOVA did not respect the assumption of normality or variance homoscedasticity of variance between the phenotypes, we used instead a linear regression for each phenotype according to the light level. After transforming the dependent variable data (square-root transformation), we could obtain a normal distribution of the residuals.

For the Mann–Whitney U test, it is important to note that unequal group sizes might have led to an increase of the type I error (false positive), especially when the variance of the smaller group was superior to that of the bigger group (Adusah and Brooks, 2011). Conversely, normal distribution decreases the risk of errors. Consequently, results of the Shapiro tests, as well as an evaluation of the variance and difference in group sizes are still presented in table C.1. Variances of the same magnitude were judged to be similar (as the Leven test does not perform well for small groups). Groups with a difference in replicate number above 15% were judged to have strongly different sizes.
For all tests, we reject the null hypothesis (e.g., non-significant difference between the distribution of two datasets or between the distribution of a dataset and the normal distribution) if p-value $\leq$ 0.05.

4-2-2 Model description

In this section, we present the models and calibration methods used for the *in silico* study. In summary, the FSPM CPlantBox (Giraud et al., 2023) was expanded to include an auxin flow module (see section 4-2-2-2) and a regulatory network module (see section 4-2-2-3) that simulates the plant branching dynamic. These new modules aim to recreate the selected (and simplified) processes driving plant branching–see Fig.4-1 and section 4-2-2-1.
It is important to note that we used a preliminary version of the model described by Giraud et al. (2023). Therefore, this model does not include the water potential-limited growth and the (de)synthesis of starch.

4-2-2-1 Assumptions and simplifications

The objective of the simulation was to represent the branching phenotypes of pea plants under different scenarios while focusing on the effect of sucrose and auxin.

A description of the main assumptions used in the model is given in table 4-2. The method used to represent the different phenotypes *in silico* is given in table 4-1. More details on the model setup and simplifications are given in the following sections.

Table 4-2: List of the main assumption and simplifications implemented for the auxin flow and bud release modules

id.	hypotheses	reference(s)
1	auxin concentration in the stem is mainly dependent on its biosynthesis in young expending leaves	(Barbier et al., 2015b)
2	auxin flow is slow, active and basipetal	(Barbier et al., 2019, 2015b, Chabikwa et al., 2018, Renton et al., 2012)
3	auxin metabolism has a negligible effect on the shape of the unmetabolized auxin waves (relative drop in auxin concentration)	(Renton et al., 2012)
4a	auxin flow in the main shoot is not limited by the number of transporter carriers. Therefore, auxin flow rate from one stem section to the next is a constant proportional rate of its concentration in the upper segment	(Renton et al., 2012)
4b	the cross section of the tissues containing auxin is constant in the shoot	NA
5	branching can be divided between bud growth (bud swelling, slower growth) and sustained branch growth (elongation, quicker growth)	(Bertheloot et al., 2020, Cao et al., 2022, Chabikwa et al., 2018)
6	a signal is needed for the onset of bud swelling (see definition in section C.1) and for the sustained growth onset	(Bertheloot et al., 2020, Cao et al., 2022)
7	during bud swelling, the laterals can go back into dormancy	(Barbier et al., 2015b, Stafstrom et al., 1998)
8	after the sustained growth onset, the lateral cannot go back into dormancy	(Bertheloot et al., 2020)
9	sucrose signaling promotes the start of bud swelling	(Barbier et al., 2019, Cao et al., 2022, Fichtner et al., 2017)
10	sucrose signaling promotes the elongation onset	(Barbier et al., 2015a,b, Cao et al., 2022)

11	Auxin export from the bud promotes elongation onset (canalisation theory).	(Barbier et al., 2019, Bertheloot et al., 2020, Cao et al., 2022, Chabikwa et al., 2018)
12	canalisation theory: The auxin flow is first gradient driven. Afterwards, there is a polarisation of the carrier and the flow becomes active (Gradient-driven amplification). Therefore, high auxin concentration in the stem inhibits auxin transport from buds, thereby inhibiting the start of sustained growth.	(Barbier et al., 2019, Cao et al., 2022)
13	because auxin transport is self enhancing, as long as auxin biosynthesis occurs, we assume that active transport can only increase. Therefore, the elongation onset depends on the lowest auxin concentration experienced by the bud.	NA
16	there is partly a compensatory effect of sucrose and auxin signalling for the switch to sustained growth	(Barbier et al., 2019, Bertheloot et al., 2020, Cao et al., 2022, Chabikwa et al., 2018)
14	sucrose and auxin signalling is done (in part) via their interactions with strigolactone and cytokinin. Strigolactone impedes while cytokinin promotes bud growth and sustained growth	(Barbier et al., 2019, 2015b, Bertheloot et al., 2020, Brewer et al., 2009)
17	for *SLM*, buds are not subject to strigolactose-induced dormancy. The phenotype can be mimicked via a non-signal dependant growth (only the trophic effect of sucrose is important).	(Beveridge et al., 2003, de Saint Germain et al., 2013)
15	node 2 is bigger when not activated than the other nodes. Sucrose flows more easily into node 2 than into the other nodes.	(Husain and Linck, 1966, Muldoon, 2022)

4-2-2-2 Auxin flow

The method used to define the plant sucrose flow and balance is presented by Giraud et al. (2023). This section presents the equations defining the plant auxin flow, yielding iaa ($mmol\ cm^{-3}$), the auxin concentration in the transport tissue.

The auxin transport model is an adapted version of the compartment or "big cell" model of Renton et al. (2012).

The variation in iaa_i the auxin concentration in segment i, can be represented by

the following equation:

$$\frac{\partial iaa_i}{\partial t} = \alpha_{iaa}\left(\sum_{h}^{H->i} iaa_h - iaa_i\right) + \frac{F_{in,iaa}}{Vol_i} \tag{4-1}$$

$$F_{in,iaa} > 0, \text{ if } i \text{ carries a young leaf segment} \tag{4-2}$$

With α_{iaa} $(-)$ the auxin transport rate from one segment to the next,$H- > i$ the set of segments upstream of the segment i's basipetal flow, $F_{in,iaa}$ $(mmol\ d^{-1})$ the mean auxin production in expanding leaves. Vol (cm^3) is the volume of the tissues containing auxin.

To avoid high concentration values, the auxin that reached the root meristems was metabolized. This does not follow experimental observations. However, as we do not simulate the effect of auxin on roots, this process had no effect on the simulation outputs.

The auxin biosynthesis rate is a complex process and experimental data is limited and sometimes contradictory (Barbier et al., 2015b, Chabikwa et al., 2018, Stepanova and Alonso, 2016). For simplicity, the current implementation of the model, each stem node carrying a young expanding leaf had a set emission rate of auxin $F_{in,iaa}$. The next iteration of the model could include a decrease in auxin production for the nodes as the leaves grow older. Moreover, a (lower) auxin emission rate could be set for shoot meristems.

As the auxin flow in the plant is very slow ($1cm\ hr^{-1}$), we set a burn-in time at the beginning of the auxin flow simulation until the auxin concentration stabilised. Because the sucrose flow is much faster than the auxin flow, the sucrose module did not require a longer burn-in time than the auxin module. Moreover, a new empty segment was created every time the plant grew. This had negligible effects on the sucrose flow, which can quickly fill the new segment. This new segment created, however, a signal of low iaa, which propagated along the stems and caused bud specialisation. To correct this, during the simulations, every new segment was created with an initial auxin and sucrose concentrations equal to that of the older segment it is attached to. This added content was taken into account in the mass balance checks.

4-2-2-3 Branching model

This section presents the rules regulating the stem laterals' growth dynamic.
This branching model is summarised in Fig.4-2: After its creation, the bud remains dormant and can only grow up to a small length ($l_{dormant}$, cm), as shown in Fig. 4-2.A. If the sucrose concentration in the node carrying the bud, s_{test}

($mmol\ cm^{-3}$), exceeds the threshold $s_{lim,release}$ ($mmol\ cm^{-3}$), the bud is released from dormancy (see definition in Section C.1). Upon activation, the bud undergoes slow initial growth (see Fig. 4-2.A). Depending on the parameter k_{bud} ($-$) (see Eq.4-3), the bud may either return to dormancy (Fig. 4-2.a.2) or proceed to specialize into a branch (Fig. 4-2.c).
$s_{lim,release}$ is a set parameter and k_{bud} is computed from the following equation (Bertheloot et al., 2020):

$$k_{bud} = \frac{iaa_{above,min} + 1}{s_{test} + 0.2} \tag{4-3}$$

If $k_{bud} < k_{lim,specialization}$, the bud becomes a branch (Fig. 4-2.c)). If $k_{bud} > k_{lim,deactivation}$, the bud goes back into dormancy (Fig. 4-2.a).2.). If none of those two events occur, the bud keeps growing (Fig. 4-2.b)). Both $k_{lim,specialization}$ ($-$) and $k_{lim,deactivation}$ ($-$) are set parameters. For Eq.4-3, we did not implement the "sucrose-dependent correcting term" used by Bertheloot et al. (2020) as it decreased the accuracy of the preliminary *in silico* outputs.

Moreover, we applied for this model the "auxin canalisation theory" (see table 4-2). The bud specialisation (see definition in section C.1) is thus affected by the lowest registered exogenous auxin concentration. To not be affected by the auxin produced at the node (if it carries a young expending leaf), we evaluated the auxin concentration directly above the node iaa_{above} ($mmol\ cm^{-3}$). We also used the lowest auxin concentration registered by the bud $iaa_{above,min}$ ($mmol\ cm^{-3}$).

Moreover, several experiments found that the bud at node 2 tented to grow out more often and more quickly than the other buds (Beveridge et al., 2003, Fichtner et al., 2017, Muldoon, 2022). There is not yet any consensus regarding the reason behind this advantage. In their studies, Husain and Linck (1966) and Muldoon (2022) found that the dormant bud 2 was larger than the other dormant buds, making them a bigger sucrose sink. To represent this theory, s_{test} was scaled inversely to the buds' volumes and the maximum length of node 2 while dormant ($l_{dormant}$) was three times higher than for the other nodes.

In the current implementation of the model and for simplicity, a dormant bud cannot start growing once more.

4-2-3 Calibration and system modelled

4-2-3-1 Pre-existing modules

The structure of the plant shoot was obtained using a first rough parametrisation from the *in vivo* outputs of this study and from the literature data (Beveridge et al., 2003, Chabikwa et al., 2018, McKay et al., 1995, Muldoon, 2022). The

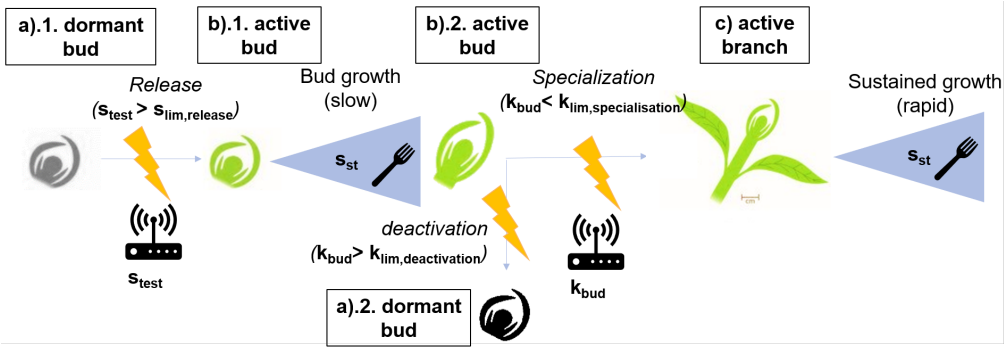

Figure 4-2: Representation of the branching model. The switch from one state to the next (text in italics, blue arrows with electricity signs) is controlled by sucrose and auxin signalling (signal signs), while the growth (blue triangle) is controlled by the trophic effect of sucrose (fork signs). The names of the different states of the lateral are given in the white rectangles.

photosynthesis and sucrose flow parameters were identical to those used in the simulation of a generic C3 plant by Giraud et al. (2023). Moreover, the parameters related to water scarcity were set to avoid water limitation on stomatal opening and growth.
Although this is a rough first calibration, the apical dominance modelised here was observed for a wide range of plants in general and environmental conditions(Barbier et al., 2019, 2015b). Therefore, the outputs should be robust to a variation in parameter values.

4-2-3-2 Auxin flow

In order to calibrate α_{iaa} in the main shoot, we set the minimum and maximum stem segment length to approximately 0.5 cm (constant segment length). We then recreated the setup described by Renton et al. (2012). Following this, we tested in parallel several values of α_{iaa} and selected the value which gave a signal propagation similar to Fig. 4-3.A (Fig.2b of Renton et al. (2014)).

Figure 4-3 shows (A) the simulation of Renton et al. (2014) (objective values) and (B) the simulation output with the selected α_{iaa} value. In our simulation, the spread of the auxin signal was wider than for Renton et al. (2014). However, we could still obtain a relative distribution similar to the objective values.

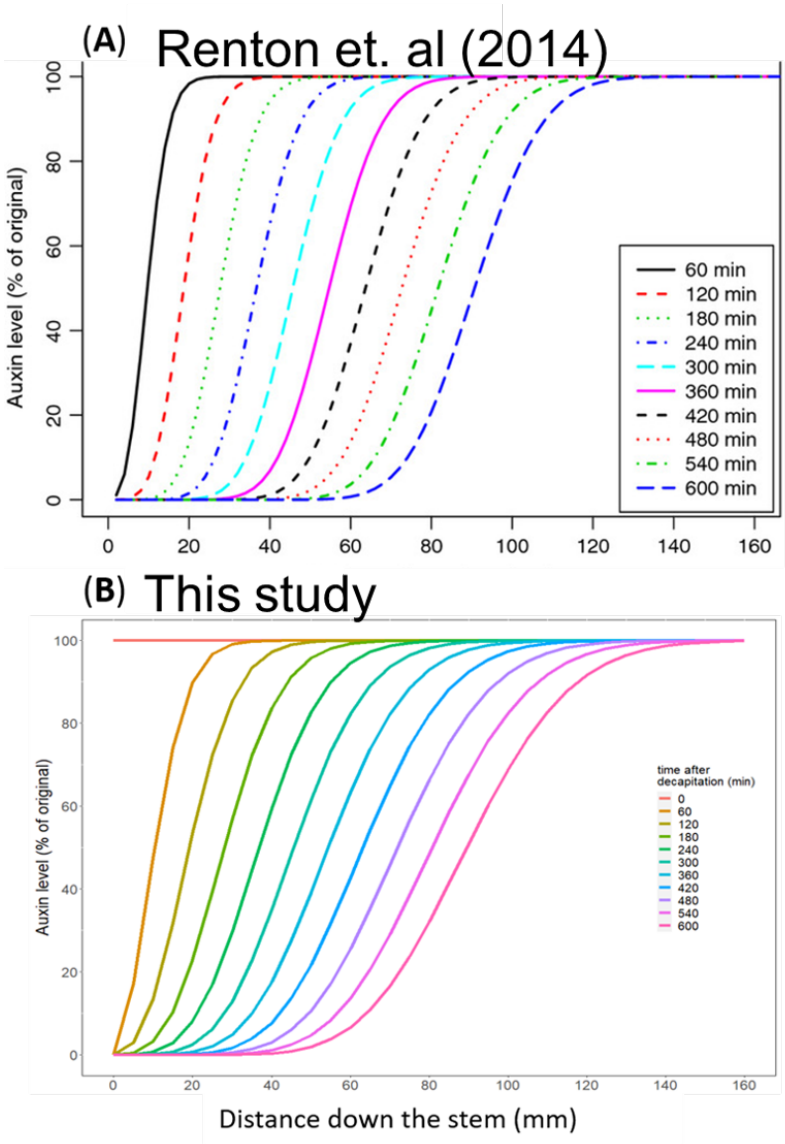

Figure 4-3: Output of the α_{iaa} calibration, with (A) the objective simulation (Renton et al., 2014), (B) the output simulation.

4-2-3-3 Branching model

Simulations were run in parallel for *WTD*, for several values of $s_{lim,release}$, $k_{lim,specialisation}$ and maximum leaf and shoot growth rates. We selected a parameter set that could recreate the simulation's objectives. Namely, the bud outgrowth dynamic followed what was expected or observed for *in vivo WTD*: bud release (resp. specialisation) within hours (resp. days) of decapitation, except for bud 2 which could happen earlier (see table 4-4).

The representation of the other phenotypes was done with the same parameter set and using characteristics given in table 4-1.

4-2-3-4 Runtime of the simulation

The simulations were run using the empirical growth until the plants had fully developed scale leaves. Then, the sucrose and auxin flow as well as the sucrose-dependent growth were activated. The *WTD* growth was simulated until the distance between the shoot nodes 6 and 7 was of 1 *cm*. Then, as for the *in vivo* setup, the decapitation was done and the growth was simulated for an extra seven days. The total simulation time of *WTD* was then used for the other scenarios.

4-3 Results and discussion

In the following sections, we present the results of the *in vivo* and *in silico* experiments and compare them to observations from the literature. The expected and observed outputs are summarised in table 4-4.

4-3-1 In vivo results

The panels 4-4.A,C and E present, for each node, the plants' bud outgrowth *in vivo* under the three light levels. Fig. 4-5 presents the total lengths of the branches for each plant according to the light level.

4-3-1-1 Variance of the data

We observed a high variability in the lengths of the branches between the replicates, especially at the nodes lower along the stem (Fig. 4-4).
This can be in part explained by the light competition between the plants–the higher branch growth for one plant likely caused a lower growth of the neighbouring plants' branches. This light competition seemed to have specifically affected the *DW* phenotype, as we observed under the high light scenario, both the lowest and highest total branch length for this phenotype (Fig. 4-5.C). Moreover, because of supposedly faulty seeds, some of the *SLM* plants did not

germinate. This reduced the number of replicates for low and medium light input (see table C.1). A higher number of replicates might have decreased the variance. Finally, the Fiji software used to evaluate the pea plants' organ lengths was less adapted for measuring dormant buds (which are much shorter), which increased the variance in the buds' measurements.

4-3-1-2 Mean total length of the laterals and main shoot

In spite of the high variance of the data, differences between the phenotypes and light levels were still observable. For *WT*, *DW*, and *SLM*, we had, as expected (Barbier et al., 2015b), a significant increase in the mean total branching length according to the light input (Fig. 4-5 and table 4-3). The light effect was especially strong for *WT* and *DW* (higher R^2 and lower p-value). On the contrary, for *WTD*, we did not have a significant increase of mean total length with the light input (p-value > 0.05, Fig. 4-5.B). This higher sensibility of the branching to light for *WT* and *DW* compared with *SLM* and *WTD* can be explained by the conceptual model: For *SLM*, there was no need for sucrose signalling. For *WTD*, sucrose was assumed to reach the signalling threshold for all light levels because of the concentration pick following the loss of the growing stem meristem (Barbier et al., 2015b). Assimilation rates therefore affected *WT* and *DW* branching through two processes (signalling and nutritional role of sucrose), against one process (nutritional role of sucrose) for *SLM* and *DW*.

This signalling limitation also explains why, as we can see in Fig.4-5, *WT* and *DW* had limited or no branching, diverging from the high branching of *WTD* and *SLM*. This follows observation from the literature (Barbier et al., 2015b, Beveridge et al., 2003, de Saint Germain et al., 2013, Fichtner et al., 2017).

Additionally, the lower leaf area of *DW* diminished their need for water. Therefore, the water added during the experiment was too high for this phenotype, causing some of the leaves to fold on themselves (see Fig. C.5). This lowered further the photosynthetic active area and thus the photosynthetic capacity.

Despite this excess watering, we also observed a significantly higher total branching length of *DW* compared with *WT* for the high light input (see table 4-3 and fig. 4-5). This follows the output of earlier studies (Arumingtyas et al., 1992, de Saint Germain et al., 2013) and can be explained by the fact that less of the carbon was used by the main shoot (shorter inter-nodal distance), lowering the sucrose-based apical dominance. This anti-correlation between stem and branch growth was also observed for *SLM*: in our study and in the literature (Arumingtyas et al., 1992, de Saint Germain et al., 2013), compared with *WT*, *SLM* was characterised by both a lower stem length and a significantly higher total branching length. This can be explained by the limited hormonal control on the branch elongation onset, which limits the resources available main shoot

growth.

4-3-1-3 Branching pattern

For the long-photoperiod conditions used in this study, it was anticipated that the plants would show increased branching at higher nodes, as documented by Arumingtyas et al. (1992), Beveridge et al. (2003), Chabikwa et al. (2018). Contrary to expectations, the long-photoperiod branching pattern was not observed. Instead, the results were consistent with the findings of Muldoon (2022) also conducted in a growth chamber. This could suggest that the differences in light quality between the glasshouses (sunlight) and growth chambers (artificial light) might cause the absence of the expected pattern (Annunziata et al., 2017).

We could observe an effect of the light input on the branching pattern along the main shoot, especially for *SLM*: for the low light level, we observed a gap in the branching pattern (at node 4), indicative of a high competition for resource between the branches (correlative dominance (Beveridge et al., 2023)). For the higher light level, we observed, on the contrary, a smooth branching pattern. The smooth branching pattern follows the expected pattern (Arumingtyas et al., 1992, Beveridge et al., 2003). Indeed, as there is no bud dormancy, the branches can elongate as soon as they are created, leading to an advantage for older buds above the scale leaves (e.g., node 3). For both *WT* and *DW*, we can observe a higher lateral development on node 2, especially under higher light level. Although the cause of this advantage of node two is not fully understood, it was observed in other studies (de Saint Germain et al., 2013, Fichtner et al., 2017, Muldoon, 2022). For *WTD* we observed, similarly to the literature data, a branching gap (Beveridge et al., 2003, Muldoon, 2022) at node 3 and a long branch at node 2 (Beveridge et al., 2003, Fichtner et al., 2017, Muldoon, 2022). This can be explained by the buds becoming activated almost simultaneously following the decapitation (limited seniority effect) because of the higher sucrose concentration. The correlative dominance (competition for sucrose) then leads to branching gaps.

4-3-2 In silico results

The panels 4-4.B,D and F present, for each node, the plants' bud outgrowth *in silico* under the three light levels.

4-3-2-1 Mean total length of the laterals and main shoot

Since the data was calibrated using *WT*, we expected to replicate the short-photoperiod branching pattern rather than the long-photoperiod pattern observed in the literature (Arumingtyas et al., 1992, Beveridge et al., 2003, Chabikwa

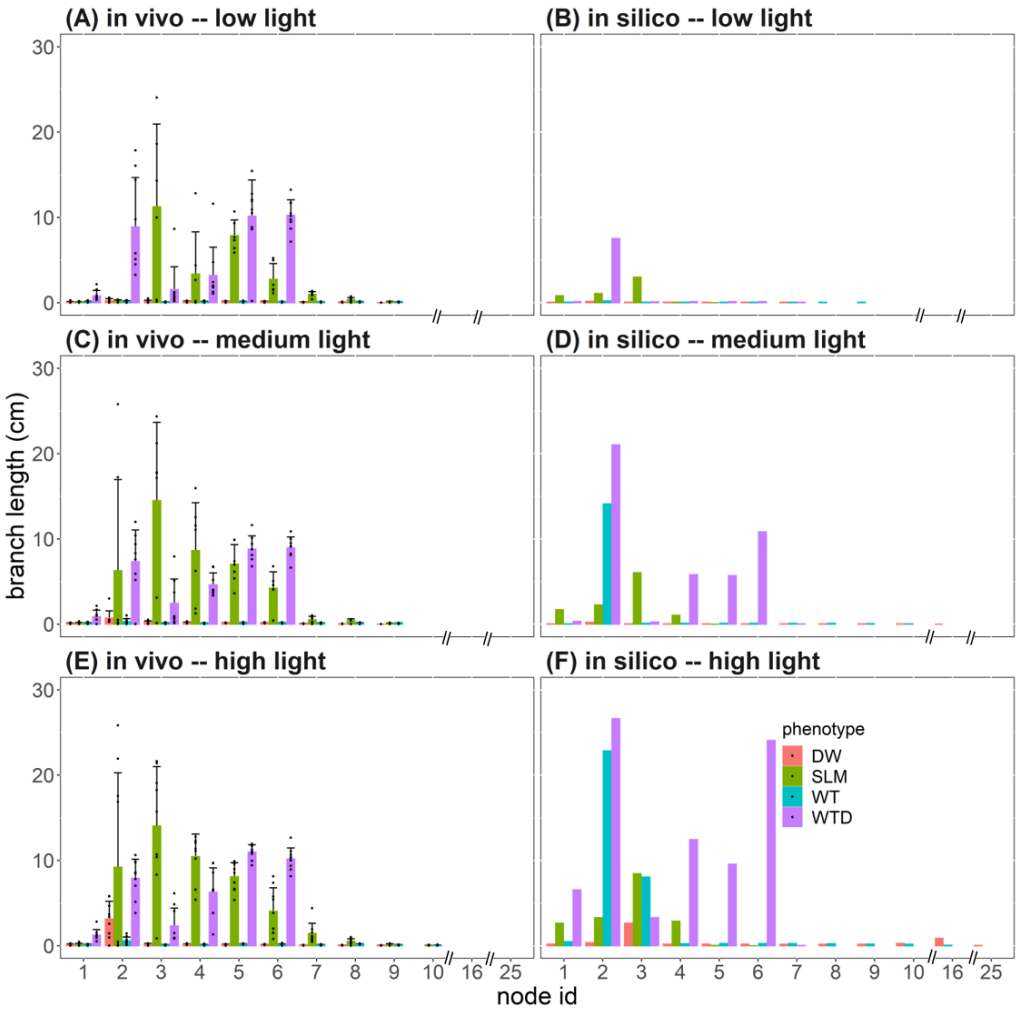

Figure 4-4: Length of the branches along the main shoot at the end of the experiments for each light level and plant phenotype. Panels (A), (C), and (E) give the *in vivo* observations. The error bars give the standard deviation. Panels (B), (D), and (F) give the *in silico* results. The x axis give the index of the pea node each branch is attached to. The distance between the branches in the graphic does **not** represent the inter-nodal distance. Represented pea phenotype: wild-type (*WT*), decapitated wild-type (*WTD*), darf mutant (*DW*), strigolactone mutant (*SLM*).

Table 4-3: Comparison of the median of the total branching length per phenotype and light level. Values in blue rectangles represent the phenotype effect. Values in yellow rectangles represent the light effect.(ns: $p > 0.05$,*: $p \leq 0.05$, **: $p \leq 0.01$, ***: $p \leq 0.001$). Represented pea phenotype: wild-type (*WT*), decapitated wild-type (*WTD*), darf mutant (*DW*), strigolactone mutant (*SLM*)

light level	phenotype	high				medium				low		
		WT	*WTD*	*DW*	*SLM*	*WT*	*WTD*	*DW*	*SLM*	*WT*	*WTD*	*DW*
high	*WTD*	***										
	DW	*	***									
	SLM	***	*	***								
medium	*WT*	ns										
	WTD		*			**						
	DW			*		ns	***					
	SLM				ns	***	ns	***				
low	*WT*	*				ns						
	WTD		ns				ns			***		
	DW			**				ns		ns	***	
	SLM				ns				ns	***	ns	***

The significant results in bold red might be caused by a type I error, because of the different group sizes.

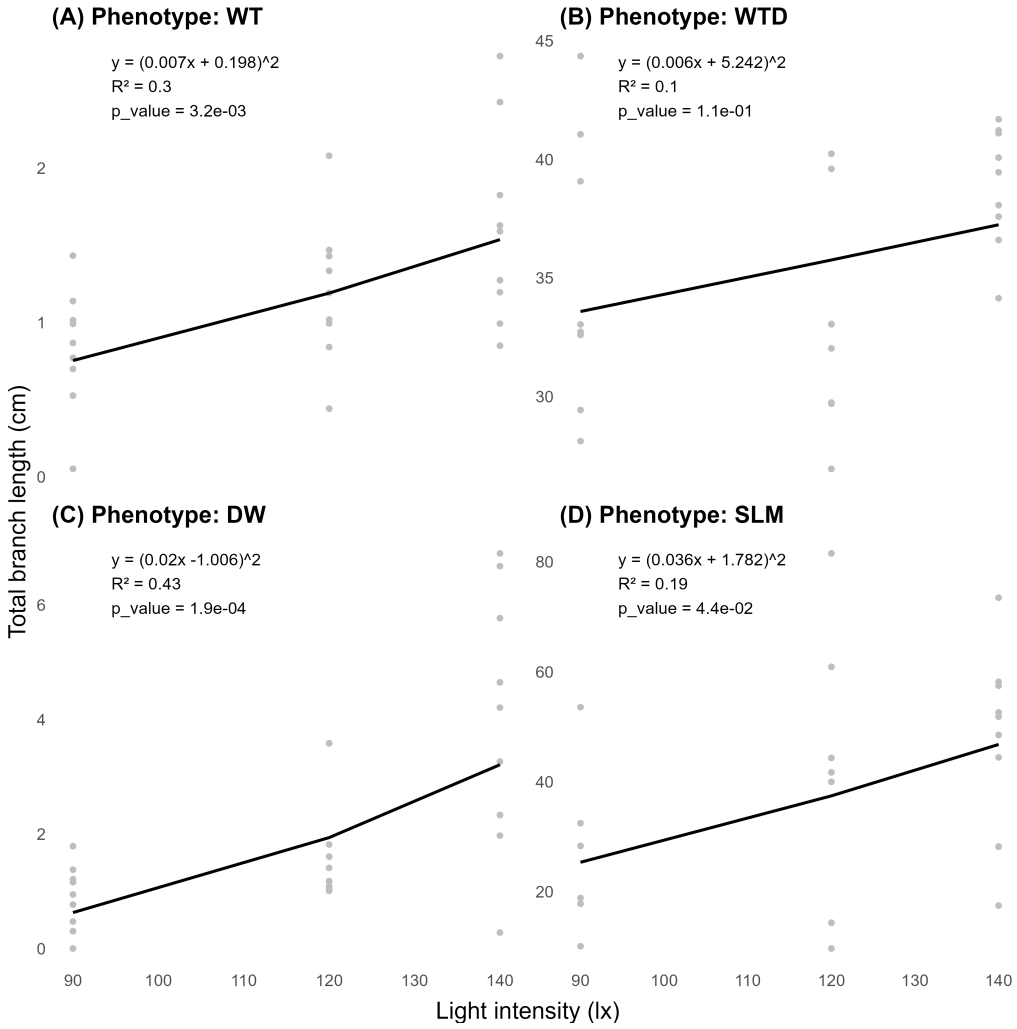

Figure 4-5: Mean total branching length per plant (cm) at the end of the experiment for each light level (in lux) and pea-plant phenotype (*WT*: wild-type, *WTD*: wild-type decapitated, *DW*: dwarf, *SLM*: strigolactone mutant), for experimental observations (grey points) and linear regressions on the square-root transformed data (black lines). The annotations give the equations of the linear regressions, their R^2 and the p-value of the slope.

et al., 2018). Consistent with our experimental results, higher light intensity led to greater branch development. However, while the overall branching dynamics matched expectations, significant quantitative discrepancies were observed in the lengths of both the lateral branches and the main shoot.

For instance, under high light conditions, the model predicted that the main shoot of *DW* would extend to node 25, while in the experimental data, *DW* only reached node 10. In contrast, for *SLM*, the model predicted a shorter total shoot length than was observed experimentally, reaching node 5 compared to node 9 under the same high light conditions.

These differences can be attributed to certain parameters in the coupled plant growth-sucrose balance model that were not precisely calibrated based on experimental data. Additionally, the model may need to better distinguish between two key processes: cell division, which consumes more sucrose, and turgor-driven cell elongation. A clearer distinction between these processes could enhance the model's ability to accurately simulate the relationship between sucrose balance, hormonal signalling, and plant growth (Coussement et al., 2020, de Saint Germain et al., 2013, Muldoon, 2022).

Especially for *SLM*, the divergences between the modelled and experimental results suggest that implementing thresholds to limit initial branch elongation could improve accuracy. The latest version of the plant model, which incorporates growth limitations based on water potential (Giraud et al., 2023), may help generate more accurate results in future simulations.

We successfully recreated the restricted branching pattern observed for *WT* and *DW*, particularly under low light levels. However, the branching in *DW* was less extensive than in *WT*, which was due to an excessively high shading parameter for *DW*.

The model plants were more sensitive to light levels than the experimental ones, leading to branch elongation in *WT*. This was however also reported for older *WT* plants in the literature (Beveridge et al., 2003). The excessive branch elongation observed under high light levels for both *WTD* and especially *WT* was driven by increased sucrose concentration as more leaves were produced. In the latest version of the plant model, a starch module has been added, improving the model's buffering capacity against variations in phloem sucrose levels, particularly in older plants. Re-implementing the hormonal regulation network in the latest version of the FSPM is expected to lead to more accurate simulations for both *WT* and *WTD*.

4-3-2-2 Branching pattern

In our simulations of *WT* and *WTD*, we were able to replicate the increased branch development at node 2, which contrasted with the higher branch development at node 3 in *SLM*. For *WTD*, the prominent branching at node 2 was associated with a branching gap at node 3 under medium and high light conditions, consistent with our experimental results. For *SLM*, we successfully recreated the smooth

branching pattern. Regarding the branching dynamics, the rapid bud release following decapitation—though not directly measured in our experiment—was accurately simulated, aligning with findings from other studies (Bertheloot et al., 2020, Chabikwa et al., 2018, Fichtner et al., 2017). Similarly, we observed a swift transition from bud activation to sustained branch growth within days of decapitation in *WTD*. In the case of *DW*, we observed increased branching below node 3. This is likely due to an excessively high shading parameter used in the model. The branch at node 2, being attached to a scale leaf, would have experienced a strong reduction in sucrose input, which could explain this pattern.

Table 4-4: Expected and observed *in silico* and *in vivo* outputs

id.	plant	expected observations[a]	reference(s)	observed[b]	
				vivo	*silico*
1	*WT* *WTD* *DW*	Long-photoperiod (16 hr): branching at higher buds	(Arumingtyas et al., 1992, Beveridge et al., 2003, Chabikwa et al., 2018)	-	-
2	*SLM*	Higher branching for higher light intensity	(Barbier et al., 2015b)	/	x
3	*WT*	Limited or no branching	(Barbier et al., 2015b, Beveridge et al., 2003, de Saint Germain et al., 2013, Fichtner et al., 2017)	x	/
4		Higher branching at node 2	(Fichtner et al., 2017, Muldoon, 2022)	x	x
5		Higher branching than *WT*	(Barbier et al., 2015b, Beveridge et al., 2003, Muldoon, 2022)	x	x
6	*WTD*	Branching gap(s) along the shoot	(Beveridge et al., 2003, Muldoon, 2022),	x	x
7		Bud release within 2 *hrs* of decapitation	(Bertheloot et al., 2020, Chabikwa et al., 2018, Fichtner et al., 2017)	NA	x
8		Sustained growth within days of decapitation	(Bertheloot et al., 2020, Chabikwa et al., 2018)	x	x
9		Higher branching at node 2	(Beveridge et al., 2003, Fichtner et al., 2017, Muldoon, 2022)	x	x
10	*DW*	higher branching than *WT*	(Arumingtyas et al., 1992, de Saint Germain et al., 2013)	x	-
11		Higher branching at node 2	(de Saint Germain et al., 2013)	x	-
12	*SLM*	higher branching than *WT*	(Barbier et al., 2015b, Beveridge et al., 2003, de Saint Germain et al., 2013, Dun et al., 2011)	x	x
13		Smooth branching pattern	(Arumingtyas et al., 1992, Beveridge et al., 2003)	x	/
14		Lower plant length than *WT*	(Arumingtyas et al., 1992, de Saint Germain et al., 2013)	x	x

[a] As the observed results did not follow the long-photoperiod patterns (observation id. 1), we compared our other outputs (observations id. 2-14) with the short-photoperiod branching patterns.

[b] observed (x) partially observed (/), not observed (-), not available (NA)

4-4 Conclusion

Branching regulation is an important and highly plastic emerging-property of a plant, that can affect its ressource use efficiency, resilience and yield. In this study, we presented an implementation of a hormonal regulatory network within a three-dimensional structural full plant model. After calibration, the model was implemented to simulate the growth and branching pattern of four pea plant phenotypes under three light levels. The model was able to recreate qualitatively several of the key processes observed either in the experiment conducted in this study or in the literature. The model's limitations, especially in recreating the quantitative results across the different light levels, also gave us hindsight into the main additional processes needed to simulate the hormone-controlled plant branching observed in laboratory and field experiments.
This work is a first step to link developmental regulatory network with a functional structural plant model. *In fine* such models could be a useful tool for breeders seeking to control plant carbon allocation.

Acknowledgement

We thank Akila Wijerathna-Yapa for his help in summarising the assumptions linked with the hormonal regulation of plant branching.

Authors' contributions

MG: Software, Visualisation, Conceptualization, Writing – original draft, Writing - Review & Editing, Investigation, Formal analysis. CB, ED: Resources, Conceptualization, Methodology for laboratory experiments, Formal analysis - support, Supervision. SC, OA, ED: Investigation - support. JH, IA, SC: Formal analysis - support, Conceptualization - support. GL, AS: Funding acquisition, Writing - Review & Editing

Chapter 5

Discussion

In this section, we discuss how the studies presented fit within the larger research landscape.

It is time to factor in the results of the calculations. It is time to restore the proper mathematics. We will stride over the numbers tumbling down from the screens, sowing the necessary disorder within them [...]. We will mix flesh with numbers. We will mix our laughter and sweat with the lines of code [...]. We will break a few windows to let the fresh air in.

Mariette Navarro *Nous Les Vagues*

5-1 Simulating water and carbon flow in the soil-rhizosphere plant continuum

At the start of this work, FSPMs with varied characteristics were available: 3D representation of shoots and roots (Seleznyova and Hanan, 2018, Zhou et al., 2020), linked carbon (C) and water fluxes (Lacointe and Minchin, 2019, Seleznyova and Hanan, 2018, Zhou et al., 2020), C respiration (Barillot et al., 2016, Gauthier et al., 2020), exudation (Zhou et al., 2020), distributed C sources, sinks, and storage (Lacointe and Minchin, 2019), water and/or C dependent growth (Coussement et al., 2020, Gauthier et al., 2020, Louarn and Song, 2020, Postma et al., 2017), coupled soil and root water flux (Khare et al., 2022), effects of the atmosphere variables and plant water status on the coupled stomatal opening and photosynthesis (Tuzet et al., 2003). Some of these models and modules became the blueprint for the implementation of new processes in CPlantBox. The novel aspect of this latest implementation of CPlantBox comes from the opportunity to simulate the interactions of these modules' respective processes–representing the C and water fluxes in the soil-plant-atmosphere-continuum–within one single user-friendly framework (Louarn and Song, 2020). This allowed us to investigate the feedback effects between plant growth and water- and C-fluxes, which was lacking in earlier models (Damour et al., 2010, De Swaef et al., 2022, Soualiou et al., 2021, Zhou et al., 2020). Processes that are usually predefined in FSPMs and for which limited experimental data are available–like C partitioning (Postma et al., 2017, Soualiou et al., 2021)–became consequently emerging properties of our model. We could therefore simulate how growth and C partitioning vary according to the growth conditions via semi-mechanistic process descriptions. This allowed us to gain insights into agronomically relevant plant characteristics, such as the C-use efficiency: from our model it is possible to evaluate the amount of C that leads to biomass production (against the amount that is respirated or exudated) according to the water uptake rates. Our model facilitates the definition of beneficial plant phenotypes leading to a higher water-use efficiency under specific local environmental conditions.

Regarding the soil-rhizosphere-plant framework, several models have been developed to simulate the root-influenced spatiotemporal distribution of C turnover and microbial activity (Pot et al., 2022, Sircan et al., 2024), the exudation from a growing 3D root system (Rees et al., 2023b), or the exudation and water uptake by a static plant, based on the C and water balance within the plant and soil (Lacointe and Minchin, 2019, Zhou et al., 2020). Rees et al. (2023a) coupled *RhizoDep* with other models on the *OpenAlea* platform to represent the root-soil C and nitrogen exchanges for a growing wheat plant, driven by its inner N and C balances. Regarding plant-soil coupling for solute flow using FSPMs, several modelling studies have represented the soil as a dynamic environment with water and solute uptake (generally phosphorus) or C releases from a static or growing root system (Gérard et al., 2017, Heppell et al., 2016, Jorda Guerra et al., 2021, Landl et al., 2021a, Mai et al., 2019, Ruiz et al., 2021, Schröder et al., 2014, Schwartz et al., 2016). Braghiere et al. (2020) set up a 3D FSPM accounting

for shoot-root-soil interactions for water and C using model coupling. However, their framework did not account for either C flow and microbial reactions in the soil or inner plant water and C balance. Some coupled models also represented inner plant water flow (Mai et al., 2019, Schröder et al., 2014, Schwartz et al., 2016), or root-shoot interactions (Braghiere et al., 2020, Heppell et al., 2016), and Mai et al. (2019) used a sequential implementation of the multi-scale setup. Our framework stands out by representing a dynamic whole plant model and a dynamic soil model for both water and C flows (Rees et al., 2018, Ruiz et al., 2021, Schnepf et al., 2022), including biological and physical reactions (such as adsorption and the interactions with microbial communities) in the soil domain. For comparison, tables 5-1 and 5-2 give an overview of studies using FSPMs that include both the root and shoot organs explicitly and in a 3D space, as well as at least one function.

5-2 Simulation of plant growth and development

As discussed above, the mechanistic representation of 3D plant growth and its link with other modules is one of the novel aspects of CPlantBox. Linking the plant water and C balance with its 3D growth is also a new type of modelling output for full plant FSPMs in general (Coussement et al., 2020). Indeed, the precise dynamic of cell division and (reversible) expansion is not precisely understood (Beveridge et al., 2023). Using the precise water and C flow simulation of CPlantBox and implementing the big-cell model (Cieslak et al., 2022) method to simulate how the time-dependent supply of water and C affects plant growth in the different organs (volume and density) could yield new insights into plant water and C use efficiency.

In chapter 3, simulation results indicate that plant expansion growth is strongly influenced by changes in water potential during the diurnal cycle and drought periods, consistent with processes described in previous studies (Barillot et al., 2020, Coussement et al., 2018, De Swaef et al., 2022, Verbančič et al., 2018). However, it is hypothesised that cell wall biosynthesis (biosynthetic growth) predominantly occurs during the day using photoassimilates, while being much more limited at night when it relies on starch reserves (Verbančič et al., 2018). Although our simulations did not explicitly separate biosynthetic growth from expansion growth, the parametrization of the plant C module allowed us to qualitatively reproduce these dynamics. For this simulation, the virtual plant's starch pool can be interpreted as representing both actual starch reserves and newly synthesised wall material, thereby enabling expansion growth to occur at night. To achieve robust results and better recreate typical C dynamics across a wider range of parameter sets, it could be beneficial to explicitly represent biosynthetic growth in future models. Following the analyses of Verbančič et al. (2018) and Barillot et al. (2020), high biosynthetic growth requires higher C supply but results in the creation of new cells more flexible and capable of expanding under lower turgor pressure. This higher amount of cells with high cell

Table 5-1: Overview of FSPM studies, part 1: models with an explicit representation of shoot and root organs in a 3D space as well as at least one function[a]. W: water, C: carbon (and C-derived compounds), N: nitrogen (and nitrogen-derived compounds). -: none , NA: information not available. Update from the overview of Zhou et al. (2020).

Model name	References	Plant species	Additional organs[b]	Growth mechanisms considered	Elements in the plant[c]
CPlantBox (this study)	(Giraud et al., 2023, 2025)	generic	-	C and W-dependent	**W, C**
CPlantBox	(Baker et al., 2025, Bauer et al., 2024, Zhou et al., 2020)	generic	-	Genetic	**W, C**
PiafMunch	(Daudet et al., 2002, Lacointe and Minchin, 2019)	generic	fruit	-	**W, C**
PlaNet-Maize	(Lobet et al., 2014b)	generic	-	C-dependent	**W**, C
CN-wheat+RhizoDep	(Gauthier et al., 2020, Rees et al., 2023a, 2025)	wheat	grain	C and N-dependent	**C**[e], N
CN-Maiz	(Lu et al., 2024)	generic[d]	grain	C and N-dependent	C, N
RoCoCau+TOY	(Masson et al., 2021)	generic	-	light, C and W-dependent	W, C
GRAAL-CN	(Drouet and Pagès, 2003, Drouet and Pagès, 2007)	Maiz	-	temperature, N and C-dependent	**C, N**
alfalfa	(Zhang et al., 2018)	alfalfa	flower, bud	photosynthesis and degree day-dependent	C
L-grass	(Rouet et al., 2022)	perennial grass	flower	temperature and light-dependent	-
Archisimple + Min3P +shoot FSP	(Braghiere et al., 2020)	generic		potential transpiration dependent	W
GrapevineXL_V2	(Seleznyova and Hanan, 2018, Zhu et al., 2021)	grapevine	fruit	temperature and C-dependent	**C**
L-PEACH(-h)	(Allen et al., 2005, DeJong, 2022)	peach trees	flower, fruit, bud	water and C-dependent	W, **C**
L-ALMOND	(DeJong, 2022, DeJong et al., 2017)	almond trees	flower, fruit, bud	water and C-dependent	W, **C**

[a] Some models have additional modules, but which were not implemented in studies with both a 3D shoot and root.

[b] In addition to root, leaf and stem.

[c] Underlined letters in bold represent elements whose inner plant flows are represented, as opposed to e.g., distribution via allocation rules.

[d] Generic model in spite of the repository name.

[e] Element flow represented in the root system.

Table 5-2: Overview of FSPM studies, part 2: models with an explicit representation of shoot and root organs in a 3D space as well as at least one function[a]. W: water, C: carbon (and carbon-derived compounds), N: nitrogen (and nitrogen-derived compounds). -: none , NA: information not available.

name	plant processes[b]	soil processes	language	availability	parent framework
CPlantBox (this study)	photosynthesis&transpiration, stomatal regulation, auxin-dependent branching, respiration	3D flow of water and several elements, adsorption, reactions	Python, C++	open source	-
CPlantBox (other)	light interception	-	Python, C++	open source	-
PiafMunch	pressure-dependent reversible growth	-	C++	upon request	-
PlaNet-Maize	transpiration&stomatal regulation	simplified 3D water flow	Java, R	open source	-
CN-Wheat+RhizoDep	senescence, photosynthesis&transpiration&stomatal regulation, light distribution, root system secondary growth, respiration	-	Python	respective modules: open source	OpenAlea
CN-Maiz	photosynthesis, light interception	1D soil N flow	XL	open source	GroImp
RoCoCau+TOY	senescence	-	Python	open source	AMAPstudio
GRAAL-CN	seed C remobilisation, photosynthesis, respiration	-	C	NA	-
alfalfa	photosynthesis	-	NA	upon request	NA
L-grass	root-shoot C partitioning, cutting, light interception	-	Python (L-Py)	open-source	OpenAlea
Archisimple + Min3P +shoot FSP	photosynthesis&transpiration	3D soil water and several elements' flows and reactions	Fortran, C, Java, Python	upon request	GroImp
GrapevineXL_V2	secondary growth	-	XL	open source	GroImp
L-PEACH(-h)	secondary growth, pruning, fruit thinning, light interception, photosynthesis	soil water balance, available space for root growth	L-C	upon request	Lstudio/vlab
L-ALMOND	secondary growth, pruning, fruit thinning, light interception, photosynthesis	soil water balance, available space for root growth	L-C	upon request	Lstudio/vlab

[a] Some models have additional modules, but which were not implemented in studies with both a 3D shoot and root.

[b] Apart from growth and inner plant flows (processes already mentioned in Table 5-1).

wall flexibility can help maintain plant growth in case of drought (Blum, 2017). Another mechanism supporting growth under low turgor pressure is osmotic adjustment, which has been identified as a critical process during drought conditions (Blum, 2017, Coussement et al., 2018). Not including this process in our model could explain the high growth limitation caused by drought observed in our simulation.

In chapter 4, despite the model's simplified representation of hormonal transport pathways and limited calibration, it replicated key qualitative results from both our study and previous literature. This supports the hypothesis that sucrose plays a central role in regulating branching at the whole-plant scale (Barbier et al., 2019, 2015b) under laboratory conditions and when neither water nor nutrients are limiting. For this study as well, a more precise representation of the plant growth module could allow for more accurate (quantitative) results under a wider range of scenarios. Indeed, the balance between cell division and elongation can be affected by strigolactone signalling (de Saint Germain et al., 2013) and changes the relationship between plant C usage and branch elongation. However, there is a lack of empirical data regarding the dynamic of cell division and elongation in shoot branching (Beveridge et al., 2023).
We used the model of Bertheloot et al. (2020), which implicitly integrates the effect of cytokinin and strigolactone in a variable computed from the concentration of sucrose and auxin. However, as mentioned by Beveridge et al. (2023), the long-distance signalling of cytokinin and strigolactone in the plant plays an important role in the branching regulation. Expanding the plant hormonal module to include the representation and transport of those hormones could allow for a more precise simulation of the inter-organ and shoot-root interactions. To determine which (hormonal) processes are relevant at the plant scale for producing observed phenotypes, our *in silico* outputs could be compared with a broader range of laboratory data, such as the experiments of Ferguson and Beveridge (2009) or the review by Beveridge et al. (2003). Additional known hormonal processes could be integrated as needed.

Implementing the plant hormonal control (chapter 4) module within the CPlantBox plant-soil (chapter 3) framework could allow the simulations scenarios presented in both chapters to yield more accurate results. For instance, as discussed in chapter 3, this version of CPlantBox includes the simulation of water-pressure-limited growth and the storage of plant sucrose as starch. Water limitation on growth is expected to establish a new threshold for lateral growth, while sucrose storage as starch should help stabilize sucrose concentration. Both modules could correct the excessively high lateral development observed in certain scenarios from chapter 4. Additionally, the stabilisation of sucrose concentration should enhance the model's robustness across a broader range of parameters.

5-3 Software engineering

CPlantBox represents the 3D plant structure using a graph formalism, a widely used concept (Allen et al., 2005, Braghiere et al., 2020, Lacointe and Minchin, 2019, Postma et al., 2017, Rouet et al., 2022, Zhu et al., 2021). This representation allows us to implement existing solvers created for graphs or 1-dimensional meshes (Guennebaud et al., 2010, Hindmarsh et al., 2005, Koch et al., 2021). These solvers greatly increase the efficiency of the flow computation (Lacointe and Minchin, 2019). Likewise, the implementation of CPlantBox in C++ with Python binding allows us to use the rapidity of C++ and the flexibility and clarity of Python. This is an important advantage as computational power becomes a significant limitation for the development of FSPMs (Coussement et al., 2020, Soualiou et al., 2021). CPlantBox is also a flexible model: the spatial and temporal resolution (respectively plant segment length and time step) can be defined at run-time by the user. CPlantBox can also represent a wide variety of plants, contrary to some of the other FPSMs available (Coussement et al., 2020, Louarn and Song, 2020). Similarly to other frameworks like SIMPLACE (Enders et al., 2023) and OpenAlea (Pradal et al., 2008), users can select the modules to implement according to their research question. For instance, Baker et al. (2023) implemented the plant shoot structure module to create synthetic data for machine learning. Bauer et al. (2024) used the whole-plant water flow, and Baker et al. (2025) made use of the photosynthesis module. This makes CPlantBox a tool to [a] test the effect of the interactions between plant genotype, environmental conditions, and agricultural management, [b] help understand how/why these interactions lead to emerging properties (like plant structure and photosynthetic capacity), [c] return output parameters used as inputs by crop models (like C partitioning).

The multi-scale framework is a further advantages of this setup (Ruiz et al., 2021), increasing the resolution in the soil areas near the root-soil interface to balance accuracy and computing speed. Moreover, the use of fixed-point iteration (with implicit time stepping) for the plant-soil coupling allowed for larger time steps, increasing therefore not only the model accuracy but also its speed for specific scenarios (Schnepf et al., 2023). However, as the simulation of the water flow was the main bottleneck for model convergence, application of the model to more sandy soil or larger water flows will lead to shorter time steps and, therefore, longer computation time. The usage of the DuMu^x solver for the soil models and the representation of independent 1D perirhizal zones make the parallelisation of the soil-rhizosphere-plant framework (chapter 3) especially relevant. For the system modelled, optimal speed was reached when using 32 cores. Further updates of the framework to reduce the overhead caused by sharing information across processes could allow the simulation to run optimally on a higher number of cores, increasing the computation speed and making better usage of high-performance computing.

The modular nature of the framework also opens several possibilities for

the implementation of machine learning algorithms to increase computing speed, as some of the modules could be replaced by surrogate models. Physics-informed neural networks could for instance be efficient surrogate models of the different flow simulations (Baker et al., 2019, Stock et al., 2024). The flow simulation could also be improved by implementing neural networks to update during the simulations the hyperparameters of the flow solver, such as the grid size or the time step (Baker et al., 2019). For instance, the optimal number of cell in out 1D perirhizal zone models (chapter 3) is likely to be strongly problem-dependent. Moreover, our current soil-rhizosphere-plant models relies currently on two fixed-point iteration loops: one for the coupled FvCB-stomatal opening and one for the plant water flow and soil processes (see Fig. 3-4). An algorithm using reinforcement learning, such as the actor-critic algorithm, could be used to try and reduce the number of iterations necessary for convergence (Mnih et al., 2016). The 'actor' agent would return guesses for the most relevant input data of each loop (stomatal opening for the FvCB-stomata module, plant water uptake for the soil-plant loop) according to the results of the previous loops. The 'reward' used by both agents would be computed from the error and non-convergence indexes of each iteration (see section B.6). Either convergence or reaching the maximal number of allowed iterations would represent the end of a learning 'episode'. Finally, because of its high number of parameters, CPlantBox could profit from the development of calibration pipelines, which could include machine-learning elements (see section 5-4).

5-4 Calibration and validation of CPlantBox

Due to its detailed representation of plant structure and processes, CPlantBox requires a large number of parameters (see Table 5-3). Several CPlantBox parameters represent implicitly several processes, e.g. the organ tropism strength *TropismT*. Such fitting parameters have no explicit physical definition, cannot be measured directly and require therefore reverse calibration. This challenge is common to FSPMs (De Reffye et al., 2010, Soualiou et al., 2021) but is particularly evident for CPlantBox as it forms are large framework for soil-rhizosphere-plant simulation. The need for a calibration pipeline will become more critical as new functional modules are introduced, necessitating robust parameter estimation strategies and databases. Accurately representing root systems in FSPMs is particularly challenging. Unlike shoot organs, which can be directly measured and calibrated, root system traits are largely hidden underground and difficult to quantify (Takahashi and Pradal, 2021). Models can be calibrated using local traits (e.g., root radius, lateral root spacing), but a sufficient number of measurement points is needed to capture the mean and standard deviation of stochastic structural parameters. Validation also requires root system-scale data. Moreover, the model must incorporate both dynamic traits (e.g., growth rate) and three-dimensional traits (e.g., tropism), which cannot be easily inferred from local measurements. For plants like wheat, reconstructing the entire root system is essential to classify root types

accurately, as their diameters often overlap. However, few experimental methods provide full 3D root system evaluations. Techniques such as MRI and X-ray CT, while precise, are impractical for field studies. Alternative methods—soil coring, excavation, trenches, and rhizoboxes—offer limited perspectives and risk damaging root structures (Freschet et al., 2021, Landl et al., 2021a, Takahashi and Pradal, 2021). Wheat root systems pose additional difficulties due to their fibrous nature and small root diameters (Chen et al., 2020). Non-destructive methods struggle to detect fine roots, while destructive techniques risk data loss during cleaning and scanning.

Divers workflows have been implemented to facilitate the calibration of CPlantBox by users. First of all, several CPlantBox parameter sets have been established for different plant species, particularly for the structural description of root systems (Schnepf et al., 2018b). For the soil biokinetic parameters, Sircan et al. (2024) defined a parameter space fulfilling biogeochemical constraints.
Moreover, to help define the most relevant parameters in future calibration, Schnepf et al. (2018a), Landl et al. (2018), and Morandage et al. (2019) conducted statistical and sensitivity analysis of the root structural module: Schnepf et al. (2018a) presented the correlations between CPlantBox's root parameters and common root system observations. Landl et al. (2018) conducted a study on the effects of using 2D images to parameterise the 3D CPlantBox model. They could determine rules linking the 2D root distribution to the model's tropism parameters. In the study of Morandage et al. (2019), it was evaluated which root parameters had the strongest effect on the resulting aggregated root system observations (e.g., root length density). Giraud et al. (2023) did a simpler analysis of the sensitivity of selected outputs of the C and water modules to the plant parameters (see section A.7). These studies can help users evaluate which CPlantBox parameters have to be parameterised with the most care according to the simulation objectives, and which parameters can be the most easily calibrated via inverse modeling.
Inverse modeling (also known as simulation-based inference) was already used to calibrate root-scale CPlantBox parameters using aggregated variables such as root length density. In their study, Morandage et al. (2021) implemented a version of DREAM_ZS for Python (Laloy et al., 2017, Laloy and Vrugt, 2012), accounting for the stochasticity of the CRootBox FSPM (Schnepf et al., 2018b). This method effectively calibrated key root system parameters using root length density data from field experiments. The workflow developed by Morandage et al. (2021) was later re-implemented and updated to remain compatible with CPlantBox. Ensuring access to calibration tools and standardized workflows is essential for the long-term usability and adoption of FSPMs in the scientific community (Bonan, 2019d, Soualiou et al., 2021, Stock et al., 2024). Efforts to develop a user-friendly calibration implementation for CPlantBox are underway. Due to the computational expense of running the model, simulation-based inferences that require fewer model runs could also provide significant advantages (Rangarajan et al., 2022).
Future implementations could also profit from new studies and experimental

methods developed to evaluate the plant and soil C dynamic. In their study, le Gall et al. (2024) used plant-scale columns and transpiration chambers as well as isotopic measurements to evaluate plant transpiration, assimilation and the root water uptake profiles during their growth. Moreover, the root structure was evaluated using non-destructive NMR measurements and destructive root system scanning. This dataset would allow for a calibration of the model's structural, water and FvCB modules. Similarly, Metzner et al. (2022) could obtain plant C flow data using non-destructive isotopic measurements, which could lead to a precise calibration of CPlantBox's C flow model. Finally, microbial data from studies like the one of Lattacher et al. (2025) can be used to calibrate the soil C model: microbial biomass can be linked directly with the outputs of our model, while the simulated microbial activity can be compared with the experimentally observed enzymatic activity.

Table 5-3: Number of CPlantBox input parameters. The number of parameters required by the plant depends partly on the resolution selected by the user (e.g., water conductivity constant per organ type or age-dependent). The parameter numbers given here correspond to the resolution used in this work. Parameters corresponding to physical constant (e.g., H_2O to CO_2 ratio of molecular diffusivity in air) are not counted. Parameters corresponding to user selection (e.g., whether the plant does C3 or C4 photosynthesis) are not counted. NA: module not applicable.

	organ type specific			Plant	Soil	Total
	root	stem	leaf			
Structure	11	13	12	6	2	44
FvCB-stomata	0	0	0	13	NA	13
Water flow	2	2	2	0	5	11
Carbon dynamic	4	4	4	16	28	56
Total	17	19	18	35	35	**124**

Chapter 6

Conclusion and Outlook

In this section, we summarise the key outputs of the studies presented, including directions for future research.

for the authors, [books] could be called 'Conclusions' and for the reader 'Incentives'. We feel very well that our wisdom begins where the author's ends, and we would like him to give us answers, when all he can do is give us desires.

PROUST *Sur la Lecture*

6-1 Conclusions

Adapting our agricultural practices to maintain food production under resource shortages, increasing uncertainty, and extreme weather events requires a deeper understanding of the interrelated plant processes and higher predictive capability of future resulting phenotypes. Modelling is a valuable tool to achieve these objectives by recreating observed results or predicting new outcomes under novel genotype-environment-management combinations.

The overall aim of this thesis was to set up a framework capable of simulating at the individual plant scale the interactions between water flow and carbon balance in the soil and plant domains, mediated by the soil and atmosphere abiotic conditions, as well as selected plant and microbial traits and processes. We strove to make the framework precise enough to represent the main relevant processes while remaining flexible and user-friendly (straightforward calibration and implementation). The main objectives of this work were: [1] to couple the water and carbon balances in the shoot and root system (chapter 2), [2] to set up a framework representing the water and carbon balance in the soil-rhizosphere-plant continuum (chapter 3), and [3] to link the plant carbon balance with its branching regulation and test (*in silico*) assumptions taken from the literature (chapter 4).

Objective [1]: As described in chapter 2 of this thesis, we implemented new modules within the functional structural plant model CPlantBox. The water and carbon balances of the plant were then coupled via the stomatal-opening FvCB module and the water- and carbon-limited growth module. Moreover, the simulation of the xylem and phloem flows allowed us to couple the shoot and root system balances. With this new framework, we connected domains and processes that are typically simulated in isolation and we gained insights into complex interaction processes. For instance, dry spells can have both positive and negative effects on exudation: while they may increase the carbon available for exudation due to reduced growth, stomatal closure and decreased leaf area growth also lower the supply of photosynthates. The simulation of the plant water- and carbon-related processes underlined the central role of plant growth when representing the interactions between those two resources. A more precise representation of the water and carbon coupling could consequently be obtained by updating the plant growth model, allowing for an asynchronous supply of resources.
Objective [2]: As presented in chapter 3 of this thesis we implemented the plant model within an updated multiscale soil model, considering microbial activity. This framework allowed for an in-depth analysis of the interrelated processes driving soil respiration and carbon stabilisation under different weather scenarios and microbial traits. We used the model outputs to understand how the traits of the microbial community affected the changes in the carbon balance caused by a drying-wetting cycle. The set up of the fixed point iteration proved to be a key lever to increase model accuracy and speed.

Objective [3]: In chapter 4 of this thesis, we set up a semi-mechanistic representation of shoot branching using the signalling role of sucrose and auxin and the nutritional role of sucrose. Comparing simulation outputs with our experimental results and observations from the literature allowed us to test hypotheses regarding the main processes affecting shoot branching regulation under specific weather scenarios. In spite of the limited calibration, we could re-create key experimental results. This similarities indicate that representing sucrose and auxin transport could be sufficient to simulate semi-mechanistically plant branching patterns under non-stress conditions. The simulation of the plant sucrose as a signaling molecule rendered more important the plant processes linked to the regulation of its concentration.

6-2 Outlook

Building on the discussion and conclusion sections, we present here suggestions for further research.

6-2-1 Model implementation

This work focused on the different aspects of model development, from process representation to numerical schemes and software engineering while it only exemplified the models' capabilities for specific applications. Future work on CPlantBox will focus on the use of the model to answer more complex scientific questions that take advantages of the wide range of output variables computed by the model. For example, the continuation of the work presented in chapter 4 would help evaluate the importance of inner plant carbon, not only as a biomass building block but also as signal. More generally, the model could be used to test hypothesis regarding the possible redundancy between phytohormones and physical processes: The model can allow us to evaluate when the water potential-driven flow is sufficient to explain observed water and carbon allocation within the plant and when other plant processes–plant signaling–have a significant effect on the plant's development. The soil-rhizosphere-plant framework could be used to evaluate the effect of various plant phenotypes on the carbon allocation in the system and specifically soil carbon stabilisation. It would thus be possible to define phenotypes and specific parameters leading to the most efficient use of water and carbon under specific environmental conditions.

6-2-2 Simulation of the soil and plant nitrogen flows

Future developments of the CPlantBox framework could focus on improving its representation of plant growth by incorporating additional key physiological processes. One important step will be the integration of a nitrogen balance module for both the plant and the soil. Nitrogen availability strongly influences plant growth, root system architecture, and carbon allocation, making it a crucial factor in simulating realistic plant-soil interactions. Including a nitrogen model will allow for a more accurate representation of how plants adjust their growth strategies in response to nutrient availability, complementing the existing carbon and water balance modules. Since nitrogen uptake is closely linked to root development, this addition will also help refine simulations of root growth dynamics, particularly under varying soil conditions. Furthermore, nitrogen availability interacts with microbial activity, influencing processes such as plant carbon release and water uptake. By incorporating these feedback mechanisms, the model will provide a more comprehensive tool for studying plant-soil interactions across different environmental conditions.

6-2-3 Model calibration

For the calibration, developing standardised methods and user-friendly tools will help more researchers use the model effectively without requiring extensive technical expertise. Since running the model can be time-consuming and computationally expensive, exploring simulation-based inference that require fewer model runs could make the calibration faster while maintaining accuracy. In addition, future implementation of the soil-rhizosphere-plant framework will lead to the creation of parameter sets that can then be adapted for plants and soils with similar characteristics. Regarding the data gathering, incorporating plant and soil isotopic measurements could be key to evaluating the water and carbon dynamic *in vivo*, providing valuable data for calibration CPlantBox's functional modules. Expanding existing parameter databases and improving the calibration pipeline will support wider adoption of CPlantBox for different plant species and environmental conditions. These improvements will make CPlantBox a more reliable and practical tool for studying plant-soil interactions.

Acknowledgments

This work would not have been possible without the dedication and countless hours of support provided by many individuals along the way.

My deepest gratitude goes to my supervisors, Prof. Dr. Guillaume Lobet and Prof. Dr. Andrea Schnepf, for making this doctoral project possible and for their unwavering support throughout. Their feedback and patience were instrumental not only in helping me complete this work, but also in shaping my development as a young researcher.

I am also grateful to the other supervisors of the CROP project—Prof. Dr. Mathieu Javaux, Prof. Dr. Youri Rothfuss, Prof. Dr. Ellen Kandeler, Prof. Dr. Christian Poll, Prof. Dr. Thilo Streck, and Prof. Dr. Holger Pagel—for their expertise and support. Many thanks as well to the other members of the CROP project: Samuel Le Gall, Adrian Lattacher, Moritz Harrings, and Ahmet Sircan. It was a wonderful opportunity to undertake this work within such a supportive team.

Furthermore, I would like to thank Prof. Dr. Harry Vereecken and Prof. Dr. Jan Vanderborght for their willingness to invest time in reviewing and improving the work of the many PhD students under their supervision.

I am also thankful to the members of the University of Queensland—Dr. Nicole Fortuna, Dr. Stephanie Conway, Dr. Inigo Auzmendi, Olalekan Amoo, Dr. Elisabeth Dun, Dr. Jim Hanan, and Prof. Dr. Christine Beveridge—for welcoming me so warmly and generously sharing their time and knowledge.

My sincere gratitude to the entire ROSI team for creating such an enjoyable working environment: Dirk Norbert Baker, Felix Bauer, Juan Carlos Baca Cabrera, Magdalena Landl, Tobias Selzner, Ullah Sibghat, Anna Heck, and Erik Kopp. My special thanks to Daniel Leitner for helping me learn how to develop scientific software.

Heartfelt thanks to Herbert and Sigrid for welcoming me in their home and taking care of me, to Julien for being the best kind of eccentric, and to Till, for being

my partner on this journey. Lastly, I thank my friends and family, and especially my parents Armand and Domnine and siblings Ysé and Aurélien for their lovingly biased support.

Funding

The author acknowledge funding by the German Federal Ministry of Education and Research (BMBF) in the framework of the funding measure "Plant roots and soil ecosystems, significance of the rhizosphere for the bio-economy" (Rhizo4Bio), subproject CROP phase I (FKZ 031B0909). Further funding is appreciated from the German Research Foundation (DFG) within the priority program 2322 "Soil Systems" (STR 481/12-1) and under Germany's Excellence Strategy (EXC 2070-390732324).

Bibliography

Adusah, A. and Brooks, G. (2011). Type i error inflation of the separate-variances welch t test with very small sample sizes when assumptions are met. *Journal of Modern Applied Statistical Methods*, 10:362–372.

Ahrens, B., Guggenberger, G., Rethemeyer, J., John, S., Marschner, B., Heinze, S., Angst, G., Mueller, C. W., Kögel-Knabner, I., Leuschner, C., Hertel, D., Bachmann, J., Reichstein, M., and Schrumpf, M. (2020). Combination of energy limitation and sorption capacity explains 14c depth gradients. *Soil Biology and Biochemistry*, 148.

Ahusborde, E., Kern, M., and Vostrikov, V. (2015). Numerical simulation of two-phase multicomponent flow with reactive transport in porous media: application to geological sequestration of co2. *ESAIM: Proceedings and surveys*, 49:21–39.

Albasha, R., Fournier, C., Pradal, C., Chelle, M., Prieto, J. A., Louarn, G., Simonneau, T., and Lebon, E. (2019). HydroShoot: a functional-structural plant model for simulating hydraulic structure, gas and energy exchange dynamics of complex plant canopies under water deficit—application to grapevine (Vitis vinifera). *in silico Plants*, 1(1):diz007.

Allen, H. R. and Ptashnyk, M. (2020). Mathematical modelling of auxin transport in plant tissues: Flux meets signalling and growth. *Bulletin of Mathematical Biology*, 82(2):17.

Allen, M. T., Prusinkiewicz, P., and DeJong, T. M. (2005). Using l-systems for modeling source–sink interactions, architecture and physiology of growing trees: the l-peach model. *New Phytologist*, 166(3):869–880.

Allen, R., Pereira, L., Raes, D., and Smith, M. (1998). Guidelines for computing crop water requirements-fao irrigation and drainage paper 56, fao-food and agriculture organisation of the united nations, rome (http://www. fao. org/docrep)

arpav (2000), la caratterizzazione climatica della regione veneto, quaderni per. *Geophysics*, 156:178.

Amthor, J. S. (2000). The McCree–de Wit–Penning de Vries–Thornley Respiration Paradigms: 30 Years Later. *Annals of Botany*, 86(1):1–20.

Annunziata, M. G., Apelt, F., Carillo, P., Krause, U., Feil, R., Mengin, V., Lauxmann, M., Koehl, K., Nikoloski, Z., Stitt, M., and Lunn, J. (2017). Getting back to nature: A reality check for experiments in controlled environments. *Journal of experimental botany*, 68.

Aqeel, M., Ran, J., Hu, W., Irshad, M. K., Dong, L., Akram, M. A., Eldesoky, G. E., Aljuwayid, A. M., Chuah, L. F., and Deng, J. (2023). Plant-soil-microbe interactions in maintaining ecosystem stability and coordinated turnover under changing environmental conditions. *Chemosphere*, 318:137924.

Arumingtyas, E., Floyd, R., Gregory, M.J., and Murfet, I. (1992). Branching in pisum: inheritance and allelism tests with 17 ramosus mutants. *Pisum Genetics*, 24:17–31.

Badri, D. and Vivanco, J. (2009). Regulation and function of root exudates. *Plant, Cell & Environment*, 32(6):666–681.

Baker, D. N., Bauer, F. M., Giraud, M., Schnepf, A., Göbbert, J. H., Scharr, H., Hvannberg, E. P., and Riedel, M. (2023). A scalable pipeline to create synthetic datasets from functional–structural plant models for deep learning. *in silico Plants*, 6(1):diad022.

Baker, D. N., Giraud, M., Göbbert, J. H., Scharr, H., Riedel, M., Hvannberg, E. Þ., and Schnepf, A. (2025). Virtual world coupling with photosynthesis evaluation for synthetic data production. *bioRxiv*.

Baker, N., Alexander, F., Bremer, T., Hagberg, A., Kevrekidis, Y., Najm, H., Parashar, M., Patra, A., Sethian, J., Wild, S., et al. (2019). Workshop report on basic research needs for scientific machine learning: Core technologies for artificial intelligence. Technical report, USDOE Office of Science (SC), Washington, D.C. (United States).

Barbier, F., Dun, E., and Beveridge, C. (2017). Apical dominance. *Current Biology*, 27:R864–R865.

Barbier, F., Peron, T., Lecerf, M., Perez Garcia, M. D., Barriere, Q., Rolcik, J., Boutet, S., Citerne, S., Lemoine, R., Porcheron, B., Roman, H., Leduc, N., Gourrierec, J., Bertheloot, J., and Sakr, S. (2015a). Sucrose is an early modulator of the key hormonal mechanisms controlling bud outgrowth in rosa hybrida. *Journal of Experimental Botany*, 66.

Barbier, F. F., Dun, E. A., Kerr, S. C., Chabikwa, T. G., and Beveridge, C. A. (2019). An update on the signals controlling shoot branching. *Trends in Plant Science*, 24(3):220–236.

Barbier, F. F., Lunn, J. E., and Beveridge, C. A. (2015b). Ready, steady, go! a sugar hit starts the race to shoot branching. *Current Opinion in Plant Biology*, 25:39–45.

Bardgett, R. and Caruso, T. (2020). Soil microbial community responses to climate extremes: Resistance, resilience and transitions to alternative states. *Philosophical Transactions of the Royal Society B: Biological Sciences*, 375:20190112.

Bardgett, R., Manning, P., Vries, F., and Morriën, E. (2013). Hierarchical responses of plant-soil interactions to climate change: Consequences for the global carbon cycle. *Journal of Ecology*, 101:334–343.

Barillot, R., Chambon, C., and Andrieu, B. (2016). CN-Wheat, a functional–structural model of carbon and nitrogen metabolism in wheat culms after anthesis. I. Model description. *Annals of Botany*, 118(5):997–1013.

Barillot, R., De Swaef, T., Combes, D., Durand, J.-L., Escobar-Gutiérrez, A. J., Martre, P., Perrot, C., Roy, E., and Frak, E. (2020). Leaf elongation response to blue light is mediated by stomatal-induced variations in transpiration in festuca arundinacea. *Journal of Experimental Botany*, 72(7):2642–2656.

Batchelor, C. K. and Batchelor, G. (2000). *An introduction to fluid dynamics*. Cambridge university press.

Bauer, F. M., Baker, D. N., Giraud, M., Baca Cabrera, J. C., Vanderborght, J., Lobet, G., and Schnepf, A. (2024). Root system architecture reorganization under decreasing soil phosphorus lowers root system conductance of zea mays. *bioRxiv*.

Bazot, S., Mikola, J., Nguyen, C., and Robin, C. (2005). Defoliation-induced changes in carbon allocation and root soluble carbon concentration in field-grown lolium perenne plants: do they affect carbon availability, microbes and animal trophic groups in soil? *Functional Ecology*, 19(5):886–896.

Bear, J. and Bachmat, Y. (1967). A generalized theory on hydrodynamic dispersion in porous media. *Int. Union Geod. Geophys. Publ.*, 72.

Benes, B., Guan, K., Lang, M., Long, S., Lynch, J., Marshall-Colon, A., Peng, B., Schnable, J., Sweetlove, L., and Turk, M. (2020). Multiscale computational models can guide experimentation and targeted measurements for crop improvement. *The Plant Journal*, 103.

Benjamini, Y. and Hochberg, Y. (1995). Controlling the false discovery rate: A practical and powerful approach to multiple testing. *Journal of the Royal Statistical Society. Series B (Methodological)*, 57(1):289–300.

Bertheloot, J., Barbier, F., Boudon, F., Perez-Garcia, M. D., Péron, T., Citerne, S., Dun, E., Beveridge, C., Godin, C., and Sakr, S. (2020). Sugar availability suppresses the auxin-induced strigolactone pathway to promote bud outgrowth. *New Phytologist*, 225(2):866–879.

Beveridge, C. A., Rameau, C., and Wijerathna-Yapa, A. (2023). Lessons from a century of apical dominance research. *Journal of Experimental Botany*, 74(14):3903–3922.

Beveridge, C. A., Weller, J. L., Singer, S. R., and Hofer, J. M. (2003). Axillary Meristem Development. Budding Relationships between Networks Controlling Flowering, Branching, and Photoperiod Responsiveness. *Plant Physiology*, 131(3):927–934.

Bidel, L. P. R., Pagès, L., Rivière, L. M., Pelloux, G., and Lorendeau, J. Y. (2000). MassFlowDyn I: A Carbon Transport and Partitioning Model for Root System Architecture. *Annals of Botany*, 85(6):869–886.

Bingham, I. J. and Wu, L. (2011). Simulation of wheat growth using the 3d root architecture model spacsys: validation and sensitivity analysis. *European journal of agronomy*, 34(3):181–189.

Blum, A. (2017). Osmotic adjustment is a prime drought stress adaptive engine in support of plant production. *Plant, Cell & Environment*, 40(1):4–10.

Blyth, M. G. and Morris, R. J. (2018). *Fluid Transport in Plants*, pages 15–36. Springer International Publishing, Cham.

Bonan, G. (2019a). *Appendices*, page 381–390. Volume 1 of Bonan (2019b).

Bonan, G. (2019b). *Climate Change and Terrestrial Ecosystem Modeling*, volume 1. Cambridge University Press, San Diego, California.

Bonan, G. (2019c). *Leaf Photosynthesis*, page 167–188. Volume 1 of Bonan (2019b).

Bonan, G. (2019d). *Terrestrial Biosphere Models*, pages 167–188. Volume 1 of Bonan (2019b).

Bonkowski, M., Tarkka, M., Razavi, B., Schmidt, H., Blagodatskaya, E., Koller, R., Yu, P., Knief, C., Hochholdinger, F., and Vetterlein, D. (2021). Spatiotemporal dynamics of maize (zea mays l.) root growth and its potential consequences for the assembly of the rhizosphere microbiota. *Frontiers in Microbiology*, 12.

Borken, W. and Matzner, E. (2009). Reappraisal of drying and wetting effects on c and n mineralization and fluxes in soils. *Global Change Biology*, 15(4):808–824.

Bouvry, A. and Lebeau, F. (2023). Digital twin of a smart plant factory for plant phenotyping : Data assimilation between measured and simulated 3d point cloud data in the cplantbox fspm. In *10th International Conference on Functional-Structural Plant Models (FSPM)*.

Boyer, J. S. and Kramer, P. J. (1995). *Water relations of plants and soils*. Academic Press., San Diego, California.

Braghiere, R. K., Gérard, F., Evers, J. B., Pradal, C., and Pagès, L. (2020). Simulating the effects of water limitation on plant biomass using a 3d functional-structural plant model of shoot and root driven by soil hydraulics. *Ann Bot*, 126(4):713–728.

Bramley, H. (2006). *Water flow in the roots of three crop species: The influence of rootnstructure, aquaporin activity and waterlogging*. Thesis, The University of Western Australia.

Bramley, H., Turner, D., Tyerman, S., and Turner, N. (2007). Water flow in the roots of crop species: The influence of root structure, aquaporin activity, and waterlogging. In *Advances in Agronomy*, volume 96 of *Advances in Agronomy*, pages 133–196. Academic Press.

Brewer, P. B., Dun, E. A., Ferguson, B. J., Rameau, C., and Beveridge, C. A. (2009). Strigolactone Acts Downstream of Auxin to Regulate Bud Outgrowth in Pea and Arabidopsis. *Plant Physiology*, 150(1):482–493.

Brown, R. W., Chadwick, D. R., Bending, G. D., Collins, C. D., Whelton, H. L., Daulton, E., Covington, J. A., Bull, I. D., and Jones, D. L. (2022). Nutrient (c, n and p) enrichment induces significant changes in the soil metabolite profile and microbial carbon partitioning. *Soil Biology and Biochemistry*, 172.

Cabrita, P. (2011). *Experimental and theoretical studies of phloem transport with the inclusion of lateral solute exchange and apoplastic conditions*. PhD thesis, Justus-Liebig-UniversitÃ¤t, Otto-Behaghel-Str. 8, 35394 Giessen.

Canarini, A., Kaiser, C., Merchant, A., Richter, A., and Wanek, W. (2019). Root exudation of primary metabolites: Mechanisms and their roles in plant responses to environmental stimuli. *Front Plant Sci*, 10:157.

Cannell, M. G. R. and Thornley, J. H. M. (2000). Modelling the Components of Plant Respiration: Some Guiding Principles. *Annals of Botany*, 85(1):45–54.

Cao, D., Barbier, F., Dun, E. A., Fichtner, F., Dong, L., Kerr, S. C., and Beveridge, C. A. (2022). Auxin-independent effects of apical dominance induce temporal changes in phytohormones. *bioRxiv*.

Chabikwa, T. G., Brewer, P. B., and Beveridge, C. A. (2018). Initial Bud Outgrowth Occurs Independent of Auxin Flow from Out of Buds. *Plant Physiology*, 179(1):55–65.

Chen, X., Zhu, Y., Ding, Y., Pan, R., Shen, W., Yu, X., and Xiong, F. (2021). The relationship between characteristics of root morphology and grain filling in wheat under drought stress. *PeerJ*, 9:e12015.

Chen, Y., Palta, J., Prasad, P. V. V., and Siddique, K. H. M. (2020). Phenotypic variability in bread wheat root systems at the early vegetative stage. *BMC Plant Biology*, 20(1):185.

Cieslak, M., Owens, A., and Prusinkiewicz, P. (2022). Computational models of auxin-driven patterning in shoots. *Cold Spring Harb Perspect Biol*, 14(3).

Cieslak, M., Seleznyova, A., Prusinkiewicz, P., and Hanan, J. (2011). Towards aspect-oriented functional–structural plant modelling. *Annals of botany*, 108:1025–41.

Corso, D., Delzon, S., Lamarque, L. J., Cochard, H., Torres-Ruiz, J. M., King, A., and Brodribb, T. (2020). Neither xylem collapse, cavitation, or changing leaf conductance drive stomatal closure in wheat. *Plant, Cell & Environment*, 43(4):854–865.

Coussement, J., De Swaef, T., Lootens, P., and Steppe, K. (2020). Turgor-driven plant growth applied in a soybean functional–structural plant model. *Annals of Botany*, 126(4):729–744. © The Author(s) 2020. Published by Oxford University Press on behalf of the Annals of Botany Company. All rights reserved. For permissions, please e-mail: journals.permissions@oup.com.

Coussement, J., Swaef, T., Lootens, P., Roldán-Ruiz, I., and Steppe, K. (2018). Introducing turgor-driven growth dynamics into functional-structural plant models. *Annals of botany*, 121.

Damour, G., Simonneau, T., Cochard, H., and Urban, L. (2010). An overview of models of stomatal conductance at the leaf level. *Plant, Cell and Environment*, 33(9):1419–1438.

Darrah, P. R. (1991). Models of the rhizosphere. *Plant and Soil*, 133(2):187–199.

Daudet, F. A., Lacointe, A., Gaudillere, J. P., and Cruiziat, P. (2002). Generalized muench coupling between sugar and water fluxes for modelling carbon allocation as affected by water status. *Journal of Theoretical Biology*, 214(3):481–498.

de la Fuente Cantó, C., Simonin, M., King, E., Moulin, L., Bennett, M., Castrillo, G., and Laplaze, L. (2020). An extended root phenotype: the rhizosphere, its formation and impacts on plant fitness. *The Plant Journal*, 103.

De Reffye, P., Heuvelink, E., Guo, Y., Hu, B.-G., and Zhang, B. (2010). *Coupling Process-Based Models and Plant Architectural Models: A Key Issue for Simulating Crop Production*, pages 130–147. Springer.

de Saint Germain, A., Ligerot, Y., Dun, E. A., Pillot, J.-P., Ross, J. J., Beveridge, C. A., and Rameau, C. (2013). Strigolactones Stimulate Internode Elongation Independently of Gibberellins. *Plant Physiology*, 163(2):1012–1025.

De Schepper, V., De Swaef, T., Bauweraerts, I., and Steppe, K. (2013). Phloem transport: a review of mechanisms and controls. *Journal of Experimental Botany*, 64(16):4839–4850.

De Swaef, T., Pieters, O., Appeltans, S., Borra-Serrano, I., Coudron, W., Couvreur, V., Garré, S., Lootens, P., Nicolaï, B., Pols, L., Saint Cast, C., Šalagovič, J., Van Haeverbeke, M., Stock, M., and wyffels, F. (2022). On the pivotal role

of water potential to model plant physiological processes. *in silico Plants*, 4(1). diab038.

de Vries, J. (2021). Using evolutionary functional–structural plant modelling to understand the effect of climate change on plant communities. *in silico Plants*, 3(2). diab029.

Debnath, L. (2005). *Linear Partial Differential Equations*, pages 1–148. Birkhäuser Boston, Boston, MA.

DeJong, T. (2022). Simulating fruit tree growth, structure, and physiology using l-systems. *Crop Science*, 62(6):2091–2106.

DeJong, T. M., Da Silva, D., Negron, C., Cieslak, M., and Prusinkiewicz, P. (2017). The l-almond model: a functional-structural virtual tree model of almond tree architectural growth, carbohydrate dynamics over multiple years. In *X International Symposium on Modelling in Fruit Research and Orchard Management*, pages 43–50. International Society for Horticultural Science (ISHS), Leuven, Belgium.

Deng, L., Peng, C., Kim, D.-G., Li, J., Liu, Y., Hai, X., Liu, Q., Huang, C., Shangguan, Z., and Kuzyakov, Y. (2021). Drought effects on soil carbon and nitrogen dynamics in global natural ecosystems. *Earth-Science Reviews*, 214.

Dewar (2002). The ball–berry–leuning and tardieu–davies stomatal models: synthesis and extension within a spatially aggregated picture of guard cell function. *Plant, Cell and Environment*, 25(11):1383–1398.

Dilkes, N. B., Jones, D. L., and Farrar, J. (2004). Temporal dynamics of carbon partitioning and rhizodeposition in wheat. *Plant Physiology*, 134(2):706–715.

Drake, J. E., Darby, B. A., Giasson, M.-A., Kramer, M. A., Phillips, R. P., and Finzi, A. C. (2013). Stoichiometry constrains microbial response to root exudation- insights from a model and a field experiment in a temperate forest. *Biogeosciences*, 10(2):821–838.

Drouet, J.-L. and Pagès, L. (2003). Graal: a model of growth, architecture and carbon allocation during the vegetative phase of the whole maize plant: model description and parameterisation. *Ecological Modelling*, 165(2-3):147–173.

Drouet, J.-L. and Pagès, L. (2007). Graal-cn: A model of growth, architecture and allocation for carbon and nitrogen dynamics within whole plants formalised at the organ level. *Ecological Modelling*, 206(3):231–249.

Dubitzky, W., Wolkenhauer, O., Cho, K.-H., and Yokota, H., editors (2013). *Functional-Structural Plant Modeling*, pages 778–781. Springer New York, New York, NY.

Dun, E. A., de Saint Germain, A., Rameau, C., and Beveridge, C. A. (2011). Antagonistic Action of Strigolactone and Cytokinin in Bud Outgrowth Control. *Plant Physiology*, 158(1):487–498.

Dunbabin, V. M., Postma, J. A., Schnepf, A., Pagès, L., Javaux, M., Wu, L., Leitner, D., Chen, Y. L., Rengel, Z., and Diggle, A. J. (2013). Modelling root–soil interactions using three–dimensional models of root growth, architecture and function. *Plant and soil*, 372:93–124.

Dupuy, L. X. and Silk, W. K. (2016). Mechanisms of early microbial establishment on growing root surfaces. *Vadose Zone Journal*, 15(2).

Enders, A., Vianna, M., Gaiser, T., Krauss, G., Webber, H., Srivastava, A. K., Seidel, S. J., Tewes, A., Rezaei, E. E., and Ewert, F. (2023). Simplace—a versatile modelling and simulation framework for sustainable crops and agroecosystems. *in silico Plants*, 5(1):diad006.

Evers, J. B., van der Krol, A. R., Vos, J., and Struik, P. C. (2011). Understanding shoot branching by modelling form and function. *Trends in Plant Science*, 16(9):464–467.

Evers, J. B. and Vos, J. (2013). Modeling branching in cereals. *Frontiers in Plant Science*, 4.

FAO (2021). *The impact of disasters and crises on agriculture and food security: 2021*. FAO.

Farquhar, G. D., von Caemmerer, S., and Berry, J. A. (1980). A biochemical model of photosynthetic co2 assimilation in leaves of c3 species. *Planta*, 149(1):78–90.

Ferguson, B. and Beveridge, C. (2009). Roles for auxin, cytokinin, and strigolactone in regulating shoot branching. *Plant physiology*, 149:1929–44.

Fichtner, F., Barbier, F., Feil, R., Watanabe, M., Annunziata, M. G., Chabikwa, T., Hoefgen, R., Stitt, M., Beveridge, C., and Lunn, J. (2017). Trehalose 6-phosphate is involved in triggering axillary bud outgrowth in garden pea (pisum sativum l.). *The Plant Journal*, 92.

Freschet, G. T., Pagès, L., Iversen, C. M., Comas, L. H., Rewald, B., Roumet, C., Klimešová, J., Zadworny, M., Poorter, H., Postma, J. A., Adams, T. S., Bagniewska-Zadworna, A., Bengough, A. G., Blancaflor, E. B., Brunner, I., Cornelissen, J. H. C., Garnier, E., Gessler, A., Hobbie, S. E., Meier, I. C., Mommer, L., Picon-Cochard, C., Rose, L., Ryser, P., Scherer-Lorenzen, M., Soudzilovskaia, N. A., Stokes, A., Sun, T., Valverde-Barrantes, O. J., Weemstra, M., Weigelt, A., Wurzburger, N., York, L. M., Batterman, S. A., Gomes de Moraes, M., Janecek, S., Lambers, H., Salmon, V., Tharayil, N., and McCormack, M. L. (2021). A starting guide to root ecology: strengthening ecological concepts and standardising root classification, sampling, processing and trait measurements. *New Phytologist*, 232(3):973–1122.

Galindo-Castañeda, T., Lynch, J. P., Six, J., and Hartmann, M. (2022). Improving soil resource uptake by plants through capitalizing on synergies between root architecture and anatomy and root-associated microorganisms. *Frontiers in Plant Science*, 13.

Galindo-Castañeda, T., Hartmann, M., and Lynch, J. P. (2023). Location: root architecture structures rhizosphere microbial associations. *Journal of Experimental Botany*, 75(2):594–604.

Gaudio, N., Louarn, G., Barillot, R., Meunier, C., Vezy, R., and Launay, M. (2021). Exploring complementarities between modelling approaches that enable upscaling from plant community functioning to ecosystem services as a way to support agroecological transition. *in silico Plants*, 4.

Gauthier, M., Barillot, R., Schneider, A., Chambon, C., Fournier, C., Pradal, C., Robert, C., and Andrieu, B. (2020). A functional structural model of grass development based on metabolic regulation and coordination rules. *Journal of Experimental Botany*, 71(18):5454–5468.

George, T. S., Bulgarelli, D., Carminati, A., Chen, Y., Jones, D., Kuzyakov, Y., Schnepf, A., Wissuwa, M., and Roose, T. (2024). Bottom-up perspective – the role of roots and rhizosphere in climate change adaptation and mitigation in agroecosystems. *Plant and Soil*.

Giraud, M., Le Gall, S., Harings, M., Javaux, M., Leitner, D., Meunier, F., Rothfuss, Y., van Dusschoten, D., Vanderborght, J., Vereecken, H., Lobet, G., and Schnepf, A. (2023). CPlantBox: a fully coupled modeling platform for the water and carbon fluxes in the Soil-Plant-Atmosphere-Continuum. *in silico Plants*, page diad009.

Giraud, M., Sırcan, A. K., Streck, T., Leitner, D., Lobet, G., Pagel, H., and Schnepf, A. (2025). In silico analysis of carbon stabilisation by plant and soil microbes for different weather scenarios. *EGUsphere*, 2025:1–76.

Grafahrend-Belau, E., Junker, A., Eschenröder, A., Müller, J., Schreiber, F., and Junker, B. H. (2013). Multiscale Metabolic Modeling: Dynamic Flux Balance Analysis on a Whole-Plant Scale. *Plant Physiology*, 163(2):637–647.

Guennebaud, G., Jacob, B., et al. (2010). Eigen v3. http://eigen.tuxfamily.org.

Guyer, J. E., Wheeler, D., and Warren, J. A. (2009). Fipy: Partial differential equations with python. *Computing in Science & Engineering*, 11(3):6–15.

Gérard, F., Blitz-Frayret, C., Hinsinger, P., and Pagès, L. (2017). Modelling the interactions between root system architecture, root functions and reactive transport processes in soil. *Plant and Soil*, 413(1):161–180.

Hall, A. J. and Minchin, P. E. H. (2013). A closed-form solution for steady-state coupled phloem/xylem flow using the lambert-w function. *Plant, Cell & Environment*, 36(12):2150–2162.

Hartmann, H., Bahn, M., Carbone, M., and Richardson, A. D. (2020). Plant carbon allocation in a changing world – challenges and progress: introduction to a virtual issue on carbon allocation. *New Phytologist*, 227(4):981–988.

Helmig, R. (1997). *Multiphase Flow and Transport Processes in the Subsurface: A Contribution to the Modeling of Hydrosystems*. Springer.

Heppell, J., Payvandi, S., Talboys, P., Zygalakis, K. C., Langton, D., Sylvester-Bradley, R., Edwards, A. C., Walker, R., Withers, P., Jones, D. L., and Roose, T. (2016). Use of a coupled soil-root-leaf model to optimise phosphate fertiliser use efficiency in barley. *Plant and Soil*, 406(1):341–357.

Hindmarsh, A. C., Brown, P. N., Grant, K. E., Lee, S. L., Serban, R., Shumaker, D. E., and Woodward, C. S. (2005). SUNDIALS: Suite of nonlinear and differential/algebraic equation solvers. *ACM Transactions on Mathematical Software (TOMS)*, 31(3):363–396.

Hirschberg, K., Miller, C. M., Ellenberg, J., Presley, J. F., Siggia, E. D., Phair, R. D., and Lippincott-Schwartz, J. (1998). Kinetic analysis of secretory protein traffic and characterization of golgi to plasma membrane transport intermediates in living cells. *J Cell Biol*, 143(6).

Hobbie, J. E. and Hobbie, E. A. (2013). Microbes in nature are limited by carbon and energy: the starving-survival lifestyle in soil and consequences for estimating microbial rates. *Frontiers in Microbiology*, 4.

Husain, S. M. and Linck, A. J. (1966). Relationship of apical dominance to the nutrient accumulation pattern in pisum sativum var. alaska. *Physiologia Plantarum*, 19(4):992–1010.

Hölttä, T., Lintunen, A., Chan, T., Mäkelä, A., and Nikinmaa, E. (2017). A steady-state stomatal model of balanced leaf gas exchange, hydraulics and maximal source-sink flux. *Tree physiology*, 37:1–18.

Hölttä, T., Vesala, T., Sevanto, S., Perämäki, M., and Nikinmaa, E. (2006). Modeling xylem and phloem water flows in trees according to cohesion theory and münch hypothesis. *Trees*, 20:67–78.

ISSS (1976). Bulletin of the international society of soil science no. 49.

Iwanaga, T., Usher, W., and Herman, J. (2022). Toward SALib 2.0: Advancing the accessibility and interpretability of global sensitivity analyses. *Socio-Environmental Systems Modelling*, 4:18155.

Jensen, K. H., Savage, J. A., and Holbrook, N. M. (2013). Optimal concentration for sugar transport in plants. *Journal of The Royal Society Interface*, 10(83):20130055.

Jiang, C., Séquaris, J.-M., Wacha, A., Bóta, A., Vereecken, H., and Klumpp, E. (2014). Effect of metal oxide on surface area and pore size of water-dispersible colloids from three german silt loam topsoils. *Geoderma*, 235-236:260–270.

Jones, S. and Cox, P. (2019). The Impact of a Simple Representation of Non-Structural Carbohydrates on the Simulated Response of Tropical Forests to Drought. *Biogeosciences*.

Jorda Guerra, H., Huber, K., Kunkel, A., Vanderborght, J., Javaux, M., Oberdörster, C., Hammel, K., and Schnepf, A. (2021). Mechanistic modeling of pesticide uptake with a 3d plant architecture model. *Environmental Science and Pollution Research*, 28.

Khare, D., Selzner, T., Leitner, D., Vanderborght, J., Vereecken, H., and Schnepf, A. (2022). Root system scale models significantly overestimate root water uptake at drying soil conditions. *Frontiers in Plant Science*, 13:798741.

Kirby, E. J. M. (1988). Analysis of leaf, stem and ear growth in wheat from terminal spikelet stage to anthesis. *Field Crops Research*, 18(2):127–140.

Koch, T., Glaser, D., Weishaupt, K., Ackermann, S., Beck, M., Becker, B., Burbulla, S., Class, H., Coltman, E., Emmert, S., Fetzer, T., Grüninger, C., Heck, K., Hommel, J., Kurz, T., Lipp, M., Mohammadi, F., Scherrer, S., Schneider, M., Seitz, G., Stadler, L., Utz, M., Weinhardt, F., and Flemisch, B. (2021). Dumux 3 – an open-source simulator for solving flow and transport problems in porous media with a focus on model coupling. *Computers & Mathematics with Applications*, 81:423–443. Development and Application of Open-source Software for Problems with Numerical PDEs.

Koch, T., Heck, K., Schröder, N., Class, H., and Helmig, R. (2018). A new simulation framework for soil–root interaction, evaporation, root growth, and solute transport. *Vadose Zone Journal*, 17:1–21.

Kramer, P. J. and Boyer, J. S. (1995). *Cell Water Relations*, chapter 3. Academic press.

Kravchenko, L. V., Strigul, N. S., and Shvytov, I. A. (2004). Mathematical simulation of the dynamics of interacting populations of rhizosphere microorganisms. *Microbiology*, 73(2):189–195.

Kuppe, C. W., Schnepf, A., von Lieres, E., Watt, M., and Postma, J. A. (2022). Rhizosphere models: their concepts and application to plant-soil ecosystems. *Plant and Soil*, 474(1):17–55.

Kutschera-Mitter, L., Barmicheva, K. M., and Sobotik, M. (1998). *The Importance of Root-Cap Mucilage for Plant And Soil*, pages 673–683. Springer Netherlands, Dordrecht.

Kuzyakov, Y. and Cheng, W. (2004). Photosynthesis controls of co2 efflux from maize rhizosphere. *Plant and Soil*, 263(1):85–99.

Kuzyakov, Y. and Razavi, B. S. (2019). Rhizosphere size and shape: Temporal dynamics and spatial stationarity. *Soil Biology and Biochemistry*, 135:343–360.

Lacointe, A. and Minchin, P. E. H. (2019). *A Mechanistic Model to Predict Distribution of Carbon Among Multiple Sinks*, pages 371–386. Springer New York, New York, NY.

Lacointe, A. and Minchin, P. P. (2008). Modelling phloem and xylem transport within a complex architecture. *Functional Plant Biology*, 35(10):772–780.

Laloy, E., Beerten, K., Vanacker, V., Christl, M., Rogiers, B., and Wouters, L. (2017). Bayesian inversion of a crn depth profile to infer quaternary erosion of the northwestern campine plateau (ne belgium). *Earth Surface Dynamics*, 5(3):331–345.

Laloy, E. and Vrugt, J. A. (2012). High-dimensional posterior exploration of hydrologic models using multiple-try dream(zs) and high-performance computing. *Water Resources Research*, 48(1).

Landl, M., Haupenthal, A., Leitner, D., Kroener, E., Vetterlein, D., Bol, R., Vereecken, H., Vanderborght, J., and Schnepf, A. (2021a). Simulating rhizodeposition patterns around growing and exuding root systems. *in silico Plants*, 3(2). diab028.

Landl, M., Phalempin, M., Schlüter, S., Vetterlein, D., Vanderborght, J., Kroener, E., and Schnepf, A. (2021b). Modeling the impact of rhizosphere bulk density and mucilage gradients on root water uptake. *Frontiers in Plant Science*, 3.

Landl, M., Schnepf, A., Vanderborght, J., Bengough, A., Bauke, S., Lobet, G., Bol, R., and Vereecken, H. (2018). Measuring root system traits of wheat in 2d images to parameterize 3d root architecture models. *Plant and Soil*, 425.

Landsberg, J. J. and Fowkes, N. D. (1978). Water Movement Through Plant Roots. *Annals of Botany*, 42(3):493–508.

Lattacher, A., Le Gall, S., Rothfuss, Y., Gao, C., Harings, M., Pagel, H., Giraud, M., Alahmad, S., Hickey, L. T., Kandeler, E., and Poll, C. (2025). Rooting for microbes: impact of root architecture on the microbial community and function in top- and subsoil. *Plant and Soil*.

le Gall, S., van Duschoten, D., Lattacher, A., Giraud, M., Harings, M., Deseano Diaz, P., Sircan, A., Poll, C., Lobet, G., Javaux, M., et al. (2024). Investigating the impact on water fluxes and physiological development of the combination of contrasted root wheat cultivars from isotopic analysis. In *EGU General Assembly Conference Abstracts*, page 15966.

Leitner, D., Klepsch, S., Bodner, G., and Schnepf, A. (2010). A dynamic root system growth model based on l-systems: Tropisms and coupling to nutrient uptake from soil. *Plant and soil*, 332:177–192.

Lemoine, R., La Camera, S., Atanassova, R., Dédaldéchamp, F., Allario, T., Pourtau, N., Bonnemain, J.-L., Laloi, M., Coutos-Thévenot, P., Maurousset, L., Faucher, M., Girousse, C., Lemonnier, P., Parrilla, J., and Durand, M. (2013). Source-to-sink transport of sugar and regulation by environmental factors. *Frontiers in Plant Science*, 4.

Leuning, R. (1995). A critical appraisal of a combined stomatal-photosynthesis model for c3 plants. *Plant, Cell and Environment*, 18(4):339–355.

Lobet, G., Pagès, L., and Draye, X. (2014a). A modeling approach to determine the importance of dynamic regulation of plant hydraulic conductivities on the water uptake dynamics in the soil-plant-atmosphere system. *Ecological Modelling*, 290:65–75. Special Issue of the 4th International Symposium on Plant Growth Modeling, Simulation, Visualization and Applications (PMA'12).

Lobet, G., Pagès, L., and Draye, X. (2014b). A modeling approach to determine the importance of dynamic regulation of plant hydraulic conductivities on the water uptake dynamics in the soil-plant-atmosphere system. *Ecological Modelling*, 290:65–75. Special Issue of the 4th International Symposium on Plant Growth Modeling, Simulation, Visualization and Applications (PMA'12).

Louarn, G. and Song, Y. (2020). Two decades of functional–structural plant modelling: now addressing fundamental questions in systems biology and predictive ecology. *Annals of Botany*, 126(4):501–509.

Lu, J., Stomph, T. J., Mi, G., Yuan, L., and Evers, J. (2024). Identifying and quantifying the contribution of maize plant traits to nitrogen uptake and use through plant modelling. *in silico Plants*, 6(2):diae018.

Lu, Z., Xie, K., Pan, Y., Ren, T., Lu, J., Wang, M., Shen, Q., and Guo, S. (2019). Potassium mediates coordination of leaf photosynthesis and hydraulic conductance by modifications of leaf anatomy. *Plant Cell and Environment*, 42.

Lynch, J. (2021). Harnessing root architecture to address global challenges. *The Plant Journal*, 109.

Lynch, J. M. and Whipps, J. M. (1990). Substrate flow in the rhizosphere. *Plant and Soil*, 129(1):1–10.

Lynch, J. P., Strock, C. F., Schneider, H. M., Sidhu, J. S., Ajmera, I., Galindo-Castañeda, T., Klein, S. P., and Hanlon, M. T. (2021). Root anatomy and soil resource capture. *Plant and Soil*, 466(1):21–63.

Ma, W., Tang, S., Dengzeng, Z., Zhang, D., Zhang, T., and Ma, X. (2022). Root exudates contribute to belowground ecosystem hotspots: A review. *Frontiers in Microbiology*, 13.

Mai, T. H., Schnepf, A., Vereecken, H., and Vanderborght, J. (2019). Continuum multiscale model of root water and nutrient uptake from soil with explicit consideration of the 3d root architecture and the rhizosphere gradients. *Plant and Soil*, 439(1):273–292.

Mammeri, Y. and Sellier, D. (2017). A surface model of nonlinear, non-steady-state phloem transport. *Mathematical Biosciences and Engineering*, 14:1055–1069.

Marshall-Colon, A., Long, S. P., Allen, D. K., Allen, G., Beard, D. A., Benes, B., von Caemmerer, S., Christensen, A. J., Cox, D. J., Hart, J. C., Hirst, P. M., Kannan, K., Katz, D. S., Lynch, J. P., Millar, A. J., Panneerselvam, B., Price,

N. D., Prusinkiewicz, P., Raila, D., Shekar, R. G., Shrivastava, S., Shukla, D., Srinivasan, V., Stitt, M., Turk, M. J., Voit, E. O., Wang, Y., Yin, X., and Zhu, X.-G. (2017). Crops in silico: Generating virtual crops using an integrative and multi-scale modeling platform. *Frontiers in Plant Science*, 8.

Masson, A. L., Caraglio, Y., Nicolini, E., Borianne, P., and Barczi, J.-F. (2021). Modelling the functional dependency between root and shoot compartments to predict the impact of the environment on the architecture of the whole plant: methodology for model fitting on simulated data using deep learning techniques. *in silico Plants*, 4(1):diab036.

Mathlouthi, M. and Reiser, P., editors (1995). *Rheological properties of sucrose solutions and suspensions*, pages 126–154. Springer US, Boston, MA.

McDougall, B. M. and Rovira, A. D. (1970). Sites of exudation of 14c-labelled compounds from wheat roots. *New Phytologist*, 69(4):999–1003.

McKay, M., Ross, J., Lawrence, N., Cramp, R., Beveridge, C., and Reid, J. (1995). Control of internode length in pisum sativum (further evidence for the involvement of indole-3-acetic acid). *Plant physiology*, 106:1521–1526.

Metzner, R., Chlubek, A., Bühler, J., Pflugfelder, D., Schurr, U., Huber, G., Koller, R., and Jahnke, S. (2022). In vivo imaging and quantification of carbon tracer dynamics in nodulated root systems of pea plants. *Plants*, 11(5).

Meunier, F., Draye, X., Vanderborght, J., Javaux, M., and Couvreur, V. (2017). A hybrid analytical-numerical method for solving water flow equations in root hydraulic architectures. *Applied Mathematical Modelling*, 52:648–663.

Michelena, V. A. and Boyer, J. S. (1982). Complete Turgor Maintenance at Low Water Potentials in the Elongating Region of Maize Leave. *Plant Physiology*, 69(5):1145–1149.

Millington, R. J. and Quirk, J. P. (1961). Permeability of porous solids. *Transactions of the Faraday Society*, 57(0):1200–1207.

Mnih, V., Badia, A. P., Mirza, M., Graves, A., Lillicrap, T. P., Harley, T., Silver, D., and Kavukcuoglu, K. (2016). Asynchronous methods for deep reinforcement learning.

Morandage, S., Laloy, E., Schnepf, A., Vereecken, H., and Vanderborght, J. (2021). Bayesian inference of root architectural model parameters from synthetic field data. *Plant and Soil*, 467(1):67–89.

Morandage, S., Schnepf, A., Leitner, D., Javaux, M., Vereecken, H., and Vanderborght, J. (2019). Parameter sensitivity analysis of a root system architecture model based on virtual field sampling. *Plant and Soil*, 438(1):101–126.

Morandage, S., Schnepf, A., Leitner, D., Javaux, M., Vereecken, H., and Vanderborght, J. (2022). Correction to: Parameter sensitivity analysis of a root system architecture model based on virtual field sampling. *Plant and Soil*, 477(1):849–850.

Moyano, F. E., Manzoni, S., and Chenu, C. (2013). Responses of soil heterotrophic respiration to moisture availability: An exploration of processes and models. *Soil Biology and Biochemistry*, 59:72–85.

Mualem, Y. (1976). A new model for predicting the hydraulic conductivity of unsaturated porous media. *Water Resources Research*, 12(3):513–522.

Muldoon, C. (2022). *Characterisation of Pea Axillary Bud–Anatomy and Ontogenetic Progression*. Master thesis, School of Biological Sciences.

Narsilio, G. A., Buzzi, O., Fityus, S., Yun, T. S., and Smith, D. W. (2009). Upscaling of navier–stokes equations in porous media: Theoretical, numerical and experimental approach. *Computers and Geotechnics*, 36(7):1200–1206.

Neumann, G. and Römheld, V. (2009). *The release of root exudates as affected by the plant's physiological status*, pages 23–54. CRC Press.

Nguyen, C. (2009). *Rhizodeposition of Organic C by Plant: Mechanisms and Controls*, volume 23, pages 97–123. Springer Netherlands.

Nikinimaa, E., Hölttä, T., Hari, P., Kolari, P., Mäkelä, A., Sevanto, S., and Vesala, T. (2013). Assimilate transport in phloem sets conditions for leaf gas exchange. *Plant, Cell & Environment*, 36(3):655–669.

Nikinmaa, E., Sievänen, R., and Hölttä, T. (2014). Dynamics of leaf gas exchange, xylem and phloem transport, water potential and carbohydrate concentration in a realistic 3-d model tree crown. *Annals of botany*, 114.

Nobel, P. S. (2009a). *Chapter 1 - Cells and Diffusion*, pages 2–43. Volume 1 of Nobel (2009e), fourth edition.

Nobel, P. S. (2009b). *Chapter 2 - Water*, pages 2–43. Volume 1 of Nobel (2009e), fourth edition.

Nobel, P. S. (2009c). *Chapter 8 - Leaves and Fluxes*, pages 364–437. Volume 1 of Nobel (2009e), fourth edition.

Nobel, P. S. (2009d). *Chapter 9 - Plants and Fluxes*, pages 438–505. Volume 1 of Nobel (2009e), fourth edition.

Nobel, P. S. (2009e). *Physicochemical and Environmental Plant Physiology (Fourth Edition)*, volume 1. Academic Press, San Diego, fourth edition.

Pagel, H., Kriesche, B., Uksa, M., Poll, C., Kandeler, E., Schmidt, V., and Streck, T. (2020). Spatial control of carbon dynamics in soil by microbial decomposer communities. *Frontiers in Environmental Science*, 8.

Personeni, E., Nguyen, C., Marchal, P., and Pagès, L. (2007). Experimental evaluation of an efflux–influx model of C exudation by individual apical root segments. *Journal of Experimental Botany*, 58(8):2091–2099.

Poeplau, C. and Don, A. (2023). A simple soil organic carbon level metric beyond the organic carbon to clay ratio. *Soil Use and Management*, 39.

Postma, J. A., Kuppe, C., Owen, M. R., Mellor, N., Griffiths, M., Bennett, M. J., Lynch, J. P., and Watt, M. (2017). Opensimroot: widening the scope and application of root architectural models. *New Phytologist*, 215(3):1274–1286.

Postma, J. A. and Lynch, J. P. (2012). Complementarity in root architecture for nutrient uptake in ancient maize/bean and maize/bean/squash polycultures. *Annals of Botany*, 110(2):521–534.

Pot, V., Portell, X., Otten, W., Garnier, P., Monga, O., and Baveye, P. C. (2022). Accounting for soil architecture and microbial dynamics in microscale models: Current practices in soil science and the path ahead. *European Journal of Soil Science*, 73(1).

Powell, O. M., Barbier, F., Voss-Fels, K. P., Beveridge, C., and Cooper, M. (2022). Investigations into the emergent properties of gene-to-phenotype networks across cycles of selection: a case study of shoot branching in plants. *in silico Plants*, 4(1):diac006.

Pradal, C., Dufour-Kowalski, S., Boudon, F., Fournier, C., and Godin, C. (2008). Openalea: a visual programming and component-based software platform for plant modelling. *Functional plant biology*, 35(10):751–760.

Prescott, C. E., Grayston, S. J., Helmisaari, H.-S., Kaštovská, E., Körner, C., Lambers, H., Meier, I. C., Millard, P., and Ostonen, I. (2020). Surplus carbon drives allocation and plant–soil interactions. *Trends in Ecology & Evolution*, 35(12):1110–1118.

Prusinkiewicz, P., Crawford, S., Smith, R. S., Ljung, K., Bennett, T., Ongaro, V., and Leyser, O. (2009). Control of bud activation by an auxin transport switch. *Proc Natl Acad Sci U S A*, 106(41):17431–6.

Prusinkiewicz, P. and Lindenmayer, A. (2012). *The algorithmic beauty of plants*. Springer Science & Business Media.

Puetz, T., Kiese, R., Wollschläger, U., Groh, J., Rupp, H., Zacharias, S., Priesack, E., Gerke, H., Gasche, R., Bens, O., Borg, E., Baessler, C., Kaiser, K., Herbrich, M., Munch, J., Sommer, M., Vogel, H.-J., Vanderborght, J., and Vereecken, H. (2016). Tereno-soilcan: a lysimeter-network in germany observing soil processes and plant diversity influenced by climate change. *Environmental Earth Sciences*, 74.

Putten, W., Bardgett, R., Bever, J., Bezemer, T., Casper, B., Fukami, T., Kardol, P., Klironomos, J., Kulmatiski, A., Schweitzer, J., Suding, K., Voorde, T., and Wardle, D. (2013). Plant-soil feedbacks: the past, the present and future challenges. *Journal of Ecology*, 101:265–276.

Přikryl, Z. and Vančura, V. (1980). Root exudates of plants. *Plant and Soil*, 57(1):69–83.

Qian, X., Liu, L., Croft, H., and Chen, J. (2021). Relationship between leaf maximum carboxylation rate and chlorophyll content preserved across 13 species. *Journal of Geophysical Research: Biogeosciences*, 126(2):e2020JG006076. e2020JG006076 2020JG006076.

Qiushuang, S., Yaping, W., Heng, T., Na, S., Xiansheng, Z., and Fang, W. (2021). Genetic, hormonal, and environmental control of tillering in wheat. *The Crop Journal*, 9(5):986–991.

R Core Team, . (2019). R: A language and environment for statistical computing.

Radcliffe, D. E. and Simunek, J. J. (2010). *Soil physics with HYDRUS: Modeling and applications*. CRC Press.

Radde, N. and Hütt, M.-T. (2016). The physics behind systems biology. *EPJ Nonlinear Biomedical Physics*, 4.

Rakshit, A., Singh, S., Abhilash, P. C., and Biswas, A., editors (2021). *Soil Science: Fundamentals to Recent Advances*. Springer, Singapore.

Rambla, C., Van Der Meer, S., Voss-Fels, K. P., Makhoul, M., Obermeier, C., Snowdon, R., Ober, E. S., Watt, M., Alahmad, S., and Hickey, L. T. (2022). A toolkit to rapidly modify root systems through single plant selection. *Plant Methods*, 18(1):2.

Rangarajan, H., Hadka, D., Reed, P., and Lynch, J. P. (2022). Multi-objective optimization of root phenotypes for nutrient capture using evolutionary algorithms. *The Plant Journal*, 111(1):38–53.

Rees, F., Barillot, R., Gauthier, M., Pagès, L., Pradal, C., and Andrieu, B. (2023a). Simulating rhizodeposition as a function of shoot and root interactions within a new 3d functional-structural plant model. In *9th International Conference on Functional-Structural Plant Models (FSPM)*.

Rees, F., Gauthier, M., Barillot, R., Richard-Molard, C., Jullien, A., Chenu, C., Pradal, C., and Andrieu, B. (2023b). Quantitative importance of various rhizodeposition processes: lessons from a mechanistic functional-structural root model. In *FSPM 2023 - 10th International Conference on Functional-Structural Plant Models*, Berlin, Germany.

Rees, F., Gérault, T., Gauthier, M., Barillot, R., Richard-Molard, C., Jullien, A., Chenu, C., Pradal, C., and Andrieu, B. (2025). Deciphering spatiotemporal patterns of rhizodeposition with a functional-structural root model: Rhizodep.

Rees, F., Richard-Molard, C., Chenu, C., and Andrieu, B. (2018). Modelling rhizodeposition with functional-structural plant models. In *10th International Society on Root Research Conference (ISRR-10)*.

Renton, M., Hanan, J., Ferguson, B. J., and Beveridge, C. A. (2012). Models of long-distance transport: how is carrier-dependent auxin transport regulated in the stem? *New Phytologist*, 194(3):704–715.

Renton, M., Hanan, J., Ferguson, B. J., and Beveridge, C. A. (2014). Corrigendum. *New Phytologist*, 203(2):705–705.

Reyes, F., Pallas, B., Pradal, C., Vaggi, F., Zanotelli, D., Tagliavini, M., Gianelle, D., and Costes, E. (2019). MuSCA: a multi-scale source–sink carbon allocation model to explore carbon allocation in plants. An application to static apple tree structures. *Annals of Botany*, 126(4):571–585.

Richards, L. A. (1931). Capillary conduction of liquids through porous mediums. *Physics*, 1(5):318–333.

Roose, T. and Fowler, A. (2004). A model for water uptake by plant roots. *Journal of Theoretical Biology*, 228(2):155–171.

Roose, T., Keyes, S., Daly, K., Carminati, A., Otten, W., Vetterlein, D., and Peth, S. (2016). Challenges in imaging and predictive modeling of rhizosphere processes. *Plant and Soil*, 407.

Rouet, S., Durand, J.-L., Leclercq, D., Bernicot, M.-H., Combes, D., Escobar-Gutiérrez, A., and Barillot, R. (2022). L-grassf: a functional–structural and phenological model of lolium perenne integrating plant morphogenesis and reproductive development. *in silico Plants*, 4(2):diac012.

Rougier, M. (1981). *Secretory Activity of the Root Cap*, volume 13/B of *Encyclopedia of Plant Physiology*, page 772. Springer, Berlin, Heidelberg.

Roux, X., Lacointe, A., Escobar-Gutiérrez, A., and Dizès, S. (2001). Carbon-based models of individual tree growth: A critical appraisal. *Annals of Forest Science*, 58:469–506.

Ruiz, S., Fletcher, D. M., Williams, K., and Roose, T. (2021). *Plant–Soil Modelling*, pages 127–198. John Wiley & Sons, Ltd.

Saliendra, N. Z. and Meinzer, F. C. (1991). Symplast Volume, Turgor, Stomatal Conductance and Growth in Relation to Osmotic and Elastic Adjustment in Droughted Sugarcane 1. *Journal of Experimental Botany*, 42(10):1251–1259.

Schindelin, J., Arganda-Carreras, I., Frise, E., Kaynig, V., Longair, M., Pietzsch, T., Preibisch, S., Rueden, C., Saalfeld, S., Schmid, B., Tinevez, J.-Y., White, D. J., Hartenstein, V., Eliceiri, K., Tomancak, P., and Cardona, A. (2012). Fiji: an open-source platform for biological-image analysis. *Nature Methods*, 9(7):676–682.

Schneider, A., Godin, C., Boudon, F., Demotes-Mainard, S., Sakr, S., and Bertheloot, J. (2019). Light regulation of axillary bud outgrowth along plant axes: An overview of the roles of sugars and hormones. *Frontiers in Plant Science*, 10.

Schneider, H., Postma, J., Kochs, J., Pflugfelder, D., Lynch, J., and Dusschoten, D. (2020). Spatio-temporal variation in water uptake in seminal and nodal root systems of barley plants grown in soil. *Frontiers in Plant Science*, 11:1247.

Schnepf, A., Black, C. K., Couvreur, V., Delory, B. M., Doussan, C., Heymans, A., Javaux, M., Khare, D., Koch, A., Koch, T., Kuppe, C. W., Landl, M., Leitner, D., Lobet, G., Meunier, F., Postma, J. A., Schäfer, E. D., Selzner, T., Vanderborght, J., and Vereecken, H. (2023). Collaborative benchmarking of functional-structural root architecture models: Quantitative comparison of simulated root water uptake. *in silico Plants*, 5(1):diad005.

Schnepf, A., Carminati, A., Ahmed, M. A., Ani, M., Benard, P., Bentz, J., Bonkowski, M., Knott, M., Diehl, D., Duddek, P., Kröner, E., Javaux, M., Landl, M., Lehndorff, E., Lippold, E., Lieu, A., Mueller, C. W., Oburger, E., Otten, W., Portell, X., Phalempin, M., Prechtel, A., Schulz, R., Vanderborght, J., and Vetterlein, D. (2022). Linking rhizosphere processes across scales: Opinion. *Plant and Soil*, 478(1):5–42.

Schnepf, A., Huber, K., Landl, M., Meunier, F., Petrich, L., and Schmidt, V. (2018a). Statistical characterization of the root system architecture model crootbox. *Vadose Zone Journal*, 17(1).

Schnepf, A., Leitner, D., Landl, M., Khare, D., Heck, A., Giraud, M., Selzner, T., Helmrich, D., Lobet, G., Zhou, X., Bouvri, A., Ullah, S., Feron, T., Heymans, A., and Koch, T. (2025a). Cplantbox, branch giraud2025_carbonstabilisation. Zenodo [code].

Schnepf, A., Leitner, D., Landl, M., Khare, D., Heck, A., Giraud, M., Selzner, T., Helmrich, D., Lobet, G., Zhou, X., Bouvri, A., Ullah, S., Feron, T., Heymans, A., and Koch, T. (2025b). dumux-rosi, branch giraud2025_carbonstabilisation. Zenodo [code].

Schnepf, A., Leitner, D., Landl, M., Lobet, G., Mai, T. H., Morandage, S., Sheng, C., Zörner, M., Vanderborght, J., and Vereecken, H. (2018b). CRootBox: a structural–functional modelling framework for root systems. *Annals of Botany*, 121(5):1033–1053.

Schopfer, P. (2006). Biomechanics of plant growth. *American journal of botany*, 93:1415–25.

Schröder, N., Lazarovitch, N., Vanderborght, J., Vereecken, H., and Javaux, M. (2014). Linking transpiration reduction to rhizosphere salinity using a 3d coupled soil-plant model. *Plant and Soil*, 377(1):277–293.

Schwartz, N., Carminati, A., and Javaux, M. (2016). The impact of mucilage on root water uptake—a numerical study. *Water Resources Research*, 52(1):264–277.

Seki, M., Feugier, F., Song, X.-J., Ashikari, M., Nakamura, H., Ishiyama, K., Yamaya, T., Inari-Ikeda, M., Kitano, H., and Satake, A. (2014). A mathematical model of phloem sucrose transport as a new tool for designing rice panicle structure for high grain yield. *Plant and Cell Physiology*, 56.

Seleznyova, A. and Hanan, J. (2017). Carbon transport revisited: A novel approach for solving quasi-stationary carbon transport in a system with michaelis-menten sources and sinks. *Acta Horticulturae*, 1160:269–276.

Seleznyova, A. N. and Hanan, J. (2018). Mechanistic modelling of coupled phloem/xylem transport for L-systems: combining analytical and computational methods. *Annals of Botany*, 121(5):991–1003.

Sellier, D. and Harrington, J. (2012). Phloem sap flow and carbohydrate transport in vascular plants: A generic surface model. In *Plant Growth Modeling, Simulation, Visualization and Applications (PMA)*, pages 332–339.

Sevanto, S., Hoelttae, T., and Holbrook, N. M. (2011). Effects of the hydraulic coupling between xylem and phloem on diurnal phloem diameter variation. *Plant Cell Environ*, 34(4):690–703. 1365-3040 Sevanto, Sanna Hoelttae, Teemu Holbrook, N Michele Journal Article Research Support, Non-U.S. Gov't United States 2011/01/19 Plant Cell Environ. 2011 Apr;34(4):690-703. doi: 10.1111/j.1365-3040.2011.02275.x. Epub 2011 Feb 18.

Sievänen, R., Godin, C., Dejong, T., and Nikinmaa, E. (2014). Functional-structural plant models: A growing paradigm for plant studies. *Annals of botany*, 114:599–603.

Silva, L. and Lambers, H. (2021a). Soil-plant-atmosphere interactions: structure, function, and predictive scaling for climate change mitigation. *Plant and Soil*, 461.

Silva, L. C. R. and Lambers, H. (2021b). Soil-plant-atmosphere interactions: structure, function, and predictive scaling for climate change mitigation. *Plant and Soil*, 461(1):5–27.

Sircan, A. K., Streck, T., Schnepf, A., Giraud, M., Lattacher, A., Kandeler, E., Poll, C., and Pagel, H. (2024). Trait-based modeling of microbial interactions and carbon turnover in the rhizosphere. *Social Science Research Network (SSRN)*.

Soualiou, S., Wang, Z., Sun, W., de Reffye, P., Collins, B., Louarn, G., and Song, Y. (2021). Functional–structural plant models mission in advancing crop science: Opportunities and prospects. *Frontiers in Plant Science*, 12.

Stafstrom, J., Ripley, B., Devitt, M., and Drake, B. (1998). Dormancy-associated gene expression in pea axillary buds. *Planta*, 205:547–552.

Stanfield, R. C. and Bartlett, M. K. (2022). Coordination between phloem loading and structure maintains carbon transport under drought. *Frontiers in Plant Science*, 13.

Stepanova, A. N. and Alonso, J. M. (2016). Auxin catabolism unplugged: Role of iaa oxidation in auxin homeostasis. *Proceedings of the National Academy of Sciences*, 113(39):10742–10744.

Stock, M., Pieters, O., De Swaef, T., and wyffels, F. (2024). Plant science in the age of simulation intelligence. *Frontiers in Plant Science*, 14.

Succi, S. (2015). Lecture 10: Finite volumes.

Swart, N. C., Cole, J. N., Kharin, V. V., Lazare, M., Scinocca, J. F., Gillett, N. P., Anstey, J., Arora, V., Christian, J. R., Jiao, Y., Lee, W. G., Majaess, F., Saenko, O. A., Seiler, C., Seinen, C., Shao, A., Solheim, L., von Salzen, K., Yang, D., Winter, B., and Sigmond, M. (2019). Cccma canesm5 model output prepared for cmip6 cmip.

Sze, T.-K., Liu, J., and Dutta, P. (2013). Numerical modeling of flow through phloem considering active loading. *Journal of Fluids Engineering*, 136:021206.

Takahashi, H. and Pradal, C. (2021). Root phenotyping: Important and minimum information required for root modeling in crop plants. *Breeding Science*, 71.

Tardieu, F., Granato, I., Oosterom, E., Parent, B., and Hammer, G. (2020). Are crop and detailed physiological models equally 'mechanistic' for predicting the genetic variability of whole-plant behaviour? the nexus between mechanisms and adaptive strategies. *in silico Plants*, 2.

Thompson, M. and Holbrook, N. (2003). Scaling phloem transport: Water potential equilibrium and osmoregulatory flow. *Plant, Cell & Environment*, 26:1561 – 1577.

Thompson, M. V. (2006). Phloem: the long and the short of it. *Trends in Plant Science*, 11(1):26–32.

Thornley, J. H. M. (2011). Plant growth and respiration re-visited: maintenance respiration defined – it is an emergent property of, not a separate process within, the system – and why the respiration : photosynthesis ratio is conservative. *Annals of Botany*, 108(7):1365–1380.

Thornley, J. H. M. and Cannell, M. G. R. (1997). Temperate Grassland Responses to Climate Change: an Analysis using the Hurley Pasture Model. *Annals of Botany*, 80(2):205–221.

Thornley, J. H. M. and Cannell, M. G. R. (2000). Modelling the components of plant respiration: Representation and realism. *Annals of Botany*, 85(1):55–67.

Thorpe, M., Lacointe, A., and Minchin, P. (2011). Modelling phloem transport within a pruned dwarf bean: A 2-source-3-sink system. *Functional Plant Biology*, 38:127–138.

Tixier, A., Forest, M., Prudent, M., Durey, V., Zwieniecki, M., and Barnard, R. L. (2023). Root exudation of carbon and nitrogen compounds varies over the day–night cycle in pea: The role of diurnal changes in internal pools. *Plant, Cell & Environment*, 46(3):962–974.

Trofymow, J. A., Coleman, D. C., and Cambardella, C. (1987). Rates of rhizodeposition and ammonium depletion in the rhizosphere of axenic oat roots. *Plant and Soil*, 97(3):333–344.

Tshikunde, N. M., Odindo, A., Shimelis, H., and Mashilo, J. (2018). Leaf gas exchange and water-use efficiency of dry-land wheat genotypes under water stressed and non-stressed conditions. *Acta Agriculturae Scandinavica, Section B — Soil & Plant Science*, 68(8):738–748.

Tuzet, A., Perrier, A., and Leuning, R. (2003). A coupled model of stomatal conductance, photosynthesis and transpiration. *Plant, Cell and Environment*, 26(7):1097–1116.

Uys, L., Hofmeyr, J.-H. S., and Rohwer, J. M. (2021). Coupling kinetic models and advection–diffusion equations. 1. Framework development and application to sucrose translocation and metabolism in sugarcane. *in silico Plants*, 3(1).

van Berkel, K., de Boer, R. J., Scheres, B., and ten Tusscher, K. (2013). Polar auxin transport: models and mechanisms. *Development*, 140(11):2253–68. 1477-9129 van Berkel, Klaartje de Boer, Rob J Scheres, Ben ten Tusscher, Kirsten Journal Article Research Support, Non-U.S. Gov't England 2013/05/16 Development. 2013 Jun;140(11):2253-68. doi: 10.1242/dev.079111.

van Dusschoten, D., Kochs, J., Kuppe, C. W., Sydoruk, V. A., Couvreur, V., Pflugfelder, D., and Postma, J. A. (2020). Spatially Resolved Root Water Uptake Determination Using a Precise Soil Water Sensor. *Plant Physiology*, 184(3):1221–1235.

van Genuchten, M. T. (1980). A closed-form equation for predicting the hydraulic conductivity of unsaturated soils. *Soil Science Society of America Journal*, 44(5):892–898.

Van Rossum, G. and Drake Jr, F. L. (1995). *Python tutorial*. Centrum voor Wiskunde en Informatica Amsterdam, The Netherlands.

Vanderborght, J., Leitner, D., Schnepf, A., Couvreur, V., Vereecken, H., and Javaux, M. (2024). Combining root and soil hydraulics in macroscopic representations of root water uptake. *Vadose Zone Journal*, 23(3):e20273.

Verbančič, J., Lunn, J. E., Stitt, M., and Persson, S. (2018). Carbon supply and the regulation of cell wall synthesis. *Molecular Plant*, 11(1):75–94.

Verdouw, C., Tekinerdogan, B., Beulens, A., and Wolfert, S. (2021). Digital twins in smart farming. *Agricultural Systems*, 189:103046.

Vos, J., Evers, J. B., Buck-Sorlin, G. H., Andrieu, B., Chelle, M., and de Visser, P. H. B. (2009). Functional–structural plant modelling: a new versatile tool in crop science. *Journal of Experimental Botany*, 61(8):2101–2115.

Vos, J., Marcelis, L., and Evers, J. (2007). Functional-structural plant modelling in crop production. In *Functional-structural plant modelling in crop production*, pages 1–12. Springer.

Wang, G., Li, W., Wang, K., and Huang, W. (2021). Uncertainty quantification of the soil moisture response functions for microbial dormancy and resuscitation. *Soil Biology and Biochemistry*, 160:108337.

Wang, J., Bogena, H. R., Vereecken, H., and Brüggemann, N. (2018). Characterizing redox potential effects on greenhouse gas emissions induced by water-level changes. *Vadose Zone Journal*, 17(1).

Wang, X., Hua, J., Kang, M., Wang, H., and Reffye, P. (2024). Functional–structural plant model "greenlab": A state-of-the-art review. *Plant Phenomics*, 6:0118.

Wass, T., Fortuna, N., Auzmendi, I., Hanan, J., and Beveridge, C. (2023). Computational modelling approach to understanding shoot architecture including plant branching and flowering. In *7th International Plant Dormancy Symposium*.

Wiesenbauer, J., König, A., Gorka, S., Marchand, L., Nunan, N., Kitzler, B., Inselsbacher, E., and Kaiser, C. (2024). A pulse of simulated root exudation alters the composition and temporal dynamics of microbial metabolites in its immediate vicinity. *Soil Biology and Biochemistry*, 189.

Windt, C. W., Vergeldt, F. J., De Jager, P. A., and Van As, H. (2006). Mri of long-distance water transport: a comparison of the phloem and xylem flow characteristics and dynamics in poplar, castor bean, tomato and tobacco. *Plant, Cell & Environment*, 29(9):1715–1729.

Zhang, W., Wang, G., Han, J., Li, F., Zhang, Q., and Doonan, J. (2018). A functional-structural model for alfalfa that accurately integrates shoot and root growth and development. In *2018 6th International Symposium on Plant Growth Modeling, Simulation, Visualization and Applications (PMA)*, pages 134–140.

Zhou, X.-R., Schnepf, A., Vanderborght, J., Leitner, D., Lacointe, A., Vereecken, H., and Lobet, G. (2020). CPlantBox, a whole-plant modelling framework for the simulation of water- and carbon-related processes. *in silico Plants*, 2(1). diaa001.

Zhu, J., Gou, F., Rossouw, G., Begum, F., Henke, M., Johnson, E., Holzapfel, B., Field, S., and Seleznyova, A. (2021). Simulating organ biomass variability and carbohydrate distribution in perennial fruit crops: a comparison between the common assimilate pool and phloem carbohydrate transport models. *in silico Plants*, 3(2):diab024.

Zubairova, U., Nikolaev, S., Penenko, A., Podkolodnyy, N., Golushko, S., Afonnikov, D., and Kolchanov, N. (2016). Mechanical behavior of cells within a cell-based model of wheat leaf growth. *Frontiers in Plant Science*, 7.

Appendix A: Further development of an FSPM

A.1 Water potentials, conductivities, and conductances

We evaluate the water potentials in four domains: the soil, the xylem, the sieve tubes, and the atmosphere, respectively denoted with the subscripts *soil*, *x*, *st*, and *atm*. For clarity, we define here the total potential ψ_t and its components in each of those domains. We define ψ_t as

$$\psi_t \quad = \quad \frac{\eta - \eta_{ref}}{\bar{V}} \quad = \quad \psi_p + \psi_g + \psi_o,$$

where η and η_{ref} are the chemical potentials of the considered and reference water respectively, ψ_p is the pressure potential, ψ_g is the gravitational potential and ψ_o is the osmotic potential (Nobel, 2009b). ψ_p includes all the potentials except the osmotic and gravitational ones and can be positive (absolute ψ_p $>$ absolute $\psi_{p,ref}$) or negative (absolute ψ_p $<$ absolute $\psi_{p,ref}$). In unsaturated soils,

$$\psi_{p,soil} = \psi_{m,soil} + \psi_{a,soil} < 0$$

with ψ_m the matric potential and ψ_a the pneumatic potential. The pneumatic potential corresponds to the over-pressure of the air: $\psi_a = P_{atm} - P_{soil\ air}$. P_{atm} (hPa) is the atmospheric pressure at ground level, dependent on the pressure of all the gases in the Earth's atmosphere. The reference water (denoted with the subscripts *ref*) is pure, at ground level (z_{ref} $=$ 0), and the hydrostatic potential equals the atmospheric pressure. In the plant, $\psi_p = \psi_h$, with ψ_h the hydrostatic potential. ψ_p is generally positive in the plant tissues and is also called the turgor pressure. For specific cells, like the xylem $\psi_{p,x}$ is usually under tension. All the water potentials are given in hPa (corresponding to $100 \times Joule/m^3$).

In this paper, the flow of fluids considered can be computed with either the lateral conductivity ($k_{lat,Y}$, in $L\ P^{-1}T^{-1}$, here in $cm\ hPa^{-1}\ d^{-1}$), or the intrinsic axial conductance ($K_{ax,Y}$, in $L^4P^{-1}T^{-1}$, here in $cm^4\ hPa^{-1}\ d^{-1}$) (Meunier et al., 2017). *lat* stands for lateral and *ax* for axial. Y is a stand in for the denomination of the flow channel (compartment, tissue, membrane...) considered.
For the photosynthesis module, we use the stomatal conductance in molar units ($g_{Z,Y}$, in $N\ L^{-2}T^{-1}$, here in $mmol\ cm^{-2}\ d^{-1}$), with Z standing in for either *h2o* or *co2*.
For the soil module, the hydraulic conductivity (κ_{soil}), units are in $cm^2\ hPa^{-1}\ d^{-1}$ ($L^2\ P^{-1}T^{-1}$) given the definition of the soil water potential.

A.2 Computation of the plant shape variable

An organ's length is equal to the sum of the length of its segments: $L_{seg} \leq L_{org}$, with L in cm. Root and stem organs are defined as cylinders, which shapes are computed from their lengths and radii (a in cm). In the current CPlantBox implementation, a is constant for all segments of the organ: $a_{seg} = a_{org}$.
Leaf organs are defined as cuboids which shapes are computed from their thicknesses (a in cm) and widths (w in cm). The leaf organs are separated in two regions: the sheath and the blade. a and w of the sheath can be different to that of the blade.
The seed is represented by one node linking the main stem (and tillers) with the 0-order roots. The sieve tubes and xylem tissues are defined as cylinders. Each organ can have one or more sieve tube or xylem cylinders. Finally, the shape of the mesophyll is assumed to be equal to that of the leaf blade it is in (for instance with v, the volume in cm^3: $v_{meso} = v_{blade}$).

A_{cross} (cross-sectional area, cm^2), v (volume, cm^3), and p (perimeter of the exchange surface, cm) of all the organs, segments, sieve tubes, and xylem tissues are calculated thus:

$$v_Y = \begin{cases} v_{sheath} + v_{blade} & \text{for leaf organs} \\ A_{cross,Y} \times L_Y & \text{else} \end{cases} \tag{A-1}$$

$$A_{cross,Y} = \sum_i^{n_\mathcal{X}} A_{cross,Y,i} \tag{A-2}$$

$$p_Y = \sum_i^{n_\mathcal{X}} p_{Y,i} \tag{A-3}$$

$$A_{cross,Y,i} = \begin{cases} w_Y a_Y & \text{for leaf blades and sheaths} \\ \pi a_{Y,i}^2 & \text{else} \end{cases} \tag{A-4}$$

$$p_{Y,i} = \begin{cases} 2w_i & \text{for leaf blades and sheaths} \\ 2\pi a_{Y,i} & \text{else} \end{cases} \tag{A-5}$$

with Y as a stand-in for either *st* (sieve tube tissues), x (xylem tissues), *seg* (segment), *org* (organ), *sheath* (leaf sheath), and *blade* (leaf blade). i represent one cylinder of the tissue type in the studied segment. n_Y corresponds to the number of tissue unit of segment (or vessel) per cross section of segment. Thus $n_{seg} = 1$. In our parameterised model, n_{st} (resp. n_x) corresponds to the number of vascular bundles per cross-section times the number of sieve (resp. xylem) tubes of a specific radius per bundle. As p corresponds to the perimeter of the lateral exchange surface, we only take into account the width of the leaf and not its thickness, as, for our virtual plant, the stomatas are located on the upper and lower side of the leaf blade.

A.3 Photosynthesis: auxiliary equations

We present below complementary equations that are used in the photosynthesis module.

A.3-1 Raoult's law

The area-specific water vapor flow rate $j_{lat,ox-atm}$ ($cm^3\ cm^{-2}\ d^{-1}$) can be driven by the gradient of water vapor pressure (ea in hPa) or of total water potential (ψ_t in hPa). We convert ψ_t to ea using Raoult's law (Nobel, 2009b):

$$\psi_{t,Y} = \frac{RT_Y \rho_{h2o}}{Mm_{h2o}} ln(\frac{ea_Y}{es(T_Y)}) + \psi_{g,Y} \tag{A-6}$$

with, for the domain Y, Mm_{h2o} ($kg\ mmol^{-1}$) and ρ_{h2o} ($kg\ cm^{-3}$) respectively the water molar mass and density, $es(T_Y)$ (hPa) the saturation vapor pressure at temperature T_Y (K), the ideal gas constant R ($cm^3\ hPa\ K^{-1} mmol^{-1}$), and the gravitational potential $\psi_{g,x}$ (hPa).

A.3-2 Plant functions

Several photosynthesis variables are dependent on the temperature. This temperature dependence can be described by the Arrhenius and the temperature inhibition functions (Bonan, 2019c): The Arrhenius function (Bonan, 2019c):

$$\text{Arrhenius}(T_{seg}, E_{a,X}) = exp\left(\frac{E_{a,X}}{0.1 \times RT_{25}}(1 - \frac{T_{25}}{T_{seg}})\right) \tag{A-7}$$

$$TempInhib(T_{seg}, E_{d,X}) = \frac{1}{1 + exp\left(\frac{ST_{seg} - E_{d,X}}{0.1 \times RT_{seg}}\right)} \tag{A-8}$$

with $E_{a,j}$ and $E_{d,j}$ ($mJ\ mmol^{-1}$), respectively the activation and deactivation energy. S ($mJ\ mmol^{-1}\ K^{-1}$) is an entropy term. The factor 0.1 is used to go from $hPa\ cm^3\ K^{-1}\ mmol^{-1}$ to $mJ\ K^{-1}\ mmol^{-1}$.

M_{co2}, M_{o2} and $\Gamma*$ can be calculated with the following equation:

$$X_x = X_x^{25} \times Arrhenius(T_{seg}, E_{a,x}) \tag{A-9}$$

where $E_{a,x}$ is the activation energy for X_x (either M_{co2}, M_{o2}, R_d, or $\Gamma*$) in $mJ\ mmol^{-1}$, and X_x^{25} is the value of X_x for $T = 298.15\ K$.

A.3-3 Air conductance

We separate the area outside the leaf in three zones: the laminar layer directly outside the leaf (boundary layer), the turbulent layer between the leaf boundary layer and the canopy induced zero displacement height, the turbulent layer between the canopy induced zero displacement height and the point of measurement. The effect of each layer is represented by a resistivity to the water vapor flow, respectively: $Res_{h2o,bl}$, $Res_{h2o,canopy}$, and $Res_{h2o,atm}$, all in $d\ cm^{-1}$.

$Res_{h2o,atm}$ is computed according to Allen et al. (1998):

$$Res_{atm,h2o} = \frac{ln\left[\frac{z_m - \frac{2}{3}h_p}{0.123 \times h_p}\right] \times ln\left[\frac{z_m - \frac{2}{3}h_p}{0.1 \times h_p}\right]}{k_{Karman}^2 u_z} \tag{A-10}$$

with z_m (cm) height of wind and humidity measurements, h_p (cm) the height of the highest plant node, k_{Karman} $(0.41\ -)$ the von Karman's constant, u_z $(cm\ d^{-1})$ wind speed at height z_m. $\frac{2}{3}h_p$ is the canopy induced zero displacement height.

We set the mean canopy resistance as (Nobel, 2009d):

$$Res_{h2o,canopy} = \frac{\frac{1}{3}h_p}{k_{eddy,canopy}} \tag{A-11}$$

with $\frac{1}{3}h_p$ the mean length of the canopy turbulent layer between the leaf boundary layer and the canopy induced zero displacement height, $k_{eddy,canopy}$ $(8.64e8\ cm^2 d^{-1})$ the mean eddy covariance value, corresponding to the value given by Nobel (2009d) for the space 1 m below the top of a maize canopy. And, assuming a constant leaf boundary layer thickness of 0.03 cm, we obtain

$$Res_{h2o,bl} = \frac{0.03}{Diff_{h2o}} = 1.5e-6$$

with $Diff_{h2o} \approx 2e3\ cm^2 d^{-1}$, the diffusion coefficient of water vapor in air (Nobel, 2009c).
We can then convert the physical conductances ($\frac{1}{Res_{h2o,Y}}$ in $d\ cm^1\ cm^{-2}$) in molar conductances ($g_{h2o,Y}$ in $mmol\ cm^{-2}\ d^{-1}$) (Nobel, 2009c, Tuzet et al., 2003):

$$g_{h2o,Y} = \frac{P_{atm}}{Res_{h2o,Y} \times RT_Y} \tag{A-12}$$

A.4 Assumption of local water equilibrium

Thompson and Holbrook (2003) presented a mathematical model to justify the assumption of water equilibrium between the xylem and the phloem. Briefly, when their $\hat{R}\hat{F}$ coefficient is above unity, equilibrium can be assumed.
In their model, they looked at a sieve tube with a constant radius and viscosity, where the loading and unloading of sucrose occurred at the boundaries. Those simplifications can be applied to our model when focusing on the segment level. Indeed, the (un)loading of sucrose occurs in the nodes at the segments' extremities. The $\hat{R}\hat{F}$ coefficient can be computed thus:

$$\hat{R}\hat{F}_{ij} = \frac{p_{st}}{A_{cross,st}} \times R\ T_{seg}\ s_{st,\cdot} \times \frac{l_{seg}}{j_{ij}} \times k_{lat,st-x,w} \tag{A-13}$$

$$s_{st,\cdot} = \begin{cases} s_{st,j} & \text{if} \quad j_{ij} \geq 0 \\ s_{st,i} & \text{else} \end{cases} \tag{A-14}$$

with $k_{lat,st-x,w}$ the water permeability of the membrane linking the xylem and phloem tissues.
In order to have $\hat{R}\hat{F} \geq 1$ we had to adapt our parameter set to have $Fu = 0\ mmol\ ml^{-1}\ d^{-1}$ (no usage of carbon) when $s_{st} < 0.4\ mmol\ ml^{-1}$. This fits with observations for wheat plant where s_{st} was observed to be above this value (Thompson and Holbrook, 2003). For our four simulations, after a burn-in time of 3 hours, we needed to have an area-specific conductance between the xylem and the phloem $k_{lat,st-x,w}$ at least equal to $1.1e-4\ cm\ d^{-1}\ hPa^{-1}$ so that $\hat{R}\hat{F} \geq 1$ for all segments. This value was found to be plausible for wheat plants (Boyer and Kramer, 1995). This confirms the analysis of Thompson and Holbrook (2003): in their study, they found this simplification to be acceptable for the transport system of most plants, including wheat.

Likewise, in the study of Lacointe and Minchin (2008) for $s_{st} > 0.15\ mmol\ cm^{-3}$, decreasing the permeability of the membrane between the xylem and phloem had no effect on the outputs.
The assumption of local water equlibrium between xylem and phloem was also tested in experimental studies and found to be acceptable (Cabrita, 2011, Sevanto et al., 2011, Section 2.2.1.5).

A.5 Calibration and notations

A.5-1 Experiments for direct calibration

A.5-1-1 Plant growth conditions

The wheat phenotype studied in this experiment (UQR15) was obtained from the Hickey lab (University of Queensland, Australia) (Rambla et al., 2022). 13 PVC columns (diameter = 8 cm, height = 45 cm) were filled with silty loam soil from

one testing site of the Research Center Jülich, located in Selhausen (50.8659 N, 6.4471 E). The columns received two seeds each (equivalent to a sowing density of 400 seeds/m^2) and were afterwards installed in a climate chamber (20°C day, 18°C night, 50% RH, 1000 $\mu mol\ m^{-2}s^{-1}$ of PAR from 6am to 8pm). The mean initial soil gravimetric water content (θ_{soil}) was of 0.40 $cm^3\ cm^{-3}$. Water was added twice a week to keep the θ_{soil} value between 0.30 $cm^3\ cm^{-3}$ to 0.44 $cm^3\ cm^{-3}$. Fertiliser (7% Nitrate, 19% Ammonium) was added at 6 and 34 days after sowing (stage Z11 and Z25 of the Zadok's growth scale, respectively) in liquid solution supplied at a rate of 3 $kg\ m^{-2}$.

A.5-1-2 Non-destructive measurements

The plant development was evaluated two to three times a week via the following measurements: number of tillers and leaves, plant stage (on the Zadok scale), and length and width of the leaves' blade. The chlorophyll content of the lowest and second highest leaf of each plant tiller was also recorded using a chlorophyll meter (SPAD502, Konika Minolta, Bremen, Germany). The mean θ_{soil} value for each column was measured by weighting the column on a scale.

A.5-1-3 Soil Water Profiler

In order to measure the transpiration rate, we used the Soil Water Profiler (SWaP) developed by van Dusschoten et al. (2020). At 4, 5, and 6 weeks after sowing (stages Z24, Z25, and Z33, respectively) four of the soil columns were randomly selected. The measurements lasted 36 hours (two day- and one night-periods). The sensor temporal and spatial (vertical) resolutions were 15 min and 1cm, respectively. The day-light intensity alternated between high and low irradiation level every 4 hours. The variation in total θ_{soil} allowed us to measure the root water uptake rate (assumed equal to the transpiration) at those irradiation levels. The soil surface was covered and the evaporation was thus assumed to be negligible. The same transpiration measurements were done while progressively increasing the irradiation level in order to measure the light saturation point.

A.5-1-4 Destructive measurement

Following the SWaP measurements, we extracted the root systems from the soil. The fresh weight of the roots, stems and leaves was measured. The roots were then stored in 30% Ethanol solutions. The fresh weight of the root, stems and leaf was measured via a weighing scale (precision = 1 mg; Kern 572-30, Kern & Sohn GmbH, Balingen, Germany). The stems and leaves were stored in a freezer at $-20°C$. Afterwards, the leaves were scanned (Canon, 4 Krefeld, Germany) for analysis with ImageJ (Schindelin et al., 2012) to measure the leaf blade and sheath surface together with the position and number of the nodes along the stems. The volume of the leaves and stems were obtained by immersing them in a graduated cylinder containing water and measuring the variation of the water level. Lateral

cuts of the leaf blades (at 5cm to the leaf sheath, on the second leaf of the tiller), stems (at 1cm above the soil, when the stems were present) and roots (at a 9-18cm depth) were done with a cryomicrotome (CM 3050S; Leica Microsystems GmbH, Wetzlar, Germany). The images were analysed with ImageJ to measure the number of vascular bundles and the average shape of the xylem and phloem tissues in each bundle.

A.5-2 Input parameters and other variables and parameters

The tables below present the input parameters and variables of the model. The source used for the parameter estimation can be either [a] direct calibration—direct experimental measurements (see section above), [b] indirect calibration—value set to fit with objective outputs, [c] from the literature (copying the value or recomputing it from the dataset of the publication), in which case the reference is given. The shoot shape parameters were obtained from the experiments described above while the root shape parameters (except for the phloem and xylem tissues) were taken from Bingham and Wu (2011), as adapted by Schnepf et al. (2018b).

Table A.1: Soil parameters.

Symbol	Description	Values and units	Source
$\theta_{lat,soil}$	residual water content	$0.08\,\mathrm{cm^3 cm^{-3}}$	illustrative
$\theta_{s,soil}$	saturated water content	$0.43\,\mathrm{cm^3 cm^{-3}}$	illustrative
α_{soil}	parameter related to the inverse of the air entry suction	$0.04\,\mathrm{hPa^{-1}}$	direct calibration
n_{soil}	measure of the pore-size distribution	$1.503\,-$	illustrative
$\kappa_{s,soil}$	soil conductivity at saturation	$1.6\,\mathrm{cm^2\,hPa^{-1}\,d^{-1}}$	illustrative

Table A.2: Input parameters of the structural CPlantBox modules: Notation, symbols, values(std) and units

Symbol	Description	Values and units	Source	Remarks
		General		
delayB	time delay between the basal root emergence	3 d	direct	
delayTi	time delay between tiller emergence	10 d	direct	
firstB	emergence of first basal root	1 d	direct	
firstTi	emergence of first tiller	6 d	direct	
maxB	maximal number of basal roots	15	direct	
maxTi	maximal number of tiller	5	direct	
seedPos	Coordinate of the seed	(0, 0, −0.3) *cm*	direct	
delayDefinition	method used to define the growth delay of the laterals	time-based (use time constant defined per organ type)		could also be distance based (computed from l_{apical}, $l_{internodal}$, and r)
		Leaves		
a	thickness	0.03 cm	direct	
bendingN	bending strength	18	illustrative	number of trials for bending computation
bendingS	change in growth direction per *cm* of organ length	$0.02\,\mathrm{cm^{-1}}$	illustrative	
dx_{max}	maximal segment length	2 cm		
dx_{min}	minimal segment length	1 cm		
gf	growth function	negative exponential		
$l_{max,blade}$	maximal blade length	35 cm	direct	
$l_{max,sheath}$	maximal sheath length	8 cm	direct	

pseudoStem	whether to implement pseudostem growth	True		The leaf sheaths grow upward, bending starts at the blade
r	initial growth rate used during the empirical growth period	$4\,\mathrm{cm\,d^{-1}}$	direct	used during the empirical growth period
shapeType	method to represent surface of the leaf	ribon (use mean w_{blade} and w_{sheath})		could also define precisely the distance between the leaf border and the mid-vein along the leaf's length
theta	branching angle from parent organ	0.2 rad	illustrative	
w_{blade}	blade width	0.9 cm	direct	
w_{sheath}	sheath width	0.35 cm	direct	
		main shoot and tillers		
a	radius	0.03 cm	direct	
bendingN	bending strength	1	illustrative	number of trials for bending computation
bendingS	change in growth direction per *cm* of organ length	$0.01\,\mathrm{cm^{-1}}$	illustrative	
delayNGEnd	time span between growth stop and stem elongation start	24 d	direct	
delayNGStart	time span between stem create and growth stop	4 d	direct	
dx_{max}	maximal segment length	2 cm	direct	
dx_{min}	minimal segment length	1 cm	direct	
gf	growth function	negative exponential	direct	
l_{apical}	maximal apical length	0 cm	direct	
l_{basal}	maximal basal length	1 cm	direct	
$l_{internodal}$	maximal internodal length	8.75 cm	direct	
l_{max}	maximal length	35 cm	direct	
latDelay	phyllochron	10 d	direct	
nodalGrowth	implement stem elongation?	True		
r	initial growth rate used during the empirical growth period	$4\,\mathrm{cm\,d^{-1}}$	direct	used during the empirical growth period
theta	branching angle from parent organ	0.2 rad	illustrative	
		root		
primary and basal root				

a	radius	0.05 cm	(Bingham and Wu, 2011, Schnepf et al., 2018b)	
dx_{max}	maximal segment length	3 cm		
dx_{min}	minimal segment length	1 cm		
gf	growth function	negative exponential	(Bingham and Wu, 2011, Schnepf et al., 2018b)	
l_{apical}	maximal apical length	12 cm	(Bingham and Wu, 2011, Schnepf et al., 2018b)	
l_{basal}	maximal basal length	0.8 cm	(Bingham and Wu, 2011, Schnepf et al., 2018b)	
$l_{internodal}$	maximal internodal length	0.4 cm	(Bingham and Wu, 2011, Schnepf et al., 2018b)	
l_{max}	maximal length	60 cm	(Bingham and Wu, 2011, Schnepf et al., 2018b)	
latDelay	growth delay of the laterals	4 d	(Bingham and Wu, 2011, Schnepf et al., 2018b)	
r	initial growth rate used during the empirical growth period	2.4 cm d^{-1}	(Bingham and Wu, 2011, Schnepf et al., 2018b)	used during the empirical growth period
theta	branching angle from parent organ	0.4 rad	(Bingham and Wu, 2011, Schnepf et al., 2018b)	
TropismN	tropism strength	1	(Bingham and Wu, 2011, Schnepf et al., 2018b)	number of trials for tropism computation

TropismS	change in growth direction per *cm* of organ length	0.261799	(Bingham and Wu, 2011, Schnepf et al., 2018b)	
TropismT	tropism type	gravitropism	(Bingham and Wu, 2011, Schnepf et al., 2018b)	
1st order lat				
a	radius	0.02 cm	(Bingham and Wu, 2011, Schnepf et al., 2018b)	
dx_{max}	maximal segment length	3 cm		
dx_{min}	minimal segment length	1 cm		
gf	growth function	negative exponential	(Bingham and Wu, 2011, Schnepf et al., 2018b)	
l_{apical}	maximal apical length	5 cm	(Bingham and Wu, 2011, Schnepf et al., 2018b)	
l_{basal}	maximal basal length	1 cm	(Bingham and Wu, 2011, Schnepf et al., 2018b)	
$l_{internodal}$	maximal internodal length	0.25 cm	(Bingham and Wu, 2011, Schnepf et al., 2018b)	
l_{max}	maximal length	10 cm	(Bingham and Wu, 2011, Schnepf et al., 2018b)	
latDelay	growth delay of the laterals	5 day	(Bingham and Wu, 2011, Schnepf et al., 2018b)	
r	initial growth rate used during the empirical growth period	1 cm d^{-1}	(Bingham and Wu, 2011, Schnepf et al., 2018b)	used during the empirical growth period

theta	branching angle from parent organ	0.79 rad	(Bingham and Wu, 2011, Schnepf et al., 2018b)	
TropismN	tropism strength	1	(Bingham and Wu, 2011, Schnepf et al., 2018b)	number of trials for tropism computation
TropismS	change in growth direction per *cm* of organ length	0.5	(Bingham and Wu, 2011, Schnepf et al., 2018b)	
TropismT	tropism type	gravitropism	(Bingham and Wu, 2011, Schnepf et al., 2018b)	
2nd order lateral				
a	radius	0.02 cm	(Bingham and Wu, 2011, Schnepf et al., 2018b)	
dx_{max}	maximal segment length	3 cm		
dx_{min}	minimal segment length	1 cm		
gf	growth function	negative exponential	(Bingham and Wu, 2011, Schnepf et al., 2018b)	
l_{apical}	maximal apical length	3 cm	(Bingham and Wu, 2011, Schnepf et al., 2018b)	
l_{basal}	maximal basal length	1 cm	(Bingham and Wu, 2011, Schnepf et al., 2018b)	
l_{max}	maximal length	4 cm	(Bingham and Wu, 2011, Schnepf et al., 2018b)	
r	initial growth rate used during the empirical growth period	$0.6\,\mathrm{cm\,d^{-1}}$	(Bingham and Wu, 2011, Schnepf et al., 2018b)	used during the empirical growth period

theta	branching angle from parent organ	0.96 rad	(Bingham and Wu, 2011, Schnepf et al., 2018b)	
TropismN	tropism strength	1	(Bingham and Wu, 2011, Schnepf et al., 2018b)	number of trials for tropism computation
TropismS	change in growth direction per *cm* of organ length	0.1	(Bingham and Wu, 2011, Schnepf et al., 2018b)	
TropismT	tropism type	gravitropism	(Bingham and Wu, 2011, Schnepf et al., 2018b)	

Table A.3: Input parameters of the functional CPlantBox modules: Notation, symbols, values and units

Symbol	Description	Values and units	Source	Remarks
		Photosynthesis		
Chl	leaf chlorophyll content	50.5×10^{-3} $\mathrm{mmol^{-1}\,cm^{-2}}$	direct calibration	
$E_{a,c}$	activation energy for M_{co2}	$59\,430\,\mathrm{mJ\,mmol^{-1}}$	(Tuzet et al., 2003)	
$E_{a,d}$	activation energy for δ	$59\,430\,\mathrm{mJ\,mmol^{-1}}$	(Bonan, 2019c)	
$E_{a,j}$	activation energy J_{max}	$37\,000\,\mathrm{mJ\,mmol^{-1}}$	(Tuzet et al., 2003)	
$E_{a,o}$	activation energy M_{o2}	$36\,000\,\mathrm{mJ\,mmol^{-1}}$	(Tuzet et al., 2003)	
$E_{a,rd}$	activation energy for R_d	$53\,000\,\mathrm{mJ\,mmol^{-1}}$	(Tuzet et al., 2003)	
$E_{a,v}$	activation energy F_{cmax}	$58\,520\,\mathrm{mJ\,mmol^{-1}}$	(Tuzet et al., 2003)	
$E_{d,j}$	deactivation energy J_{max}	$220\,000\,\mathrm{mJ\,mmol^{-1}}$	(Tuzet et al., 2003)	
$E_{d,v}$	deactivation energy F_{cmax}	$220\,000\,\mathrm{mJ\,mmol^{-1}}$	(Tuzet et al., 2003)	
f_{w1r}	residual water scarcity factor of the stomatal model	9.308×10^{-2} –	(Corso et al., 2020)	computed from their dataset
g_0	residual stomatal conductance to CO_2	$69\,\mathrm{mmol\,cm^{-2}\,d^{-1}}$	indirect calibration	from night transpiration

$g_{h2o,ox-stomata}$	conductance of the pathway between the xylem surface and the stomata	$86.4\,\mathrm{mmol\,cm^{-2}\,d^{-1}}$	indirect calibration	
k_{chl1}	fitting parameter for Eqn.(2-9)	$2\,\mathrm{d^{-1}}$	indirect calibration	from nitrogen-limited transpiration
k_{chl2}	fitting parameter for Eqn.(2-9)	$9\,\mathrm{mmol\,cm^{-2}\,d^{-1}}$	indirect calibration	from nitrogen-limited transpiration
k_{fw1}	plant sensibility to water stress for stomatal opening	$6 \times 10^{-4}\,\mathrm{hPa}$	(Corso et al., 2020)	
k_{g1}	fitting parameter for Eqn.(2-27)	$1.5\,-$	indirect calibration	from transpiration
k_{g2}	H_2O to CO_2 ratio of molecular diffusivity in air	$1.6\,-$	(Tuzet et al., 2003)	
k_{jmax}	J^{25}_{max} to F^{25}_{cmax} ratio	$1.5\,-$	indirect calibration	from light saturation point
$l_{rootExchange}$	root exchange (immature) zone	0.8 *cm* from the tip	direct	zone without root hair
M^{25}_{co2}	reference Michaelis coefficient for CO_2 at 25°C	302×10^{-6} $\mathrm{mmol\,mmol^{-1}}$	(Tuzet et al., 2003)	
M^{25}_{o2}	reference Michaelis coefficient for O2 at 25°C	256×10^{-3} $\mathrm{mmol\,mmol^{-1}}$	(Tuzet et al., 2003)	
Mm_{h2o}	molar mass of H_2O	$18 \times 10^{-3}\,\mathrm{kg\,mmol^{-1}}$	-	
o_i	substomatal O_2 molar fraction	210×10^{-3} $\mathrm{mmol\,mmol^{-1}}$	(Tuzet et al., 2003)	
S	entropy term for J_{max} and F_{cmax}	$700\,\mathrm{mJ\,mmol^{-1}\,K^{-1}}$	(Tuzet et al., 2003)	
α	fitting parameter for Eqn.(2-15)	$0.2\,-$	(Tuzet et al., 2003)	
$\Gamma*^{25}$	reference $\Gamma*$ at 25°C	$4.275 \times 10^{-5}\,\mathrm{mmol\,mmol^{-1}}$	(Bonan, 2019c)	
$\psi_{o,symplasm}$	osmotic water potential in the symplasm	$10\,000\,\mathrm{hPa}$	(Schopfer, 2006)	
$\psi_{t,crit,1}$	critical total water potential of the leaf xylem for stomatal opening	$-2500\,\mathrm{hPa}$	indirect calibration	
ω	fitting parameter for Eqn.(2-15)	0.95	(Tuzet et al., 2003)	
		Organ-specific		
$k_{lat,st,root}$	root membrane permeability to sucrose	1×10^{-2} $\mathrm{cm\,d^{-1}}$	indirect calibration	to get realistic ratio of exudated sucrose

$k_{lat,x,root0}$	xylem membrane permeability to water for 0-order roots	6.37×10^{-5} cm hPa^{-1}d^{-1}	direct calibration	Based on the concentric membrane model of (Bramley, 2006)
$k_{lat,x,root1}$	xylem membrane permeability to water for 1-order roots	7.9×10^{-5} cm hPa^{-1}d^{-1}	direct calibration	
$k_{lat,x,root2}$	xylem membrane permeability to water for 2-order roots	7.9×10^{-5} cm hPa^{-1}d^{-1}	direct calibration	
$k_{lat,x,stem}$	xylem membrane permeability to water for stems	0 cm hPa^{-1}d^{-1}	-	-
$k_{lat,x,leaf}$	leaf xylem membrane permeability to water	3.83×10^{-4} cm hPa^{-1}d^{-1}	(Lu et al., 2019)	
$r_{st,max,leaf}$	growth rate used by the phloem module for leaves	10 cm d^{-1}	indirect calibration	
$r_{st,max,root0}$	growth rate used by the phloem module for 0-order roots	14.4 cm d^{-1}	indirect calibration	to recreate observed growth once
$r_{st,max,root1}$	growth rate used by the phloem module for 1-order roots	9 cm d^{-1}	indirect calibration	carbon-limited module is used
$r_{st,max,root2}$	growth rate used by the phloem module for 2-order roots	8 cm d^{-1}	indirect calibration	
$r_{st,max,stem}$	growth rate used by the phloem module for stems	1 cm d^{-1}	indirect calibration	
$\rho_{s,leaf}$	sucrose content per volume of leaf fresh tissue	6.72 mmol cm^{-3}	direct calibration	
$\rho_{s,root}$	sucrose content per volume of root fresh tissue	6.12 mmol cm^{-3}	direct calibration	
$\rho_{s,stem}$	sucrose content per volume of plant fresh tissue	7.8 mmol cm^{-3}	direct calibration	
		Other		
$F_{in,max}$	maximum loading rate into the sieve tube	0.5 mmol d^{-1}	indirect calibration	
$F_{max,starch,X}$	maximum value of *starch* synthesis in X (sieve tube or mesophyll) according to the Michaelis-Menten dynamic	0 mmol cm^{-3} d^{-1}	(Daudet et al., 2002), illustrative	
g	gravitational acceleration	980 hPacm^{2}kg^{-1}	-	

$k_{hyd,starch,X}$	relative starch hydrolyse rate in X (sieve tube or mesophyll)	$0\,\mathrm{d}^{-1}$	(Daudet et al., 2002), illustrative
$k_{targ,starch,X}$	starch hydrolyse or biosynthesis rate in X (sieve tube or mesophyll) according to $s_X - s_{targ,X}$	$0.21\,\mathrm{d}^{-1}$	(Daudet et al., 2002), illustrative
k_{m1}	fitting parameters for $R_{m,max}$	$0.25\,-$	indirect
k_{m2}	fitting parameters for $R_{m,max}$	$2 \times 10^{-5}\,-$	indirect calibration
$l_{leaf,growthZone}$	leaf zone with intercalar meristem	2 *cm* from the leaf base	(Zubairova et al., 2016)
M_{meso}	Michaelis-Menten coefficient for the active loading of sucrose	$0.2\,\mathrm{mmol\,cm^{-3}}$	indirect calibration
M_{out}	Michaelis-Menten coefficient for the active unloading of sucrose	$0.1\,\mathrm{mmol\,cm^{-3}}$	indirect calibration
$M_{starch,X}$	Michaelis constant for *starch* synthesis in X (sieve tube or mesophyll)	$\mathrm{Inf mmol\,cm^{-3}}$	(Daudet et al., 2002), illustrative
$Q10$	temperature coefficient for R_m	$2\,-$	(Barillot et al., 2016)
R	ideal gas constant	83.14 $\mathrm{hPa\ cm^3K^{-1}mmol^{-1}}$	
$s_{st,min}$	minimum sucrose concentration in the sieve tube below which no loss of carbon occurs	$0.4\,\mathrm{mmol\,cm^{-1}}$	indirect calibration
s_{soil}	mean soil soluble carbon concentration in sucrose equivalent content	$1 \times 10^{-4}\,\mathrm{mmol\,cm^{-1}}$	direct calibration
$s_{targ,X}$	target s_X in X (sieve tube or mesophyll) defining *starch* synthesis or hydrolysis	$0.4\,\mathrm{mmol\,cm^{-3}}$	illustrative
$T_{ref,Q10}$	reference temperature for $Q10$	293.15 K	(Barillot et al., 2016)
Y	plant sucrose use efficiency for growth	$0.9\,-$	indirect
β	ratio of axial conductance with sieve plates to that without	$1\,-$	indirect calibration

β_{meso}	down-regulation factor for the active loading of sucrose	$0.1-$	indirect calibration
ρ_{h2o}	water density	$1 \times 10^{-3}\,\mathrm{kg\,cm^{-3}}$	-
$\psi_{t,crit,2}$	critical total water potential of the xylem for growth	$-2000\,\mathrm{hPa}$	(Zubairova et al., 2016)
$\psi_{t,max}$	water potential above which water is not limiting for growth	$0\,\mathrm{hPa}$	(Zubairova et al., 2016)

Table A.4: Xylem tubes' shapes

organ type	tube(s) per vascular bundle	bundle(s) per cross section	resulting n_i	xylem radius, $a_{x,i}$ (cm)	Source
leaf	2	32	64	0.0015	direct calibration
leaf	2	32	64	0.0005	direct calibration
stem	3	52	156	0.0017	direct calibration
stem	1	52	52	0.0008	direct calibration
root0	4	1	4	0.0015	direct calibration
root1, root2	4	1	4	0.00041	direct calibration
root1, root2	1	1	1	0.00087	direct calibration

Table A.5: Sieve tubes' shapes

organ type	tube(s) per vascular bundle	bundle(s) per cross section	resulting n_i	sieve tube radius, $a_{st,i}$ (cm)	Source
leaf	18	32	576	0.00025	direct calibration
stem	21	52	1092	0.00019	direct calibration
root0	33	1	33	0.00039	direct calibration
root1, root2	25	1	25	0.00035	direct calibration

Table A.6: Variables and other parameters: Notation, symbols and units

Symbol	Description	Units
	Photosynthesis	
A_g	gross carbon assimilation rate per unit of surface	$\mathrm{mmol\,cm^{-2}\,d^{-1}}$
$A_{g,q}$	daily gross carbon assimilation	$\mathrm{mmol\,d^{-1}}$
c_i	substomatal CO_2 molar fraction	$\mathrm{mmol^{-1}\,mmol^{-1}}$
c_{atm}	CO_2 molar fraction at the site of measurment	$\mathrm{mmol^{-1}\,mmol^{-1}}$
D	vapor deficit coefficient	$-$
E_v	water vapor flow rate per leaf area	$\mathrm{cm^3\,cm^{-2}\,d^{-1}}$
ea	actual vapor pressure	hPa
es	saturated vapor pressure	hPa
f_{w1}	water scarcity factor of the stomatal model	$-$
g_{co2}	conductance to CO_2	$\mathrm{mmol\,cm^{-2}\,d^{-1}}$
g_{ho2}	conductance to HO2	$\mathrm{mmol\,cm^{-2}\,d^{-1}}$
h	relative humidity	$-$
Je	electron transport rate for a set for a set PAR	$\mathrm{mmol\,cm^{-2}\,d^{-1}}$
Je_{max}	maximal electron transport rate	$\mathrm{mmol\,cm^{-2}\,d^{-1}}$
Je^{25}_{max}	maximal electron transport rate at 25°C	$\mathrm{mmol\,cm^{-2}\,d^{-1}}$
M_{co2}	Michaelis coefficient for CO_2	$\mathrm{mmol\,mmol^{-1}}$
M_{o2}	Michaelis coefficient for O2	$\mathrm{mmol\,mmol^{-1}}$
P_{atm}	atmospheric air pressure	hPa
PAR	photosynthetic active radiation absorbed by the plant	$\mathrm{mmol\,photons\,cm^{-2}\,d^{-1}}$
R_d	dark respiration rate	$\mathrm{mmol\,cm^{-2}\,d^{-1}}$
Res	resistivity	$\mathrm{d\,cm^2\,cm^{-3}}$
F_c	carboxylation rate	$\mathrm{mmol\,cm^{-2}\,d^{-1}}$
F_{cmax}	maximal carboxylation rate	$\mathrm{mmol\,cm^{-2}\,d^{-1}}$
F^{25}_{cmax}	maximal carboxylation rate at 25°C	$\mathrm{mmol\,cm^{-2}\,d^{-1}}$
V_j	electron transport rate	$\mathrm{mmol\,cm^{-2}\,d^{-1}}$
Γ	CO_2 compensation point	$\mathrm{mmol\,mmol^{-1}}$
$\Gamma*$	CO_2 compensation point in the absence of mitochondrial respiration	$\mathrm{mmol\,mmol^{-1}}$
	Other	
a	element's radius or leaf thickness	cm
A_{cross}	cross-sectional area	$\mathrm{cm^2}$
$Exud$	sucrose sink for exudation	$\mathrm{mmol\,d^{-1}}$
$[Exud]$	sucrose sink for exudation	$\mathrm{mmol\,cm^{-3}\,d^{-1}}$
F_{in}, F_{out}, $F_{out,MM}$	source terms for s_{st} loading, total unloading, and unloading with Michaelis-Menten	$\mathrm{mmol\,d^{-1}}$
$[F_{in}]$, $[F_{out}]$, $[F_{out,MM}]$	source terms for s_{st} loading, total unloading, and unloading with Michaelis-Menten	$\mathrm{mmol\,cm^{-3}\,d^{-1}}$

G_{tot}	sucrose sink for growth	$\mathrm{mmol\,d^{-1}}$
$[G_{tot}]$	sucrose sink for growth	$\mathrm{mmol\,cm^{-3}\,d^{-1}}$
j_{lat}	solution lateral flux	$\mathrm{cm^1 d^{-1}}$
J	solution volumetric flow rate	$\mathrm{cm^3 d^{-1}}$
K_{ax}	intrinsic axial conductance for the solution	$\mathrm{cm^4 hPa^{-1} d^{-1}}$
k_{lat}	area specific conductance of the membrane	$\mathrm{cm\,hPa^{-1} d^{-1}}$
L, l	total length, arbitrary small length	cm
p	perimeter	cm
r	growth rate	$\mathrm{cm\,d^{-1}}$
R_m	sucrose sink for maintenance	$\mathrm{mmol\,d^{-1}}$
$[R_m]$	sucrose sink for maintenance	$\mathrm{mmol\,cm^{-3}\,d^{-1}}$
$s, \bar{s}$	sucrose concentration, residual between actual and minimum sucrose concentration	$\mathrm{mmol\,cm^{-3}}$
s_q	sucrose content	mmol
$starch$	starch concentration	$\mathrm{mmol\,cm^{-3}}$
t	time	d
v	volume	$\mathrm{cm^3}$
W	leaf blade's or sheath's width	cm
T	temperature	K
z	height, z = 0 at the soil surface, upward-pointing axis	cm
μ	dynamic viscosity	hPa d
ξ	local axial coordinate of the plant	cm
ψ	water potential	hPa
Ω, $\partial\Omega$	studied domain and its boundaries	–

Subindices

0	initial or residual value
atm	atmosphere
ax	axial
bl	leaf boundary layer
$blade$	leaf blade
$canopy$	canopy
$Clim$	carbon limited
$CWlim$	carbon and water limited
$crit$	critical
h	hydrostatic (in phloem: turgor)
g	gravitational
i, j	plant node index
in	entering the sieve tube
l	value over the length l
lat	lateral
lim	limited
m	matric potential

max	maximum (potential) value
$meso$	mesophyll
o	osmotic potential
ox	outer xylem
org	organ
out	outside of plant (value) or leaving the plant (flow)
p	turgor pressure (in xylem: hydraustatic potential)
$sheath$	leaf sheath
ref	reference
$sheath$	leaf sheath
$soil$	soil
seg	plant segment (discretised model) studied plant zone (continuous model)
st	phloem sieve tube
$stomata$	stomata
t	total
x	xylem
$wlim$	water limited

A.6 Numerical solution

In this section, we first give an overview of the main notations used to describe the numerical solutions. We then define the analytical solution for the xylem water flow, leaf outer-xylem water flow (transpiration), and phloem flow for one segment. Finally, we describe the matrix notation and solving scheme. Numerical details of the soil water flow are described in Koch et al. (2021).

A.6-1 Mathematical definitions

The branched plant structure is divided into connected line segments with N_s segments and N_n nodes. From the point of view of a mathematical graph, it corresponds to a directed tree (see section 2-2-1-2). According to the graph (or mesh) terminology, a CPlantBox-node is a graph-node (mesh-vertex) and a CPlantBox-segment is a graph-edge (mesh-cell). For the definition of segment or node variables: We define the segment ij as the segment going from i to j.
We have for the segment flows: $J_{ij} = -J_{ji}$ For other segment variables, $X_{ij} = X_{ji}$. Subscripts of brackets or parenthesis $([...]_{ij}$, $(...)_{ij})$ apply to all the variables within. For the definition of matrices, the subscript *seg* indicates vectors of size $[N_s, 1]$ containing segment data. *node* indicates vectors of size $[N_s + 1, 1]$ containing node data. The sign "$\cdot$" indicates a hadamard product, "$\oslash$" a hadamard division and ^{T} indicates a transposition.

The FvCB-stomatal regulation variables (such as A_g, $g_{co2,stomata}$, see Section 2-2-1-4-1), the xylem water flux variables ($J_{ax,x}$, $j_{lat,x-soil}$, $j_{lat,x-atm}$, see Section 2-2-1-4-2) and the phloem solution axial flux ($J_{ax,st}$, see Section 2-2-1-4-3) are solved for each segment. The other sucrose-related variables (s_{st}, s_{meso}, F_{in}, F_{out} see Sections 2-2-1-4-3, 2-2-1-4-5) and $\psi_{t,x}$ (see Section 2-2-1-4-2) are solved for each node.

IM is the incidence matrix of the directed graph (of size $[N_n, N_s]$) and IM^T is its transposition (of size $[N_s, N_n]$). Thus we have:

$$IM[j,k] = \begin{cases} -1 & \text{if} \quad \text{a segment k has j as begin-node} \\ 1 & \text{if} \quad \text{a segment k has j as end-node} \\ 0 & \text{else} \end{cases} \tag{A-15}$$

BM is a boolean matrix of size $[N_s, N_n]$. It gives for each segment the index of the upflow node:

$$BM[k,j] = \begin{cases} 1 & \text{if} \quad IM[j,k] \times J_{w,seg}[k] < 0 \\ 0 & \text{else} \end{cases} \tag{A-16}$$

with $J_{w,seg}[k]$ the net water flow of the segment k going from the begin-node to the end-node. Therefore, $BM[k,j] = 1$ only if the water flow in the segment k goes from the node j to the other node of the segment k.

A.6-2 Analytical solution for one segment

In this following section, we present the definition of the driving equations of Sections 2-2-1-4-2, 2-2-1-4-3 and 2-2-1-4-1, discretized for one plant segment (graph edge) or node (graph vertex).

A.6-2-1 Plant water flow

A.6-2-1-1 Axial flow

The analytical solution to Eqn.(2-36) presented below is based on the approach of Landsberg and Fowkes (1978) and Meunier et al. (2017, Appendix B). However, contrary to them, [a] we define the xylem axial flow according to $\psi_{p,x}$ and not $\psi_{t,x}$ [b] we use an exponential function instead of an hyperbolic function.
When $k_{lat,x} > 0$ and $K_{ax,x} > 0$ we use the analytical continuous solution

$$\psi_{p,x}(l) = \psi_{out} + d_i e^{\tau l} + d_j e^{-\tau l} \tag{A-17}$$

$$\psi_{out} = \begin{cases} \psi_{m,soil} \text{ if belowground} \\ \psi_{p,ox} \text{ if leaf} \end{cases} \tag{A-18}$$

with ψ_{out} (hPa) the water potential outside of the plant, uniform over the axial distance l. The above equation is solved with

$$\tau = \sqrt{p_{org} \times k_{lat,x}/K_{ax,x}} \tag{A-19}$$

where the constants d_i, and d_j (hPa) can be calculated from the boundary conditions.
To discretise the equation for each segment ij, the Dirichlet top ($l = 0$), and bottom ($l = L$) boundary conditions are given by the begin- and end-nodes of the segment: $\psi_{p,x}(0) = \psi_{p,x,i}$ and $\psi_{p,x}(L) = \psi_{p,x,j}$. They are inserted into the analytic solution and yield the two equations

$$\begin{pmatrix} 1 & 1 \\ e^{\tau L} & e^{-\tau L} \end{pmatrix}_{ij} \begin{pmatrix} d_i \\ d_j \end{pmatrix}_{ij} = \begin{pmatrix} \psi_{p,x,i} - \psi_{out,ij} \\ \psi_{p,x,j} - \psi_{out,ij} \end{pmatrix}. \tag{A-20}$$

Each plant segment is given a mean $\psi_{m,soil,ij}$ ($\psi_{m,soil,ij}$ of the voxel were the segment center is located) or $\psi_{p,ox,ij}$. Therefore, $\psi_{out,ij}$ is a constant. From these equations we can calculate the constants $d_{i,ij}$, and $d_{j,ij}$ of the segment ij as

$$\begin{pmatrix} d_i \\ d_j \end{pmatrix}_{ij} = \delta_{ij}^{-1} \begin{pmatrix} e^{-\tau L} & -1 \\ -e^{\tau L} & 1 \end{pmatrix}_{ij} \begin{pmatrix} \bar{\psi}_{p,i} \\ \bar{\psi}_{p,j} \end{pmatrix}_{ij} \tag{A-21}$$

with

$$\delta_{ij} := [e^{-\tau L} - e^{\tau L}]_{ij}, \tag{A-22}$$

and

$$\bar{\psi}_{p,i,ij} = \psi_{p,x,i} - \psi_{out,ij} \tag{A-23}$$

$$\bar{\psi}_{p,j,ij} = \psi_{p,x,j} - \psi_{out,ij} \tag{A-24}$$

Thus, $\bar{\psi}_{p,i,ij}$ and $\bar{\psi}_{p,j,ij}$ are constants.
Putting the constants $d_{i,ij}$ and $d_{j,ij}$ into the solution for $\psi_{p,x}$ (Eqn.(A-17)) we can write down the exact axial flow in the segment ij, as (Meunier et al., 2017, B2):

$$J_{ax,x,ij}(l) = -[K_{ax,x}\left(d_i\tau e^{\tau l} - d_j\tau e^{-\tau l} + d\psi_g(l)\right)]_{ij} \tag{A-25}$$

with $d\psi_g(l)$ the gradient of gravitational water potential between the nodes i and the point at l cm from i. Replacing the constants $d_{i,ij}$ and $d_{j,ij}$ with their definition yields the explicit axial flow equation:

$$\begin{aligned} J_{ax,x,ij}(l) = &- K_{ax,x,ij}[\delta^{-1}\tau[(e^{-\tau L}\bar{\psi}_{p,x,i} - \bar{\psi}_{p,x,j})e^{\tau l} \\ &- (-e^{\tau L}\bar{\psi}_{p,x,i} + \bar{\psi}_{p,x,j})e^{-\tau l}] + d\psi_g(l)]_{ij} \end{aligned} \tag{A-26}$$

Evaluation of the axial flow at $l = 0$ (node i) yields

$$J_{ax,x,ij}(0) = -K_{ax,x,ij}\left(\delta^{-1}\tau[(e^{-\tau L} + e^{\tau L})\bar{\psi}_{p,i} - 2\bar{\psi}_{p,j}] + d\psi_g(0)\right)_{ij} \tag{A-27}$$

For conservation of mass in each node i, the summed exact axial flows have to equal zero,

$$\sum_{j \in N(i)} J_{ax,x,ij}(0) = 0 \tag{A-28}$$

where N(i) are the indices of the segments starting from node index i to j. We can solve this system of equations (see appendix A.6-2-5) and obtain thus $\psi_{p,x}$ and $J_{ax,x}$ for each plant node and segment, respectively.

$\psi_{p,x}$ and $J_{ax,x}$ are then used by the photosynthesis and phloem module (Eqns.(2-25) and (2-38)) and by the core CPlantBox-module to compute the water-limited growth rate (Eqn.(2-2)).

A.6-2-1-2 Lateral flow

Once $\psi_{p,x}$ is known, the exact lateral water flow ($J_{lat,x-out}$, in $cm^3 d^{-1}$) for a segment ij with length L_{ij} and lateral conductivity $k_{lat,x,ij}$ can be computed with the following equations:

$$J_{lat,x-out,ij} = -[p_{org}\ k_{lat,x}]_{ij} \int_0^{L_{ij}} \psi_{out,ij} - \psi_{p,x} dl \tag{A-29}$$

$$J_{lat,x-out,ij} = [p_{org}\ k_{lat,x}\left(\frac{d_i}{\tau}(e^{\tau L} - 1) + \frac{d_i}{\tau}(1 - e^{-\tau L})\right)]_{ij} \tag{A-30}$$

Inserting the definition of $d_{i,ij}$ and $d_{i,ij}$ into the exact lateral flow yields

$$\begin{aligned} J_{lat,x-out,ij} = &[p_{org}\ k_{lat,x}\frac{1}{\delta\tau} \\ &\times \left(\bar{\psi}_{p,i}(1 - e^{-\tau L} - e^{\tau L} + 1) + \bar{\psi}_{p,j}(-e^{\tau L} + 1 + 1 - e^{-\tau L})\right)]_{ij} \end{aligned} \tag{A-31}$$

and

$$J_{lat,x-out,ij} = [p_{org}\ k_{lat,x}\frac{1}{\delta\tau}(\bar{\psi}_{p,i}+\bar{\psi}_{p,j})(2-e^{-\tau L}-e^{\tau L})]_{ij} \quad \text{(A-32)}$$

The $J_{lat,x-out}$ values from root segments can then be used as source term in the soil module (see Section 2-2-1-5). The $J_{lat,x-out}$ values from leaf segments corresponds to the transpiration rate (see Section 2-2-1-4-1-1).

A.6-2-2 Stomatal regulation, photosynthesis, and transpiration

Once $\psi_{p,x}$ and $j_{lat,x-atm}$ are known, we can compute $\psi_{p,ox}$ (hPa), the water potential on the surface of the leaf vascular bundle-sheath, by implementing Eqns.(A-31), and solving for ψ_{out} (here, equivalent to $\psi_{p,ox}$):

$$\psi_{p,ox,ij} = \left(\left[\frac{j_{lat,x-atm}\times L\times p}{k_{lat,x}\frac{1}{\tau\delta}(2-e^{-\tau L}-e^{\tau L})}\right]_{ij}+(\psi_{h,x,i}+\psi_{h,x,j})\right)\times 0.5 \quad \text{(A-33)}$$

$j_{lat,x-atm}$ is obtained from Eqn.(2-7). $\psi_{p,ox}$ can then used in the xylem flow module (see Eqn.(2-35)) at the next computation loop.

A.6-2-3 Sucrose balance

As explained above, s_{st}, s_{meso}, F_{in}, F_{out} are node variables. When segment-defined variables or parameters are needed to compute them (such as v_{st}, A_g, $k_{lat,st}$), we allocate to the node i the variable from the segment .i which has i as end node: $X_{i,node} = X_{.i,seg}$.

We set $s_{Y,q}$ $(mmol\ sucrose)$ the sucrose content in the compartment Y, either the mesophyll or the sieve tube.
$\frac{ds_{q,j}}{dt}$ $(mmol\ sucrose\ d^{-1})$, the variation of sucrose content in the node j, is defined thus:

$$\frac{ds_{st,q,j}}{dt} = J_{ax,st,q,j.}+(F_{in,j}-F_{out,j}) \quad \text{(A-34)}$$

$$J_{ax,st,q,j} = \sum_{i}^{N_n}(s_{ij}\times J_{ax,st,h2o,ij}) \quad \text{(A-35)}$$

$$J_{ax,st,h2o,ij} = \frac{K_{ax,st,ij}}{L_{ij}}\times(RT\times(s_j-s_i)+(\psi_{xj}-\psi_{xi})) \quad \text{(A-36)}$$

$$s_{ij} = \begin{cases} s_i & \text{, if } J_{w,ij}<0 \\ s_j & \text{, if } J_{w,ij}\geq 0 \end{cases}, \quad \text{(A-37)}$$

$$\frac{ds_{meso,q,j}}{dt} = (F_{Ag,i}-F_{in,i})\times v_{meso,i}. \quad \text{(A-38)}$$

ψ_{xj} and ψ_{xi} are obtained thanks to the xylem flow computation (see Sections 2-2-1-4-2 and A.6-2-1). $F_{Ag,i}$ corresponds to the sucrose assimilation rate computed according to Eqns.(2-22),(2-46). $F_{in,i}$ and $F_{out,i}$ are computed according to

the equations in Eqns.(2-48) and (2-57) respectively. $J_{ax,st,q,j.}$ (resp. $J_{ax,st,h2o,ij}$) corresponds to the axial flow in the sieve tube of sucrose content (resp. water) at the node i.

A.6-2-4 Matrix form and solving scheme

In the following section, we present the discretized system of equations and the solving schemes to obtain $\psi_{p,x}$, $\frac{ds_{st,q,j}}{dt}$ and $\frac{ds_{meso,q,j}}{dt}$.

A.6-2-5 Xylem water flow

From Eqns.(A-27-A-28) we can construct a system of equations, that can be solved for $\psi_{p,x}$:

$$\psi_{h,x,node} = C^{-1} \times b_{node} \tag{A-39}$$

With C and b_{node} matrices of size $[N_n,\, N_n]$ and $[N_n,\, 1]$ respectively. They are filled with zeros except at the following locations:

$$\begin{aligned}
C[i,\, i] &= C[i,\, i] + c_{i,ij} && \text{(A-40)}\\
C[i,\, j] &= 2[K_{ax,x}\delta^{-1}\tau]_{ij} && \text{(A-41)}\\
b_{node}[i,\, 1] &= b_{node}[i,\, 1] + [K_{ax,x} \times d\psi_g]_{ij} + (c_{i,ij} + C[i,\, j])\psi_{out,ij} && \text{(A-42)}\\
c_{i,ij} &= [K_{ax,x}\delta^{-1}\tau(e^{-\tau L} + e^{\tau L})]_{ij} && \text{(A-43)}
\end{aligned}$$

for each segment ij going from node i to node j.

This system of equation is solved for the steady state solution of $\psi_{p,x}$ with the sparse linear solver (SParseLU) of the C++ Eigen library (Guennebaud et al., 2010). The $\psi_{p,x}$ are then used to compute the variables from the FvCB-stomatal regulations module. The fixed point iteration between the computation continues until convergence.

A.6-2-6 Sucrose balance

The equations from Section A.6-2-3 can be set in matricial form:

$$\begin{aligned}
\left[\frac{ds_{st,q}}{dt}\right]_{node} &= IM \times (J_{w,seg} \cdot s_{st,seg}) + (F_{in,node} - F_{out,node}) \cdot v_{st,node} && \text{(A-44)}\\
s_{st,seg} &= BM \times s_{st,node} && \text{(A-45)}\\
s_{st,node} &= s_{st,q,node} \oslash v_{st,node} && \text{(A-46)}\\
J_{w,seg} &= Co_{ax,st,seg}(IM^T \times RTs_{st,node} + IM^T \times \psi_{x,node}) && \text{(A-47)}\\
\left[\frac{ds_{meso,q}}{dt}\right]_{node} &= (F_{Ag,node} - F_{in,node}) \cdot v_{st,node} && \text{(A-48)}
\end{aligned}$$

with $Co_{ax,st,seg}$ the vector defining the conductance ($cm^3hPa^{-1}d^{-1}$) per sieve tube segment.

The system of equations is solved numerically using an implicit method: the value of $s^{m,n}_{q,node}$ (the vector containing the estimation m at time step n of s_q per node) is used to compute $\left[\frac{ds_q^{m,n}}{t_n - t_{n-1}}\right]_{node}$. This value is sent to the implicit Sundials-CVODE solver (Hindmarsh et al., 2005) which then yields $s^{m+1,n}_{q,node}$. This loops continues until convergence is reached. The solver then moves on the the next time step.

A.7 Sensitivity analysis

The program contains a high number of plant parameters which cannot be measured directly and which are highly correlated between them with regards to the outputs. Therefore, to have a better idea of which parameters need to be (re)calibrated in priority, a first sensitivity analysis was run for [a] the coupled water flow and FvCB-stomatal regulations modules (water modules), [b] the phloem flow and carbon usage modules (carbon modules). A sensitivity analysis of the root system parameters only can be found in the work of Morandage et al. (2022) .

As the computation time of the full coupled simulation is too long to run a sensitivity analysis, we evaluated the effect of the water (resp. carbon) modules' parameters for one time step of 3 hours. We moreover focused on a selected number of outputs variables of interest, namely [a] the total transpiration and gross assimilation rates for the water modules and [b] carbon usage rate for growth ($G_{tot,CWlim}$) for the carbon modules.

This sensitivity analysis is limited to a short time span and evaluates each module separately. Nonetheless, water (resp. phloem) parameters which have a strong influence on the transpiration and assimilation rates (resp. growth rate) will also influence strongly the other modules on the long term. For this evaluation, we did not include plant parameters which could be considered as physical constants, like E_a and E_d, respectively the activation and deactivation energy parameters used in the photosynthesis model.

Like for our example of simulation, we only represented a starch dynamic in the sieve tube (resp. mesophyll) dependent on the gradient between s_{st} (resp. s_{meso}) and the target value $s_{targ,st}$ ($s_{targ,meso}$). The starch-related parameters representing other dynamics (e.g., $F_{max,starch}$, $k_{hyd,starch}$) were set to 0. To diminish the number of parameters to evaluate, some where regrouped. Consequently, k_{Chl} represent the influence of Chl, $kchl1$, and $kchl2$; k_{starch} represents the influence of the starch-related parameters; X_{root} represent the influence of the parameter X for all the root types. We only selected key structural parameters. Moreover, some pre-tests allowed us to take out of the analysis parameters which

had a very limited effect on the outputs (like *oi*) to lower as well the number of parameters evaluated.

The sample range of each evaluated parameter was set to $[\frac{1}{2},2]$ of their value used in this study, except for the values of α and ω. For these two variables, ranges were set to make sure that a solution for Eqn. (2-15) could be found. We used $\Delta\psi_{o,symplast}$ as parameter(which corresponds to $\psi_{o,symplast} - \psi_{t,crit2}$) instead of $\psi_{o,symplast}$ to avoid ever having $|\psi_{o,symplast}| > |\psi_{t,crit2}|$ which would have led to computation errors.
Moreover, a first analysis showed that the environmental conditions and the plant's development stage influenced the sensitivity of the outputs to the parameters. Therefore, the analysis was run for each plant age at the beginning of the simulations (11 or 18 days) and each weather type (*baseline*, *dry spell*) using the environmental variables for noon.

The analysis was done with the SALib python module (Iwanaga et al., 2022). The number of samples was set according to the trade-off between precision gain and computation speed loss (see table A.7). Therefore, the simulations using slower modules were run with a lower number of parameter samples.

Table A.7: Number of samples per parameter for each simulation for the Sobol sensitivity analysis.

	water modules		carbon modules	
scenario \ plant age	11d	18d	11d	18d
baseline	2^{12}	2^{12}	2^{11}	2^{11}
dry spell	2^{12}	2^{12}	2^{11}	2^{11}

Figure A.1 presents the outputs of the analysis. The variation of the sensitivity index according to the plant and environment's characteristics indicate that such analysis could be necessary for each model setup. The difference in the width of the confidence intervals is in part linked to the different number of samples used for each analysis (see Table A.7).

For the water modules, we can observe that $g_{h2o,ox,max}$ is especially important. This parameter represents the conductivity between the leaf xylem bundle sheath and the substomatal cavity. Currently, $g_{h2o,ox,max}$ is a set constant. The results indicate therefore that it is necessary to represent the variation of $g_{h2o,ox,max}$ to evaluate more precisely the plant transpiration rate. For the assimilation rate, Chl (the leaf chlorophyll content), k_{chl1} and k_{chl2} (parameters linking the chlorophyll content to the potential assimilation rate), have a strong influence on the output of the simulation, because the affect the carboxylation rate (V_c). Similarly, α and k_{jmax} affect the photon-limited assimilation rate V_j. Moreover, the leaf structural parameters (l_{max} the maximum length, r_{leaf} the growth rate,

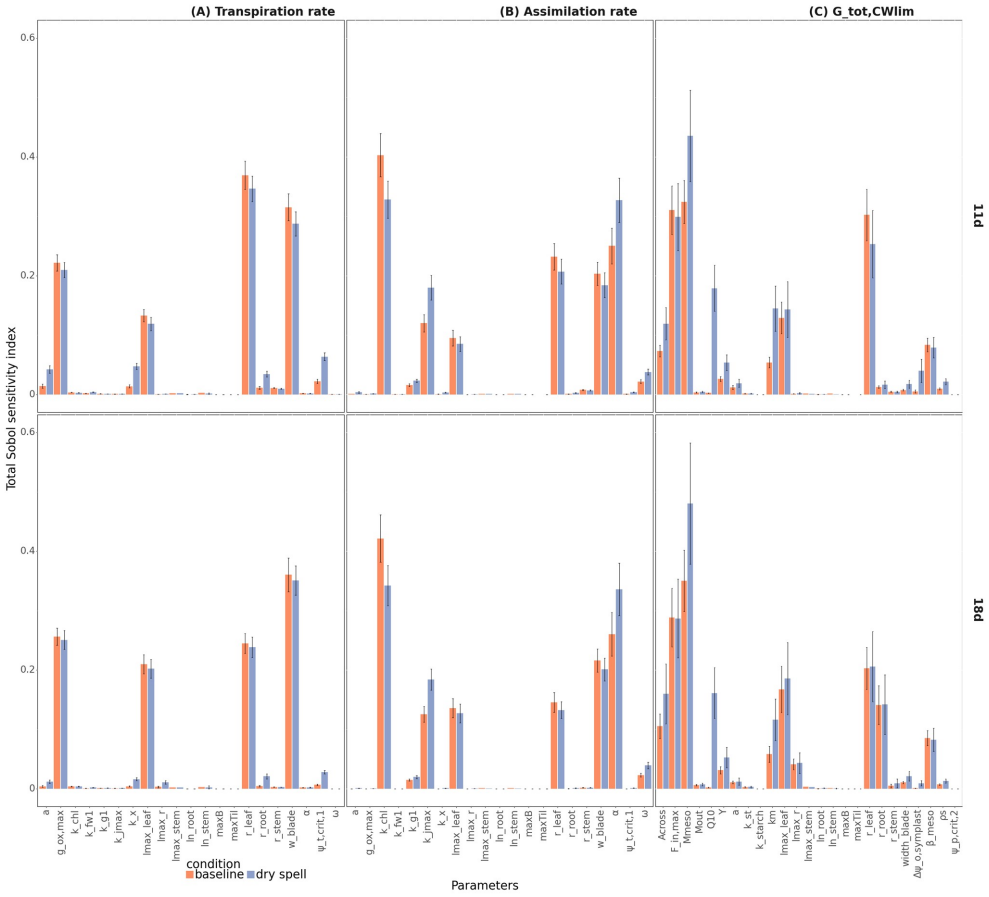

Figure A.1: Sensitivity analysis of the plant's (A) transpiration and (B) gross assimilation rate to the water modules' parameter and (C) carbon usage rate for growth ($G_{tot,CWlim}$) to the carbon modules' parameters for 11d and 18d plants under the two weather scenarios presented in the study. The sensitivity index includes both first order effects and interactions with the other parameters. The error bars show the limits of the confidence interval (confidence level of 95%).

w_{blade} the blade width) also had a strong influence on the outputsboth the assimilation and the transpiration.

For the carbon modules, we can observe for instance that $G_{tot,CWlim}$ is especially sensible to the parameters defining the flow of sucrose from the mesophyll to the sieve tubes: $F_{in,max}$, M_{meso} and β_{meso}. This defines how quickly the assimilated sucrose flows in the sieve tube and has a strong influence on the plant's capacity to buffer changes in assimilation rate
Surprisingly, $\psi_{p,crit,2}$ which defines the water limitation on growth, was found to have no influence on the outputs. It is likely caused by the fact that, for the simulated period, sucrose was more limiting than water for growth. Running a longer simulation for the sensitivity analysis should give a better evaluation of the influence of $\psi_{p,crit,2}$ on $G_{tot,CWlim}$.

A.8 Other simulation Results

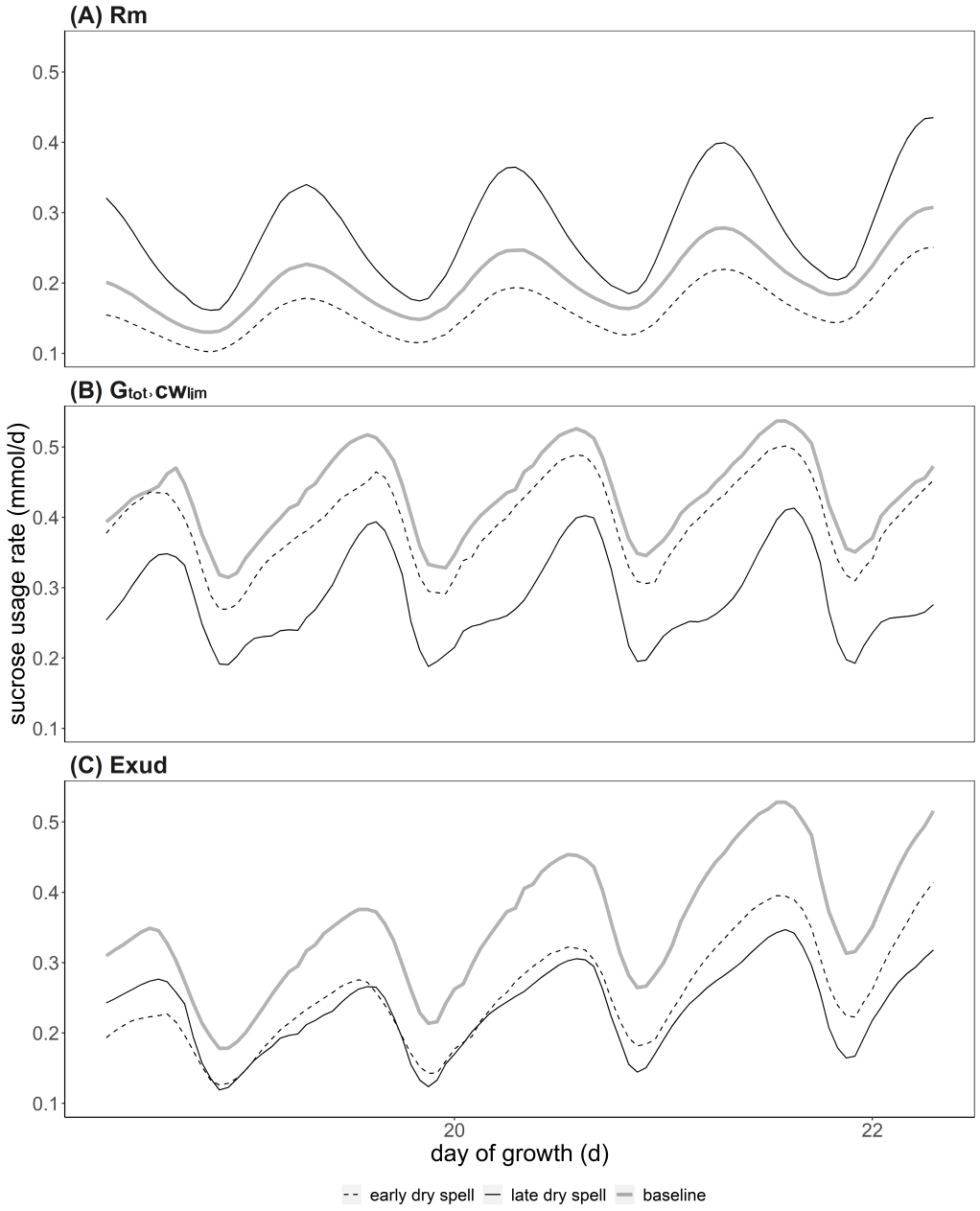

Figure A.2: Partitioning of the carbon loss between the three sinks according to time between day 19 and 23: maintenance respiration (Rm), growth and growth respiration ($G_{tot,CWlim}$), root exudation ($Exud$). We compare an early (thin dashed lines) and late dry spells (thin lines) against against a baseline scenario (thick lines).

Appendix B: Simulated carbon balance in the soil and plant

B.1 List of the parameters and variables

Table B.1: Represented carbon pools.

Output variables	Definition	Unit
C_L^l / C_L^s	Concentration of carbon from compounds with low molecular weight (in the liquid/solid phase)	$mol\ C\ cm^{-3}\ water$ / $mol\ C\ cm^{-3}\ scv$
C_H^l	Concentration of carbon from compounds with high molecular weight	$mol\ C\ cm^{-3}\ water$
C_O (C_O^a, C_O^d)	Concentration of oligotrophs (active, dormant)	$mol\ C\ cm^{-3}\ scv$
C_C (C_C^a, C_C^d)	Concentration of copiotrophs (active, dormant)	$mol\ C\ cm^{-3}\ scv$
CO_2	Unit of emitted CO_2 per volume of soil	$mol\ C\ cm^{-3}\ scv$

Table B.2: TraiRhizo input parameters. When the source is not given, the parameter values are taken from the sets defined by Sircan et al. (2024) and selected in section B.9. HMW: high molecular weight organic carbon compound.

Symbol	Definition (and source)	Value per selected parameter set			Unit
		highCO2	*highMB*	*lowMUptake*	
a	Sharpness parameter for the switch function from active to dormancy	0.1			–
$C^l_{H,init}$	Initial concentration of high molecular weight organic carbon concentration	$5.94e^{-4}$	$6.94e^{-4}$	$6.47e^{-4}$	$mol\ C\ cm^{-3}\ water$
$C^l_{L,init}$	Initial dissolved low molecular weight organic carbon	$4.71e^{-6}$	$5.15e^{-6}$	$5.1e^{-6}$	$mol\ C\ cm^{-3}\ water$
$C^s_{L,max}$	Maximum sorption capacity	$8.9e^{-4}$			$mol\ C\ cm^{-3}\ scv$
$C_{thres,C}$	Threshold C^l_L for microbial (de)activation	$1.42e^{-5}$	$9.90e^{-6}$	$2.19e^{-5}$	$mol\ C\ cm^{-3}\ water$
$C_{thres,O}$		$8.58e^{-6}$	$7.71e^{-6}$	$9.76e^{-6}$	
D_{HW}	Diffusion coefficient of high molecular weight organic carbon	$3.456e^{-3}$			$cm^2\ d^{-1}$
D_{LW}	Diffusion coefficient of dissolved low molecular weight organic carbon	2.07	0.92	1.45	$cm^2\ d^{-1}$
k_{ads}	Adsorption rate	$2.7e^{-7}$			$cm^3\ scv\ mol\ C^{-1}\ d^{-1}$
$k_{d,C}$	Deactivation rate coefficient	2.73	1.49	1.37	d^{-1}
$k_{d,O}$		0.24	4.04	0.11	
k_{des}	Desorption rate	$5e^{-5}$			d^{-1}
$k_{C,S}$	Substrate affinity to dissolved low molecular weight organic C	$4.93e^4$	$1.50e^5$	$7.72e^4$	$mol\ C\ cm^{-3}\ scv$
$k_{O,S}$		$1.02e^6$	$1.16e^7$	$9.55e^4$	
K_L	Half-saturation coefficients of enzymes targeting HMW	$1.98e^{-6}$	$1.02e^{-7}$	$6.23e^{-4}$	$mol\ C\ cm^{-3}\ scv$
$k_{max,C}$	Maximum maintenance rate coefficient	$7.07e^{-3}$	$1.38e^{-3}$	$1.46e^{-3}$	d^{-1}
$k_{max,O}$		$2.30e^{-4}$	$6.57e^{-4}$	$1.14e^{-3}$	
$k_{r,C}$	Reactivation rate coefficient	86.3	95.9	54.3	d^{-1}
$k_{r,O}$		1.17	54.9	0.181	

$v_{max,depoly}$	Maximum reaction rate of enzymes targeting HMW	0.108	$1.31e^{-2}$	$1.69e^{-3}$	d^{-1}
Y	Maintenance yield	0.372	$2.54e^{-2}$	0.397	–
Y_C	Growth yield on dissolved low molecular weight organic carbon	$1.08e^{-2}$	0.108	0.422	–
Y_O		$2.43e^{-2}$	0.142	0.896	
α	Empirical parameter determining the curvature of Eq.B-43 (Moyano et al., 2013)	1.47			–
β_C	Reduction factor of maintenance requirements in dormant state	$1.64e^{-3}$	$5.13e^{-3}$	$1.09e^{-4}$	–
β_O		0.592	$9.32e^{-2}$	$3.31e^{-2}$	
$\mu_{max,C}$	Maximum growth rate coefficient	0.83	1.42	0.25	d^{-1}
$\mu_{max,O}$		$1.03e^{-2}$	$3.56e^{-2}$	$1.26e^{-2}$	
ρ_L	Proportion of high molecular weight organic carbon formed from dead microbial biomass due to maintenance	$2.16e^{-2}$	0.579	$1.51e^{-2}$	–
ρ_b	Soil bulk density	1.51			$g\ mineral\ soil\ cm^{-3}\ scv$
τ	$\tau = \frac{\psi_{m,soil,D2A}}{\psi_{m,soil,A2D}}$, with $\psi_{m,soil,D2A}$ the threshold soil matric potential for microbial activation (Wang et al., 2021)	0.39			–
$\psi_{m,soil,A2D}$	Threshold soil matric potential for microbial deactivation (Wang et al., 2021)	4600			hPa
$\psi_{m,soil,opt}$	Threshold soil matric potential above which water is not limiting for microbial activity (Moyano et al., 2013)	-30			hPa
$\psi_{m,soil,th}$	Threshold soil matric potential bellow which microbial activity ceases (Moyano et al., 2013)	-158000			hPa
ω_{DA}	Empirical exponent for Eqs.B-62,B-63 (Wang et al., 2021)	3.38			–

B.2 Soil water flow

In the sections below, we present the implementation of the equations given in section 3-2-2-2 to the 1D axisymmetric and 3D soil domains.

B.2-1 3D soil model

For the 3D macroscale soil model, the sink term of Eq. (3-6) $S_\theta = S_{w,root-3DS}$ (cm^3 $water$ cm^{-3} scv d^{-1}), the water uptake or release by the roots:

$$S_{w,root-3DS,init} = \frac{1}{V_{3DS,scv}} \sum_{i=1}^{nr} \frac{\partial \theta_i V_{1DS,scv,i}}{\partial t} \tag{B-1}$$

$$S_{w,root-3DS} = \mathbf{Lim}(S_{w,root-3DS,init}) \tag{B-2}$$

where nr $(-)$ is the number of root segments in the soil control space of volume $V_{3DS,scv}$ (cm^3 scv), the i subscript is the identification of the ith root, $V_{1DS,scv,i}$ (cm^3 scv) is the volume of the perirhizal zone i and θ_i its water content. Instead of using $q_{w,root-soil}$ (see Eq. (3-3)) like Mai et al. (2019), in this study $S_{w,root-3DS}$ is obtained from $\frac{\partial \theta_i V_{1DS,scv,i}}{\partial t}$. This helps avoid computation errors when simulating the macro-soil flows and diminishes the divergence between the macro- and microscale models. Indeed, the plant-prescribed $q_{w,root-soil}$ was already potentially limited during the computation of $\frac{\partial \theta_i V_{1DS,scv,i}}{\partial t}$ according to $\psi_{x,crit}$ (see Eq. (B-12)). We then set a second limitation on the net sink (resp. source) using the maximum potentially available water (resp. space) in the voxel–equal to the water (resp. space) volume at the beginning of the time step and to the maximum amount of water that could be gained (resp. lost) according to the inter-voxel flow at the last time step. The driving equation for the water flow is defined thus at the macroscale (Koch et al., 2021, Mai et al., 2019):

$$\frac{\partial \theta}{\partial t} = K_{sat} \nabla \cdot (\kappa_m (\nabla \psi_{m,3DS} - \nabla \psi_{g,3DS})) + S_{w,root-3DS} \quad \text{for} \quad \Omega \backslash \partial\Omega,\ t(3-4) \tag{B-3}$$

$$S_{w,root-3DS} = S_{w,root-3DS,0} \quad \text{at} \quad t = t_0 \tag{B-4}$$

A boundary condition completes the model and can represent, for instance, the net gain or loss of water resulting from rainfall and soil evaporation.

B.2-2 1D axisymmetric soil models

Because of the small radii of the microscale domains, we assume that the gravitational gradient along the radial coordinate is negligible compared with the matric potential gradient: $abs(\frac{\partial \psi_{g,1DS}}{\partial r}) << abs(\frac{\partial \psi_{m,1DS}}{\partial r})$. We thus get (Debnath, 2005, Eq. 1.10.4):

$$\frac{\partial \theta}{\partial t} = \frac{1}{r} \frac{\partial}{\partial r} (r K_{sat} \kappa_m \frac{\partial \psi_{m,1DS}}{\partial r}) + \frac{1}{r} S_{w,3DS-1DS} \tag{B-5}$$

with r (cm) the radial coordinate along the axisymmetric domain, where $r = 0$ corresponds to the center of root segment associated with the microscale soil domain. $r \in [r_{in}, r_{out}]$, with r_{in} (cm) the inner boundary of the domain, corresponding to the root radius, and r_{out} (cm) the outer boundary of the 1D domain. The water flow at the inner boundary of 1D domain corresponds to $q_{root-soil}$ (see Eq. (3-3)). $S_{w,3DS-1DS}$ is obtained from the bulk soil water flow. For the segment i in the voxel k:

$$S_{w,1DS-3DS,i} = -\frac{Q_{w,1DS-3DS,i}}{V_{1DS,scv,i}} \tag{B-6}$$

$$Q_{w,1DS-3DS,i} = -\,Q_{w,3DS-3DS,k} \cdot W_w(i,k) \tag{B-7}$$

$$W_w(i,k) = \begin{cases} \frac{(\theta_s-\theta_i)V_{1DS,scv,i}+Q_{w,root-soil,i}dt}{\sum_j^n(\theta_s-\theta_j)V_{1DS,scv,j}+Q_{w,root-soil,j}dt} & \text{if} \quad Q_{w,3DS-3DS,k} > 0 \\ \frac{(\theta_i-\theta_r)V_{1DS,scv,i}-Q_{w,root-soil,i}dt}{\sum_j^{nr}(\theta_j-\theta_r)V_{1DS,scv,j}-Q_{w,root-soil,j}dt} & \text{else} \end{cases} \tag{B-8}$$

$$V_{1DS,scv,i} = \pi\,(r_{out,i}^2 - r_{in,i}^2)\,L_{r,i} \tag{B-9}$$

$$Q_{w,root-soil,i} = q_{w,root-soil,i} 2\pi r_{in,i} L_i \tag{B-10}$$

$Q_{w,3DS-3DS,k}$ $(cm^3\ water\ d^{-1})$ corresponds to the net water change in the subcontrol volume caused by the exchange with neighbouring voxels. The second element on the right-hand side of Eq. (B-7), W_w $(-)$ is a weighting factor dividing the net water flow between the microscale domains of the macroscale voxel k. W_w is computed from the maximal potentially available water (resp. space), which is the sum of [a] the net root water release (resp. uptake) over the evaluated period, and [b] the water (resp. air) volume available at the beginning of the evaluated period. In Eq. (B-6), the volume of the microscale domain ($V_{1DS,scv}$, $cm^3\ scv$) is used to convert the net water sink from $cm^3\ water\ d^{-1}$ to $cm^3\ water\ cm^{-3}\ scv\ d^{-1}$. $S_{w,1DS-3DS,i}$ is then divided between the 1D segments of the microscale domains using the same weighting method. We obtain the following driving equation for the microscale soil domains (Koch et al., 2021, Mai et al., 2019):

$$r\frac{\partial\theta}{\partial t} = \frac{\partial}{\partial r}(rK_{sat}\kappa_m\frac{\partial\psi_{m,1DS}}{\partial r}) + rS_{w,1DS-3DS} \quad \text{for} \quad r \in]r_{in}, r_{out}[,\ t > t_0 \tag{B-11}$$

$$K_{sat}\kappa_m\frac{\partial\psi_{m,1DS}}{\partial r} = max(q_{w,root-soil},\ K_{sat}\kappa_m\frac{(\psi_{crit,x}-\psi_{m,1DS})}{\Delta r_{root-1DS}}) \quad \text{at} \quad r = r_{in} \tag{B-12}$$

$$K_{sat}\kappa_m\frac{\partial\psi_{m,1DS}}{\partial r} = 0 \quad \text{at} \quad r = r_{out} \tag{B-13}$$

$$S_{w,3DS-1DS} = S_{w,3DS-1DS,0} \quad \text{at} \quad t = t_0 \tag{B-14}$$

with $\psi_{crit,x}$ (hPa) the critical (minimum) xylem water potential. Therefore, if both $\psi_{m,soil}$ and $q_{w,root-soil}$ are low, the realised net water uptake might be more limited than prescribed via $q_{w,root-soil}$.

B.3 Soil carbon transport

In the sections below, we present the implementation of the equations given in section 3-2-2-4 to the 1D axisymmetric and 3D soil domains.

B.3-1 3D soil model

For the 3D macroscale soil domain, S_X can be computed in two ways:

1. If there are no roots in the voxel i ($len(nr_i) = 0$), S_X corresponds to the sources computed at the voxel scale ($S_{X,3DS}$, $mol\ cm^{-3}\ scv\ d^{-1}$).

2. If there is at least one root in the voxel, S_X corresponds to the sources computed at the microscale ($S_{X,1DS}$, $mol\ cm^{-3}\ scv\ d^{-1}$).

This method is represented by the following equations:

$$S_X = \begin{cases} \frac{1}{V_{3DS}} \sum_{i=1}^{nr_k} V_{1DS} S_{X,1DS} & \text{if} \quad len(nr_k) > 0 \\ S_{X,3DS} & \text{else} \end{cases} \tag{B-15}$$

This allows us to achieve similar results at the micro- and macroscales and to profit from the higher resolution of the microscale models, leading to more accurate results in the soil voxels containing roots. $S_{X,1DS}$ is computed similarly to $S_{w,root-3DS}$ (see Eq. (B-1)), by computing the mean C variation rate and limiting the sink according to the C potentially available in the voxel. The driving equation for dissolved low molecular weight organic C is (Mai et al., 2019):

$$\frac{\partial \theta C_L^l}{\partial t} - K_{sat} \nabla \cdot \left(\kappa_m C_L^l (\nabla \psi_m - \nabla \psi_g) \right) \tag{B-16}$$

$$-\nabla \cdot (D_L(\theta, \phi) \nabla C_L^l) - S_L = 0 \text{ for } \Omega \backslash \partial\Omega,\ t > t_0,$$

$$C_L^l = C_{L,0}^l, \text{ at } t = t_0 \tag{B-17}$$

For high molecular weight organic C compounds, we have:

$$\frac{\partial \theta C_H^l}{\partial t} - \nabla \cdot (D_H(\theta, \phi) \nabla C_H^l) - S_H = 0$$

$$\text{for } \Omega \backslash \partial\Omega,\ t > t_0, \tag{B-18}$$

$$C_H^l = C_{H;0}^l, \text{ at } t = t_0 \tag{B-19}$$

For both equation sets, the boundary conditions can be used to represent an input of organic matter in the soil.

B.3-2 1D axisymmetric soil models

For 1D axisymmetric microscale soil domains, we get (Mai et al., 2019):

$$\frac{\partial \theta C_X^l}{\partial t} = -\frac{1}{r}\frac{\partial}{\partial r} r C_X^l \vec{u}_X + \frac{1}{r}\frac{\partial}{\partial r} r (D_X(\theta,\ \phi)\frac{\partial C_X^l}{\partial r}) \quad + S_X + S_{1DS-3DS,X} \tag{B-20}$$

$S_{1DS-3DS,X}$ represents the net source of solutes from inter-voxel exchanges at the macroscale. For the segment i in the voxel k:

$$S_{1DS-3DS,X,i} = -\ \frac{Q_{X,1DS-3DS,i}}{V_{1DS,scv,i}} \tag{B-21}$$

$$Q_{X,1DS-3DS,i} = -Q_{X,3DS-3DS,k}\ W_X(i,k) \tag{B-22}$$

$$W_X(i,k)\ =\ \begin{cases} \frac{m_{X,pot,i}}{\sum_j^n m_{X,pot,j}} & \text{if} \quad Q_{X,3DS-3DS,k} < 0 \\ \frac{1/max(m_{X,pot,i},\epsilon)}{(\sum_j^n 1/max(m_{X,pot,j},\epsilon))} & \text{else} \end{cases} \tag{B-23}$$

$$m_{X,pot,i}\ =\ \theta_i V_{1DS,scv,i} C_{X,i}^l + Q_{X,root-soil,i} dt \tag{B-24}$$

$$Q_{X,root-soil,i}\ =\ 2\pi r_{in,i} L_i\ \cdot \begin{cases} q_{exud,i} & \text{if} \quad \text{X is } C_L^l \\ q_{mucil,i} & \text{if} \quad \text{X is } C_H^l \end{cases} \tag{B-25}$$

$m_{X,pot}$ $(mol\ C)$ is the potentially available solute content. $Q_{X,3DS-3DS,k}$ $(mol\ C/d)$ corresponds to the net solute transport into the sub-control volume from other soil voxels. The second element of Eq. (B-22) is a weighting factor dependent on the solute content of the microscale domains in the voxel. $V_{1DS,scv,i}$ is used to convert the net solute transport from $mol\ d^{-1}$ to $mol\ cm^{-3}\ d^{-1}$. For solutes we could have $m_{X,pot} = 0$, we, therefore, set a minimum value of $\epsilon \approx 0$ when using ${C_{X,pot}^q}^{-1}$ to avoid a division by 0. The same method is used to divide the net sinks between the 1D segments of the microscale domain.

Eq. (B-20) for dissolved low molecular weight organic C gives:

$$\begin{aligned} r\frac{\partial \theta C_L^l}{\partial t}\ -\ \frac{\partial}{\partial r}(r C_L^l K_{sat} \kappa_m(S_w)\frac{\partial \psi_m}{\partial r}) & \\ -\frac{\partial}{\partial r} r (D_L(\theta,\ \phi)\frac{\partial C_L^l}{\partial r}) & \\ -r(S_L + S_{1DS-3DS,L}) \quad &= \quad 0 \text{ for } \Omega \backslash \partial\Omega,\ t > t_0, \end{aligned} \tag{B-26}$$

$$K_{sat}\frac{\partial}{\partial r}\left(\kappa_m C_L^l \frac{\partial \psi_m}{\partial r}\right) + \frac{\partial}{\partial r}(D_L(\theta,\ \phi)\frac{\partial C_L^l}{\partial r}) \quad = \quad q_{exud,1DS-root} \text{ for } r = r_{in}, \tag{B-27}$$

$$K_{sat}\frac{\partial}{\partial r}\left(\kappa_m C_L^l \frac{\partial \psi_m}{\partial r}\right) + \frac{\partial}{\partial r}(D_L(\theta,\ \phi)\frac{\partial C_L^l}{\partial r}) \quad = \quad 0 \text{ for } r = r_{out}, \tag{B-28}$$

$$C_L^l \quad = \quad C_{L,0}^l, \text{ at } t = t_0 \tag{B-29}$$

Eq. (B-20) for high molecular weight organic C compounds gives:

$$r\frac{\partial \theta C_H^l}{\partial t} - \frac{\partial}{\partial r} r(D_H(\theta,\ \phi)\frac{\partial C_H^l}{\partial r}) \tag{B-30}$$

$$- r(S_H + S_{1DS-3DS,H}) = 0 \text{ for } \Omega \backslash \partial\Omega,\ t > t_0,$$

$$\frac{\partial}{\partial r}(D_H(\theta,\ \phi)\frac{\partial C_H^l}{\partial r}) = q_{mucil,1DS-root} \text{ for } r = r_{in}, \tag{B-31}$$

$$\frac{\partial}{\partial r}(D_H(\theta,\ \phi)\frac{\partial C_H^l}{\partial r}) = 0 \text{ for } r = r_{out}, \tag{B-32}$$

$$C_H^l = C_{H,0}^l, \text{ at } t = t_0 \tag{B-33}$$

The solute transport at the inner boundary of the domain corresponds to the exchange with the root (q_{exud} or q_{mucil}, see Eq. (3-16), (3-20)).

B.4 Soil reactions and microbial pools

Microorganisms can be modeled as a system of ordinary differential equations in time, (Pot et al., 2022), representing the to SOC mineralisaiton and CO_2 release caused by microbes (Pagel et al., 2020). We can describe the microbial behaviour by looking at community-level microbial traits (Bardgett and Caruso, 2020): recent studies indicate that soil bacterial communities are dominated by relatively few taxa with strong environmental preferences. Therefore a focus on the functional traits of dominant taxa can improve our understanding.
The equations in this section were adapted from the ones setup by Sircan et al. (2024). They present the microbe-driven soil reactions. The microbial community is divided in two main groups: oligotrophs (slower development and higher substrate affinity) and copiotrophs (quicker development and lower substrate affinity). The main differences with the equations presented by Sircan et al. (2024) are the explicit representation of the soil water content and its influence on microbial processes, and the non-instantaneous C sorption. We present below the list of reactions which sum up to $S_{microbe,X}$ for the organic C concentration of dissolved low molecular weight concentration (C_L^l) and high molecular weight compounds (C_H^l), as well as the connected microbial pools:

$$S_{microbe,L} = S_{depoly} + (1 - p_L)S_{decay} - S_{growth,L} - S_{Muptake,L} \tag{B-34}$$

$$S_{microbe,H} = -S_{depoly} + p_L S_{decay} \tag{B-35}$$

with S_{depoly} the depolymerisation rate of high molecular weight organic C compounds, S_{decay} the solute gain from microbial decay, $S_{growth,S}$ the dissolved low molecular weight organic C uptake for microbial growth, and $S_{Muptake,L}$ the dissolved low molecular weight organic C uptake for maintenance (all in $mol\ C\ C^{-3}\ scv\ d^{-1}$). p_L (mol/mol) is the proportion of high molecular weight organic C compounds to total C compounds formed from dead microbial biomass due to maintenance.
The reaction rates are dependent on the concentration of microbial pools. Like

Pagel et al. (2020), we define four microbial pools in the solid, described by their C concentration in the soil phase C_Z^Y ($mol\ C\ microbes/cm^3\ scv$). Y stands either for a (active microbes) or d (dormant microbes). Z stands for O (oligotrophes) or C (copiotrophes).
We define their respective variation thus:

$$\frac{\partial C_O^a}{\partial t} = S_{growth,O} - S_{deact,O} + S_{react,O} - \frac{1}{Y_M} S_{Mdecay,O}^a \tag{B-36}$$

$$\frac{\partial C_O^d}{\partial t} = S_{deact,O} - S_{react,O} - \frac{1}{Y_M} S_{Mdecay,O}^d \tag{B-37}$$

$$\frac{\partial C_C^a}{\partial t} = S_{growth,C} - S_{deact,C} + S_{react,C} - \frac{1}{Y_M} S_{Mdecay,C}^a \tag{B-38}$$

$$\frac{\partial C_C^d}{\partial t} = S_{deact,C} - S_{react,C} - \frac{1}{Y_M} S_{Mdecay,C}^d \tag{B-39}$$

$S_{growth,Z}$ corresponds to the growth of C_Z^a, $S_{decay,Z}^Y$ corresponds to the decay of $C_Z^{Y,s}$, $S_{deact,Z}$ represents the switch of C_Z^a to C_Z^d and $S_{react,Z}$ represents the switch of C_Z^d to C_Z^a . $S_{Mdecay,Z}^Y$ represents the loss of $C_Z^{Y,s}$ C because of maintenance. All rates are in $mol\ C\ cm^{-3}\ scv\ d^{-1}$. Y_M $(-)$ is the maintenance yield. The growth reaction rates are defined thus:

$$S_{growth,L} = \frac{1}{Y_O} S_{growth,O} + \frac{1}{Y_C} S_{growth,C} \tag{B-40}$$

$$S_{growth,O} = f_A(\psi_{m,soil}) \frac{\mu_{max,O}\ C_L^l\ k_{O,L}}{\mu_{max,O} + C_L^l k_{O,L}} C_O^a \tag{B-41}$$

$$S_{growth,C} = f_A(\psi_{m,soil}) \frac{\mu_{max,C}\ C_L^l\ k_{C,L}}{\mu_{max,C} + C_L^l\ k_{C,L}} C_C^a \tag{B-42}$$

$$f_A(\psi_{m,soil}) = \begin{cases} 1 - \left(\frac{log_{10}(\psi_{m,soil}/\psi_{m,soil,opt})}{log_{10}(\psi_{m,soil,th}/\psi_{m,soil,opt})} \right)^{\alpha}, & \psi_{m,soil} \in [\psi_{m,soil,th}, \psi_{m,soil,opt}] \\ 1, & \psi_{m,soil} > \psi_{m,soil,opt} \\ 0, & \psi_{m,soil} < \psi_{m,soil,th} \end{cases} \tag{B-43}$$

With Y_Z $(-)$ the growth yield of C_Z. $\mu_{max,Z}$ $(1/d)$ is the maximum growth rate of C_Z^a. $k_{O,L}$ $(cm^3\ scv\ d\ mol^{-1}\ C)$ is the C_Z^a affinity to C_L^l. $f_A(\psi_{m,soil})$ $(-)$ defines the water limitation on the access of the microorganisms and enzymes to the solutes (Moyano et al., 2013). The maintenance decay rates are defined thus:

$$S_{Mdecay} = S_{Mdecay,O}^a + S_{Mdecay,O}^d + S_{Mdecay,C}^a + S_{Mdecay,C}^d \tag{B-44}$$

$$S_{Mdecay,O}^a = k_{max,O} \overline{C_O^a} - S_{Muptake,L,O}^a \tag{B-45}$$

$$S_{Mdecay,O}^d = k_{max,O} \beta_O C_O^d - S_{Muptake,L,O}^d \tag{B-46}$$

$$S_{Mdecay,C}^a = k_{max,C} \overline{C_C^a} - S_{Muptake,L,C}^a \tag{B-47}$$

$$S_{Mdecay,C}^d = k_{max,C} \beta_C C_C^d - S_{Muptake,L,C}^d \tag{B-48}$$

$$\overline{C_O^a} = max(0., C_O^a - C_{O,lim}^a) \tag{B-49}$$

$$\overline{C_C^a} = max(0., C_C^a - C_{C,lim}^a) \tag{B-50}$$

$k_{max,Z}$ $(1/d)$ is the maximum maintenance rate coefficient for C_Z. β_Z $(-)$ is the reduction factor of maintenance requirements in dormant state for C_Z. $C^a_{Z,lim}$ $(mol\ C/cm^3\ scv)$ corresponds to the minimal value of C^a_Z below which the microbial pool can only be subjected to growth. This limitation allows us to have a re-development of the pool even if we have no solute in the soil for a period of time. We use consequently the limited $\overline{C^a_Z}$ $(mol\ C/cm^3\ scv)$ value for all reaction rates except for $S_{growth,Z}$. The uptake rates are defined thus:

$$S_{uptake,L} = S^a_{uptake,L,O} + S^d_{uptake,L,O} + S^a_{uptake,L,C} + S^d_{uptake,L,C} \tag{B-51}$$

$$S^a_{uptake,L,O} = f_A(\psi_{m,soil}) \frac{k_{max,O} C^l_L k_{O,L}}{k_{max,O} + C^l_L k_{O,L}} \overline{C^a_O} \tag{B-52}$$

$$S^d_{uptake,L,O} = f_A(\psi_{m,soil}) \frac{k_{max,O} C^l_L k_{O,L}}{k_{max,O} + C^l_L k_{O,L}} \beta_O C^d_O \tag{B-53}$$

$$S^a_{uptake,L,C} = f_A(\psi_{m,soil}) \frac{k_{max,C} C^l_L k_{C,L}}{k_{max,C} + C^l_L k_{C,L}} \overline{C^a_C} \tag{B-54}$$

$$S^d_{uptake,L,C} = f_A(\psi_{m,soil}) \frac{k_{max,C} C^l_L k_{C,L}}{k_{max,C} + C^l_L k_{C,L}} \beta_C C^d_C \tag{B-55}$$

The deactivation and reactivation rates are defined thus:

$$S_{deact,O} = \max((1-\phi_O), f_{A2D}(\psi_{m,soil})) k_{d,O} \overline{C^a_O} \tag{B-56}$$

$$S_{deact,C} = \max((1-\phi_C), f_{A2D}(\psi_{m,soil})) k_{d,C} \overline{C^a_C} \tag{B-57}$$

$$S_{react,O} = \min(\phi_O, f_{D2A}(\psi_{m,soil})) k_{r,O} C^d_O \tag{B-58}$$

$$S_{react,C} = \min(\phi_C, f_{D2A}(\psi_{m,soil})) k_{r,C} C^d_C \tag{B-59}$$

$$\phi_O = \frac{1}{e^{\frac{C^l_{thres,O} - C^l_L}{aC^l_{thres,O}}} + 1} \tag{B-60}$$

$$\phi_C = \frac{1}{e^{\frac{C^l_{thres,C} - C^l_L}{aC^l_{thres,C}}} + 1} \tag{B-61}$$

$$f_{A2D}(\psi_{m,soil}) = \frac{1}{1 + [\psi_{m,soil,A2D}/\psi_{m,soil}]^{\omega_{DA}}} \tag{B-62}$$

$$f_{D2A}(\psi_{m,soil}) = \frac{1}{1 + [\psi_{m,soil}/(\tau\ \psi_{m,soil,A2D})]^{\omega_{DA}}} \tag{B-63}$$

with $k_{d,Z}$ and $k_{r,Z}$ $(1/d)$ respectively the deactivation and reactivation rate coefficients for C_Z. $C^l_{thres,Z}$ $(mol\ C/cm^3\ water)$ is the C^l_L threshold for ϕ_Z. ϕ_Z $(-)$ is the switch function defining the effect of C^l_L on microbial dormancy ($S_{deact,Z}$ and $S_{react,Z}$), while f_{A2D} and f_{D2A} $(-)$ define the effect of soil water content (see Wang et al. (2021)). The increase of the deactivation (resp. decrease of the activation) is defined by the most limiting resource between dissolved low molecular weight organic C and water. For instance, when water limiting for microbial activation, we will have $\min(\phi_Z, f_{D2A}(\psi_{m,soil})) = f_{D2A}(\psi_{m,soil})$ or

$\max((1-\phi_Z), f_{A2D}(\psi_{m,soil})) = f_{A2D}(\psi_{m,soil})$. Finally, we get the depolymerisation rate (Pagel et al., 2020):

$$S_{depoly} = f_A(\psi_{m,soil}) v_{max,depoly} \frac{C_H^l}{K_L + C_H^l} \overline{C_O^a} \tag{B-64}$$

With $v_{max,depoly}$ $(1/d)$ is the maximum reaction rate of enzymes targeting high molecular weight organic C compounds, K_L $(mol/cm^3\ water)$ half-saturation coefficients of enzymes targeting high molecular weight organic C compounds.
From the reactions defined above, we also get C_{co2} $(mol\ C/cm^3\ scv)$, the amount of C released:

$$\frac{\partial C_{co2}}{\partial t} = \frac{1-Y_O}{Y_O} S_{growth,O} + \frac{1-Y_C}{Y_C} S_{growth,C} + \frac{1-Y_M}{Y_M} S_{Mdecay} + S_{Muptake} \tag{B-65}$$

Although we do compute the amount of C released, we do not simulate its transport in the domain.

B.5 Growth of existing 1D axisymmetric soil models

Once the 1D domain volumes at time step N have been computed (see Eq. (3-26)), the redistribution of the water and C between the microscale domains of a voxel are done in 2 steps:

1. Compute the new water volume and solute content in the pre-existing microscale domains that have shrunk while trying to maintain the radial concentration gradients.

2. Compute the water volume and C content of the new microscale domains and of the pre-existing microscale domaines that have grown. We define for each voxel a mean water content and C concentration from the leftover water volume, C content, and voxel space. There is no concentration gradient in the newly added microscale space.

We set m_X (mol) as the content of the C element X with the concentration C_X, and V_w $(cm^3\ water)$ the water volume.

B.5-1 Shrinking 1D axisymmetric soil models

For perirhizal zone with a volume decrease between time step $N-1$ and N, we adapt m_X in each soil voxel so that, for the segment k:

$$ChangeRatioS_k = \frac{m_{x,k}^N}{m_{X,k}^{N-1}}$$

$$ChangeRatioW_k = \frac{V_{w,k}^N}{V_{w,k}^{N-1}}$$

We set $ChangeRatioS$ and $ChangeRatioW$ so that the microscale domain will lose or gain water and solute according to the volume change. $ChangeRatioW$ is also adapted to keep $\theta \in [\theta_{wiltingpoint}, \theta_s]$. $\theta_{wiltingpoint}$ is the soil water content when $\psi = \psi_{crit}$ the critical plant water potential. Consequently:

$$ChangeRatioS_k = min(\frac{V_{1DS,scv,k}^N}{V_{1DS,scv,k}^{N-1}}, 1) \tag{B-66}$$

$$ChangeRatioW_k = max(min(ChangeRatioS_k, \frac{\theta_s\ V_{1DS,scv,k}^N}{V_{w,k}^{N-1}}), \frac{\theta_{wiltingpoint}\ V_{1DS,scv,k}^N}{V_{w,k}^{N-1}}) \tag{B-67}$$

We also want to keep the radial concentration gradients:

$$\frac{\partial C_k^N}{\partial r} = \frac{\partial C_k^{N-1}}{\partial r} \tag{B-68}$$

$$\frac{\partial \theta_k^N}{\partial r} = \frac{\partial \theta_k^{N-1}}{\partial r} \tag{B-69}$$

For the discretised microscale domain made of n segments, this gives us a set of equations that can be solved analytically. In matricial form:

$$\mathcal{B} = Q^{-1}G \tag{B-70}$$

With Q a matrix of size $[n, n]$:

$$Q = \begin{bmatrix} -1 & 1 & 0 & ... & 0 \\ 0 & -1 & 1 & ... & 0 \\ 0 & ... & ... & ... & 0 \\ 0 & ... & ... & -1 & 1 \\ V_{0,k}^N & V_{1,k}^N & ... & V_{n-1,k}^N & V_{n-1,k}^N \end{bmatrix} \tag{B-71}$$

And G an array of size n:

$$G = \begin{bmatrix} b_{r_{1,k}^N}^{N-1} - b_{r_{0,k}^N}^{N-1} \\ ... \\ ... \\ b_{r_{n,k}^N}^{N-1} - b_{r_{n-1,k}^N}^{N-1} \\ B_k^{N-1} ChangeRatio_k^N \end{bmatrix} \tag{B-72}$$

B_k^N is the total amount of the solute or of water (in mol or cm^3) and b is the solute concentration or water content. The last lines of G and Q assure that we

obtain the correct total solute and water amount, the other lines represent the wished for gradient between the new location of the segment centers. The value of $b^{N-1}_{r^N_{1,k}} - b^{N-1}_{r^N_{0,k}}$ give the changes of b (at $N-1$) between the segment centers (distance at N). It is obtained by interpolation of the concentration gradients between the segments centers at the end of time step $N-1$.
$ChangeRatioW_k$ and $ChangeRatioS_k$ ensure that the overall θ and m_k in the whole microscale domain remains within the needed range, but not for each segment. Consequently, when implementing the new water value for each microscale segment, we adapt the distribution of the water between the segments to have for each segment $\theta \in [\theta_{wiltingpoint}, \theta_s]$. Likewise, we ensure that $min(m_k) \geq 0$.
This yields $C^{N,0,-1}_{1DS}$ and $\theta^{N,0,-1}_{1DS}$ to be used at the beginning of the next fixed point loop iteration, see section B.6.

B.5-2 New and expanding 1D axisymmetric soil models

From the concentration of the existing microscale domains per voxel, we compute the mean θ_{new} and C_{new}, the water and concentration in the newly freed soil space. θ_{new} and C_{new} will define the initial conditions of the added volume in the expanding or new microscale domains. For this, we compute the total volume of the newly freed volume in the voxel ($V^N_{3DS,scv,leftover}$, cm^3):

$$V^N_{3DS,scv,i,leftover} = \sum_{j}^{nr^N_{shrunk,i}} L_{j,N}\pi({r^N_{out,j}}^2 - r^2_{in,j}) \tag{B-73}$$

with $nr^N_{shrunk,i}$ the sets of microscale domains in voxel i that have shrunk at time step N. We then get the content of water and C that are not in the old microscale domains of voxel i anymore:

$$V^N_{3DS,w,i,leftover} = \sum_{j}^{nr^N_{shrunk,i}} V^{N-1}_{1DS,w,j} - V^N_{1DS,w,j} \tag{B-74}$$

$$m^N_{3DS,X,i,leftover} = \sum_{j}^{nr^N_{shrunk,i}} m^{N-1}_{1DS,X,j} - m^N_{1DS,X,j} \tag{B-75}$$

We can then get θ_{new} and C_{new}:

$$\theta^N_{k,new} = \begin{cases} \frac{V^N_{3DS,w,i,leftover}}{V^N_{3DS,scv,i,leftover}} & \text{if} \quad len(nr^{N-1}_i) > 0 \\ \frac{V^{N-1}_{3DS,w,i}}{V^{N-1}_{3DS,scv,i}} & \text{else} \end{cases} \tag{B-76}$$

$$C^{y,N}_{k,new} = \begin{cases} \frac{X^N_{i,leftover}}{V^N_{3DS,i,leftover}} & \text{if} \quad len(nr^{N-1}_i) > 0 \\ \frac{X^{N-1}_i}{V^{N-1}_{3DS,i}} & \text{else} \end{cases} \tag{B-77}$$

$$V_{3DS,i,leftover} = \begin{cases} V_{3DS,w,i,leftover} & \text{if} \quad C^y = C^l \\ V_{3DS,scv,i,leftover} & \text{if} \quad C^y = C^s \end{cases} \tag{B-78}$$

$$V_{3DS,i} = \begin{cases} V_{3DS,w,i} & \text{if} \quad C^y = C^l \\ V_{3DS,scv,i} & \text{if} \quad C^y = C^s \end{cases} \tag{B-79}$$

We can then add the C and water to the growing microscale domains (the C concentration is null for newly created domains):

$$\theta^{N,0,-1}_{1DS} = \theta^{N-1}_{1DS} + \theta^N_{k,new}\Delta V_{1DS,scv,k} \tag{B-80}$$

$$C^{N,0,-1}_{1DS} = C^{N-1}_{1DS} + C^N_{k,new}\Delta V_{1DS,scv,k} \tag{B-81}$$

We then use the method presented in section B.5-1 to obtain the θ and C_X value for each microscale segment respecting the new content and trying to maintain the old concentration gradients. This yields $C^{N,0,-1}_{1DS}$ and $\theta^{N,0,-1}_{1DS}$ to be used at the beginning of the next fixed point loop iteration, see section B.6.

B.6 Pseudo-code of the iterative computation loop

The three models (plant, 1D microscale soil, 3D macroscale soil) are coupled using an iterative approach based on the method Jorda Guerra et al. (2021). In the following section, we present the implementation of the equations defined above, in matricial form and for one time step N. Although the water and C balances are computed together, for clarity, the descriptions of their respective computation loops are presented separately.

B.6-1 Definition of matrices

For the section below, M represents a matrix of size $[ns,\ nr]$, with ns the number of soil voxels and nr the number of root segments belowground (equal to the number of microscale domains). Other variables include vectors of size nr with root, root-soil interface or microscale soil values (with respectivelly the subscripts $root$, rsi, $1DS$). The root-soil interface corresponds to the 1D segment at the inner boundary of the microscale models. Vectors with the subscript $3DS$ give the macroscale soil values and are of size ns. $V_{V,w}$ (cm^3 $water$), θ, ψ, C_X and $\mathbf{m_x}$

($mol\ C$), K_{sri} ($cm^2\ hPa^{-}1\ d^{-1}$) are vectors giving respectively the water volume, water content, water potential, component concentration, component content, and hydraulic conductivity at the soil-root interface. $V_{surf,out}$ (cm^2) is a vector of size nr and $V_{surf,out}[i] = 2\pi\ r_{out,i}\ L_{r,i}$, giving the surface at the outer boundary of the perirhizal zone i. Similarly, $V_{surf,in}[i] = 2\pi\ r_{in,i}\ L_{r,i}$ gives the surface at the inner boundary. $V_{V,scv,3DS}$ (resp. $V_{V,scv,1DS}$) is a vector of size ns (resp. nr) giving the volume of each voxel (resp. of each microscale domain). The source vector is obtained from $\mathbf{S} = SV_V$ and is thus in $cm^3\ water\ d^{-1}$ or in $mol\ d^{-1}$. M_c is a binary matrix. M_c is filled with 0 except for $M_c[i,\ j] = 1$, when the j^{th} root segment (and corresponding 1D soil domain) is in the i^{th} soil voxel. $V_{hasRoot}$ is a vector of size ns with 1 for the macroscale soil voxels with at least one root and 0 elsewhere. We set:

$$M_{surf,in} = M_c \circ V_{surf,in}$$

with $\circ$ the hadamard product and $M_{surf,in}$ a matrix of size $[ns,\ nr]$ giving the inner surface of the microscale domain for each soil voxel. $Q_{w,3DS-3DS}$ ($cm^3\ water\ d^{-1}$), and $Q_{X,3DS-3DS}$ ($mol\ C\ d^{-1}$) are vectors of size ns giving, for all the voxels containing at least one root, the changes in water or C (for a specific component)caused by exchanges with other voxels (i.e., not caused by input from a root or from biochemical reactions). $M_{weight,X}$ is the weight matrices used to divide voxel flows ($Q_{3DS-3DS}$) between the microscale domains in each voxel (see Eq. (B-8),(B-23))

B.6-2 Fixed point iteration for the water flow

The pseudo-code below presents the implementation of the fixed-point iteration loop for the water flow.

(A) $L^N_{root}, M^N_c = \mathbf{Growth}(\mathrm{Env}^N, \mathbf{C}^{st,N-1}_L,\ \psi^{N-1}_x)$

$M^N_{surf,in}, V^N_{surf,in}, V^N_{surf,out}, \theta^{N,0,-1}_{1DS}, \psi^{N,0,-1}_{rsi} =$

$\mathbf{Distribute}(L^N_{root}, M^N_c, \theta^{N-1}_{1DS})$

$Q^{N,0,-1}_{w,3DS} = Q^{N-1}_{w,3DS},\ \theta^{N,0,-1}_{3DS} = \theta^{N-1}_{3DS}$ (B-82)

for n in range($\frac{\Delta\ t}{\delta\ t}$):

while any($\mathrm{err}_{...} > \epsilon_{...}$), and $k < k_{max}$:

(B) $q^{N,n,k}_{w,root-soil},\ \psi^{N,n,k}_x = \mathbf{FlowPhoto}(\mathrm{Env}^{N,n},\ \psi^{N,n,k-1}_{rsi})$ (B-83)

(C) $S^{N,n,k}_{w,1DS-3DS} = -\ M^{N,n,k,T}_{weight,w} Q^{N,n,k-1}_{w,3DS}$ (B-84)

$K^{N,n,k}_{sri}, \theta^{N,n,k}_{1DS}, q^{N,n,k,limited}_{w,root-soil} = \mathbf{Flow}(V^N_{surf,in} q^{N,n,k}_{w,root-soil}\delta t,$

$\mathbf{S}^{N,n,k}_{w,1DS-3DS}\delta t,\ \theta^{N,n,k-1}_{1DS}, V^N_{V,scv,1DS})$ (B-85)

$\mathbf{S}^{N,n,k}_{w,3DS} = M^N_{surf,in} q^{N,n,k,limited}_{w,root-soil}$ (B-86)

(D) $\theta^{N,n,k}_{3DS}, Q^{N,n,k}_{w,3DS} = \mathbf{Flow}(\mathbf{S}^{N,n,k}_{w,3DS}\delta t,\ \theta^{N,n,k-1}_{3DS}, V_{V,scv,3DS})$ (B-87)

(E) $\mathrm{errW}^{N,n,k}_{1DS,3DS,cumul} = \mathbf{Err}(M_c[\theta^{N,n,k}_{1DS}\ V^N_{V,scv,1DS}] -$

$[\theta^{N,n,k}_{3DS}\ V_{V,scv,3DS}])$ (B-88)

$\mathrm{errW}^{N,n,k}_{1DS,3DS} = \mathrm{errW}^{N,n,k}_{1DS,3DS,cumul} - \mathrm{errW}^{N,n-1}_{1DS,3DS,cumul}$ (B-89)

$\mathrm{errW}_{k,k-1} = \mathbf{Err}(X^{N,n,k} - X^{N,n,k-1})$ (B-90)

$\mathrm{errW}_{qroot} = \mathbf{Err}(q^{N,n,k,limited}_{w,root-soil} - q^{N,n,k}_{w,root-soil})$ (B-91)

$\mathrm{errW}_{mass1DS} = \mathbf{Err}(\theta^{N,n,k}_{1DS} V^N_{V,scv,1DS} - [\theta^{N,n,IC}_{1DS} V^N_{V,scv,1DS} +$

$(V^N_{surf,in} q^{N,n,k}_{w,root-soil} + \mathbf{S}^{N,n,k}_{w,1DS-3DS} S^{N,n,k}_{w,1DS-1DS})\Delta t])$ (B-92)

$\mathrm{errW}_{mass3DS} = \mathbf{Err}(\sum^{segments} (\theta^{N,n,k}_{3DS} V_{Vscvw,3DS} - [\theta^0_{3DS} V_{V,scv,3DS}$

$+ \sum^{N}_{j} (M^j_{surf,in} q^j_{w,root-soil}\delta t^j)]))$ (B-93)

assert $\mathrm{err}_{...} \leq \epsilon_{...}$ (B-94)

$\psi^{N,n+1,-1}_{rsi} = \psi^{N,n,k}_{rsi},\ \theta^{N,n+1,-1}_{1DS} = \theta^{N,n,k}_{1DS}$

$Q^{N,n+1,-1}_{w,3DS} = Q^{N,n,k}_{w,3DS},\ \theta^{N,0,-1}_{3DS} = \theta^{N-1}_{3DS}$ (B-95)

N (resp. Δt) is the step index (resp. time step) of the whole computation loop and n (resp. δt) is the step index (resp. time step) of the fixed point iteration. k is the iteration number of the fixed point iteration and k_{max} the maximum amount of iteration allowed. Env represents other environmental conditions, L_{root} (cm) is a vector which contains the length of each root segment (and thus microscale domain).

The T superscript gives the transpose of a matrix. **Flow** represents a function computing the water flow and **FlowPhoto** the coupled plant water flow and

photosynthesis. **Distribute** corresponds to the division of the voxel volume and water between the microscale domains according to the methods presented in section 3-2-2-6. $\text{err}_{1DS,3DS,cumul}$ gives the difference between the water content values computed at the micro- and macroscale and $\text{err}_{1DS,3DS}$ the difference added at the last time step. err_{qroot} is the difference between the root water uptake rates computed by the plant and the microscale soil. err_{mass} gives the mass balance error, $\text{err}_{k,k-1}$ the output differences between the last two iterations (non-convergence). **Err** is a function to sum and normalise the error. $\text{err}_{...}$ corresponds to each of the errors computed within the iteration loop, and $\epsilon_{...}$ is their respective maximum value allowed.

B.6-3 Fixed point iteration for the solutes transport

The pseudo-code below presents the implementation of the fixed-point iteration loop for the C transport.

(A) $L^N_{root}, M^N_c, q^N_{X,root-soil},\ C^{st,N}_{X,root} = \mathbf{Growth} \circ \mathbf{TransportReac}(\mathrm{Env}^N,$
$\sum_j^n (A^{N-1,j}_n \delta t^{N,j}),\ C^{N-1}_{X,rsi})$ (B-96)

$M^N_{surf,in}, V^N_{surf,in}, V^N_{surf,out}, C^{N,0,-1}_{X,1DS} =$
$\mathbf{Distribute}(L^N_{root}, M^N_c, C^{N-1}_{X,1DS})$ (B-97)

$Q^{N,0,-1}_{X,3DS} = Q^{N-1}_{X,3DS},\ C^{N,0,-1}_{X,3DS} = C^{N-1}_{X,1DS}$ (B-98)

for n in range($\frac{\Delta\ t}{\delta\ t}$):

while any(err$_{...}$ $>$ $\epsilon_{...}$), and k $<$ k_{max}:

(B) $q^{N,n,k}_{X,root-soil},\ A^{N,n,k}_n = \mathbf{TransportPhoto}(\mathrm{Env}^{N,n},\ \psi^{N,n,k-1}_{rsi})$ (B-99)

(C) $\mathbf{S}^{N,n,k}_{X,1DS-3DS} = -M^{N,n,k,T}_{weight,X} Q^{N,n,k-1}_{X,3DS}$ (B-100)

$C^{N,n,k}_{X,1DS}, \mathbf{m}^{N,n,k}_{X,1DS} = \mathbf{TransportReac}(V^N_{surf,in} q^N_{X,root-soil}\delta t,$
$\mathbf{S}^{N,n,k}_{X,1DS-3DS}\delta t, C^{N,n,k}_{X,1DS}, \theta^{N,n,k}_{1DS})$ (B-101)

$\mathbf{S}^{N,k}_{X,3DS} = M^N_c((\mathbf{m}^{N,n,k}_{X,1DS} - \mathbf{m}^{N,n-1}_{X,1DS})/\delta t + \mathbf{S}^{N,n,k}_{X,1DS-3DS})$ (B-102)

(D) $C^{N,n,k}_{X,3DS}, Q^{N,n,k}_{X,3DS} = V_{hasRoot}\mathbf{Transport}(\mathbf{S}^{N,n,k}_{X,3DS}\delta t,\ \mathbf{C}^{N,n-1}_{X,3DS})$
$+ (1 - V_{hasRoot})\mathbf{TransportReac}(\mathbf{C}^{N,n-1}_{X,3DS})$ (B-103)

(E) $\mathrm{errC}_{1DS,3DS,cumul} = \mathbf{Err}(M^N_c \mathbf{m}^{N,k}_{\mathbf{x}1DS} - \mathbf{m}^{N,k}_{\mathbf{x}3DS})$ (B-104)

$\mathrm{errC}^{N,n,k}_{1DS,3DS} = \mathrm{errC}^{N,n,k}_{1DS,3DS,cumul} - \mathrm{errC}^{N,n-1}_{1DS,3DS,cumul}$ (B-105)

$\mathrm{errC}_{k,k-1} = \mathbf{Err}(X^{N,n,k} - X^{N,n,k-1})$ (B-106)

$\mathrm{errC}_{mass1DS} = \mathbf{Err}(\sum_{comp}^{NComp} (\mathbf{m}^{N,k}_{X,1DS} - [\mathbf{m}^{N-1}_{X,1DS}$
$+ (V^N_{surf,in} q^{N,k}_{X,root-soil} + S^{N,k}_{x,1DS-1DS} + S^{N,k}_{x,1DS-3DS})\Delta t]))$ (B-107)

$\mathrm{errC}_{mass3DS} = \mathbf{Err}(\sum^{segments}\ (\sum_{comp}^{NComp} (\mathbf{m}^N_{X,3DS} - [\mathbf{m}^0_{X,3DS}$ (B-108)
$+ \sum_n^N M^n_{surf,in} q^n_{X,root-soil}\Delta t)]))))$

assert err$_{...} \leq \epsilon_{...}$ (B-109)

$\mathbf{m}^{N,n+1,-1}_{X,1DS} = \mathbf{m}^{N,n,k}_{X,1DS},\ C^{N,n+1,-1}_{X,1DS} = C^{N,n,k}_{X,1DS}$ (B-110)

$Q^{N,n+1,-1}_{X,3DS} = Q^{N,n,k}_{X,3DS},\ C^{N,n+1,-1}_{X,3DS} = C^{N,n,k}_{X,3DS}$ (B-111)

TransportReac represents the implementation of a function computing biochemical reactions and solute transport according to input variables. We need to sum all the components for the solute mass balance (err_{mass}). A_n is the net assimilation of sucrose, thus $A_n \neq 0$ only for dissolved low molecular weight

organic C (C_L^l and $\mathbf{m}_L$). $Q_{X,3DS} \neq 0$ only for the C of dissolved low molecular weight organic compounds and high molecular weight organic compounds.

B.7 Soil parameters and process constraints

The tables below present the parameter and process constraints defined for TraiRhizo by Sircan et al. (2024). Baseline soil corresponds to the soil outside the rhizosphere.

Table B.3: TraiRhizo parameter constraints defined by Sircan et al. (2024)

	Constraint	Description/ Explanation
1	$\mu_{max,C} > \mu_{max,O}$	Maximum growth rate of copiotrophs is higher than maximum growth rate of oligotrophs.
2	$k_{O,S} > k_{C,S}$	Specific substrate affinity to small molecules for oligotrophs is higher than for copiotrophs.
3	$k_{max,C} > k_{max,O}$	Maximum maintenance rate coef. must be higher for copiotrophs than for oligotrophs.
4	$C_{thresh,C} > C_{thresh,O}$	Oligotrophs (K-strategists) are adapted to low carbon and nutrient availability.
5	$k_{max,i} < \mu_{max,i}$ $i \in \{O, C\}$	It is a logical constraint to ensure organisms "fit to survive".
6	$k_{r,i} \geq k_{d,i}$ $i \in \{O, C\}$	Transition to dormant (or potentially active) state is typically slower than reactivation.
7	$k_{j,i} > \mu_{max,i}$ $i \in \{O, C\}$, $j \in \{r, d\}$	Changes of metabolic state are faster than growth, death, and changes in composition
8	$Y_O > Y_C$	Oligotrophs are slow growing at high yield, copiotrophs are fast-growing at low yield

B.8 Lateral root water conductivity in the mature root zone

The mature root area as well as the root water conductivity ($k_{lat,x}$, $cm\ hPa^{-1}\ d^{-1}$) values for the immature zone are taken from Giraud et al. (2023). However, in that study, $k_{lat,x} = 0$ in the mature root area (more than 0.8 cm away from the root tip). To obtain more realistic results, we used the work of Bramley et al. (2007) to evaluate the $\frac{k_{lat,x,mature}}{k_{lat,x,immature}}$ ratio. Bramley et al. (2007, Fig. 4.15) defines the surface-normalised root resistance $k_{tot,x}$ in $m\ s^{-1}\ MPa\ 10^{-8}$ over the length l (m) from the tip as: $k_{tot,x}(l) = (-83 \times l + 20.9) \times 1e-8$ and the mean root conductance (in $m^3\ s^{-1}\ MPa\ 10^{-11}$) as $K_{tot,x}(l) = (0.7 \times l + 2.4) \times 1e-11$. We can therefore obtain the side surface of the root segment (A in m) up to l cm from $A(l) = \frac{K_{tot,x}(l)}{k_{tot,x}(l)}$. Moreover, in their study, the root axial

Table B.4: TraiRhizo process constraints adapted from the ones defined by Sircan et al. (2024). [a]: The lower bound of the constraints was decreased by 10% compared with the value defined by Sircan et al. (2024). [b]: The lower bound of the constraints was decreased by 10% compared with the value defined by Sircan et al. (2024).

	Constraint	Description/ Explanation
1	$3.33e^{-6} < (C_O + C_C)_R < 1e^{-4}\ mol\ cm^{-3}$	The range for the concentration of microbial biomass in the rhizosphere from literature for different soil types, textures, experimental conditions.
2^a	$0.9 < (\frac{(C_O+C_C)_R}{(C_O+C_C)_B} < 2.5$	Microbial biomass is higher in the rhizosphere than baseline soil and lower than a threshold value which is set up from literature.
3^b	$3.33e^{-4} < (C_L^l + C_H^l)_R < 1.33e^{-3} \times 1.1\ mol\ cm^{-3}$	The range for soil organic carbon in the rhizosphere for different soil types, textures, experimental conditions.
4^b	$0.66 < \frac{(C_L^l+C_H^l)_R}{(C_L^l+C_H^l)_B} < 2 \times 1.1$	The range for ratio of soil organic carbon in the rhizosphere to baseline soil for different soil types, textures, experimental conditions.
5	$6e^{-4} < (\frac{C_O^a+C_C^a}{C_O+C_C})_R < 0.6$	The range for ratio of active microbial biomass to total microbial biomass for different soil types, textures, experimental conditions.
6	$C_{L,R}^l < 4.58e^{-5}\ mol\ cm^{-3}$	Based on water extractable organic carbon measurements. Water extractable organic carbon should include dissolved organic carbon (DOC) together with some sorbed carbon mass therefore it must be higher than the DOC concentration.
7^a	$0.9C_{L,B}^l < C_{L,R}^l$	Based on water extractable organic carbon measurements.
8^a	$0.9C_{C,R} > C_{O,R}$	The rhizosphere is dominated by copiotrophs.
9	$\frac{C_{C,B}}{C_{O,B}} < \frac{C_{C,R}}{C_{O,R}}$	

resistance was found to be negligible, and we get therefore $k_{lat,x}(l) = k_{tot,x}(l)$ and $K_{lat,x}(l) = K_{tot,x}(l)$. We assumed that the mean $k_{lat,x}$ over the assumed immature root zone could be defined as $k_{lat,x,immature} \approx k_{lat,x}(0.008)$. We then evaluated $K_{lat,x}$ between $l_1 = 0.07\ m$ from the tip and $l_2 = 0.18\ m$ from the tip, which were the range of distances used in their study. We then computed $\int_{l1}^{l2} A(l)dl$ and $\int_{l1}^{l2} K_{lat,x}(l)dl$. From this we could get $\int_{l1}^{l2} k_{lat,x}(l)dl = \frac{\int_{l1}^{l2} K_{lat,x}(l)dl}{\int_{l1}^{l2} A(l)dl}$. This yielded $\frac{k_{lat,x,mature}}{k_{lat,x,immature}} = \frac{\int_{l1}^{l2} k_{lat,x}(l)dl}{k_{lat,x}(0.008)} \times 100 = 1.45\% \approx 1.5\%$. We consequently set $k_{lat,x,mature} = 0.015 k_{lat,x,immature}$ for our modelling study.

B.9 Calibration of the soil carbon dynamic

This section describes the method used to calibrate the soil C dynamic. The objective was to implement a simple method allowing us to select sets representing different dynamics. A summary of the characteristics of each of the three selected microbial parameter sets is given in table 3-2.

B.9-1 Selection of the TraiRhizo parameter sets

In their study, Sircan et al. (2024) defined 1650 parameter sets for TraiRhizo model according to a series of parameter and process constraints, which are given in appendix B.7. The 1650 parameter sets were divided in three groups according to the resulting gradients of C_L^l directly at the root surface—small, medium, or strong gradient. [a] We randomly selected 33 sets in each of the three gradient categories. Then, we ran the coupled model on the (adapted) parameterised plant of Giraud et al. (2023) between days 10 and 14 of growth (with dynamic soil water and C flows). [b] Sets that did not respect the process constraints defined by Sircan et al. (2024) were removed–see Table B.4. [c] From the 12 remaining sets, we selected three sets representing different soil C dynamics. For step [a], we ran the simulation without water scarcity effect–meaning, without implementing the effect of water on microbial (de)activation (Eq. (B-62), (B-63)) and access to soil solutes (Eq. (B-43)). For step [b], following the method of (Sircan et al., 2024) and the analysis of Kuzyakov and Razavi (2019), we defined the rhizosphere as the soil volume up to 3 mm from the root surface. The baseline soil (soil outside of the rhizosphere) values were taken from the macroscale voxel data at the bottom of the soil column. We retained the sets that respected all the constraints for all the rhizosphere units at the end of the simulation. In some cases, some perirhizal zone units were slightly outside the constraints' bounds. To retain those sets, some constraint bounds were enlarged by 10%. These bounds-relaxations are indicated in table B.4.

Figure B.1 gives the concentration of different C pools along the soil depth. The first set led to a high CO_2 production in spite of a low microbial development, and was named *highCO2*. The second set led to a high development of the microbial biomass and was named *highMB*. The last set led to low solute mineralisation and microbial development. It was named *lowMUptake*.

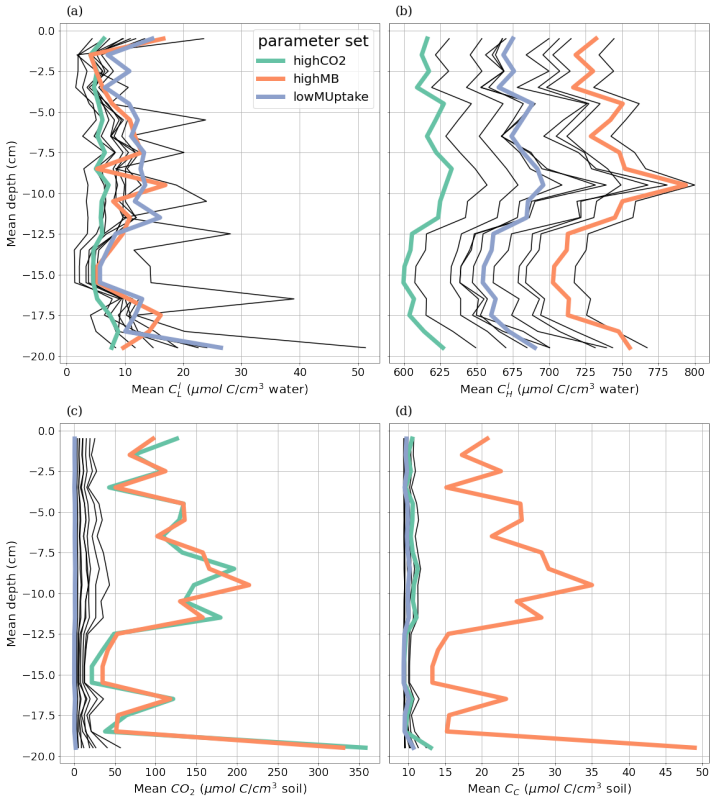

Figure B.1: Mean carbon concentration along the depth after four days of simulation (day 10 to 14) for concentrations of carbon from high (C_H^l) and dissolved low (C_L^l) molecular weight organic compounds, emitted CO_2, and copiotroph carbon (C_C), in the 3D soil voxels which contain at least one root segment (perirhizal zone). The line colour gives the index of the parameter set. Only parameter sets that respect the process constraints defined by Sircan et al. (2024) after four simulation days are represented. The selected sets are *highCO2* (green line), *highMB* (orange line) and *lowMUptake* (purple line).

B.9-2 Description of the selected TraiRhizo parameter sets

B.9-2-1 Distribution of the parameter values

Figs. B.2 and B.3 present frequency histograms for each of the parameters in the 1650 sets. The parameters pointed by the numbered arrows correspond to the parameters of the three selected sets (*highCO2*, *highMB*, *lowMUptake*). As we can see, several of the parameter distributions are strongly skewed to the right, making some of the higher values outliers. Therefore, the sets containing the higher parameter values are more likely to give different outputs when compared with the other sets.
From the parameter values, we can give a description of the selected sets:
All three parameter sets offer low β_C (activity of dormant copiotrophs), $k_{C,S}$ (copiotroph affinity to dissolved low molecular weight organic C compounds), $k_{d,C}$, $k_{d,O}$ (deactivation rates), $k_{max,C}$, $k_{max,O}$ (maintenance rates), $\mu_{max,C}$, $\mu_{max,O}$ (growth rates), $v_{max,depoly}$ (depolymerisation rates of high molecular weight organic C compounds) values. This follows the average values of the 1650 sets and lead to a lower microbial activity and slower deactivation. Moreover, the sets have higher than average D_{LW} values, which should smooth the distribution of C_L^l. As can be seen more clearly in Fig. B.3, we have an equilibrium between $k_{d,O}$ and $k_{r,O}$: the sets with higher $k_{d,O}$ also have higher $k_{r,O}$. All sets have a higher $k_{r,C}$ leading to a quick reactivation rate of the copiotrophs. Finally, the three sets have similar C_{init}^l values, and, in particular, a higher than average $C_{L,init}^l$.
highCO2 stands out by its higher β_O value, leading to a higher activity for dormant oligotrophs. Moreover, this sets has the higher D_{LW} values. Finally, the low growth yield (Y_C, Y_O) may lead to higher C usage and CO_2 emission rates.
highMB has higher activation rate parameters ($k_{r,O}$, $k_{r,C}$) linked with low C_{thres} parameters, which should lead to a high activated-to-total microbial biomass, although the deactivation parameter for oligotrophs ($k_{d,O}$) is also high. The relatively higher affinity parameters ($k_{C,S}$, $k_{O,S}$) and growth parameters ($\mu_{max,C}$, $\mu_{max,O}$) should lead to a quicker increase of the microbial biomass. The low Y (yield parameters) should also lead to higher C usage and CO_2 emissions.
lowMUptake stands out for its low activation rate parameters ($k_{r,O}$, $k_{r,C}$) linked with high C_{thres} parameters, which should lead to a high activated-to-total microbial biomass, although the deactivation parameters ($k_{d,C}$, $k_{d,O}$) are also low. Low maintenance need for dormant microbes (β_C, $beta_O$) and high yield parameters (Y, Y_C, Y_O) should also lead to a lower C usage and CO_2 emissions.

B.9-2-2 Distribution of output variables under different values of dissolved low molecular weight organic carbon

We computed for a range of C_L^l values intermediary outputs describing the microbial dynamic:

- ϕ_O (ϕ_C), $-$: ratio of oligotrophs (copiotrophs) which will be activated
- S_{decay}, $mol\ C\ cm^{-3}\ d^{-1}$: decay rate

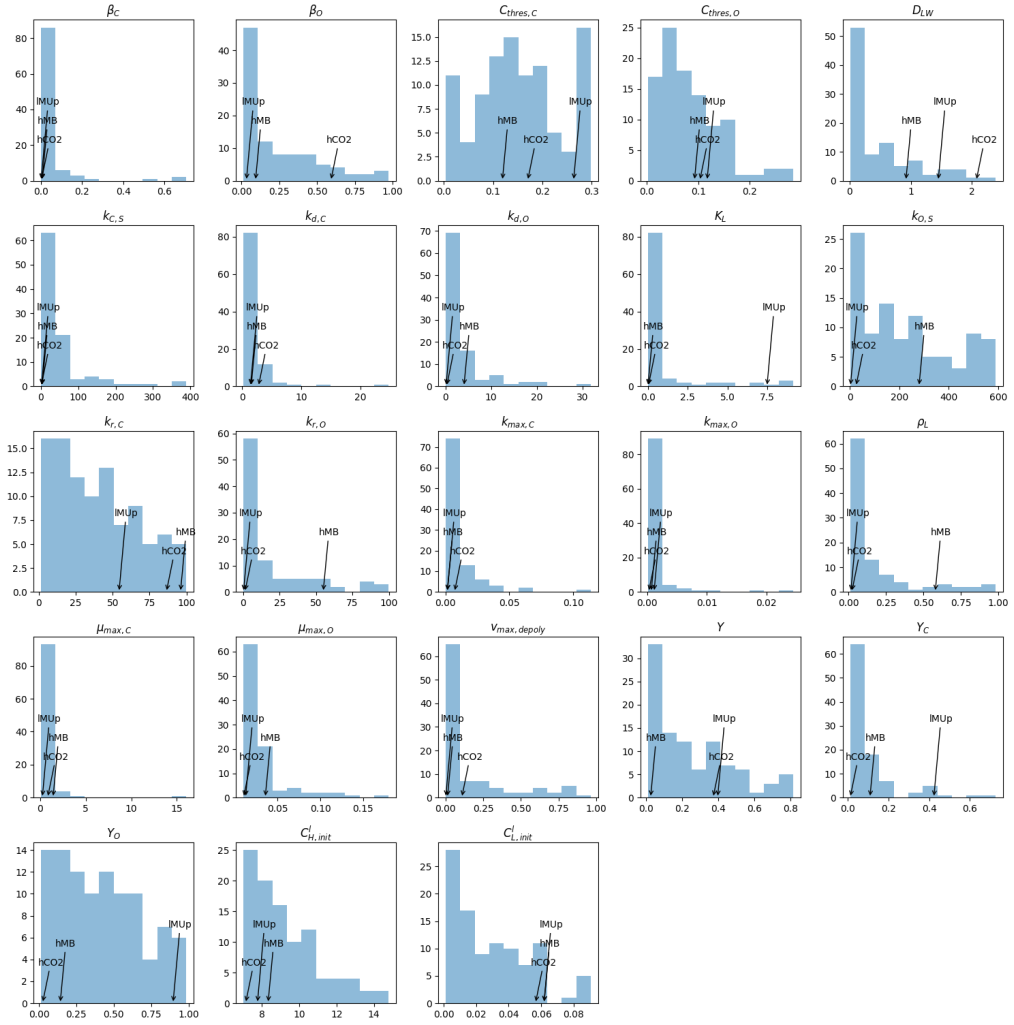

Figure B.2: Histogram of the TraiRhizo input parameters. The parameters pointed by the numbered arrows correspond to the parameters of the three selected sets, *highCO2*, *highMB*, *lowMUptake*, respectively called *hCO2*, *hMB*, *lMUp*.

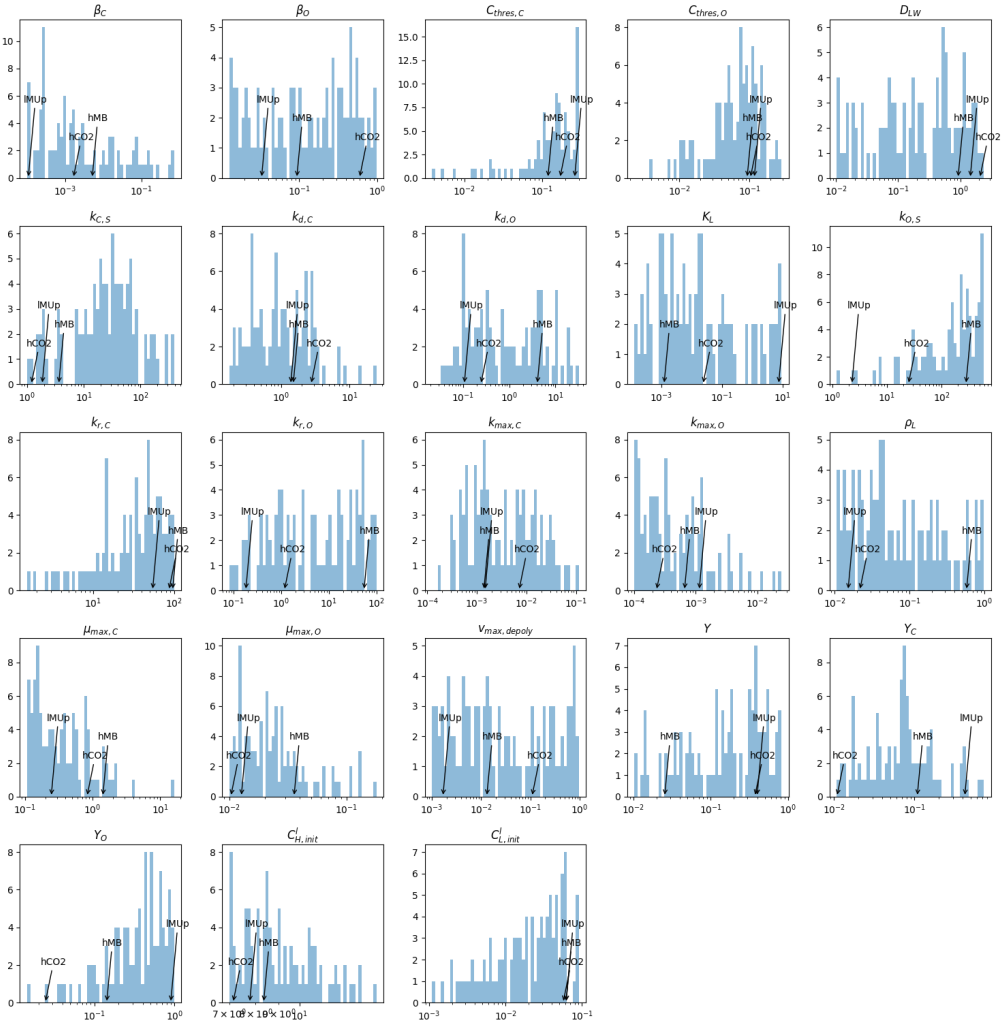

Figure B.3: Logarithmic histogram of the TraiRhizo input parameters. he parameters pointed by the numbered arrows correspond to the parameters of the three selected sets, *highCO2*, *highMB*, *lowMUptake*, respectively called *hCO2*, *hMB*, *lMUp*.

- S_{growth}, $mol\ C\ cm^{-3}\ d^{-1}$: growth rate
- S_{deact}, $mol\ C\ cm^{-3}\ d^{-1}$: deactivation rate of active microbes
- S_{react}, $mol\ C\ cm^{-3}\ d^{-1}$: reactivation rate of dormant microbes
- $dCO2dt$, $mol\ C\ cm^{-3}\ d^{-1}$: production rate of CO2
- $dMBdt$, $mol\ C\ cm^{-3}\ d^{-1}$: total absolute amount of change in the mass of microbial biomass C per unit of time

Fig.B.4 give the ratio between the related intermediary variables for all the parameter sets with the selected sets being colored. Fig. B.5 shows the same data but only for the selected sets. Subgraphics d to i use a logarithmic scale on the y-axis. As we can observe, *highCO2* led to a higher relative advantage of the oligotroph compared with the copiotroph regarding their fitness (decay-to-growth rate ratio). This was driven by the higher copiotroph decay-to-growth rate ratio. This was partly compensated by the lower ratio $\frac{S_{growthC}+S_{decayC}}{S_{deactC}+S_{reactC}}$ indicating that the copiotroph dynamic was more driven by (de)activation than by growth and decay. Moreover, we can note a higher CO_2 emission rate per unit of transformed microbial C.
highMB had lower ϕ values for both copiotrophs and oligotrophs, indicating that lower C_L^l values was necessary for an activation of the microbial community. This led in part to the lower $\frac{S_{deact}}{S_{react}}$ for both microbial group, causing a quicker reactivation compared with the deactivation. *highMB* also led to relatively low decay-to-growth ratio when compared with the other two sets. Finally, for lower C_L^l values, *highMB* had the highest relative importance of (de)activation on the copiotroph dynamic, when compared with the other two sets. *lowMUptake* offered the highest copiotroph fitness and the lowest oligotroph-to-copiotroph fitness ratio, giving a relative advantage to the copiotrophs. However, this set had the highest ϕ and $\frac{S_{deact}}{S_{react}}$ values, leading to a stronger deactivation of the microbes. For this set, we have a higher importance of the growth and decay over the (de)activation when comparing with the other two sets.

B.10 Complementary results

B.10-1 Model runtime

The model was implemented on the Institute of Bio- and Geosciences (IBG-3) computer cluster, Forschungszentrum Jülich. Each simulation was run on one node (shared memory) and 32 cores (Mainboard Supermicro H12DSU-iN), using all 32 cores for the simulation of the 1D and 3D soil domains (respectively the micro- and macroscale) and one core for the plant domain. The run-time of the simulation lasted between 9 h (*baseline* with *highSolutes*) and 13 h (*lateDry* with *highCO2*). The time step of the fixed point iteration remained at 20 mn for the baseline scenarios, went several times down to 7 mn for the *earlyDry* and

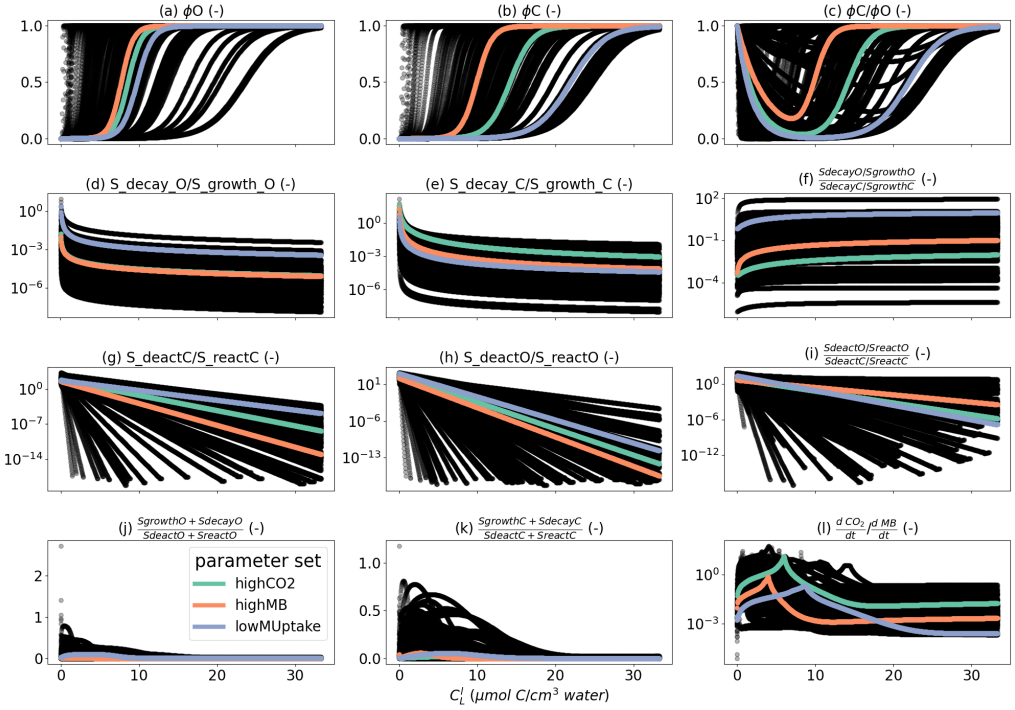

Figure B.4: Distribution of specific microbial-related reaction rate for a range of C_L^l for all 99 parameter sets. The coloured values correspond to the three selected sets: *highCO2* (green line), *highMB* (orange line) and *lowMUptake* (purple line). Graphics d to i use a logarithmic scale for the y-axis.

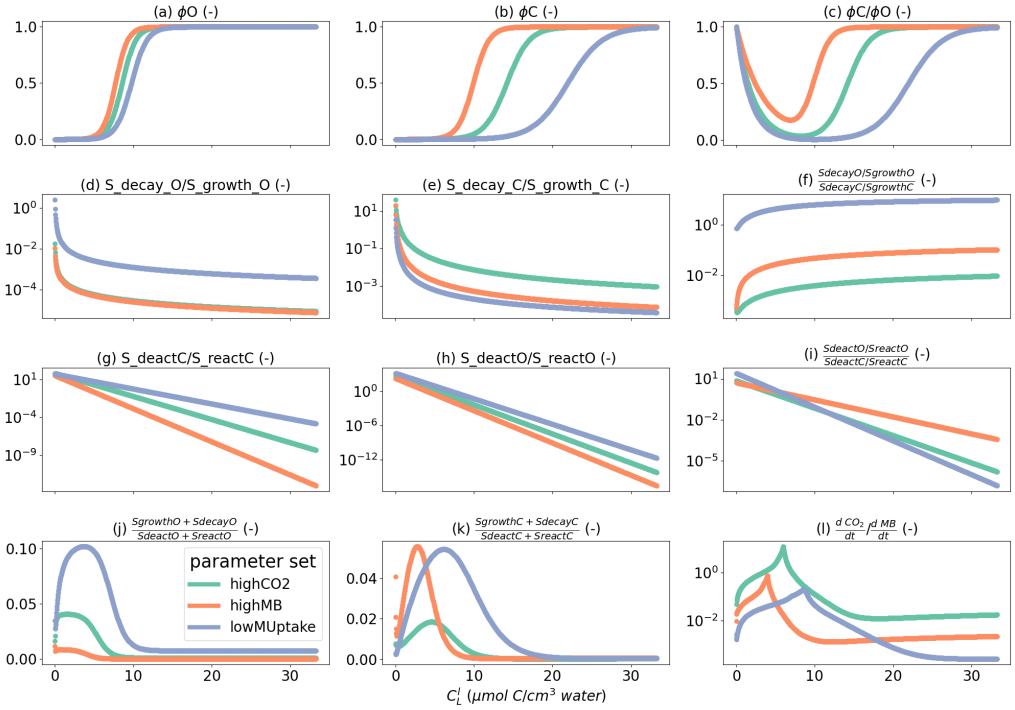

Figure B.5: Distribution of specific microbial-related reaction rate for a range of C_L^l for the selected parameter sets. The coloured values correspond to the three selected sets: *highCO2* (green line), *highMB* (orange line) and *lowMUptake* (purple line). Graphics d to i use a logarithmic scale for the y-axis.

lateDry scenarios. The computation of the water flows and content was the main bottleneck for the convergence of the iteration loop. For *baseline*, respectively 17%, 10%, and 27% of the runtime was spent solving the 3D soil domain, 1D soil domain, and plant models. For *earlyDry*, on average, 36%, 9%, and 14% of the runtime was spent solving the 3D soil domain, 1D soil domains, and plant models. For *lateDry*, on average, 38%, 11%, and 15% of the runtime is spent solving the 3D soil domain, 1D soil domain, and plant model. In total, between 54% and 64% of the runtime was dedicated to solving the models.

B.10-2 Normalised root length density

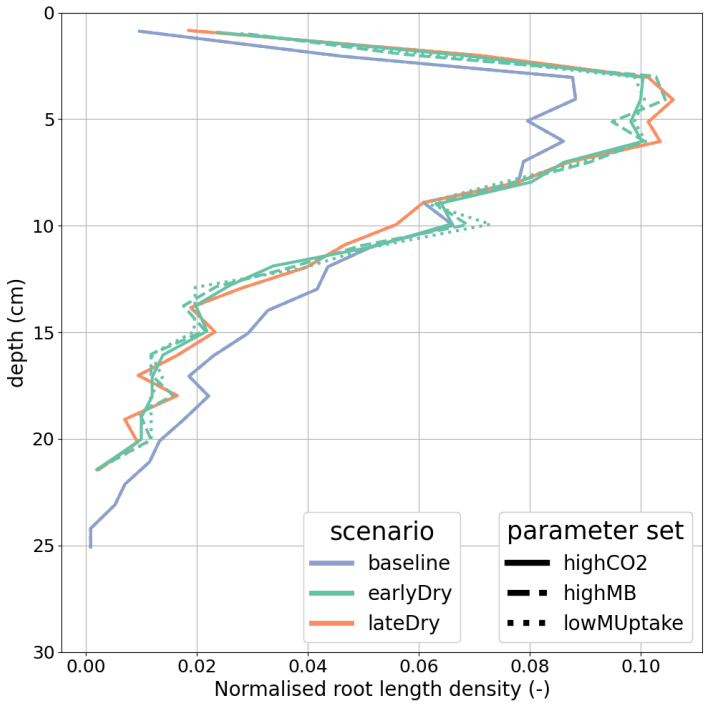

Figure B.6: Normalised root length density at the end of the simulation. Line colours indicate the weather scenarios: baseline (blue) against an early (green) and late (red) dry spell. Line types represent different biokinetic parameter sets.

B.11 Radial carbon concentration profiles

To evaluate how C_L^l is linked with the development and activation of the most important microbial pool (copiotrophs), Fig. B.7 presents the radial concentration profile of the C_C and C_C^a:C_C ratio at the end of the simulations. We observed a very steep gradient of C_C according to the distance from the root surface for *highMB* and *highCO2*. Indeed, the microbes developed around the C source. As

they were not motile, they remained on this segment even once the root segment had become older and its C releases and water uptake decreased. For *lowMUptake*, the C_C gradient (like the C_l^l gradient, see Fig. 3-11) was smoother than the other two parameter sets for all weather scenarios. Therefore, even though C_C directly at the root-soil interface is higher with *highCO2* than with *lowMUptake*, we observed similar C_C at the bulk soil and perirhizal$_{trunc}$ scales (Figs. 3-7(e) and 3-8(d)).

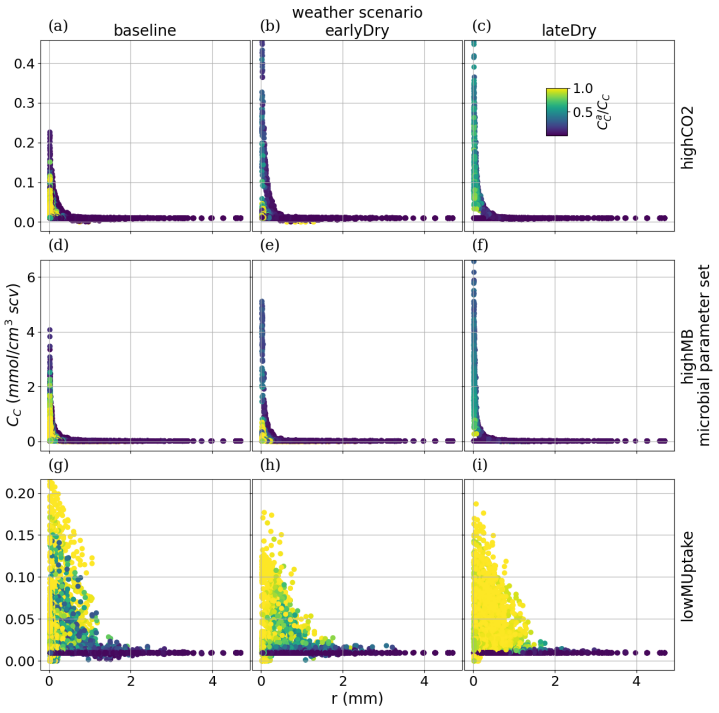

Figure B.7: Radial concentration profile of copiotroph carbon at the end of the simulation for each plant perirhizal zone. r (mm) corresponds to the distance to the root surface. The colour gives the ratio of active-to-total oligotroph biomass. Each column corresponds to a specific weather scenario and each row corresponds to a specific biokinetic parameterisation. We have a different y-axis for each row.

Appendix C: Mechanistic representation of plant branching

C.1 Glossary

- Apical dominance: the process by which the shoot tip inhibits auxiliary bud outgrowth. (Barbier et al., 2019, Beveridge et al., 2023)
- Branch: An arbitrary unit that is larger than a bud. (Barbier et al., 2019). It is defined here as a lateral that has passed the bud specialisation phase and cannot go into dormancy because of hormonal signalling related to apical dominance.
- Branch elongation\sustained growth: growth of the branch, quicker than the bud swelling.
- Branching gap: branching phenotype where at least one shorter lateral is above and below longer laterals.
- Bud: an embryonic shoot in the axil of a leaf. (Barbier et al., 2019)
- Bud dormancy: Quiescent condition with reduced metabolism. Although not represented in this study, may be followed by bud release. (Barbier et al., 2019)
- Bud growth: slow growth phase between bud release and sustained growth, sometimes termed post-activation or subsequent growth (Beveridge et al., 2023).
- Bud specialisation\sustained growth onset: Switch from bud to branch, start of the sustained branch growth.

- Bud swelling: Slow growth subsequent to the bud activation. (Barbier et al., 2019)
- Bud release: switch from dormant to active/growing bud, start of the bud swelling phase. Sometimes called bud activation (Barbier et al., 2019, Beveridge et al., 2023).
- Deactivation: In the context of this study, released bud becoming dormant
- Decapitation: Experimental procedure whereby the shoot tip (shoot meristem and connected immature leaf) is removed to promote the growth of buds below. (Barbier et al., 2019)
- Smooth branching pattern: in the context of this study, shoot phenotype with no significant branching gap along the main shoot.
- Specialisation: In the context of this study, the transition from bud growth to sustained (branch) growth
- Sustained growth: growth of the branch, no longer clearly subject to (hormonal) control by apical dominance, but may be affected by growth resource scarcity. (Beveridge et al., 2023).

Figure C.1 presents the terms used to define the parts of a pea plant shoot. Notably, pea plant stems are made of a series of nodes linked by internodes. Each node is made of a leaf and of a bud. the two small leaves at the base of the plant are called scales leaves. Nodes were numbered acropetally from the first scale leaf as node 1.

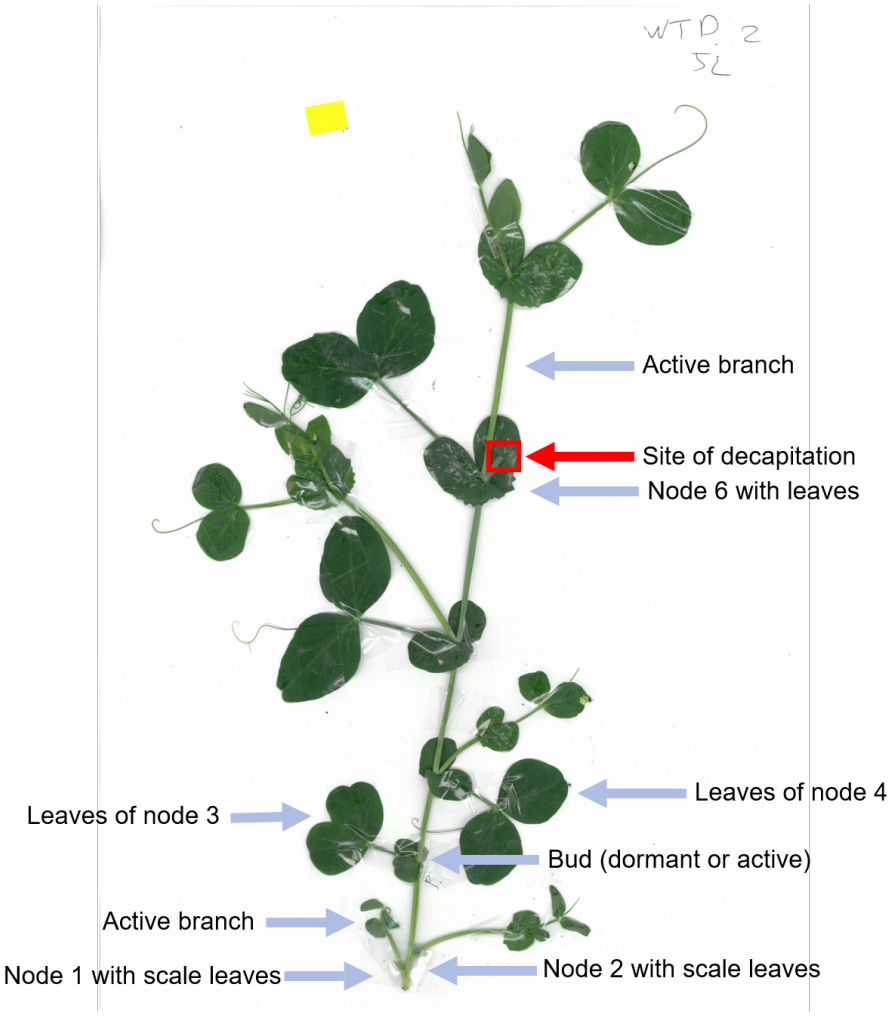

Figure C.1: Conceptual structure of a pea plant for the decapitated wild type (*WTD*) phenotype at the end of the experiment.

C.2 Complementary results

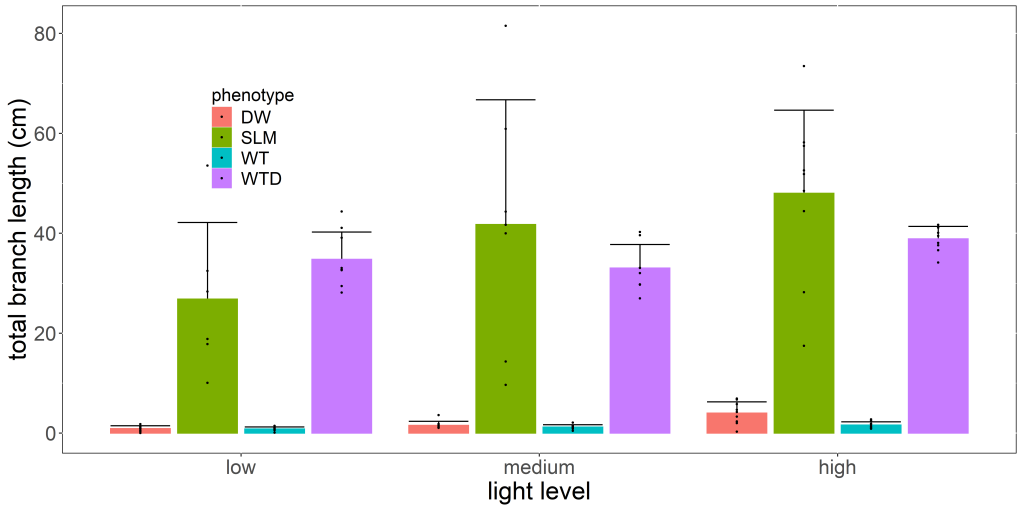

Figure C.2: Total branching length per plant at the end of the experiment for each light level and plant phenotype. Represented pea phenotype: wild-type (*WT*), decapitated wild-type (*WTD*), dwarf mutant (*DW*), strigolactone mutant (*SLM*).

Table C.1: Characteristics of the groups taken into account for the statistical analysis. The first two columns give the categories of phenotypes and light levels. The third and fifth columns give the mean and variance of the total branch length per plant. Column four gives the output of the Shapiro normality test–non-significant (ns) result indicates a data distribution similar to a normal distribution. The sixth column gives the number of replicates for each group. Represented pea phenotype: wild-type (WT), decapitated wild-type (WTD), dwarf mutant (DW), strigolactone mutant (SLM).

phenotype	light level	mean total branch length per plant (cm)		Shapiro test[a] (data)		variance		reps[b]		Shapiro test[a] (linear regression residuals)
WT	high	1.6	1.2	ns	ns	0.4	0.3	9	27	ns
	medium	1.2		ns		0.2		9		
	low	0.8		ns		0.1		9		
WTD	high	38.9	35.7	ns	ns	5.6	23	9	26	ns
	medium	33.0		ns		19.4		8		
	low	34.8		ns		26.6		9		
DW	high	4.0	2.1	ns	ns	4.5	3.6	9	27	ns
	medium	1.5		***		0.2		9		
	low	0.9		ns		0.3		9		
SLM	high	48.0	40.2	ns	ns	246.3	398.7	9	**22**	ns
	medium	41.8		ns		534.5		**7**		
	low	26.8		ns		195.8		**6**		

[a] The default assumption is that the group has a normal distribution. For $p < 0.05$, the assumption is rejected (text in red). The test was done on square-root transformed data.

[b] The red text indicates groups with size $\leq$ reps_max $\times$ 0.85. These groups are judged to be strongly smaller than the others, increasing the risks of Type I error when evaluating the distribution difference between two groups.

C.3 Example of experimental raw data

Figs. C.3-C.6 are examples of scans obtained for each phenotype at the end of the experiments.

Figure C.3: Output scan for a wild-type (WT) pea plant phenotype.

Figure C.4: Output scan for a decapitated wild-type (WTD) pea plant phenotype.

Figure C.5: Output scan for a dwarf (DW) pea plant phenotype.

Figure C.6: Output scan for a strigolactone mutant (SLM) pea plant phenotype.